



# **Metal-Catalyzed Radical Polymerization up to High Pressure**

**Dissertation**

zur Erlangung des mathematisch-naturwissenschaftlichen Doktorgrades  
"Doctor rerum naturalium"  
der Georg-August-Universität Göttingen

im Promotionsprogramm CaSuS  
der Georg-August University School of Science (GAUSS)

vorgelegt von  
**Hendrik Schröder**  
aus Oldenburg

Göttingen, 2015

## **Betreuungsausschuss**

Prof. Dr. Michael Buback	Institut für Physikalische Chemie Georg-August-Universität Göttingen
Prof. Dr. Philipp Vana, MBA	Institut für Physikalische Chemie Georg-August-Universität Göttingen
Dr. Serhiy Demeshko	Institut für Anorganische Chemie Georg-August-Universität Göttingen

## **Mitglieder der Prüfungskommission**

### **Referent**

Prof. Dr. Michael Buback	Institut für Physikalische Chemie Georg-August-Universität Göttingen
--------------------------	---

### **Korreferent**

Prof. Dr. Philipp Vana, MBA	Institut für Physikalische Chemie Georg-August-Universität Göttingen
-----------------------------	---

### **Weitere Mitglieder der Prüfungskommission**

Prof. Dr. Karlheinz Hoyerermann	Institut für Physikalische Chemie Georg-August-Universität Göttingen
Prof. Dr. Martin Suhm	Institut für Physikalische Chemie Georg-August-Universität Göttingen
PD Dr. Thomas Zeuch	Institut für Physikalische Chemie Georg-August-Universität Göttingen
Dr. Florian Ehlers	Institut für Physikalische Chemie Georg-August-Universität Göttingen

**Tag der mündlichen Prüfung:** 02. September 2015

## Table of Contents

<b>1</b>	<b>Summary</b>	<b>1</b>
<b>2</b>	<b>Introduction</b>	<b>5</b>
<b>3</b>	<b>Theoretical Background</b>	<b>9</b>
3.1	Mechanism of ATRP	9
3.2	Kinetics of ATRP	14
3.2.1	ATRP Rate, Control, and Chain-End Functionality	14
3.2.2	The Persistent Radical Effect	18
3.2.3	Kinetics under High Pressure	20
3.3	Experimental Techniques	21
<b>4</b>	<b>Kinetics of Fe-Mediated ATRP</b>	<b>29</b>
4.1	Iron-Halide-Based Catalysts	30
4.1.1	Speciation Analysis	30
4.1.2	Measurement of ATRP Rate Coefficients	39
4.1.3	Analysis of ATRP Rate Coefficients	44
4.2	Iron Halide Catalysts with Additional Ligands	50
4.2.1	<i>N</i> -Heterocyclic Carbenes	50
4.2.2	TPMA and TPMA*	51
4.2.3	Triarylphosphines	53

<b>5</b>	<b>The Interface of ATRP and OMRP</b>	<b>65</b>
5.1	RDRP Mediated by Amine- <i>bis</i> (phenolate) Iron Complexes	66
5.2	Analysis of Rate Coefficients via SP-PLP-EPR	80
5.2.1	ATRP Deactivation	80
5.2.2	Fe-Mediated Radical Termination	90
<b>6</b>	<b>Kinetics of RDRP up to High Pressure</b>	<b>105</b>
6.1	Preface	105
6.2	Modeling Cu-Mediated ATRP of Butyl Acrylate	107
6.3	Iron-Halide-Mediated ATRP up to High Pressure	118
6.3.1	Monomer-Free Model Systems	118
6.3.2	ATRP of MMA up to High Pressure	123
6.4	Kinetics with Amine- <i>bis</i> (phenolate) Iron Complexes	134
6.4.1	ATRP up to High Pressure	134
6.4.2	OMRP up to High Pressure	144
<b>7</b>	<b>Closing Remarks</b>	<b>147</b>
<b>8</b>	<b>Experimental</b>	<b>149</b>
8.1	Chemicals	149
8.2	Spectroscopic Measurements	151
8.3	Synthesis of Poly(MMA)-Br via ICAR ATRP	153
8.4	High-Pressure Equipment	154
	<b>Appendix</b>	<b>157</b>
A	Additional Figures, Tables, and Schemes	157
B	SP-PLP-EPR Measurement of Fe-CRT	175
C	Software for Modeling Procedures	181
D	Abbreviations	188
	<b>Bibliography</b>	<b>193</b>
	<b>Acknowledgements</b>	<b>209</b>
	<b>About the Author</b>	<b>211</b>

# 1

## Summary

The mechanism and kinetics of metal-catalyzed radical polymerization were investigated by spectroscopic means. A particular focus was set on Fe-mediated atom-transfer radical polymerization (ATRP) as there is a growing interest for an economic alternative to the extensively used Cu-mediated ATRP.

Experiments were started with an iron bromide-based catalyst, which simply operates without any external ligands. FT-nearIR and Mössbauer spectroscopy were used to determine the structures of  $[\text{Fe}^{\text{II}}\text{Br}_u(\text{Solv})_v]$  and  $[\text{Fe}^{\text{III}}\text{Br}_w(\text{Solv})_x]$  complexes in a variety of solvents. It was found that the tetrahedral species  $[\text{Fe}^{\text{II}}\text{Br}_3(\text{Solv})]^-$  and  $[\text{Fe}^{\text{III}}\text{Br}_4]^-$  essentially govern the activation–deactivation equilibrium of ATRP. The structure of these complexes is correlated with the measured ATRP activation rate coefficients,  $k_{\text{act}}$ , and with the equilibrium constants,  $K_{\text{ATRP}}$ , for monomer-free model systems. In weakly polar solvents such as esters, ketones, and substituted benzenes,  $k_{\text{act}}$  and also  $K_{\text{ATRP}}$  are up to two orders of magnitude higher than with strongly polar solvents, such as *N*-methylpyrrolidin-2-one (NMP), acetonitrile, and dimethylformamide, where the  $[\text{Fe}^{\text{II}}\text{Br}_3(\text{Solv})]^-$  complex is more stabilized.

Since further tuning of catalyst activity is important to access a wide range of monomers for ATRP, several types of Fe–ligand systems were tested for a potential enhancement of  $K_{\text{ATRP}}$ . The NIR spectroscopic analysis indicated that tetrahedral  $[\text{Fe}^{\text{II}}\text{Br}_u\text{L}_v]_{u+v=4}$  complexes also play a

role with external ligands, L, such as *N*-heterocyclic carbenes and phosphines. However, these compounds do not significantly improve  $K_{\text{ATRP}}$  compared with solvent molecules being the ligands. Nevertheless, the studies were helpful to clarify the role of phosphines in ATRP. The highly Lewis basic tris(2,4,6-trimethoxy-phenyl)phosphine (TTMPP) may coordinate to  $\text{Fe}^{\text{II}}$ , but primarily acts as a reducing agent for  $[\text{Fe}^{\text{III}}\text{Br}_4]^-$ , thus transforming TTMPP to TTMPP- $\text{Br}^+$ . Triphenylphosphine (TPP) is a less effective reducing agent.

An enhanced  $K_{\text{ATRP}}$  was found for amine-*bis*(phenolate) iron complexes. A combined Mössbauer, EPR, NMR, and online VIS/NIR spectroscopic analysis was carried out to determine the relevant Fe species. An interplay between ATRP and organometallic-mediated radical polymerization (OMRP), which is based on the reaction of propagating radicals with  $\text{Fe}^{\text{II}}$ , may occur depending on the monomer under investigation. Styrene polymerization operates via ATRP, whereas an interplay between ATRP and OMRP occurs for MMA polymerization.

The kinetics of ATRP and OMRP were quantitatively measured by highly time-resolved EPR spectroscopy in conjunction with pulsed-laser application for radical production, i.e., the so-called SP-PLP-EPR method. ATRP deactivation of methacrylate-type radicals by an amine-*bis*(phenolate)iron catalyst was monitored without interference by organometallic reactions. Toward higher temperatures, the ratio of deactivation to propagation rate increases, which is beneficial for ATRP control.

SP-PLP-EPR was also applied to quantify the catalytic termination (CRT) of two propagating radicals by  $\text{Fe}^{\text{II}}$  via an organometallic intermediate. In case of the  $[\text{Fe}^{\text{II}}\text{Br}_3(\text{Solv})]^-$  catalyst, the organometallic reaction plays a role for acrylate rather than for methacrylate polymerization, where CRT is by about three orders of magnitude slower. As a consequence, ATRP of acrylates should be carried out with low levels of the  $\text{Fe}^{\text{II}}$  catalyst to avoid CRT and thus improve the living character of ATRP.

The investigations into metal-catalyzed radical polymerization were expanded up to pressures of 6000 bar. Applying pressure results in a redistribution of iron bromides in favor of the charged species  $[\text{FeBr}_4]^{2-}$  and  $[\text{Fe}(\text{Solv})_6]^{2+}$ , which is particularly pronounced in polar solvents such as NMP or acetonitrile. As a consequence, the reaction volume,

$\Delta_r V(K_{\text{ATRP}})$ , is positive for  $[\text{Fe}^{\text{II}}\text{X}_i(\text{Solv})_v]$  catalysts (up to  $18 \text{ cm}^3 \text{ mol}^{-1}$ ). The studies demonstrated the advantage of the well-defined amine-*bis*(phenolate)iron system:  $\Delta_r V(K_{\text{ATRP}})$  is negative,  $(-17 \pm 2) \text{ cm}^3 \text{ mol}^{-1}$ , which is associated with a favorable shift of the ATRP equilibrium toward the side of the activated radical. Along with the increase in propagation rate, ATRP rate is thus enhanced by more than two orders of magnitude between 1 and 6000 bar.

ATRP also benefits from an improved living character under high pressure, which is due to the lowering of diffusion-controlled termination. This facilitates the synthesis of polystyrenes and polyacrylates with molar masses above  $100,000 \text{ g mol}^{-1}$  and dispersities below 1.29 under either Fe or Cu catalysis. These advantages were not compromised by an increase in the rate of intramolecular transfer, i.e., the backbiting reaction during acrylate polymerization under high pressure, which was deduced from modeling the ATRP experiments.

This thesis has improved the understanding of the mechanism and kinetics of Fe-mediated ATRP, in particular, of the potential interplay with OMRP. Moreover, the studies provide guidance for the selection of suitable reaction conditions that yield predominantly ATRP-mediated polymerizations with improved control.





# 2

## Introduction

In 2013, the worldwide polymer production exceeded ~300 million tons.<sup>1</sup> Due to their low dead weight and high resistance to corrosion, polymeric materials are used in most aspects of life, with growing demand in wind power plants, optical data chips, and the aerospace industry.<sup>2</sup> The majority of industrially produced polymers is prepared by radical polymerization, especially mass plastics such as polyethylene (PE) and polystyrene (PS).

Conventional radical polymerization, however, yields polymer without chain-end functionality and with broad molar-mass distribution, which limits the ability to control and achieve the formation of complex polymer architectures and topologies. Because of the growing interest in polymeric materials with improved and precisely tailored properties, controlled, i.e., so-called reversible deactivation radical polymerizations (RDRPs) caught the attention of scientists.<sup>3,4</sup> These methods are based on an activation–deactivation equilibrium, thereby allowing for the synthesis of polymeric materials with precisely tailored topology, chain length, functionality and with low dispersity.<sup>5–7</sup> Thus, RDRP provides access to next generation specialty polymer additives and materials. The most prominent RDRP techniques are atom-transfer radical polymerization (ATRP),<sup>6–13</sup> reversible addition-fragmentation chain-transfer (RAFT) polymerization,<sup>14–18</sup> organometallic-mediated radical polymerization (OMRP),<sup>4,19–22</sup> nitroxide-mediated polymerization,<sup>23</sup> and stable-radical-

mediated polymerization (SRMP).<sup>24</sup>

Industrially licensed and projected applications of RDRP include drug delivery systems, photonics, self-healing materials, coatings, adhesives, surfactants, dispersants, lubricants, gels, thermoplastic elastomers, sealants, organic-inorganic hybrids, nanocomposites, and electronics.<sup>5,7,10,25-29</sup> Recently, there has been considerable progress in the separation, recycling, and reduction of the amount of metal catalysts, which should foster the industrial application of RDRP.

The primary focus of the present work revolves around the mechanism and kinetics of ATRP – a technique developed by Matyjaszewski<sup>30</sup> and Sawamoto<sup>31</sup> in 1995. Mechanistically, ATRP resembles the transition-metal-catalyzed atom-transfer radical addition (ATRA) or the Kharasch-addition.<sup>32-34</sup> During ATRP, an organic radical is "activated" via halogen transfer from an organohalide to a transition-metal catalyst. Radical species are "deactivated" by the reverse transfer of the halogen atom.

Cu-mediated ATRP has been most extensively studied.<sup>35-44</sup> A variety of ligands may be used for Cu-based ATRP, which allows for the effective tuning of catalytic activity and adjustment for use with a wide range of monomers.<sup>8,13,35,45</sup> Kinetic studies have provided guidelines for the suitable selection of Cu catalyst systems. Fe-mediated ATRP appears to be an attractive alternative due to the low toxicity and broad availability of iron.<sup>4,46-51</sup> However, Fe-mediated ATRP is so far reported far less frequently.

To further advance the understanding and utility of Fe-based ATRP, detailed kinetic insights into ligated iron systems are a matter of priority and are subject of the present work. Iron catalysts for ATRP are mostly based on iron halides,<sup>4,6,47,48</sup> with phosphines,<sup>4,52-65</sup> amines,<sup>66-71</sup> and imines<sup>72-77</sup> being the ligands for the formation of Fe-based complexes.<sup>59,78</sup> Iron(II)-halide-mediated ATRP may also be carried out either in polar solvents or in the presence of ammonium salts even without the addition of specific ligands.<sup>79-84</sup>

The reversible deactivation of radicals in Fe-based ATRP is mediated by an Fe<sup>III</sup> catalyst. The reaction of Fe<sup>II</sup> with radicals is not contained in the typical ATRP scheme but is relevant in Fe-mediated OMRP.<sup>4,19-22,85</sup> Closer experimental and computational scrutiny demonstrated that both ATRP and OMRP, or organometallic reactions in general, may also operate simultaneously.<sup>4,19,21,73-76,86-89</sup> For instance, an interplay between

ATRP and catalytic chain transfer (CCT) was reported for a series of  $\alpha$ -diimine iron complexes,  $R^{1,R2}[NN]FeCl_2$ .<sup>73-77,90</sup> The nature of the ligand was found to determine the dominant polymerization mechanism, with electron-donating groups favoring ATRP and yielding halogen-terminated polymers with well-controlled molar masses. Conversely, ligands with electron-withdrawing groups were found to favor CCT, with the instability of the organometallic species resulting in  $\beta$ -hydrogen elimination to yield low molar mass, olefin-terminated polymers.

Amine-*bis*(phenolate)iron complexes,  $[O_2NN']FeCl$ , facilitate efficient RDRP of substituted styrenes and methyl methacrylate (MMA) with dispersities as low as 1.07.<sup>86,87</sup> The kinetic insight obtained from these reactions also suggests a dual mechanistic control, involving both ATRP and OMRP, which is in agreement with computational studies.<sup>91</sup> However, the expected Fe species for either of the two mechanisms have not yet been directly evidenced in the polymerization systems, e.g., via spectroscopic techniques. The relative importance of either pathway for different types of monomers has also not been spectroscopically addressed.

In this study, spectroscopic techniques will be exploited to examine the mechanism and kinetics of Fe-based RDRP. EPR spectroscopy is particularly useful for investigations into the kinetics of radical polymerization, as the relevant radical species may be quantitatively monitored online.<sup>92-94</sup> Highly time-resolved EPR spectroscopy in conjunction with laser pulsing has emerged as the state-of-the-art method for kinetic measurements, since even very fast reaction steps such as termination or deactivation may be accurately monitored.<sup>92,93</sup> In single-pulse-pulsed laser polymerization (SP-PLP), a high concentration of primary radicals is almost instantaneously produced by the laser-induced decomposition of a photoinitiator. Further helpful techniques to monitor the Fe species are UV/VIS/IR, <sup>57</sup>Fe Mössbauer, and EPR spectroscopy.

The kinetic studies will be expanded up to high pressure to gain further mechanistic insights into Fe-mediated ATRP. Applying high pressure has been reported to yield beneficial effects on both monomer conversion and dispersity in RAFT polymerization of styrene and methyl methacrylate (MMA).<sup>95,96</sup> Specifically, the observed advantages include enhanced rates of propagation<sup>97,98</sup> and diminished rates of termination, with the latter effect being associated with an increase in

viscosity toward high pressure.<sup>99-101</sup> Moreover, investigations into Cu-mediated systems revealed that the activation–deactivation equilibrium constant of ATRP,  $K_{\text{ATRP}}$ , and thus ATRP rate are significantly enhanced with increasing pressure.<sup>102-104</sup> The rate enhancement was not counterbalanced by an increase in dispersity.<sup>102,103,105</sup> The improved living character in high-pressure ATRP has been used for the synthesis of very high-molar-mass polymethacrylates and polystyrene ( $M_n \geq 10^6 \text{ g mol}^{-1}$ ).<sup>106-110</sup>

This thesis presents an in-depth investigation of the mechanism and kinetics of RDRP, focusing on Fe-mediated ATRP. The relevant Fe species will be examined by  $^{57}\text{Fe}$  Mössbauer<sup>29-31</sup> as well as FT-IR and UV/VIS spectroscopy for a variety of Fe–ligand combinations. In addition, this work provides the first measurements of  $K_{\text{ATRP}}$  in an extended pressure and temperature range, as well as of the associated rate coefficients of activation and deactivation for selected Fe–ligand systems. Wherever possible, the experiments are accompanied by simulations with the program package PREDICI.

The studies first address an iron bromide catalyst without any external ligands. The effect of adding external ligands such as phosphines or carbenes and of more robust amine–*bis*(phenolate)iron catalysts on rate and control of ATRP is then quantitatively measured. High pressure up to 6000 bar is applied to determine reaction volumes for  $K_{\text{ATRP}}$  and to study the effect of pressure on the dispersity of the polymeric product. The consequences of intramolecular transfer reactions on ATRP rate are explored in a modeling study of measured conversion vs time profiles for butyl acrylate ATRP.

The spectroscopic techniques will also be applied to capture the potential interplay between OMRP and ATRP equilibria. Along these lines, SP–PLP–EPR is used to study the catalytic termination of two propagating radicals via an organometallic R-Fe<sup>III</sup> intermediate. The results are compared to Cu catalysis.

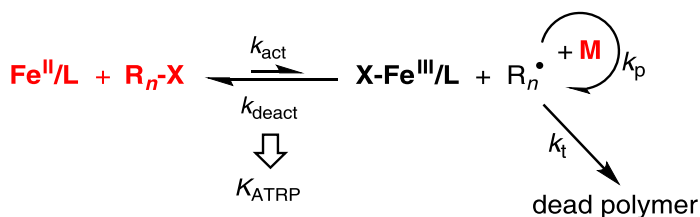
# 3

## Theoretical Background

### 3.1 Mechanism of ATRP

The kinetics of ATRP is superimposed on a conventional radical polymerization scheme. In Fe-catalyzed ATRP, radical propagation occurs concurrently with reversible deactivation of radicals mediated by Fe<sup>III</sup> and activation of alkyl halides by Fe<sup>II</sup> (Scheme 3.1). The activation rate coefficient,  $k_{\text{act}}$ , quantifies the rate of formation of the transient radical, R<sup>•</sup>, whereas the deactivation rate coefficient,  $k_{\text{deact}}$ , refers to the rate of formation of the alkyl halide, R<sub>n</sub>-X. The ratio of these two rate coefficients is defined as the equilibrium constant,  $K_{\text{ATRP}} = k_{\text{act}}/k_{\text{deact}}$ .

A "Normal ATRP" is initiated by the reaction of, e.g., an Fe<sup>II</sup> complex with an alkyl halide, R<sub>n</sub>-X, which is typically of chain length unity,  $n = 1$ . The starting materials, including the monomer, M, are marked in red. The structure of the alkyl halide initiator may resemble the structure of the monomer. However, to ensure an efficient initiation, the radicals generated from the initiator should exhibit at least the same reactivity as the radicals generated from the growing chain (i.e., generated from the monomer).<sup>10</sup> For example, methyl methacrylate (MMA) may be initiated using an *iso*-butyrate-type alkyl halide, MBriB, but even more effectively using  $\alpha$ -bromophenylacetate (EBrPA), see Figure 3.1. The associated chloride initiators may also be used, which, however, typically results in both slower activation and deactivation rate.<sup>35</sup>



**Scheme 3.1:** Mechanism of Fe-mediated ATRP; L represents the ligand to iron,  $\text{R}_n\text{-X}$  refers to the dormant alkyl halide species,  $\text{R}_n\cdot$  to the propagating radical, M to monomer,  $k_t$  to the termination rate coefficient and  $k_p$  to the propagation rate coefficient.

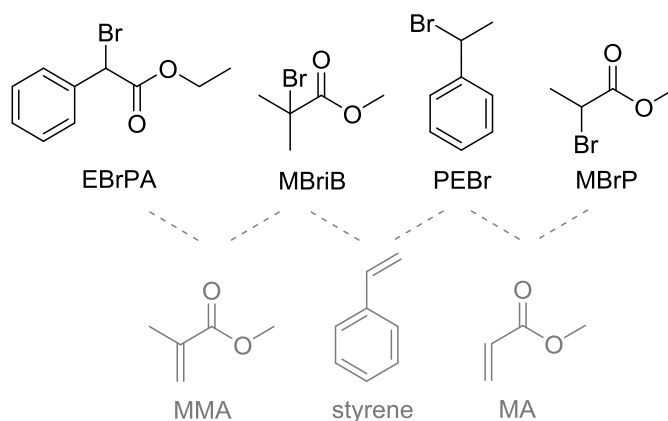


**Figure 3.1:** Common alkyl halide initiators (top) suitable for ATRP of the indicated monomers (bottom). EBrPA refers to ethyl  $\alpha$ -bromophenylacetate, MBriB to methyl 2-bromo-*iso*-butyrate, PEBr to 1-phenylethyl-bromide, and MBrP to methyl 2-bromopropionate.

Monomers with suitable substituents next to the double bond stabilize the generated radicals, which results in higher values of  $K_{\text{ATRP}}$ . Furthermore, these substituents activate the halogen-alkyl-bond of the dormant species. Substituted styrene derivatives<sup>111</sup> and methacrylates,<sup>112,113</sup> as well as acrylates,<sup>114</sup> (meth)acrylamides,<sup>115,116</sup> acrylonitriles,<sup>117</sup> and vinylpyridines<sup>118</sup> have been studied for (Cu-mediated) ATRP.

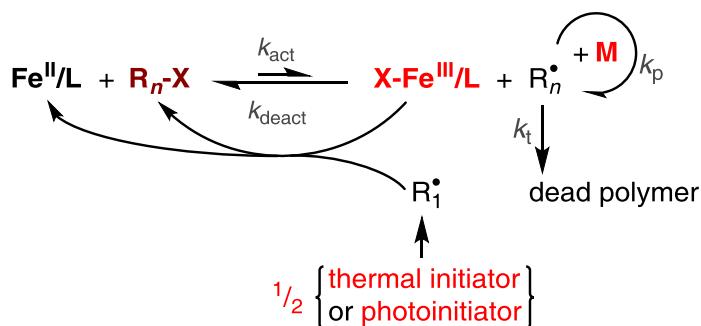
In ATRP, as with all radical polymerizations, radical–radical termination cannot be avoided (cf. Scheme 3.1). By properly selecting the reaction conditions, the amount of terminated chains will be lower than the amount of initially added alkyl halide. The concentration of the alkyl halide may thus not be reduced arbitrarily to preserve a high degree of chain-end functionality. Conversely, ATRP may efficiently be operated with substoichiometric amounts of the metal catalyst relative to the alkyl halide (see below). Such a procedure is also favorable from an economic point of view.

In the present work, Fe-mediated ATRP will be investigated in an extended temperature and pressure range as well as with various solvents and iron–ligand systems to explore suitable reaction conditions. In order to achieve a high degree of control and livingness, different ATRP procedures will also be tested.<sup>9,13</sup> For example, ATRP may be initiated in a reverse fashion, i.e., with the catalyst in the less air-sensitive, higher oxidation state, Fe<sup>III</sup>, which requires its reduction to start ATRP.<sup>8</sup> A few methodologies are explained in the following.

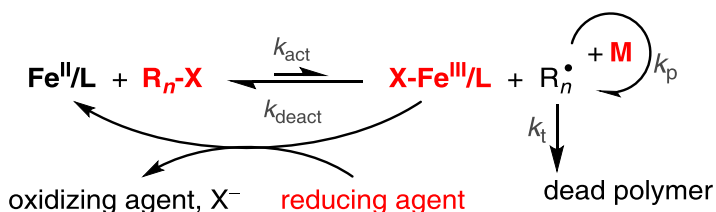
**In reverse ATRP (R-ATRP)**, the alkyl halide and the Fe<sup>II</sup>/L catalyst are produced in equal amounts *in situ* via the decomposition of an azo initiator, R<sub>1</sub>N=NR<sub>1</sub> (Scheme 3.2). The temperature stability of these azo initiators may be adjusted to provide rapid initiator decomposition at the targeted polymerization temperature and to enable an immediate initiation of the chain-growth reaction (see chapter 6.4).

Alternatively, a photoinitiator<sup>19</sup> may be used instead of a thermal one, such as in the pulsed-laser controlled experiments illustrated in chapter 5.2. The photo-induced reduction of Fe<sup>III</sup> (or Cu<sup>II</sup>) may be precisely controlled by sensible selection of the number and intensity of applied laser pulses.

**Simultaneous Reverse & Normal Initiation (SR&NI) ATRP**<sup>120</sup> combines the advantages of normal and R-ATRP: The catalyst is introduced in the higher oxidation state and reduced *in situ*. However, the majority of the chains grow from an initially added alkyl halide, analogous to Normal ATRP. Consequently, SR&NI ATRP operates with substoichiometric amounts of Fe to alkyl halide. Just like in Normal ATRP, a multifunctional chain initiator may be used as the added alkyl



**Scheme 3.2:** ATRP initiated in the reverse fashion by decomposition of either a thermal initiator or a photoinitiator. The starting materials are indicated in red. An alkyl halide initiator (brown color),  $\text{R}_1\text{-X}$ , may also be added as an initial component. The structure of the primary radicals,  $\text{R}_1^\bullet$ , depends on the type of initiator and differs from the monomer-specific radicals,  $\text{R}_r^\bullet$ .



**Scheme 3.3:** ATRP initiated in the reverse fashion by converting  $\text{X-Fe}^{\text{III}}/\text{L}$  to  $\text{Fe}^{\text{II}}/\text{L}$  and  $\text{X}^-$  using a reducing agent. The starting materials are marked in red.

halide, which allows for accessing more complex topologies such as star polymers.

**In Activators Generated by Electron Transfer (AGET) ATRP**,<sup>70,121-124</sup> reducing agents (Scheme 3.3) are used instead of thermal initiators. An actual reducing agent rules out the formation of new growing chains as a byproduct of the reduction process. As with SR&NI ATRP, the amount and type of alkyl halide initiator may be selected independently.



R-ATRP, SR&NI, and AGET ATRP are based on a rapid and single reduction of the catalyst in the higher oxidation state. The subsequent radical-radical termination results in the accumulation of the persistent radical, Fe<sup>III</sup>, (see chapter 3.2) and in the simultaneous loss of the Fe<sup>II</sup> activator species. According to *Le Chatelier's principle*, the accumulation of Fe<sup>III</sup> and the loss of Fe<sup>II</sup> and alkyl halide results in a lowering of radical concentration, [R<sub>n</sub>•], and thus in ATRP rate. It may therefore be desirable to regenerate the Fe<sup>II</sup> catalyst during ATRP in order to increase the equilibrium concentration of R<sub>n</sub>•. This may be achieved by adding thermal initiators, which decompose slowly under the selected conditions, thus progressively reducing Fe<sup>III</sup>. This method is called **Initiators for Continuous Activator Regeneration (ICAR) ATRP**.<sup>57,83,125</sup> Owing to the regeneration of Fe<sup>II</sup>, the concentration of the catalyst may be reduced to a ppm level.<sup>126</sup>

In a similar way, **Activators ReGenerated by Electron Transfer (ARGET) ATRP**<sup>125,127-130</sup> uses actual reducing agents to constantly regenerate the metal catalyst. In contrast to ARGET ATRP, the AGET methodology operates with reducing agents, which quickly reduce the catalyst in the higher oxidation state. For example, Tin(II) 2-ethylhexanoate efficiently reduces iron bromide,<sup>131</sup> whereas sulfites<sup>132</sup> such as sodium dithionite (Na<sub>2</sub>S<sub>2</sub>O<sub>4</sub>) reduce Fe<sup>III</sup>/heme catalysts (cf. Figure S1). Ascorbic acid quickly reduces Cu<sup>II</sup>/bipyridine complexes, however, more active Cu-based catalysts, as well as Fe<sup>III</sup>/heme species, and amine-*bis*(phenolate)iron(III) halide complexes are transformed slowly (Table S1 and Figure S1). In these cases, ascorbic acid may be used for ARGET ATRP procedures. The ability of different triarylphosphines to reduce iron(III) bromide will be studied in chapter 4.2.3.

Different initiation principles will be addressed throughout chapters 4–6. Normal and reverse ATRP are most suited for kinetic studies due to the absence of background initiation once the equilibrium stage is reached. On the other hand, ICAR and ARGET ATRP are attractive methods for syntheses due to the lowering of catalyst concentration and the high living character of ATRP.<sup>13,133-137</sup> The kinetics of ATRP are detailed in chapter 3.2.

## 3.2 Kinetics of ATRP

### 3.2.1 ATRP Rate, Control, and Chain-End Functionality

Equation 3.1 tells that polymerization rate in (Fe-mediated) ATRP under equilibrium conditions depends on the size of  $K_{\text{ATRP}}$  as well as on the concentrations of  $\text{Fe}^{\text{II}}/\text{L}$ ,  $\text{X-Fe}^{\text{III}}/\text{L}$ , and alkyl halide.<sup>36,111</sup>  $K_{\text{ATRP}}$  may be determined based on Equation 3.1 by measuring the polymerization rate,  $R_p$ , as well as the concentrations of the associated catalyst, alkyl halide species, and the monomer concentration (for details see chapters 4 and 6.3–6.4). Equation 3.1 applies irrespective of the ATRP procedures described in chapter 3.1. Nevertheless, there are important mechanistic features, which are characteristic of the specific ATRP methodology.

$$R_p = -\frac{d[\text{M}]}{dt} = k_p \cdot [\text{M}] \cdot [\text{R}_n^\bullet] = k_p \cdot [\text{M}] \cdot K_{\text{ATRP}} \cdot \frac{[\text{Fe}^{\text{II}}/\text{L}] \cdot [\text{R}_n\text{-X}]}{[\text{X-Fe}^{\text{III}}/\text{L}]} \quad (3.1)$$

Radical concentration and thus polymerization rate in normal, reverse, and SR&NI ATRP depend primarily on the position of the ATRP equilibrium, i.e., on  $K_{\text{ATRP}}$ . This relation is illustrated in Figure 3.2A by simulation of the associated  $\ln([\text{M}]_0/[\text{M}])$  vs time traces for different values of  $K_{\text{ATRP}}$  but identical initial concentrations of the catalyst and initiator.

A different situation is observed for ICAR ATRP, where radical concentration under equilibrium conditions primarily depends on the amount and the decomposition rate of the thermal initiator and on the termination rate coefficient (Equation 3.2).<sup>138</sup> This steady-state scenario is similar to RAFT polymerization.<sup>138</sup> Since ATRP rate is dictated by the decomposition rate of the thermal initiator, this rate becomes almost independent of the size of  $K_{\text{ATRP}}$  (Figure 3.2B). An increase in  $K_{\text{ATRP}}$  is compensated by a decrease in the equilibrium concentrations of  $\text{Fe}^{\text{II}}/\text{L}$  relative to  $\text{X-Fe}^{\text{III}}/\text{L}$ , since these concentrations conform according to the  $K_{\text{ATRP}}$  value.<sup>138</sup>

$$2k_{\text{dc}}[\text{I}_2] = 2k_t[\text{R}_n^\bullet]^2 \quad (3.2a)$$

$$[\text{R}_n^\bullet] = \sqrt{\frac{k_{\text{dc}}[\text{I}_2]}{k_t}} \quad (3.2b)$$

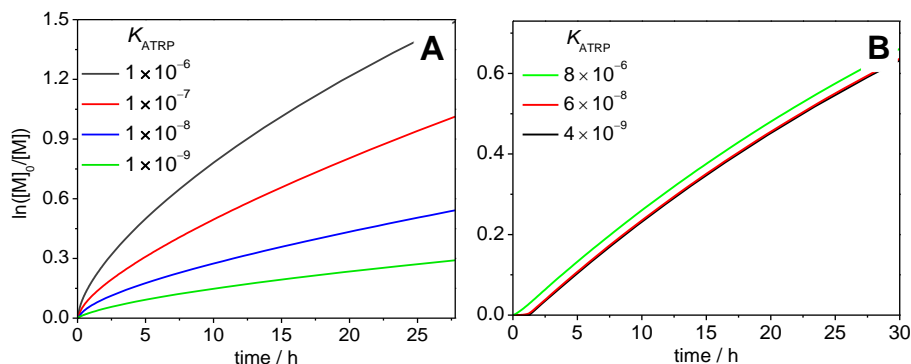


**Figure 3.2:** Simulation of  $\ln([M]_0/[M])$  vs time in (A) SR&NI ATRP at initial molar ratios of  $[M] : [R-X] : [Fe^{III}] : [R_iN=NR_i] = 250 : 1.00 : 0.50 : 0.25$ ,  $[M]_0 = 5 \text{ M}$ , with a thermal initiator decomposition rate of  $1 \times 10^{-2} \text{ s}^{-1}$ ,  $k_p = 10^3 \text{ M}^{-1}\text{s}^{-1}$ , and  $K_{ATRP}$  being varied between  $1 \times 10^{-6}$  and  $1 \times 10^{-9}$  (ref. <sup>139</sup>); (B) in ICAR ATRP according to ref. <sup>138</sup>.

Nevertheless, the value of  $K_{ATRP}$  is important for the control of ICAR ATRP. Since a very small amount of the catalyst is usually employed, catalysts with large values of  $K_{ATRP}$ , which results in high equilibrium concentrations of  $Fe^{III}$  (or  $Cu^{II}$ ), and with large deactivation rate coefficients are desirable to yield a well-controlled ICAR ATRP.<sup>140</sup>

The decomposition rate of the thermal initiator determines whether the system operates according to either SR&NI or ICAR ATRP.<sup>139</sup> In addition, there may be differences in the absolute concentration of the catalyst and/or alkyl halide.

Irrespective of the ATRP technique, the degree of polymerization,  $DP$ , of the polymer synthesized via ATRP may be predicted by the ratio of consumed monomer,  $[M]_0 \cdot conv$ , to the initial concentration of the initiator (Equation 3.3). The number average molar mass of the polymer,  $M_n$ , may be predicted based on the product of  $DP$  and the molar mass of the monomer.

$$DP = \frac{[M]_0 \cdot conv}{[R-X]_0} \quad (3.3)$$

A well-controlled ATRP yielding low dispersities,  $\mathcal{D} = M_w/M_n$ , and predictable molar mass requires a sufficient concentration of the ATRP deactivator,  $[X\text{-Fe}^{\text{III}}/\text{L}]$  (Equation 3.4).<sup>141,142</sup> Dispersity decreases with conversion, toward smaller initial concentration of the alkyl halide,  $[\text{R-X}]_0$ , and with decreasing ratio of  $k_p$  to  $k_{\text{deact}}$ . According to Equation 3.4, the effect of pressure and temperature on dispersity should be studied at otherwise identical reactions conditions (cf. chapter 6).

$$\mathcal{D} = \frac{M_w}{M_n} = 1 + \frac{1}{DP} + \left( \frac{[\text{R-X}]_0 \cdot k_p}{k_{\text{deact}} \cdot [\text{X-Fe}^{\text{III}}/\text{L}]} \right) \cdot \left( \frac{2}{\text{conv}} - 1 \right) \quad (3.4)$$

**Termination.** ATRP may be carried out to achieve narrow molar mass distributions, but perhaps even more importantly, it is desirable to obtain polymer with a high degree of preserved chain-end functionality (CEF). In ATRP, as in all radical polymerizations, radical-radical termination cannot be avoided. As a consequence, the degree of CEF decreases with time, i.e., toward higher degrees of monomer conversion. The loss in CEF, i.e., the concentration of dead chains without halogen,  $[\text{T}]$ , may be estimated via Equation 3.5,<sup>45</sup> where  $[\text{T}]$  is a function of monomer conversion,  $\text{conv}$ , and time,  $t$ .

$$[\text{T}] = 2k_t \cdot [\text{R}_n^\bullet]^2 \cdot t = \frac{2k_t \cdot d\ln(1 - \text{conv})^2}{k_p^2 \cdot dt} \quad (3.5)$$

The growing macroradicals,  $\text{R}_n^\bullet$ , are highly reactive species that terminate under diffusion control.<sup>143,144</sup> Termination may either occur by combination of two radicals,  $k_{t,\text{com}}$ , to yield  $\text{P}_{n+m}$  (Equation 3.6a) or by disproportionation,  $k_{t,\text{dis}}$ , which results in the formation saturated and unsaturated polymer,  $\text{P}_m^{\text{H}}$  and  $\text{P}_n^=$ , respectively (Equation 3.6b).



The ratio of combination and disproportionation primarily depends on the type of monomer. On the one hand, termination by combination

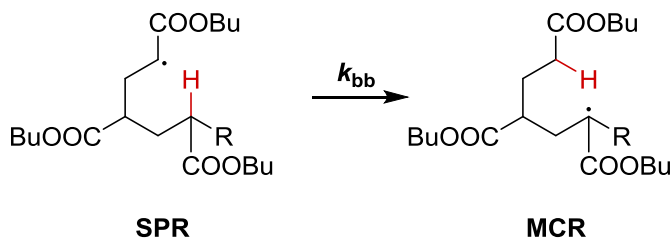
dominates in case of less sterically demanding monomers, mostly mono-substituted monomers like styrene. On the other hand, termination by disproportionation is found preferably with higher substituted monomers like MMA.<sup>145</sup> Both reaction pathways (combination and disproportionation) are included in the combined termination rate coefficient  $k_t$  (cf. Equation 3.5). The dependence of  $k_t$  on chain length,  $n$ , of  $R_n^\bullet$ , as described via the so-called composite model, is detailed elsewhere.<sup>143,144</sup>

**Transfer.** The kinetics of transfer reactions may affect the control of ATRP. In a chain-transfer reaction, the radical function is transferred ( $k_{tr,z}$ ) to another molecule, Z (Equation 3.7a), either to the monomer, an initiator molecule, a solvent molecule, the polymer, or an added chain-transfer agent. The radical function is transferred to Z simultaneously with the exchange of, for example, a hydrogen or a halogen atom. The newly formed radical,  $Z^\bullet$ , may undergo chain growth ( $k_{p,z}$ ), Equation 3.7b.



Of particular importance for the kinetics of acrylates is intramolecular transfer:<sup>146-148</sup> Via a 1,5-hydrogen shift reaction (Scheme 3.4), mostly referred to as backbiting, highly reactive secondary propagating radicals (SPRs) are transformed into weakly reactive mid-chain radicals (MCRs).<sup>149-152</sup> Propagation of MCRs, which results in the formation of SPRs, is by three orders of magnitude slower than for SPRs.<sup>153,154</sup> The consequences of backbiting for ATRP will be discussed in chapter 6.2.

**Organometallic reactions.** The ATRP scheme 3.1 contains the reaction of propagating radicals with monomer (propagation), with other propagating radicals (termination) and with the catalyst in the higher oxidation state, e.g.,  $Fe^{III}$  (ATRP deactivation). The reaction with the catalyst in the lower oxidation state,  $Fe^{II}$ , is usually not considered, even though such organometallic reaction may also play a role. This



**Scheme 3.4:** Transformation of secondary propagating radicals (SPRs) into mid-chain radicals (MCRs) in acrylate polymerization, described by the rate coefficient of the so-called backbiting reaction,  $k_{bb}$ .

this thesis will present a detailed study into the consequences of the interplay between atom transfer and organometallic reactions in chapter 5.

### 3.2.2 The Persistent Radical Effect

In (normal) ATRP, termination of radicals,  $R_n^\bullet$ , results in the accumulation of the persistent radical, i.e., the halogen-capped catalyst species in the higher oxidation state, e.g.,  $X\text{-Fe}^{\text{III}}/\text{L}$  (cf. Scheme 3.1). This is referred to as the *persistent radical effect* (PRE).<sup>155-157</sup> In contrast to the classic equation for the accumulation of the persistent radical solved by Fischer,<sup>155,156</sup> Tang et al. deduced a modified function,  $F([Y])$ , which precisely describes the accumulation of the persistent radical,  $Y$ , with time even for highly reactive systems.<sup>36</sup> Equations 3.8 and 3.10 are to be used in the equimolar case and Equations 3.8 and 3.9 in the non-equimolar one. In order to remain consistent with previous work,  $[I]_0$  represents  $[R-X]_0$ ,  $[C]_0$  refers to  $[\text{Fe}^{\text{II}}/\text{L}]_0$ , and  $[Y]$  to  $[X\text{-Fe}^{\text{III}}/\text{L}]$  in case of Fe catalysis.<sup>36</sup> It should be noted that these equations apply only in case of normal, reverse, SR&NI or AGET ATRP, provided that the equilibrium state has been reached. In ICAR and ARGET ATRP, the catalyst is progressively regenerated by reducing the persistent radical, e.g.,  $X\text{-Fe}^{\text{III}}/\text{L}$  back to  $\text{Fe}^{\text{II}}/\text{L}$ .

$$F([Y]) = \frac{([C]_0)^2}{3([C]_0 - [Y])^3} - \frac{[C]_0}{([C]_0 - [Y])^2} + \frac{1}{([C]_0 - [Y])} \quad (3.8)$$

$$F([Y]) = \left( \frac{[I]_0 [C]_0}{[C]_0 - [I]_0} \right)^2 \left( \frac{1}{([C]_0)^2 ([I]_0 - [Y])} + \frac{2}{[I]_0 [C]_0 ([C]_0 - [I]_0)} \right) \cdot \ln \left( \frac{[I]_0 - [Y]}{[C]_0 - [Y]} \right) + \frac{1}{([I]_0)^2 ([C]_0 - [Y])} \quad (3.9)$$

$$F([Y]) = 2 \cdot k_t \cdot K_{\text{ATRP}}^2 \cdot t + c' \quad (3.10)$$

The  $F([Y])$  function is therefore typically determined from normal ATRP procedures to avoid any interference of reduction reactions with the PRE. The required time-dependent concentrations of the persistent species may be observed via online UV/VIS or VIS/NIR measurements as detailed in chapter 4.1 and 6.3. By plotting  $F([Y])$  against time, the equilibrium constant,  $K_{\text{ATRP}}$ , may be determined. The analysis of  $K_{\text{ATRP}}$  requires knowledge of the termination rate coefficient,  $k_t$ . It is favorable to investigate  $K_{\text{ATRP}}$  for monomer-free model systems in order to avoid the chain-length-dependent variation of  $k_t$  (and possibly of  $K_{\text{ATRP}}$ ) underlying the  $F([Y])$  function. Analysis of  $K_{\text{ATRP}}$  for polymerization systems should be carried out according to Equation 3.1

**The Termination Rate Coefficient  $k_t$ .** The termination process in the model system involves the reaction of two small, sterically non-demanding radicals. Therefore, a reasonable approach to access the required termination rate coefficients is by assuming a translational-diffusion controlled reaction ( $k_t^D$ ). The derivation of the corresponding expression (Equation 3.11) from the Smoluchowski equation and the Stokes–Einstein relation is described elsewhere.<sup>158</sup>  $k_t^D$  may thus be estimated from fluidity, i.e., reciprocal viscosity  $\eta(T,p)$ .

$$k_t^D = \frac{R \cdot T}{3 \cdot \eta(T,p)} \quad (3.11)$$

Another approach to  $k_t$  is using the extrapolated termination rate coefficients  $k_t^{1,1}$  of two monomeric radicals, which have recently been determined via SP–PLP–EPR.<sup>93</sup>

### 3.2.3 Kinetics under High Pressure

The volume of activation,  $\Delta^\ddagger V$ , describes the pressure dependence of a rate coefficient,  $k$ , according to Equation 3.13.<sup>159-161</sup>  $\Delta^\ddagger V$  is mostly defined as the difference in the partial molar volume of the transition state structure and the sum of the partial molar volumes of the reactants. It should, however, be noted that  $\Delta^\ddagger V$  may be strongly affected by dynamic contributions, i.e., by the pressure dependence of viscosity.<sup>162</sup> Equation 3.13 precisely holds under chemical control with the rate coefficient being expressed in pressure-independent units of  $\text{kg} \times \text{mol}^{-1} \times \text{s}^{-1}$ , so that a change in density with pressure may be ignored.<sup>159</sup>

$$\left[ \frac{\partial \ln(k)}{\partial p} \right]_T = - \frac{\Delta^\ddagger V}{R \cdot T} \quad (3.13)$$

In a similar fashion, the pressure dependence of an equilibrium constant,  $K$ , is described by the reaction volume,  $\Delta_r V$ , which is defined as the difference in volume of the products vs the reactants.

As shown by Equation 3.14, there are two major contributions to the overall volume of activation.<sup>159,160</sup> The change in molar volume of the molecules or complexes, i.e., by changes in the bond lengths and angles in the transition state, is represented by  $\Delta V_M^\ddagger$ .  $\Delta V_M^\ddagger$  contributes with a negative value in a bond-forming reaction and with a positive one in a bond-cleaving reaction.

$$\Delta^\ddagger V = \Delta^\ddagger V_M + \Delta^\ddagger V_S \quad (3.14)$$

$\Delta V_S^\ddagger$  describes the change in molar volume in the transition state due to intermolecular interactions with the molecular environment, e.g., with the solvent. If a metal complex dissociates into ions, these will interact with permanent or induced dipoles of the solvent molecules, which will result in a contraction of the transition state structure and thus in a negative value of  $\Delta V_S^\ddagger$ . The latter may even outweigh the positive  $\Delta V_M^\ddagger$  to an overall negative volume of activation  $\Delta V^\ddagger$ .

The preference for ionic complexes, for species of higher charge or with enhanced ligand exchange rates (e.g., see ref.<sup>163</sup>) by increasing pressure is well understood.<sup>102-104,164</sup> Moreover, data for the pressure-dependent solubility equilibria of a variety of ubiquitous metal complexes is found in the literature.<sup>165</sup>



### 3.3 Experimental Techniques

A series of spectroscopic techniques has been applied which allow for online reaction monitoring.

**Online FT-NIR Spectroscopy up to High Pressure.** The polymerizations may be monitored in an extended pressure and temperature range via online FT-NIR spectroscopy. The high-pressure equipment is designed for pressures between 1 and 6000 bar and up to 300 °C.<sup>166,167</sup> The probing IR beam penetrates the autoclave through a sapphire window on each side as illustrated in Figure 3.3. The autoclave may either be placed directly into the FT-IR spectrometer<sup>167</sup> or, in case of larger optical path lengths, the probing light is transferred by flexible fiber optics into an autoclave positioned outside the optical compartment and back to the FT instrument.<sup>166</sup> Further details of the high-pressure equipment are given in chapter 8.4.

The concentrations of the reacting species (see Figure 3.4) were determined on the basis of Beer–Lambert’s Law (Equation 3.15), which correlates the absorbance  $A$  at a specific wavenumber,  $\tilde{\nu}$ , with the concentration,  $c$ , of the detected species. The relation is given by the optical path length,  $d$ , and the molar decadic extinction coefficient,  $\epsilon$ , which is specific for the absorption of a species at given temperature and pressure.

The linear relation between absorbance and concentration according to the Beer–Lambert’s Law precisely holds within an upper and a lower threshold of absorbance units. The validity of this relation has been checked for all detectors within the spectral range of interest as detailed in refs. <sup>168,169</sup>. The spectral analysis and the procedures of deducing integral molar absorption coefficients (vibrational intensities),  $\int \epsilon(\tilde{\nu}) d\tilde{\nu}$ , as well as an error estimate for the individual measurements is given in the results and discussion sections of chapters 4–6.

$$A(\tilde{\nu}) = \log \left( \frac{I_0}{I} \right) = \epsilon(\tilde{\nu}) \cdot c \cdot d \quad (3.15)$$

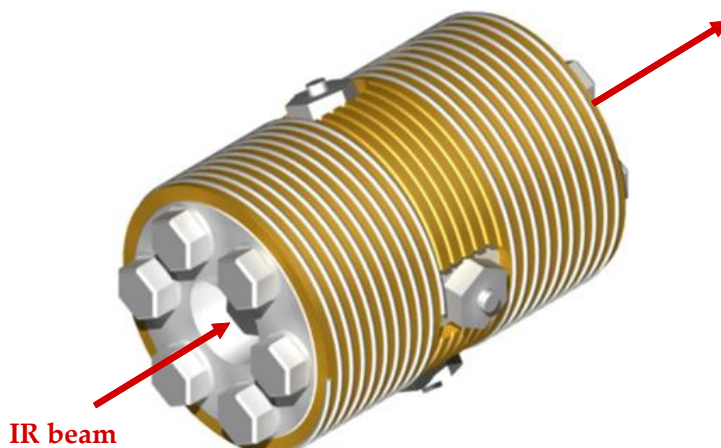


**Figure 3.3:** Schematic view of the 3 kbar autoclave embedded into an electrically heated brass jacket.<sup>170</sup> The arrows illustrate the IR light path.

---

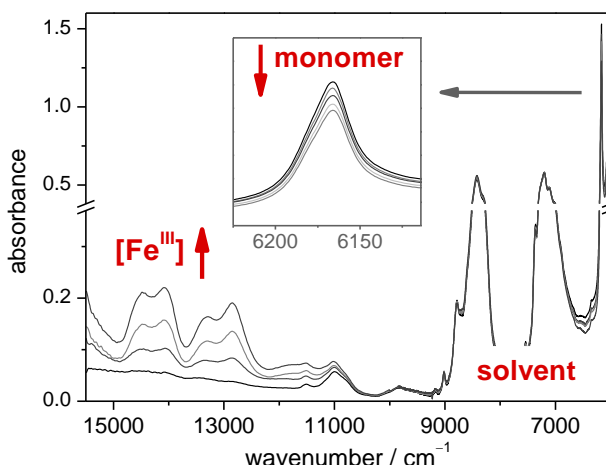


**Figure 3.4:** Typical series of FT-NIR spectra recorded online during an ATRP carried out under pressure. The absorbance of monomer, solvent and the Fe<sup>III</sup> species may be monitored at separate spectral positions. The red arrows indicate the range of major change in absorbance with time.

---

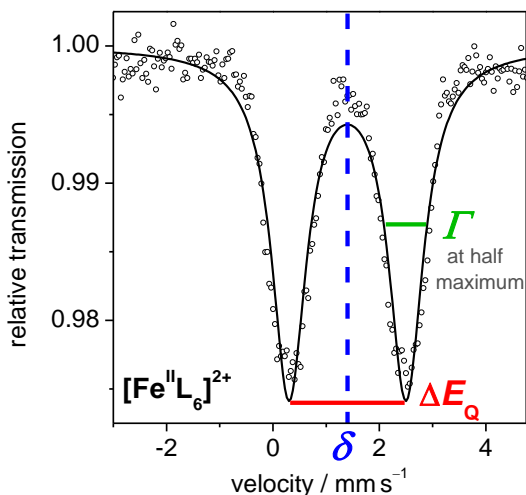


**Figure 3.5:** Mössbauer spectrum of  $[\text{Fe}^{\text{II}}(\text{NMP})_6]^{2+}$  in a flash-frozen NMP solution recorded at 80 K. The Mössbauer doublet is characterized by the isomer shift,  $\delta / \text{mm s}^{-1}$ , the quadrupole splitting,  $\Delta E_{\text{Q}}$ , and the line width,  $\Gamma$ , at half maximum.

**Mössbauer spectroscopy**<sup>171-173</sup> is based on the recoilless nuclear resonance absorption of  $\gamma$ -radiation by atomic nuclei bound in a solid phase. The radioactive source needs to be of the same element as the sample nuclei, e.g.  $^{57}\text{Fe}$ . The isomer shift (Figure 3.5),  $\delta / \text{mm s}^{-1}$ , provides direct information on the oxidation and spin state (Figure 3.6)<sup>173</sup> and may provide information about the ligand sphere of the investigated nuclei. A quadrupole splitting,  $\Delta E_{\text{Q}}$ , i.e., a doublet of the resonance line occurs in case of unsymmetrical charge distribution of the d-electrons. For example, the presence of a quadrupole splitting,  $\Delta E_{\text{Q}}$ , in the spectrum of the  $[\text{Fe}^{\text{II}}(\text{NMP})_6]^{2+}$  complex (Figure 3.5) is due to  $\text{Fe}^{\text{II}}$  being in the high spin state, where the six d-electrons are essentially located in five d-orbitals. Furthermore, the peak area of the Mössbauer doublets is proportional to the relative concentrations of the associated species (provided that relaxation rates and Lamb Mössbauer factors are identical, which is mostly the case). The line width,  $\Gamma$ , is determined at the half maximum.

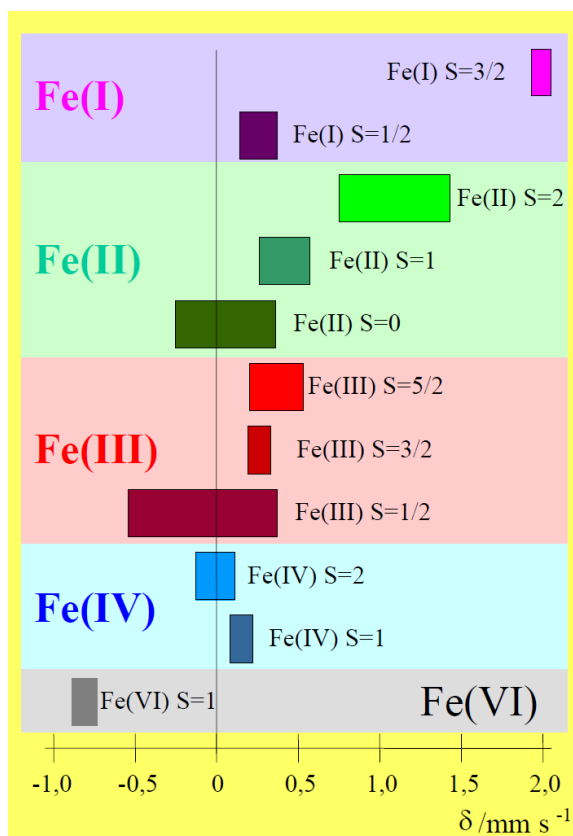


**Figure 3.6:** Expected oxidation and spin states of Fe as a function of the measured isomer shift,  $\delta / \text{mm s}^{-1}$ , according to ref. <sup>173</sup>.

**EPR spectroscopy** is used for measuring paramagnetic properties of atoms or molecules in a magnetic field.<sup>174</sup> Unpaired electrons couple with the magnetic moment of the atomic nuclei. The resulting hyperfine structure of the resonance lines provides information about the molecular structure.

EPR spectroscopy was applied in conjunction with single-pulse-laser-polymerization (SP-PLP-EPR).<sup>92,93</sup> This particular setup consists of an excimer laser (351 nm), which is placed in front of the EPR spectrometer (Figure 3.7).<sup>175</sup> The cavity resonator is equipped with a front grid for irradiation of the sample with UV light (Figure 3.7).

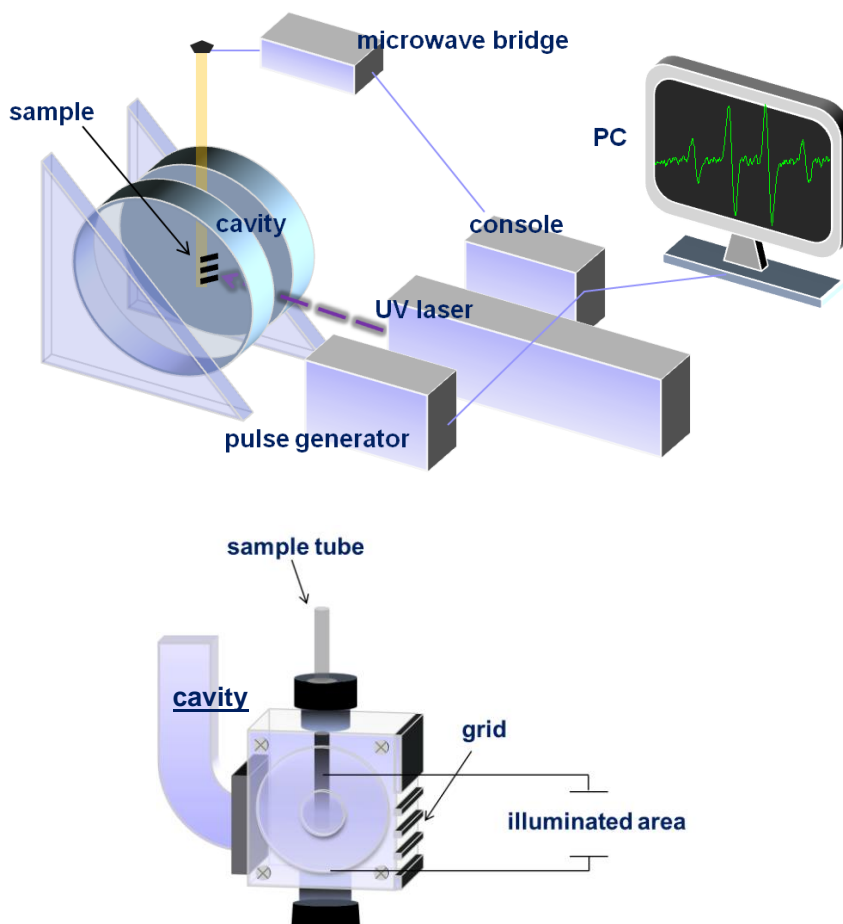


**Figure 3.7:** Schematic setup of SP-PLP-EPR.<sup>175</sup> The UV laser is placed in front of the EPR spectrometer (top). The sample placed inside the cavity (bottom) may be irradiated through a grid. The laser source and the spectrometer are synchronized using a pulse generator. The console consists of signal processing units and control electronics. The microwave bridge houses the microwave source and the detector.

The microwave bridge houses the electromagnetic radiation source and the detector. The laser source and the spectrometer are synchronized using a pulse generator (see chapter 8.2). The console consists of signal processing units and control electronics.

An EPR spectrum is typically presented as the first derivative of the absorbance spectrum (Figure 3.8). The double integral, i.e., the integral of absorbance is proportional to the concentration of the radical species (see r.h.s. of Equation 3.17 below). In addition to growing radicals, metal complexes with unpaired electrons such as  $\text{Cu}^{\text{II}}$  or high-spin  $\text{Fe}^{\text{III}}$  are EPR-active.<sup>22,176</sup> In contrast to the spectra of organic compounds (see Figure 3.8), the solid-state spectra of metal complexes are often unsymmetrical and appear at different field positions due to spin-orbit coupling of the d-electrons.<sup>174</sup>

In SP–PLP–EPR, the signal intensity,  $I_{\text{sc}}$ , of the propagating radical is recorded at a constant magnetic field ( $B_x$ ) after pulsed-laser induced radical production, with a time resolution of less than a microsecond. The index sc in  $I_{\text{sc}}$  refers to the recording of the spectrum via the signal channel. The peak intensity is directly proportional to the relative concentration of a specific type of radical species. Time-resolved monitoring may be carried out for different types of radical species which may evolve after laser-induced production of primary radical fragments (see chapter 5.2.2). The analyses of the SP–PLP–EPR experiments discussed in chapter 5.2 are mostly based on relative EPR intensity, thus not requiring calibration for absolute radical concentration.

In the case that such a quantitative analysis of radical concentration is targeted, the signal intensity,  $I_{\text{sc}}(B_x)$ , may be correlated with the double integral of the full spectrum. The proportionality given by  $h_1$  is expressed by Equation 3.16 and is characteristic for each type of radical.

$$\iint I_{\text{sc}} = h_1 \cdot I_{\text{sc}}(B_x) \quad (3.16)$$

The double integral for the species of interest may be calibrated against the measured double integral of a reference compound of known concentration (see Equation 3.17), e.g., against a solution containing 2,2,6,6-tetramethyl-1-piperidinyloxy (TEMPO). For accurate calibration, the EPR spectra of TEMPO have to be measured under exactly the same conditions (such as temperature, solvent, microwave power, modulation amplitude, sweep time, and data resolution) as used in the single-pulse experiment. Detailed descriptions of the calibration procedure may be found in the PhD theses of P. Hesse,<sup>177</sup> J. Barth,<sup>178</sup> and N. Sørensen.<sup>179</sup>

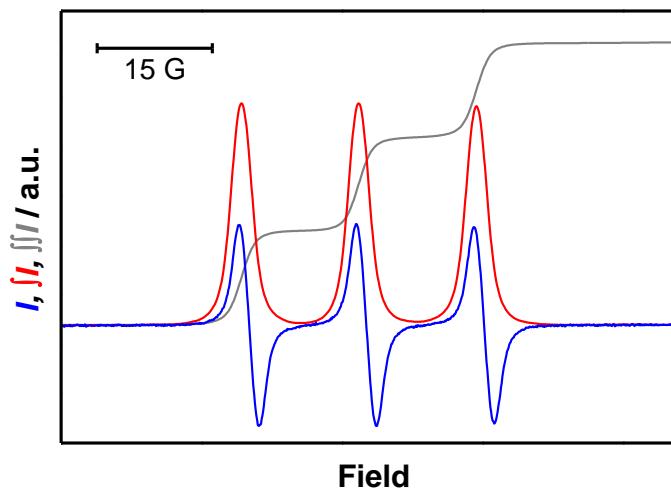


**Figure 3.8:** A typical EPR spectrum of  $1.0 \times 10^{-5} \text{ mol L}^{-1}$  TEMPO is shown in blue, the integral in red, and the double integral in gray.

$$c_R = c_{R,\text{ref}} \cdot \frac{\iint I_{\text{SC}}}{\iint I_{\text{SC,ref}}} = h_2 \cdot \iint I_{\text{SC}} \quad (3.17)$$

Kinetics in SP-PLP-EPR may be studied as a function of chain length,  $i$ , of propagating radicals.<sup>92,93</sup> The laser-induced generation of initiator-derived primary radicals is assumed to occur instantaneously with respect to the timescale of all other reactions involved. Therefore, the average chain length of propagating radicals may be estimated according to Equation 3.18, where  $k_p$  is the propagation rate coefficient,  $c_M$  the monomer concentration, and  $t$  the time after applying the laser pulse. The term (+1) represents the initiator fragment which starts the chain growth. Because of the instantaneous initiation, the molar-mass distribution of the growing radical is very narrow.

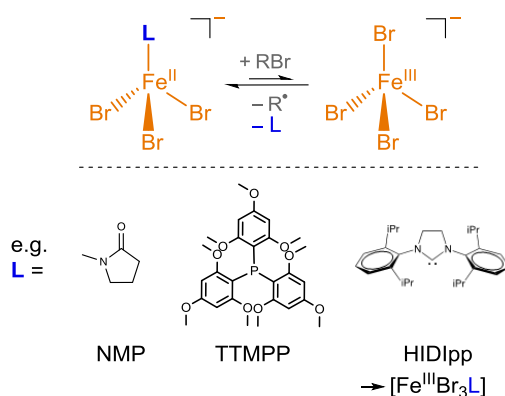
$$i = k_p \cdot c_M \cdot t + 1 \quad (3.18)$$





# 4

## Kinetics of Fe-Mediated ATRP



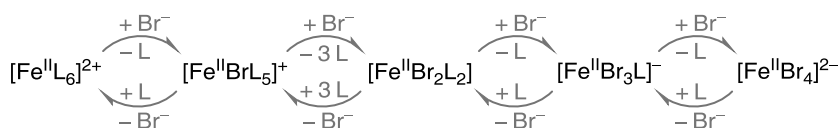
Iron halides are active and cheap catalysts for ATRP and are precursors for catalyst modifications by adding phosphines, *N*-heterocyclic carbenes (NHCs), and amines.

This chapter deals with a detailed speciation analysis of iron-halide-based complexes in different solvent environments via  $^{57}\text{Fe}$  Mössbauer and FT-IR spectroscopy. The results will be correlated with measured ATRP activation and deactivation rate coefficients. NHC and phosphine additives were also tested for the effects on rate and control of ATRP.

## 4.1 Iron-Halide-Based Catalysts<sup>1</sup>

### 4.1.1 Speciation Analysis

Iron bromides are efficient mediators of ATRP even in the absence of any external ligands.<sup>81-84</sup> Illustrated in Scheme 4.1 are the structures of monomeric Fe<sup>II</sup> complexes,<sup>180</sup> which may result from the dissolution of FeBr<sub>2</sub>. The coordination number and geometry of these complexes depend on the steric demand of the ligands. Fe<sup>II</sup> complexes containing at least two relatively large bromine atoms are tetrahedral,<sup>45,166,180,181</sup> whereas [Fe<sup>II</sup>L<sub>6</sub>]<sup>2+</sup> occurs in the typical octahedral structure.<sup>180</sup> L represents a monodentate ligand; more specifically, in the systems under investigation in this chapter, L is a solvent molecule: L = (Solv). The [FeBrL<sub>5</sub>]<sup>+</sup> species, which has not been detected in the experiments, is most likely thermodynamically labile.



**Scheme 4.1:** Monomeric Fe<sup>II</sup> complexes in solution of FeBr<sub>2</sub>. The monodentate ligand L refers in this case to a coordinated solvent molecule. Further Fe<sup>II</sup> complexes are not expected to occur in significant amounts.

The FT-NIR spectra of 30 mM FeBr<sub>2</sub> dissolved in CDCl<sub>3</sub>/CD<sub>3</sub>CN, at a molar ratio of 87.5/12.5, with different amounts of added TBA-Br are shown in Figure 4.1. This solvent mixture constitutes the best compromise of high catalyst loading and sufficient IR transmission down to 2400 cm<sup>-1</sup>, thus enabling Fe<sup>II</sup> absorption to be monitored within a wide spectral range. The optical path length, *d*, may be as high as 3.5 mm, since the small and rather symmetric solvent molecules, CDCl<sub>3</sub> and CD<sub>3</sub>CN, exhibit only a few vibrational modes. Moreover, the

<sup>1</sup> Reproduced with permission from Schroeder, H.; Buback, J.; Demeshko, S.; Matyjaszewski, K.; Meyer, F.; Buback, M. *Macromolecules* **2015**, *48*, 1981–1990, Copyright 2015 American Chemical Society. Reproduced in part with permission from Schroeder, H.; Yalalov, D.; Buback, M.; Matyjaszewski, K. *Macromol. Chem. Phys.* **2012**, *213*, 2019–2026, Copyright 2015 Wiley-VCH. The Mössbauer measurements were carried out together with S. Demeshko. J. Buback contributed to the measurements of ATRP activation and deactivation rate.

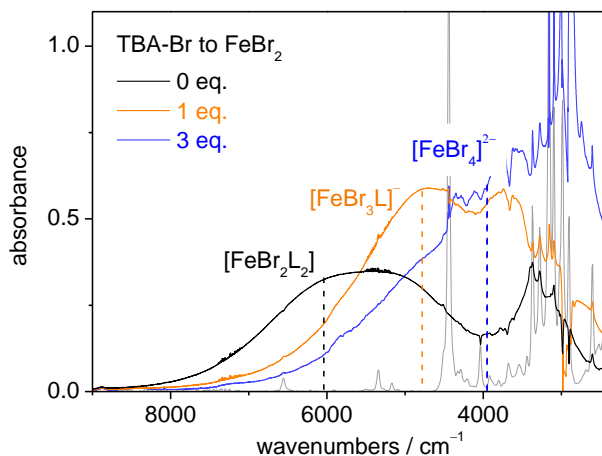


**Figure 4.1:** FT-NIR spectra of 30 mM FeBr<sub>2</sub> dissolved in CDCl<sub>3</sub>/CD<sub>3</sub>CN (molar ratio: 87.5/12.5) upon addition of either 0, 1, or 3 equiv of TBA-Br relative to FeBr<sub>2</sub>. The spectra were recorded at ambient  $p$  and  $T$  and an optical path length,  $d$ , of 3.5 mm. Solvent absorption (gray line) has been subtracted (see text). The dashed vertical lines represent the absorbance maximum positions of the indicated Fe<sup>II</sup> complexes.

solvent absorption of the deuterated solvents is shifted to lower wavenumbers as compared to the non-deuterated solvents. The spectra in Figure 4.1 do not contain the solvent absorption, given by the gray line, which has been subtracted via reference spectra measured at identical composition and TBA-Br content, but without the Fe<sup>II</sup> species. The spectra have been recorded on freshly prepared solutions to avoid halogen exchange between CDCl<sub>3</sub> and iron(II) bromide species.

Titration of the FeBr<sub>2</sub> solution with TBA-Br, as illustrated in Figure 4.1, yields NIR spectra which may be deconvoluted according to the speciation of Fe<sup>II</sup> complexes proposed in Scheme 4.1. The solubility and the complexation of Fe<sup>II</sup> species is primarily due to acetonitrile, which was used as the solvent for ATRP in reported studies.<sup>82</sup> The monomer-free catalyst system thus appears to be an adequate model system for the speciation analysis in ATRP.

The IR-NIR bands in Figure 4.1 are assigned to iron-centered d-d transitions of tetrahedral Fe<sup>II</sup> species (cf. Scheme 4.1) based on the peak positions being located between 2400 and 9000 cm<sup>-1</sup>.<sup>166,182</sup> The [FeBr<sub>4</sub>]<sup>2-</sup>

complex should be the dominant species in the FeBr<sub>2</sub> solution with the highest TBA-Br content, i.e., upon the addition of 3 equiv of TBA-Br relative to FeBr<sub>2</sub>. Hence, the absorbance around 4000 cm<sup>-1</sup> (blue line) was assigned to [FeBr<sub>4</sub>]<sup>2-</sup>. The intense absorbance at around 3200 cm<sup>-1</sup> results from the 2ν<sub>4</sub>+ν<sub>3</sub> combination mode of acetonitrile<sup>183</sup> with additional contributions to absorbance from trace amounts of water. The peak position of [FeBr<sub>4</sub>]<sup>2-</sup> may be more precisely determined via the absorbance spectra measured at higher pressure as in chapter 6.3. The absorbance around 4900 cm<sup>-1</sup> (orange line in Figure 4.1) reaches a maximum upon adding 1 equiv of TBA-Br. On the basis of the overall amount of bromide in the solution, this peak is assigned to [FeBr<sub>3</sub>L]<sup>-</sup>. The absorbance of the FeBr<sub>2</sub> solution without added TBA-Br (black line in Figure 4.1) is rather broad which indicates the simultaneous presence of the several tetrahedral [FeBr<sub>u</sub>L<sub>v</sub>]<sub>u+v=4</sub> species, i.e., with *u* = 2, 3, and 4, as proposed in Scheme 4.1. The peak position around 6100 cm<sup>-1</sup> is assigned to the neutral [FeBr<sub>2</sub>L<sub>2</sub>] complex. The octahedral species [Fe<sup>III</sup>L<sub>6</sub>]<sup>2+</sup> occurs at above 9000 cm<sup>-1</sup> (see Figure 4.2B), i.e., above the range covered in Figure 4.1.<sup>166</sup> As expected for such species bearing an inversion center, the extinction coefficient is only around ε = 5 Lmol<sup>-1</sup>cm<sup>-1</sup>,<sup>166</sup> which in turn complicates the detection of this complex in the presence of, e.g., the tetrahedral [Fe<sup>II</sup>(Br)<sub>u</sub>(NMP)<sub>v</sub>]<sub>u+v=4</sub> species (ε = 37 Lmol<sup>-1</sup>cm<sup>-1</sup> at 4820 cm<sup>-1</sup>). As explained in chapter 6.3.1, applying high pressure may assist the speciation analysis of Fe<sup>II</sup> complexes. These experiments confirm the assignment of the peak positions of the individual species.

Of major interest is to identify the ATRP mediators. Wang et al. observed highest catalyst activity in ATRP at ambient pressure upon adding 1 equiv TBA-Br.<sup>81</sup> Polymerization rate decreased upon further addition of TBA-Br, as the resulting [FeBr<sub>4</sub>]<sup>2-</sup> complex (Figure 4.1) does not activate alkyl halides, since no further bromide can coordinate to this species. Quantitative evidence for this interpretation is provided by measuring *K*<sub>ATRP</sub> at different levels of TBA-Br (see below). Since the highest catalyst activity occurs upon the addition of 1 equiv TBA-Br, where the intensity of the NIR band assigned to [FeBr<sub>3</sub>L]<sup>-</sup> is highest (cf. Figure 4.1), it may be concluded that ATRP operates predominantly by [FeBr<sub>3</sub>L]<sup>-</sup> activation of the alkyl bromide. This conclusion is in agreement with studies suggesting that the [Fe<sup>III</sup>Br<sub>4</sub>L<sub>x</sub>]<sup>-</sup> complex is the primary Fe<sup>III</sup> component<sup>184</sup> and acts as the bromide-capped

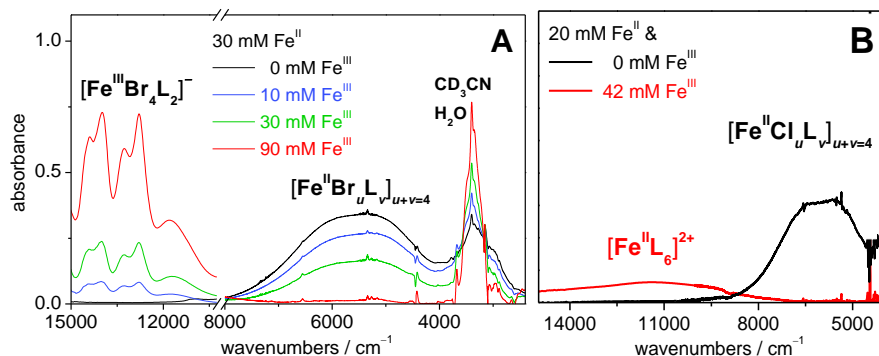


**Figure 4.2:** (A) FT-NIR spectra of  $[\text{Fe}^{\text{III}}\text{Br}_4]^-$  and  $[\text{Fe}^{\text{II}}\text{Br}_u\text{L}_v]_{u+v=4}$  complexes measured for 30 mM  $\text{FeBr}_2$  at different levels of  $\text{FeBr}_3$  in solution of  $\text{CDCl}_3/\text{CD}_3\text{CN}$  (87.5/12.5). The spectra were recorded at ambient  $p$  and  $T$  and an optical path length of 3.5 mm. Solvent absorption has been subtracted. (B) FT-NIR spectra indicating the transformation of  $[\text{Fe}^{\text{II}}\text{Cl}_u\text{L}_v]_{u+v=4}$  to  $[\text{Fe}^{\text{II}}\text{L}_6]^{2+}$  in solutions of 20 mM  $\text{FeCl}_2$  in  $\text{CDCl}_3/\text{CD}_3\text{CN}$  (2/1) without or with 2.1 equiv of  $\text{FeCl}_3$ , respectively. The optical path length was  $d \approx 5$  mm. The associated  $\text{Fe}^{\text{III}}$  absorption occurs in the UV/VIS range.

deactivator.<sup>45,166</sup> As shown in Figure 4.2A, the absorption of  $\text{Fe}^{\text{III}}$  occurs between 9000 and 15 000  $\text{cm}^{-1}$ . Such high transition energies are mostly associated with octahedral complexes, e.g.  $[\text{Fe}^{\text{III}}\text{X}_4\text{L}_2]^-$ .<sup>166,185</sup> However, this observed absorbance is actually due to tetrahedral  $[\text{Fe}^{\text{III}}\text{Br}_4]^-$ .<sup>186-188</sup> The absorption occurs at significantly higher energy as compared to the tetrahedral  $\text{Fe}^{\text{II}}$  complexes (cf. Figure 4.1) as a consequence of the  $d^5$  electron configuration in  $[\text{Fe}^{\text{III}}\text{Br}_4]^-$ . All d-d transitions are spin-forbidden and Laporte-allowed, i.e., the reverse of the usual selection rules applies.<sup>189</sup> Evidence for  $[\text{Fe}^{\text{III}}\text{Br}_4]^-$ <sup>190,191</sup> and  $[\text{Fe}^{\text{III}}\text{Cl}_4]^-$ <sup>45,192-194</sup> is also found in the Cambridge Structural Database.<sup>195</sup>

Shown in Figure 4.2A are NIR spectra of 30 mM  $\text{FeBr}_2$  to which different amounts of  $\text{FeBr}_3$  have been added in  $\text{CDCl}_3/\text{CD}_3\text{CN}$  (87.5/12.5) solution. The intensity of the signal assigned to  $[\text{Fe}^{\text{III}}\text{Br}_4]^-$  scales with the  $\text{FeBr}_3$  content. Despite the constant level of  $\text{Fe}^{\text{II}}$ , the overall intensity of tetrahedral  $[\text{Fe}^{\text{II}}\text{Br}_u\text{L}_v]$  species decreases toward higher  $\text{Fe}^{\text{III}}$  content and even disappears at the highest  $\text{Fe}^{\text{III}}$  content, i.e., at 90 mM  $\text{Fe}^{\text{III}}$ . This observation indicates bromide transfer from  $\text{Fe}^{\text{II}}$  to the Lewis acid  $\text{Fe}^{\text{III}}$ , which is accompanied by the formation of octahedral  $[\text{FeL}_6]^{2+}$ .

The occurrence of  $[\text{FeL}_6]^{2+}$  cannot be evidenced by FT-NIR but was clearly shown by  $^{57}\text{Fe}$  Mössbauer spectroscopy (see further below). Quantitative halide transfer from  $\text{Fe}^{\text{II}}$  to  $\text{Fe}^{\text{III}}$  also occurs for the associated chloride salts (Figure 4.2B) upon the addition of at least two equivalents of  $\text{FeCl}_3$  to  $\text{FeCl}_2$  (cf. Figure S2). The broad weak band at around  $11\,000\text{ cm}^{-1}$  is assigned to  $[\text{Fe}^{\text{II}}\text{L}_6]^{2+}$ . With the Cl system, this band may be observed, as the absorbance of  $[\text{Fe}^{\text{III}}\text{Cl}_4]^-$  is shifted to higher wavenumbers compared with  $[\text{Fe}^{\text{III}}\text{Br}_4]^-$  (Figure 4.2A).<sup>188</sup>

The halide transfer from  $\text{Fe}^{\text{II}}$  to  $\text{Fe}^{\text{III}}$  did not occur when 1 equiv, with respect to total Fe, of the associated halide salt, TBA-Br, was added. The additional halide results in bromide saturation to  $[\text{Fe}^{\text{III}}\text{Br}_4]^-$  irrespective of the  $\text{Fe}^{\text{III}} : \text{Fe}^{\text{II}}$  ratio. Addition of a halide salt thus may help to conduct actual ATRPs by preventing halide transfer from  $\text{Fe}^{\text{II}}$  to  $\text{Fe}^{\text{III}}$ .

It is important to check whether the solvent environment significantly affects the NIR absorption pattern of the  $\text{Fe}^{\text{II}}$  species. This being the case could result in considerable variations of  $K_{\text{ATRP}}$  with solvent composition (see chapter 4.1.2). The spectra of 22 mM  $\text{FeBr}_2$  in 16 to 100 mol%  $\text{CD}_3\text{CN}$  as the cosolvent to  $\text{CDCl}_3$ , i.e., the gray lines in the upper part of Figure 4.3, were measured. Analysis of the intensities at the peak positions indicated in Figure 4.1 for the tetrahedral  $\text{Fe}^{\text{II}}$  complexes suggests that the formation of  $[\text{FeBr}_4]^{2-}$ , along with  $[\text{FeL}_6]^{2+}$ , is favored in the most polar solvent environment, i.e., in pure  $\text{CD}_3\text{CN}$ , whereas  $[\text{FeBr}_2\text{L}_2]$  absorbance increases toward higher  $\text{CDCl}_3$  content. According to the measured absorbance at around  $4900\text{ cm}^{-1}$ , the  $[\text{FeBr}_3\text{L}]^-$  activator content remains almost unchanged and thus should not cause any changes in  $K_{\text{ATRP}}$ . Shown in the lower part of Figure 4.3 is the FT-NIR spectrum of  $\text{FeBr}_2$  dissolved in pure  $\text{CDCl}_3$  (red line). 66 mM TBA-OTf have been added to ensure the solubility of  $\text{FeBr}_2$ . The peak absorption around  $4200\text{ cm}^{-1}$  is due to  $[\text{Fe}^{\text{II}}\text{Br}_3\text{L}]^-$ , the primary component in this solvent, as confirmed by Mössbauer spectroscopy (see below). It should be noted that the peak position of  $[\text{Fe}^{\text{II}}\text{Br}_3\text{L}]^-$  is shifted by about  $700\text{--}800\text{ cm}^{-1}$ , i.e., by about  $10\text{ kJmol}^{-1}$  to lower wavenumbers in passing over to the less polar solvent environment. As detailed in chapter 4.1.2, the observed red-shift leads to an enhancement of  $K_{\text{ATRP}}$  by more than two orders of magnitude in the weakly polar solvent.<sup>105</sup>

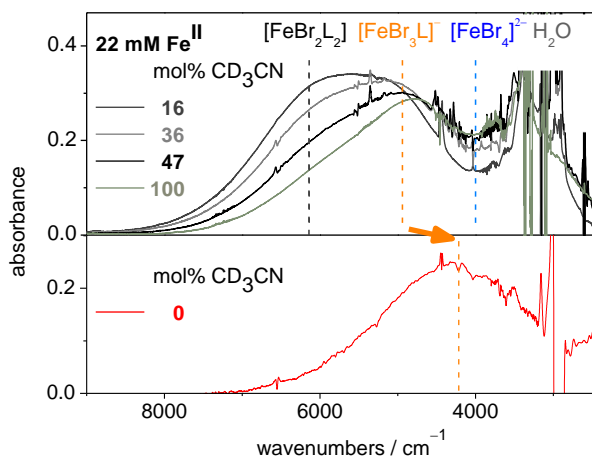


**Figure 4.3:** FT-(N)IR spectra of 22 mM  $\text{FeBr}_2$  dissolved in  $\text{CDCl}_3/\text{CD}_3\text{CN}$  solvent mixtures of different composition at ambient  $p$  and  $T$ ;  $d = 5.8$  mm. The dashed lines indicate the approximate peak positions of the tetrahedral  $\text{Fe}^{\text{II}}$  species. Solvent absorption has been subtracted. The orange arrow indicates the shift in the peak position of  $[\text{Fe}^{\text{II}}\text{Br}_3\text{L}]^-$ .

### $^{57}\text{Fe}$ Mössbauer Spectroscopy

$^{57}\text{Fe}$  Mössbauer spectroscopy has been applied for more detailed speciation analysis of iron-mediated ATRP. Due to the unfavorably large  $\gamma$ -capture cross-section of bromide, iron chloride salts were used for these measurements. The NIR spectra in Figure 4.2A–B indicate that speciation aspects should be similar for chloride and bromide salts. The Mössbauer spectra were recorded at 80 K on flash-frozen solutions which thus should closely reflect the speciation at ambient temperature.

First, two reference spectra were recorded to help with the assignment of species (Figure 4.4A–B). The Mössbauer parameters for  $[\text{FeCl}_4]^{2-}$  (green area in Figure 4.4A) were obtained by measuring  $\text{FeCl}_2$  with 4 equiv of TBA-Cl in solution of NMP. The Mössbauer parameters for  $[\text{FeL}_6]^{2+}$  (blue area Figure 4.4B) were obtained from spectra measured on a solution of 100 mM  $\text{Fe}(\text{OTf})_2$  in NMP, which contains the  $[\text{Fe}(\text{NMP})_6]^{2+}$  ( $= [\text{FeL}_6]^{2+}$ ) complex.<sup>166</sup> The parameters used for fitting the symmetric Lorentzian doublets to each single species are given in Table 4.1. The isomer shifts for  $[\text{FeCl}_4]^{2-}$ ,  $\delta = 1.05 \text{ mm s}^{-1}$ , and  $[\text{Fe}(\text{NMP})_6]^{2+}$ ,  $\delta = 1.40 \text{ mm s}^{-1}$ , are close to the reported values calculated

and measured for  $[\text{FeCl}_4]^{2-}$ :  $\delta = 0.90 \text{ mm s}^{-1}$ , and  $\delta = 1.39 \text{ mm s}^{-1}$  for  $[\text{Fe}(\text{H}_2\text{O})_6]^{2+}$  ( $= [\text{FeL}_6]^{2+}$ ).<sup>196</sup> As expected, the measured isomer shifts meet the expectation of the  $\text{Fe}^{\text{II}}$  complexes being in the high-spin state.

The Mössbauer spectrum measured on a  $\text{FeCl}_2$  solution in NMP is shown in Figure 4.4C. The spectrum is indicative of a distribution of  $\text{Fe}^{\text{II}}$  species, probably similar to the one illustrated by the series in Scheme 4.1 for the bromide system. The spectrum was fitted using the parameters for  $[\text{FeCl}_4]^{2-}$  (green area) and  $[\text{FeL}_6]^{2+}$  (blue area) from Table 4.1. The third fitted subfunction (red/gray area) refers to a combined fit for the  $[\text{Fe}^{\text{II}}\text{Cl}_2\text{L}_2]$  and  $[\text{Fe}^{\text{II}}\text{Cl}_3\text{L}]^-$  species.

Mössbauer spectroscopy is particularly useful for the detection of  $[\text{FeL}_6]^{2+}$ , which was difficult to achieve via FT-NIR (see above). Shown in Figure 4.4D is the Mössbauer spectrum of a solution of 50 mM  $\text{FeCl}_2$  and 150 mM  $\text{FeCl}_3$ . The intense (narrow) subfunction (blue curve) resulting from fitting the experimental data indicates the formation of  $[\text{Fe}(\text{NMP})_6]^{2+}$  in the  $\text{Fe}^{\text{II}}/\text{Fe}^{\text{III}}$  mixture (cf. entries 2 and 4 in Table 4.1). By calibration via the data in Figure 4.4B, the concentration of the  $[\text{Fe}(\text{NMP})_6]^{2+}$  complex is obtained to be  $47 \pm 3 \text{ mM}$ , which is in close agreement with the selected  $\text{Fe}^{\text{II}}$  concentration and thus confirms that  $[\text{Fe}(\text{NMP})_6]^{2+}$  is the dominant  $\text{Fe}^{\text{II}}$  complex. The condensed doublet of the second subfunction is assigned to high-spin  $\text{Fe}^{\text{III}}$  with the  $[\text{Fe}^{\text{III}}\text{Cl}_4]^-$  complex being the lead component. A minor amount of  $\text{Fe}^{\text{III}}$  may occur as  $[\text{Fe}(\text{NMP})_6]^{3+}$ . The isomer shift of the  $\text{Fe}^{\text{III}}$  quadrupole doublet,  $\delta = 0.20 \text{ mm s}^{-1}$ , is close to the reported values for  $[\text{FeCl}_4]^-$  in ionic liquids,  $\delta = 0.31 \text{ mm s}^{-1}$  (90 K),<sup>197</sup> and for  $[\text{FeCl}_4]^-$  with choline as the counterion,  $\delta = 0.32 \text{ mm s}^{-1}$  (4.1 K).<sup>198</sup> The integral of the subfunction for  $[\text{Fe}^{\text{III}}\text{Cl}_4]^-$  is, however, by about a factor of 8 below the expectation based on the relative concentrations of  $\text{Fe}^{\text{III}}$  (150 mM) to  $\text{Fe}^{\text{II}}$  (50 mM). As reported by König and Ritter, intermediate spin relaxation of  $\text{Fe}^{\text{III}}$  may cause such problems with quantitative measurements.<sup>199</sup> The data collected at 6 K in an extended velocity range exhibits an additional broad feature (see Figure S3), which suggests that intermediate spin relaxation also occurs with the  $\text{Fe}^{\text{III}}$  complexes. Applying an external magnetic field may help to yield the full  $\text{Fe}^{\text{III}}$  contribution with narrow line width. Irrespective of such potential further experiments, the spectrum in Figure 4.4D clearly demonstrates the formation of  $[\text{Fe}(\text{NMP})_6]^{2+}$  as the only one  $\text{Fe}^{\text{II}}$  species, which is produced by chloride



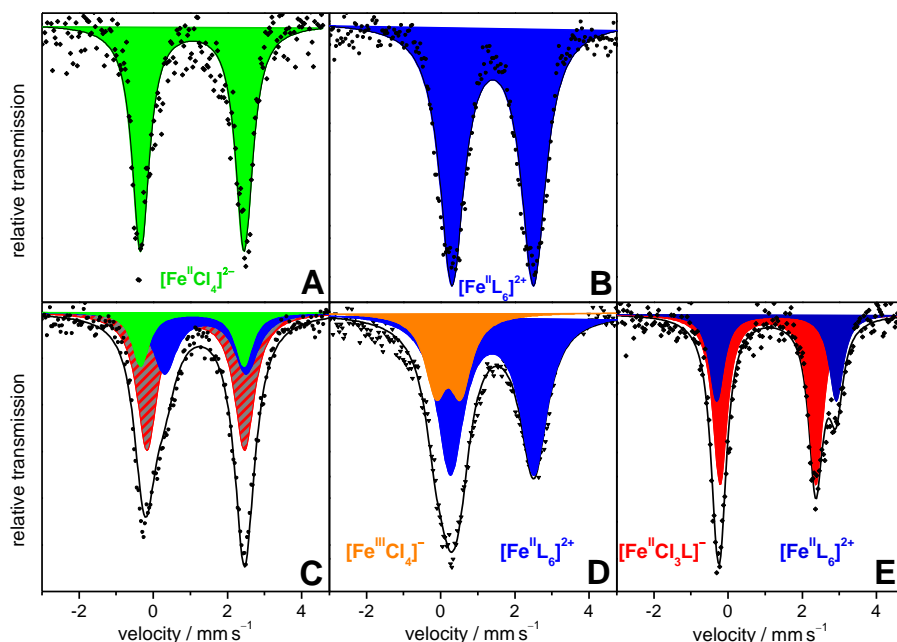


**Figure 4.4:**  $^{57}\text{Fe}$  Mössbauer spectra measured on flash-frozen solutions at 80 K. The experimental data is represented by the filled symbols. (A) Spectrum for 30 mM  $\text{FeCl}_2$  with 120 mM TBA-Cl indicating that  $[\text{Fe}^{\text{II}}\text{Cl}_4]^{2-}$  (green area) is present as the single  $\text{Fe}^{\text{II}}$  species. (B)  $[\text{Fe}^{\text{II}}\text{L}_6]^{2+} = [\text{Fe}^{\text{II}}(\text{NMP})_6]^{2+}$  (blue area) was detected after dissolving 100 mM  $\text{Fe}(\text{OTf})_2$  in NMP. (C) Spectrum of a solution of 100 mM  $\text{FeCl}_2$  in NMP. Three functions have been used to fit the experimental data (cf. Table 4.1). (D) Spectrum of a solution of 150 mM  $\text{FeCl}_3$  and 50 mM  $\text{FeCl}_2$  in NMP. The orange subfunction represents  $[\text{Fe}^{\text{III}}\text{Cl}_4]^-$  and the blue one refers to  $[\text{FeL}_6]^{2+}$ . (E) Spectrum of a solution of 50 mM  $\text{FeCl}_2$  and 50 mM TBA-OTf in 2-butanone. The red function represents  $[\text{Fe}^{\text{II}}\text{Cl}_3\text{L}]^-$  and the blue one refers to  $[\text{FeL}_6]^{2+}$ .

transfer from  $\text{Fe}^{\text{II}}$  to  $\text{Fe}^{\text{III}}$  (cf. Figure 4.2B). Moreover, the data in Figure 4.4D evidences the importance of Mössbauer spectroscopy in complementing the speciation analysis via NIR/VIS spectroscopy.

The Mössbauer spectrum in Figure 4.4E was measured with  $\text{FeCl}_2$  and 1 equiv of TBA-OTf dissolved in 2-butanone. The fitted symmetric Lorentzian doublets indicate that only two species,  $[\text{FeCl}_3\text{L}]^-$  and  $[\text{FeL}_6]^{2+}$

**Table 4.1:** Mössbauer parameters of frozen solutions containing FeCl<sub>2</sub> and the indicated amounts of TBA-Cl, FeCl<sub>3</sub>, and TBA-OTf, respectively;  $\delta$ ,  $\Delta E_Q$ , and  $\Gamma$  refer to isomer shift, quadrupole splitting, and line width, respectively. Unless stated otherwise, the spectra were measured at 80 K with NMP as the solvent.

entry	[Fe <sup>II</sup> ] / mM	[TBA-Cl] / mM	fitted species	$\delta$ / mm s <sup>-1</sup>	$\Delta E_Q$ / mm s <sup>-1</sup>	$\Gamma$ / mm s <sup>-1</sup>	rel. conc. / %
1	30	120	[Fe <sup>II</sup> Cl <sub>4</sub> ] <sup>2-</sup>	1.05	2.79	0.55	100
2	100 <sup>[a]</sup>	0	[Fe <sup>II</sup> L <sub>6</sub> ] <sup>2+</sup>	1.40	2.20	0.79	100
3	100	0	[Fe <sup>II</sup> L <sub>6</sub> ] <sup>2+</sup>	1.40 <sup>[d]</sup>	2.20 <sup>[d]</sup>	0.79 <sup>[d]</sup>	28
			[Fe <sup>II</sup> Cl <sub>4</sub> ] <sup>2-</sup>	1.05 <sup>[d]</sup>	2.79 <sup>[d]</sup>	0.55 <sup>[d]</sup>	18
			[Fe <sup>II</sup> Cl <sub>2</sub> L <sub>2</sub> ], [Fe <sup>II</sup> Cl <sub>3</sub> L] <sup>-</sup> <sup>[c]</sup>	1.14	2.63	0.66	54
<b>[Fe<sup>III</sup>]</b>							
4	50	150	[Fe <sup>II</sup> L <sub>6</sub> ] <sup>2+</sup>	1.38	2.25	0.88	24 <sup>[e]</sup>
			[Fe <sup>III</sup> Cl <sub>4</sub> ] <sup>-</sup>	0.20	0.67	0.71	≤ 76 <sup>[f]</sup>
<b>[TBA-OTf]</b>							
5	50 <sup>[b]</sup>	50	[Fe <sup>II</sup> Cl <sub>3</sub> L] <sup>-</sup>	1.07	2.59	0.46	66
			[Fe <sup>II</sup> L <sub>6</sub> ] <sup>2+</sup>	1.30	3.22	0.46	34

<sup>[a]</sup> Fe(OTf)<sub>2</sub>, <sup>[b]</sup> solvent: 2-butanone, <sup>[c]</sup> overall fit for these two species, <sup>[d]</sup> fixed parameters according to entries 1 and 2, <sup>[e]</sup> determined via calibration of [Fe<sup>II</sup>L<sub>6</sub>]<sup>2+</sup> vs the reference spectrum in Figure 4.4B (entry 2) at known overall iron content, <sup>[f]</sup> assuming [Fe<sup>III</sup>Cl<sub>4</sub>]<sup>-</sup> to be the dominant Fe<sup>III</sup> component.

occur, at a molar ratio of 2:1. The formation of [FeL<sub>6</sub>]<sup>2+</sup> is driven by the charge balance. Addition of one equivalent of TBA-Br to a solution of FeBr<sub>2</sub> in 2-butanone almost quantitatively yields [FeBr<sub>3</sub>L]<sup>-</sup> (Table 4.2). The distribution of Fe<sup>II</sup> species along the series in Scheme 4.1 thus primarily occurs in a highly polar solvent environment.

The information about the speciation of Fe<sup>II</sup> complexes in different solvent environments, as obtained from both FT-NIR and Mössbauer

**Table 4.2:** Relative amounts of Fe<sup>II</sup> complexes in different solvent environments with or without added TBA-X as determined via FT-NIR (entries 1 – 2 and 5), by Mössbauer spectroscopy (entry 3) and by a combination of both techniques (entry 4). The uncertainty of the tabulated relative amounts should be better than ±15 %.

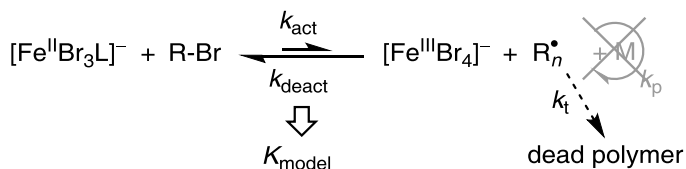
entry	MeCN / mol%	[TBA-X] / equiv of Fe <sup>II</sup>	[FeL <sub>6</sub> ] <sup>2+</sup> / % [Fe <sup>II</sup> ] <sub>tot</sub>	[FeX <sub>2</sub> L <sub>2</sub> ] % [Fe <sup>II</sup> ] <sub>tot</sub>	[FeX <sub>3</sub> L] <sup>-</sup> % [Fe <sup>II</sup> ] <sub>tot</sub>	[Fe <sup>II</sup> X <sub>4</sub> ] <sup>2-</sup> % [Fe <sup>II</sup> ] <sub>tot</sub>
1	100 [a]	0	34	15	34	17
2	16 [a]	0	21	40	36	3
3	0 [b]	0	≈ 33	-	≈ 66	-
4	0 [b]	1	-	-	> 90	-
2	16 [a]	0	21	40	36	3
5 [c]	16 [a]	0	30	22	36	12

[a] cosolvent: CDCl<sub>3</sub>, [b] solvent: 2-butanone, [c] at 2000 bar.

spectroscopy, is summarized in Table 4.2. The NIR spectra shown in Figure 4.1–4.3 provide relative changes, whereas Mössbauer spectroscopy yields absolute concentrations via the relative amounts of iron species at known overall iron content. Estimates of concentrations from NIR spectra employ charge balance considerations. The uncertainty of the molar percentages listed in Table 4.2 should be below ±15 %, irrespective of chloride or bromide being the halide species. Speciation of Fe<sup>II</sup> in pure MeCN-d<sub>3</sub> (entry 1) from FT-NIR is in remarkable agreement with the values obtained via Mössbauer spectroscopy (cf. Table 4.1, entry 3) for dissolution in pure NMP: 17 vs 18 % for [Fe<sup>II</sup>X<sub>4</sub>]<sup>2-</sup>; 34 vs 28 % for [Fe<sup>II</sup>L<sub>6</sub>]<sup>2+</sup>, and 49 vs 54 % for the sum of [FeX<sub>2</sub>L<sub>2</sub>] and [Fe<sup>II</sup>X<sub>3</sub>L]<sup>-</sup> concentrations.

#### 4.1.2 Measurement of ATRP Rate Coefficients

It appeared particularly interesting to correlate the structural analysis of the complexes in monomer-free model systems with measurements of the activation and deactivation rate coefficients,  $k_{\text{act}}$  and  $k_{\text{deact}}$ , respectively. For this purpose, a novel evaluation strategy was



**Scheme 4.2:** Mechanism for iron-bromide-mediated ATRP model systems; R-X refers to the dormant alkyl halide species, R<sup>•</sup> to the radical species and  $k_t$  to the termination rate coefficient. Due to the absence of monomer, M, propagation cannot occur.

developed, which allows for determination of  $k_{\text{act}}$  and  $k_{\text{deact}}$  in a single experiment. The ratio of  $k_{\text{act}}$  and  $k_{\text{deact}}$  is referred to as  $K_{\text{model}}$ , whereas  $K_{\text{ATRP}}$  refers to the ratio of these coefficients for an actual polymerization.

Shown in Scheme 4.2 is the mechanism for iron-bromide-mediated ATRP model systems. The absence of monomer yields a simplified scenario by excluding chain-length dependent polymerization kinetics. The reaction of  $[\text{Fe}^{\text{III}}\text{Br}_3\text{L}]^-$  with, e.g., ethyl 2-bromophenylacetate, EBrPA, as the alkyl halide results in oxidation to  $[\text{Fe}^{\text{III}}\text{Br}_4]^-$ . The accumulation of  $[\text{Fe}^{\text{III}}\text{Br}_4]^-$ , which is concurrent with termination of transient radicals according to Scheme 4.2, is referred to as *persistent radical effect* (PRE)<sup>156</sup> and may be monitored via the ligand-to-metal charge transfer (LMCT) absorption at 21 200  $\text{cm}^{-1}$  (Figure 4.5). The reaction rate may be controlled by adjusting the catalyst and initiator concentrations.

Alternatively,  $[\text{Fe}^{\text{III}}\text{Br}_4]^-$  concentration may be measured via the d-d transition between 9000 and 15 500  $\text{cm}^{-1}$  (Figure 4.6) in experiments started with higher Fe<sup>II</sup> concentrations.<sup>166</sup> The increase in  $[\text{Fe}^{\text{III}}\text{Br}_4]^-$  concentration with time is quantitatively measured by integration of the absorbance between 13 600–12 225  $\text{cm}^{-1}$  against a straight line passing through the absorbance points at these lower and higher limiting wavenumbers. Integration was performed over this low-wavenumber half-band of the Fe<sup>III</sup>-complex absorbance, as the sensitivity of the silicon diode detector is higher than in the 14 900–13 600  $\text{cm}^{-1}$  region. Quantitative analysis via integrated absorbances is mostly preferable over analysis via absorbance at the peak maximum position, as Beer-Lambert's law better holds for vibrational intensity than for absorbance

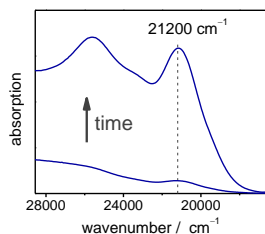


**Figure 4.5:** Plot of the  $[\text{Fe}^{\text{III}}\text{Br}_4]^-$  concentration as a function of time for the reaction of 0.67 mM  $\text{FeBr}_2$  and 0.68 mM  $\text{EBrPA}$  in solution of 2-butanone with 53 mM NMP at 60 °C.  $[\text{Fe}^{\text{III}}\text{Br}_4]^-$  is monitored via the associated absorbance at 21 200  $\text{cm}^{-1}$ .

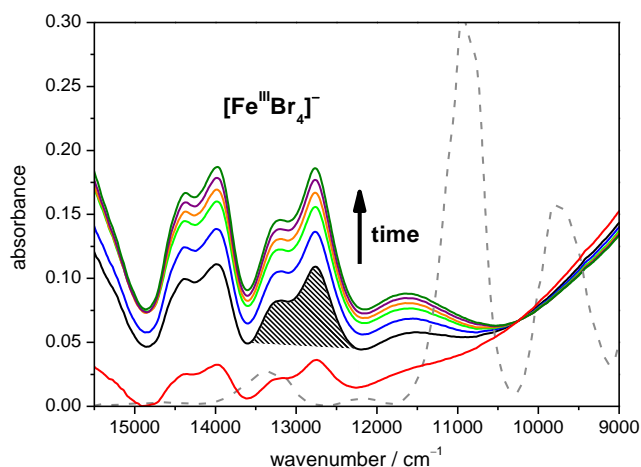


**Figure 4.6:** VIS/NIR spectral series of the  $[\text{Fe}^{\text{III}}\text{Br}_4]^-$  species as measured during the reaction of 10.0 mM  $\text{FeBr}_2$  with 33.3 mM  $\text{EBrPA}$  in NMP at 60 °C; optical path length:  $d = 35.72$  mm. By means of separately measured pure solvent spectra, the solvent absorption (dashed gray line) has been subtracted. The hatched area gives an example of the integration procedure by which  $[\text{Fe}^{\text{III}}\text{Br}_4]^-$  concentration is determined from the spectra.

at a specific wavelength. Calibration for quantitative analysis has been carried out via integrated absorbances using mixtures of 5 mM  $\text{FeBr}_3$  and of 10 mM  $\text{FeBr}_2$  without initiator.

In principle, the reaction may also be monitored via the decrease of absorbance of d–d-transitions of the  $\text{Fe}^{\text{II}}$  species centered around 4000 to

6000 cm<sup>-1</sup> (Figure 4.3). Quantitative and time-resolved analysis of the Fe<sup>III</sup> species is, however, more appropriate because of the absence of strong background absorption of the solvent.

The measurement of [Fe<sup>III</sup>Br<sub>4</sub>]<sup>-</sup> vs time consists of two parts (Figure 4.7): The pre-equilibrium state and the equilibrium state. First,  $K_{\text{model}}$  is evaluated from the equilibrium state according to a reported procedure:<sup>36</sup> Equation 4.1 presents a modified expression for the PRE, which, in contrast to the classic equations by Fischer<sup>156</sup> and Goto and Fukuda,<sup>157</sup> is also applicable to high-conversion systems.<sup>36</sup> [I]<sub>0</sub> refers to [EBrPA] at time zero, [C]<sub>0</sub> to [Fe<sup>II</sup>]<sub>0</sub>, and [Y] to [Fe<sup>III</sup>Br<sub>4</sub>]<sup>-</sup>.<sup>36</sup> The integrated expression is given by Equations 3.8–3.10 in chapter 3.2.2.

$$F([Y]) = \int_0^Y \frac{[Y]^2}{([I]_0 - [Y])^2 ([C]_0 - [Y])^2} d[Y] = 2 \cdot k_t \cdot K_{\text{ATRP}}^2 \cdot t \quad (4.1)$$

The estimate of  $k_t$ , which is required for using Equation 4.1, is carried out via the diffusion-controlled rate<sup>166</sup> which scales with fluidity.<sup>200</sup> An alternative approach for estimating  $k_t$  of the ATRP model system is based on using the composite-model parameter  $k_t^{1,1}$ , which is obtained from pulsed-laser experiments for termination of two radicals of chain length unity after adjustment to the actual solvent viscosity.<sup>92,93</sup> The  $k_t$  values deduced by these two approaches differ by a factor of four, which translates into  $K_{\text{model}}$  being uncertain within a factor of two. The uncertainty of  $k_t$  is considered to have the strongest impact on the accuracy of  $K_{\text{model}}$ . The estimates of  $k_t$  via diffusion control (i.e., via fluidity) were used to determine  $K_{\text{model}}$  if not indicated otherwise.

The evaluation proceeds via a straight-line fit of  $F(Y)$  under equilibrium conditions as illustrates in Figure 4.8. Analysis of  $F(Y)$  and the estimate of  $k_t = 3.0 \times 10^9 \text{ Lmol}^{-1}\text{s}^{-1}$  from fluidity yields  $K_{\text{model}} = 6.0 \times 10^{-7}$  for the reaction of 0.67 mM FeBr<sub>2</sub> and 0.68 mM EBrPA in solution of 2-butanone and NMP (53 mM) at 60 °C.

It should be noted that  $K_{\text{model}}$ , which refers to total Fe<sup>II</sup> content, is obtained from total Fe concentration and measured [Fe<sup>III</sup>Br<sub>4</sub>]<sup>-</sup>. The simplification of using total Fe<sup>II</sup> rather than [Fe<sup>II</sup>Br<sub>3</sub>L]<sup>-</sup> concentration is based on the fact that the individual Fe<sup>II</sup> species are in chemical equilibrium. The results are not indicative of any impact of halogen transfer from Fe<sup>II</sup> to yield the Lewis acidic complex [Fe<sup>III</sup>Br<sub>4</sub>]<sup>-</sup>, even in

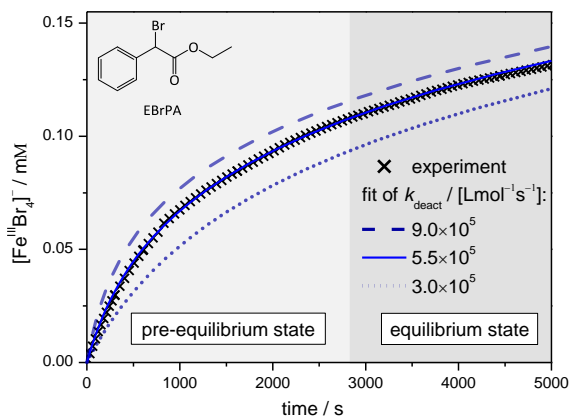


**Figure 4.7:** Plot of  $[\text{Fe}^{\text{III}}\text{Br}_4]^-$  concentration vs time for the reaction of 0.67 mM  $\text{FeBr}_2$  and 0.68 mM EBrPA in solution of 2-butanone and NMP (53 mM) at 60 °C.  $k_{\text{deact}}$  was obtained by fitting the NIR-spectroscopically measured  $[\text{Fe}^{\text{III}}\text{Br}_4]^-$  concentration vs time trace using the measured value of  $K_{\text{model}}$  obtained under equilibrium conditions.

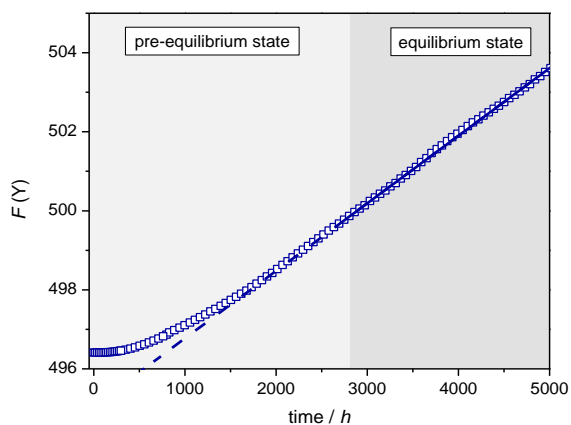


**Figure 4.8:** Plot of the function  $F[Y]$  vs time for the reaction of 0.67 mM  $\text{FeBr}_2$  and 0.68 mM EBrPA in solution of 2-butanone with 53 mM NMP at 60 °C. The close agreement of the straight-line fit with the experimental data for  $t > 2800$  s indicates that the equilibrium has been established for the activation and deactivation reactions.

the absence of TBA-Br or at high conversion, i.e., up to 90 %  $[\text{Fe}^{\text{II}}\text{Br}_3\text{L}]^-$  being transformed to  $[\text{Fe}^{\text{III}}\text{Br}_4]^-$ . Well-controlled ATRPs operate at a rather constant  $\text{Fe}^{\text{II}} : \text{Fe}^{\text{III}}$  ratio,<sup>105</sup> which prevents any major impact of halogen transfer.

The second evaluation step consists of modeling the pre-equilibrium data, according to Scheme 4.2, via the PREDICI program package. Due to monomer being absent, the ATRP mechanism reduces to only three elementary reactions of activation, deactivation, and termination.  $k_t$  is introduced as estimated via diffusion control. The measured value of  $K_{\text{model}}$  is used to substitute  $k_{\text{act}}$  by  $K_{\text{model}} \times k_{\text{deact}}$ . The rate coefficient  $k_{\text{deact}}$  is obtained by fitting the experimental  $[\text{Fe}^{\text{III}}\text{Br}_4]^-$  concentration vs time data. Figure 4.7 illustrates the close agreement of modeled and measured data by both lowering and enhancing  $k_{\text{deact}}$  by a factor of about 1.7. The simulations may also be applied toward selecting suitable catalyst and initiator concentrations. Low catalyst and initiator concentrations should be used to expand the pre-equilibrium region.

The outlined novel procedure is particularly attractive since all rate coefficients are accessible from a single experiment. With Cu catalysis, the established procedure for measuring  $k_{\text{act}}$  is by radical trapping with 2,2,6,6-tetramethyl-1-piperidinyloxy (TEMPO).<sup>35,39</sup> This approach, however, fails with Fe-mediated system, since  $\text{Fe}^{\text{II}}$  is oxidized by TEMPO.

The activation–deactivation–equilibrium constant,  $K_{\text{ATRP}}$ , may also be determined from an actual polymerization; for details see chapters 4.2.3 and 6.3.2. As with analyzing  $K_{\text{model}}$ , the measurement of  $K_{\text{ATRP}}$  involves online spectroscopic detection of the conversion of the  $\text{Fe}^{\text{III}}$  complex (or alternatively of  $\text{Fe}^{\text{II}}$ ), and additionally of polymerization rate. The results for  $K_{\text{model}}$  and  $K_{\text{ATRP}}$  measured at 60 °C and ambient pressure will be discussed in the following. Measurements over an extended pressure and temperature range are detailed in chapter 6.3.

### 4.1.3 Analysis of ATRP Rate Coefficients

According to the speciation analysis from chapter 4.1.1, the active ATRP species are  $[\text{Fe}^{\text{II}}\text{Br}_3(\text{Solv})]^- / [\text{Fe}^{\text{III}}\text{Br}_4]^-$ . As the d-d transition energy for the  $\text{Fe}^{\text{II}}$  mediator is sensitive to the type of solvent coordinated  $\text{Fe}^{\text{II}}$ , it was checked whether solvent variation also affects absolute  $K_{\text{model}}$  and  $K_{\text{ATRP}}$ .



As compared to the experiments for speciation analysis,  $\text{CDCl}_3$  was replaced by anisole or 2-butanone, as measurements were carried out at elevated temperature, i.e., at 60 °C. Such conditions are close to the ones for ATRP with the same catalyst.<sup>81,82</sup> Different amounts of NMP were added as a polar solvent, which should yield stronger coordination to  $\text{Fe}^{\text{II}}$ . TBA-OTf was added to mixtures with less than 10 mol% NMP to achieve solubility of  $\text{Fe}^{\text{II}}$ . The addition of TBA-OTf does not affect the equilibrium constant to any measurable extent, which is consistent with observations reported by the Matyjaszewski group.<sup>81</sup> This insensitivity indicates that the enhanced solubility is primarily due to the effect of charge separation by the large  $\text{OTf}^-$  ions rather than by strong metal- $\text{OTf}^-$  interactions.

Plotted in Figure 4.9A are the values of  $K_{\text{model}}$  measured for different binary NMP/anisole solvent compositions. The  $\lg(K_{\text{model}})$  data is plotted vs the molar ratio of NMP to  $\text{Fe}^{\text{II}}$ ,  $\chi_{\text{NMP}}/\chi_{\text{Fe(II)}}$ , i.e. vs the content of the highly polar solvent component relative to Fe. The dependence of  $K_{\text{model}}$  on both the NMP and  $\text{Fe}^{\text{II}}$  mole fraction is confirmed by experiments in a wide range of absolute  $\text{Fe}^{\text{II}}$  and thus NMP concentrations (cf. Figure 4.9A).  $K_{\text{model}}$  in the absence of NMP is by more than two orders of magnitude above the value measured for the highest  $\chi_{\text{NMP}}/\chi_{\text{Fe(II)}}$  in bulk NMP solution. The variation of  $K_{\text{model}}$  with  $\chi_{\text{NMP}}/\chi_{\text{Fe(II)}}$  becomes linear on a double-log scale, as shown in Figure 4.9B. The decadic logarithm ( $\lg$ ) is more easily associated with decimal numbers, and is thus used instead of the natural logarithm ( $\ln$ ). The filled symbols refer to reaction in mixtures of NMP with 2-butanone instead of NMP with anisole (open symbols). The  $K_{\text{model}}$  values are slightly above the values measured for anisole/NMP mixtures. A similar trend of  $K_{\text{ATRP}}$  vs  $\lg(\chi_{\text{NMP}}/\chi_{\text{Fe(II)}}$ ) was found for actual polymerization, i.e., for the ATRP of MMA with different levels of NMP as cosolvent (see chapter 6.3.2).<sup>105</sup>

As indicated by the straight lines in Figure 4.9B, the variation of  $\lg(k_{\text{act}})$  with  $\lg(\chi_{\text{NMP}}/\chi_{\text{Fe(II)}}$ ) is almost identical to the one of  $\lg(K_{\text{model}})$  with  $\lg(\chi_{\text{NMP}}/\chi_{\text{Fe(II)}}$ ). Thus, the variation of  $K_{\text{model}}$  with solvent composition appears to be essentially due to the associated change in  $k_{\text{act}}$  with solvent polarity, i.e., both quantities decrease toward increasing  $\lg(\chi_{\text{NMP}}/\chi_{\text{Fe(II)}}$ ). At the same time,  $k_{\text{deact}}$  increases, but only by about a factor of two in passing from low to high  $\chi_{\text{NMP}}/\chi_{\text{Fe(II)}}$  (cf. Table 4.3). As described in chapter 4.1.1, both lower  $k_{\text{act}}$  and lower  $K_{\text{ATRP}}$  in polar solvents, are not associated with a significant variation of the  $[\text{Fe}^{\text{II}}\text{Br}_3\text{L}]^-$  activator

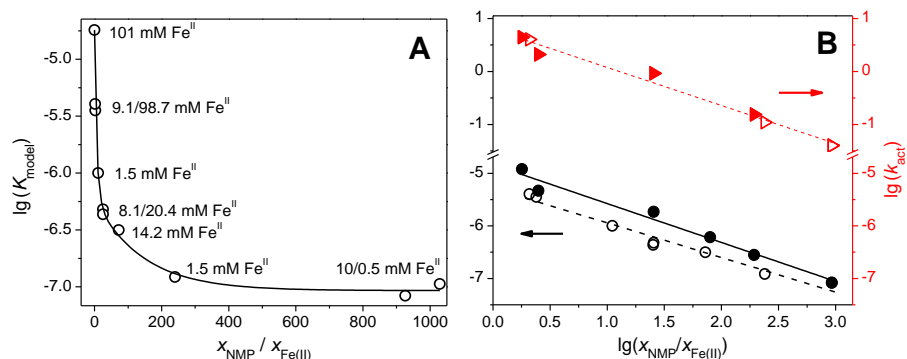


**Figure 4.9:** (A)  $\lg(K_{\text{model}})$  vs  $x_{\text{NMP}}/x_{\text{Fe(II)}}$  and (b)  $\lg(K_{\text{model}})$  vs  $\lg(x_{\text{NMP}}/x_{\text{Fe(II)}}$ ) for the reaction of EBrPA with  $\text{FeBr}_2$  in solution of anisole (empty circles) or 2-butanone (filled symbols) with NMP at 60 °C. Also shown in (B) is the plot of  $\lg(k_{\text{act}})$  vs  $\lg(x_{\text{NMP}}/x_{\text{Fe(II)}}$ ) (triangles). Straight lines have been fitted to the data in (b).

concentration (cf. Figure 4.3). The decrease of  $k_{\text{act}}$  occurs primarily at small amounts of the polar solvent component NMP, i.e., at low  $x_{\text{NMP}}/x_{\text{Fe(II)}}$  (cf. Figure 4.9A). This observation indicates coordination of NMP molecules to  $\text{Fe}^{\text{II}}$ . Similarly, the FT-NIR absorbance of the  $[\text{Fe}^{\text{II}}\text{Br}_3\text{L}]^-$  complex shifts by about  $800\text{ cm}^{-1}$  ( $10\text{ kJmol}^{-1}$ ) to higher energy (Figure 4.3) upon the addition of highly polar acetonitrile. The higher energy for the d-d transition indicates a stabilization of the  $[\text{Fe}^{\text{II}}\text{Br}_3\text{L}]^-$  species. The variations of  $k_{\text{act}}$  and  $K_{\text{ATRP}}$  correspond to a difference in Gibbs energy of about  $13\text{ kJmol}^{-1}$ . The decrease in  $k_{\text{act}}$  should thus essentially be due to the stabilization of  $[\text{Fe}^{\text{II}}\text{Br}_3\text{L}]^-$  in case of the ligand, L, being a highly polar solvent molecule, such as NMP, MeCN, or DMF.<sup>105</sup> The deactivation reaction via the  $[\text{Fe}^{\text{III}}\text{Br}_4]^-$  complex is rather insensitive toward the type of solvent due to the absence of solvent coordination. The findings suggest that iron-based ATRP should favorably be performed in less polar solvents.

The overall situation is clearly different from the one with Cu-mediated ATRP, where  $k_{\text{act}}$  is enhanced toward more polar solvents.<sup>39</sup> The measured  $\ln(k_{\text{act}}(\text{Cu}^{\text{I}}))$  values are directly proportional to non-specific solvent–solute parameters such as the Kamlet-Taft ones. The enhancement of  $k_{\text{act}}(\text{Cu}^{\text{I}})$  is primarily due to the improved stability of the

**Table 4.3:**  $K_{\text{model}}$  and  $k_{\text{deact}}$  at 60 °C for iron-halide-mediated ATRP model systems in different solvents and with added tetrabutylammonium salt.

entry	solvent <sup>[a]</sup> / (=Ligand L)	TBA salt / 1 eq.	initiator	$K_{\text{model}}$ at 60 °C	$k_{\text{deact}} /$ $\text{Lmol}^{-1}\text{s}^{-1}$
1	NMP	-	EBrPA	$1.2 \times 10^{-7}$	$8.0 \times 10^5$
2	2-Bu	TBA-OTf	EBrPA	$1.8 \times 10^{-5}$	$3.3 \times 10^5$
3	2-Bu	TBA-Br	EBrPA	$5.7 \times 10^{-5}$	$2.5 \times 10^5$
4	2-Bu	TBA-Br	PMMA-Br	$1.0 \times 10^{-5}$	$5.0 \times 10^5$

<sup>[a]</sup> 2-Bu = 2-butanone.

$\text{Cu}^{\text{II}}$  deactivator complex and of the associated transition state because of their dipolar character.<sup>39</sup>

A selection of absolute  $K_{\text{model}}$  in different solvent environments and with different amounts of added tetrabutylammonium halides is listed in Table 4.3.  $K_{\text{model}}$  and thus  $K_{\text{ATRP}}$  may be efficiently tuned by suitable selection of the solvent to yield an optimum ATRP performance for a specified class of monomers. Iron-catalyzed ATRP in the presence of NMP offers a high degree of livingness at low  $K_{\text{ATRP}}$  (cf.  $K_{\text{model}}$  entry 1).<sup>82</sup> On the other hand,  $K_{\text{ATRP}}$  may be significantly enhanced by replacement of NMP by less polar solvents such as ketones (cf.  $K_{\text{model}}$  entry 2), esters, and substituted benzenes, which may allow for high-performance ICAR-ATRP.<sup>83,84</sup> In less polar solvents, ammonium salts such as TBA-OTf were added for the better solubility of the catalyst (entry 2). Adding 1 equivalent of TBA-Br to  $\text{FeBr}_2$  in 2-butanone almost quantitatively produces  $[\text{Fe}^{\text{II}}\text{Br}_3\text{L}]^-$  and further enhances  $K_{\text{model}}$  by about a factor of three (entry 3).

Absolute  $K_{\text{ATRP}}$  depends on the type of alkyl halide and may be affected by radical chain length.<sup>102,201</sup> To mimic both the type of halide-capped radical species and chain size in the ATRP of MMA, a poly(MMA)-Br initiator with a high degree of chain-end functionality has been used (see chapter 8.3 for ICAR-ATRP synthesis of poly(MMA)-Br with  $M_n \approx 8000 \text{ g mol}^{-1}$ ).<sup>83</sup> As the degree of chain-end functionality in ICAR-ATRP may be controlled by sensible selection of the initial molar ratio of reagents, the amount of terminated chains cannot exceed 3 % of the total number of chains. Solvent selection is

particularly important for the model systems with poly(MMA)-Br, as the solvent replaces the monomer as complexing species. *Isobutyrate*, which may be looked upon as “saturated” MMA, cannot be applied due to the poor solubility provided for Fe-species, even in the presence of NMP or other ammonium salts. The number for  $K_{\text{model}}$  in solution of 2-butanone (Table 4.3, entry 4) is in excellent agreement with  $K_{\text{ATRP}}$  measured during an actual iron-mediated ATRP of MMA (Table 4.4, entry 1). It should be noted that the chain-length dependent  $k_t$  value was taken for the analysis of  $K_{\text{model}}(\text{poly(MMA)-Br})$ . The number is available from independent pulsed laser experiments<sup>202</sup> and was corrected for actual solvent viscosity.<sup>200,203-209</sup>

As seen with the monomer-free model systems, using 1 equiv TBA-Br instead of TBA-OTf enhances  $K_{\text{ATRP}}$  by about a factor of four (Table 4.4, entries 1 and 2). Addition of a second equivalent of TBA-Br reduces  $K_{\text{ATRP}}$  by about one order of magnitude (entry 3), which is assigned to  $[\text{Fe}^{\text{II}}\text{Br}_3\text{L}]^-$  being transformed into catalytically less active  $[\text{Fe}^{\text{II}}\text{Br}_4]^{2-}$  (see Figure 4.1). As with the model systems,  $K_{\text{ATRP}}$  with NMP as cosolvent (entry 4) is by more than two orders below the value in bulk MMA with the TBA-OTf additive (entry 2).

The Fe-based system  $[\text{Fe}^{\text{II}}\text{Br}_3(\text{Solv})]^-$  in less polar solvents with the TBA-Br additive,  $K_{\text{ATRP}}(\text{MMA}) \approx 1 \times 10^{-5}$  at 60 °C, may be an attractive alternative to, e.g., the Cu/PMDETA catalyst, for which the reported  $K_{\text{ATRP}}(\text{MMA})$  at 25 °C amounts to  $1.6 \times 10^{-5}$  (entry 5).<sup>102</sup> In Cu catalysis,  $K_{\text{ATRP}}$  increases upon ligand variation in passing from bipy < HMTETA < PMDETA < TPMA < Me<sub>6</sub>TREN (for the structures see ref. <sup>35</sup>) by about four orders of magnitude. Tuning of  $K_{\text{ATRP}}$  with the  $[\text{Fe}^{\text{II}}\text{Br}_3(\text{Solv})]^-$  system may be carried out by simple solvent variation without the need of adding external ligands. However,  $[\text{Fe}^{\text{II}}\text{Br}_3(\text{Solv})]^-$  cannot compete with the catalytic performance of highly active Cu catalysts such as Cu/TPMA or Cu/Me<sub>6</sub>TREN.<sup>210</sup>

Modifications of the iron halide catalyst by adding monodentate ligands, such as amines, phosphines or carbenes have been frequently used.<sup>52-55,57,59,60,63-65,80,211,212</sup> Interestingly, the reported monomer conversion vs time data suggests no significant enhancement of  $K_{\text{ATRP}}$  upon the addition of these ligands in comparison to ligand-free FeBr<sub>2</sub>/TBA-Br catalysis,<sup>14</sup> when the relative amounts of catalyst and initiator as well as polymerization temperature are taken into account.

**Table 4.4:**  $K_{\text{ATRP}}$  for iron-mediated ATRPs of MMA at 60 °C in different solvents and with the indicated additives.

entry	monomer / solvent	additives	equiv. rel. to Fe	$K_{\text{ATRP}}$ at 60 °C
1	MMA	TBA-Br	1	$9.7 \times 10^{-6}$
2	MMA	TBA-OTf	1	$2.2 \times 10^{-6}$
3	MMA/2-Bu <sup>[a]</sup>	TBA-Br	2	$6.4 \times 10^{-7}$
4	MMA/NMP <sup>[a]</sup>	-	-	$1.4 \times 10^{-8}$ <sup>[c]</sup>
<b>Cu catalysis:</b>		<b>ligand</b>	rel. to Cu	$K_{\text{ATRP}}$ at 25 °C
5	MMA/MeCN <sup>[a]</sup>	PMDETA <sup>[b]</sup>	1	$1.6 \times 10^{-5}$ <sup>[102]</sup>

<sup>[a]</sup> Ratio of MMA : solvent = 1 : 1; <sup>[b]</sup> PMDETA = *N,N,N',N'',N'''*-pentamethyldiethylenetriamine; <sup>[c]</sup> mean value from a 1:2 and 2:1 monomer/solvent mixture.<sup>105</sup>

The speciation analysis should be helpful for arriving at a better understanding of these Fe–ligand systems, which are derived from iron halides. Selected systems will be studied in the following chapters and  $K_{\text{ATRP}}$  will be determined. A novel type of Fe catalyst will be explored in chapters 5.1 and 6.4.

## 4.2 Iron Halide Catalysts with Additional Ligands

### 4.2.1 *N*-Heterocyclic Carbenes

The complexes  $[\text{Fe}^{\text{II}}\text{Br}_3\text{L}]^- / [\text{Fe}^{\text{III}}\text{Br}_4]^-$  with L being a solvent molecule are active ATRP mediators. The composition of these species is very similar in the case that the ligand, L, is a *N*-heterocyclic carbene such as HIDipp (see Figure 4.10):  $[\text{Fe}^{\text{III}}\text{Br}_3(\text{HIDipp})]$  was isolated after adding HIDipp to a solution of  $\text{FeBr}_3$ .<sup>211</sup> As compared to  $[\text{Fe}^{\text{III}}\text{Br}_4]^-$ , one bromide is replaced by the HIDipp ligand. The associated  $\text{Fe}^{\text{II}}$  complex usually occurs as a dimer,  $[\text{Fe}_2\text{Br}_2(\mu\text{-Br})_2(\text{HIDipp})_2]$ , but may be monomeric,  $[\text{FeBr}_2(\text{HIDipp})_2]$ , when two equivalents of HIDipp are added.<sup>213</sup>

ATRP of MMA in solution of anisole (50 vol%) was carried out in the reverse fashion by reaction of  $[\text{Fe}^{\text{III}}\text{Br}_3(\text{HIDipp})]$  with radicals being produced by decomposition of the azo initiator V-70. In this way, the  $\text{Fe}^{\text{II}}$  species and alkyl halide are produced *in situ*. The reaction was started at 80 °C, where rapid V-70 decomposition ensures rapid formation of alkyl halide. The short initiation interval assures a well-controlled ATRP with narrow molar mass distribution. The reaction mixture was subsequently cooled to 60 °C and ATRP continued for 25 h, which yielded 52 % monomer conversion and a dispersity of 1.04. The concentrations of  $[\text{Fe}^{\text{III}}\text{Br}_3(\text{HIDipp})]$  as well as monomer conversion were monitored via online NIR spectroscopy (Figure 4.11). The absorption pattern of  $[\text{Fe}^{\text{III}}\text{Br}_3(\text{HIDipp})]$  is similar to  $[\text{Fe}^{\text{III}}\text{Br}_4]^-$ . The  $\text{Fe}^{\text{II}}$  species does, however, not occur at a measureable intensity within the wavenumber range covered in Figure 4.11.

The mean value for  $K_{\text{ATRP}} = 2.3 \times 10^{-6}$  (r.h.s. of Figure 4.11) is close to the number measured with  $[\text{Fe}^{\text{III}}\text{Br}_4]^-$  being the catalyst,  $K_{\text{ATRP}} = 2.2 \times 10^{-6}$  (Table 4.4, entry 2). Nevertheless, *N*-heterocyclic carbenes as ligands to iron halides may be preferable in that they improve catalyst solubility and robustness at ppm concentrations.<sup>211</sup>

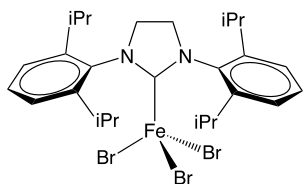


**Figure 4.10:**  $[\text{Fe}^{\text{III}}\text{Br}_3(\text{HIDipp})]$ , where  $\text{HIDipp} = 1,3\text{-bis}(2,6\text{-di-}i\text{-propylphenyl})4,5\text{-dihydroimidazol-2-ylidene}$ .

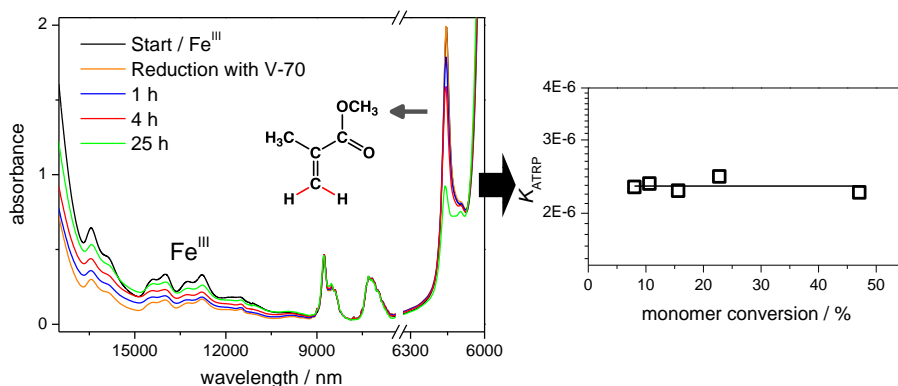


**Figure 4.11:** (L.h.s.) VIS/NIR spectra measured during a reverse ATRP of MMA at  $60\text{ }^\circ\text{C}$  mediated by  $10\text{ mM } [\text{Fe}^{\text{III}}\text{Br}_3(\text{HIDipp})]$  with  $0.6$  equiv of V-70 acting as the azo initiator in solution of anisole ( $50\text{ vol}\%$ ). The online NIR-spectroscopic monitoring of  $\text{Fe}^{\text{III}}$  and of monomer conversion yields  $K_{\text{ATRP}}$  (r.h.s. figure) as described in, e.g., chapter 4.2.3.

#### 4.2.2 TPMA and TPMA\*

Multidentate amines are common ligands for Cu-based ATRP. Conversely, such ligands are scarcely used for Fe–ligand catalyst formation.<sup>214,215</sup> Tris(2-pyridylmethyl)-amine (TPMA) and, in particular, the substituted analogue, tris([(4-methoxy-2,5-dimethyl)-2-pyridyl]methyl)amine (TPMA\*), Figure 4.12, yield highly active Cu–ligand systems and were thus screened for potential use in Fe-based catalysis.<sup>210</sup>

However, none of the two ligands provided active Fe–ligand combinations when being added in stoichiometric amounts, either to  $\text{FeBr}_2$  or to  $\text{Fe}(\text{OTf})_2$ . Attempts to polymerize MMA with EBrPA as the

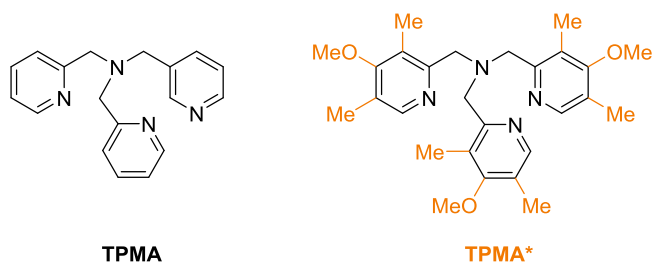


**Figure 4.12:** Tris(2-pyridylmethyl)-amine (TPMA) and tris([(4-methoxy-2,5-dimethyl)-2-pyridyl] methyl)amine (TPMA\*).

initiator at 60 °C were unsuccessful with almost no monomer conversion being observed after 20 h and with large dispersity,  $\mathcal{D} > 3$ , of the resulting oligomer. Further experiments were performed with substoichiometric amounts of the ligand to Fe. TPMA\* is preferable over TPMA due to the solubility of the resulting Fe complexes in less polar solvents such as 2-butanone, propylene carbonate or even toluene if TBA-OTf is also added (see below).

Shown in Figure 4.13 are VIS/NIR spectra measured during ATRP of MMA in solution of 2-butanone (50 vol%) at 60 °C starting with the following initial molar ratio of reagents: [MMA] : [FeBr<sub>2</sub>] : [TPMA\*] : [EBrPA] : [TBA-OTf] = 333 : 2.00 : 1.00 : 1.00 : 3.00, i.e., with just 0.5 equiv of TPMA\* with respect to FeBr<sub>2</sub>. The intensity of the absorption band at around 10 000 cm<sup>-1</sup> assigned to the Fe<sup>II</sup>/TPMA\* complex (probably [Fe<sup>II</sup>(TPMA\*)]<sup>2+</sup>)<sup>216-218</sup> remains constant in the spectra recorded over 20 h, indicating that the complex neither reacts with alkyl halide, nor equilibrates into ATRP-active Fe<sup>II</sup> species. Due to the substoichiometric amount of TPMA\*, the [Fe<sup>II</sup>Br<sub>3</sub>L]<sup>-</sup> and [Fe<sup>III</sup>Br<sub>4</sub>]<sup>-</sup> species are also present and are assigned to be the mediators of ATRP. Eckenhoff et al. came to a similar conclusion after studying several Fe-halide-based catalysts, which contained 0.5 equiv of a multidentate amine.<sup>45</sup>

$K_{\text{ATRP}}(60\text{ °C}) = 7.1 \times 10^{-6}$ , which was determined based on the concentrations of [Fe<sup>II</sup>Br<sub>3</sub>L]<sup>-</sup> and [Fe<sup>III</sup>Br<sub>4</sub>]<sup>-</sup>, is almost identical to the value found for the FeBr<sub>2</sub>/TBABr system in the absence of TPMA\*,  $K_{\text{ATRP}} = 9.7 \times 10^{-6}$  (cf. Table 4.4). Adding substoichiometric amounts of TPMA\* has no effect on  $K_{\text{ATRP}}$  and ATRP is equally well-controlled,  $\mathcal{D} = 1.10$ , with 70 % monomer conversion being reached after 20 h.



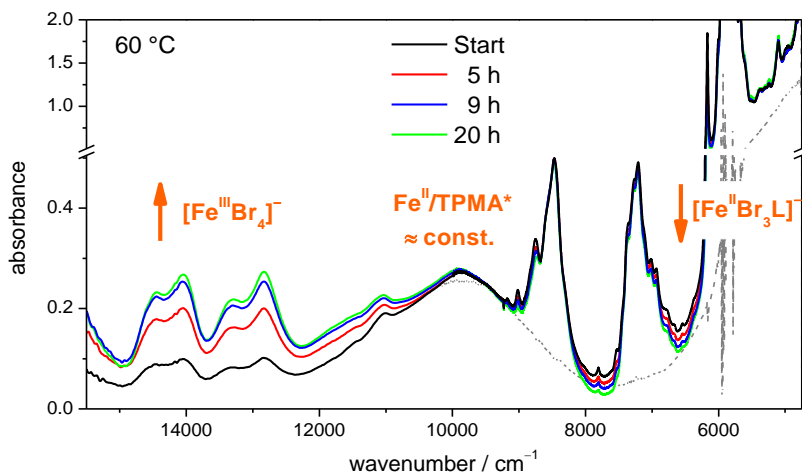


**Figure 4.13:** VIS/NIR spectra measured during ATRP of MMA starting with  $\text{FeBr}_2 : \text{TPMA}^* : \text{EBrPA} = 2 : 1 : 1$  in solution of 2-butanone (50 vol%) at 60 °C.  $[\text{Fe}^{\text{III}}\text{Br}_4]^-$ , the  $\text{Fe}^{\text{II}}/\text{TPMA}^*$  complex, and  $[\text{Fe}^{\text{II}}\text{Br}_3\text{L}]^-$  may be monitored at separate positions. The spectra recorded over 20 h indicate that  $[\text{Fe}^{\text{II}}\text{Br}_3\text{L}]^-$  is transformed to  $[\text{Fe}^{\text{III}}\text{Br}_4]^-$ , whereas the  $\text{Fe}^{\text{II}}/\text{TPMA}^*$  complex is not consumed. The dashed gray line illustrates the absorption pattern of  $[\text{Fe}^{\text{II}}\text{Br}_3\text{L}]^-$  for the initial spectrum after subtraction of solvent absorption.

### 4.2.3 Triarylphosphines<sup>2</sup>

Phosphines are among the most frequently used additives in iron-mediated ATRP<sup>4,48</sup> and generate economic and robust Fe catalysts. Their influence on the rate and degree of control over an ATRP has been studied for several monomers,<sup>52-56</sup> such as styrene<sup>53,55,59-61,219,220</sup> and methyl methacrylate (MMA).<sup>52-55,57-65,212</sup> It is recommendable to add the iron catalyst to the polymerization medium in the less air-sensitive, higher oxidation state,  $\text{Fe}^{\text{III}}$ , which requires its reduction to start ATRP. Iron-mediated ATRP with phosphines has been effectively carried out in the presence<sup>8,48,54,58,63-65,212</sup> and in the absence<sup>57,220</sup> of external reducing agents. The results suggest that phosphines themselves may reduce  $\text{Fe}^{\text{III}}$ .<sup>8,53</sup> It was found that substituted, electron-rich phosphines accelerate

<sup>2</sup> Reproduced with permission from Schroeder, H.; Matyjaszewski, K.; Buback, M. *Macromolecules* **2015**, *48*, 4431–4437, Copyright 2015 American Chemical Society.

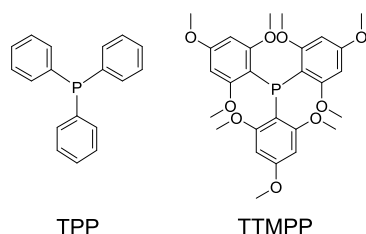
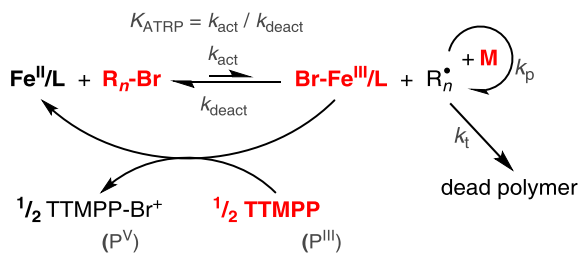


**Figure 4.14:** TPP (triphenylphosphine) and tris(2,4,6-trimethoxyphenyl)phosphine (TTMPP).

polymerization<sup>52,53</sup> and improve functional group tolerance which allowed for copolymerizations with HEMA<sup>52</sup> and enabled conducting an ATRP in the presence of methanol.<sup>54</sup> Iron/phosphine-catalyzed ATRP even operates in the absence of an alkyl halide or a thermal initiator.<sup>48,60,212,221-224</sup> Dass et al. reported that dipolar interactions between the carbonyl oxygen of MMA and the phosphorus atom are mediated by the presence of the iron(III) halide complex.<sup>222,223</sup> The so-induced catalytic formation of 1,2-dihaloisobutyrate was detected via NMR spectroscopy.<sup>60</sup> Such *in situ* initiator formation is referred to as generation of activators by monomer addition (GAMA) ATRP.<sup>48</sup> Phosphine presents an essential additive for GAMA ATRP, since FeBr<sub>3</sub> by itself retards radical polymerization.<sup>53</sup>

However, full understanding of the ability of different types of phosphines to act as ligand,<sup>4,48</sup> reducing agent<sup>48,53</sup> or assistant for chain initiation<sup>4,48,60</sup> has not yet been attained. It is a matter of priority to clarify the specific roles of phosphine and to achieve further mechanistic insight. Therefore, phosphine-assisted Fe-mediated ATRPs and associated monomer-free model systems were monitored via online VIS/NIR spectroscopy. In addition,  $K_{\text{ATRP}}$  was measured for the ATRP of styrene, MMA, and BA. Of primary interest among the triarylphosphine additives (Figure 4.14) is tris(2,4,6-trimethoxyphenyl)phosphine (TTMPP), which has been reported to reduce iron(III) halides to iron(II) compounds and is highly Lewis basic<sup>225</sup> ( $\text{p}K_{\text{a}} = 11.2$ ).<sup>48,226,227</sup> The rate of this reaction was also studied via online spectroscopic monitoring.

The ATRPs were started in the reverse fashion with the Fe catalyst added to the reaction in the higher oxidation state, Fe<sup>III</sup>, as illustrated in Scheme 4.3. The reagents marked in red, i.e., the alkyl halide initiator, the Br-Fe<sup>III</sup>/L complex, TTMPP, and monomer, M, are the initial components. The formation of the Fe<sup>II</sup>/L activator complex is expected to



**Scheme 4.3:** Iron-mediated ATRP involving  $\text{Fe}^{\text{II}}$  and  $\text{Fe}^{\text{III}}$  complexes. TTMPP acts as the reducing agent for the  $\text{Fe}^{\text{III}}$  complex. The type of ligand, L, coordinated to iron will be specified below.  $\text{R}_n\text{-Br}$  refers to deactivated chains,  $\text{R}_n^{\bullet}$  to growing radicals of chain length  $n$ , M to monomer, and  $k_p$  and  $k_t$  to the propagation and the termination rate coefficient, respectively.

occur *in situ* via the reduction of  $\text{Br-Fe}^{\text{III}}/\text{L}$  with TTMPP. The mechanism and the kinetics of this reduction will be discussed in detail below, as will be the type of ligand, L, including Br, the phosphine or solvent.

ATRPs of styrene were carried out at 100 °C in DMF solution (33 vol%) using the following initial molar ratios of reagents:  $[\text{Sty}]:[\text{MBriB}]:[\text{FeBr}_3] = 200 : 1.25 : 1.00$ . The polymerizations were carried out with different levels of TTMPP: 0.5, 1.0, and 1.5 equivalents with respect to  $\text{FeBr}_3$ . Spectroscopic measurements were started just before adding TTMPP to the reaction mixture at the target polymerization temperature. Monomer conversion was monitored between 6250 and 6000  $\text{cm}^{-1}$  via online NIR spectroscopy as illustrated in Figure 4.15A for styrene ATRP with 1.0 equiv of TTMPP. Only seven out of a multitude of spectra recorded over 21 h are shown. The  $\ln([\text{M}]_0/[\text{M}])$  vs time traces for all three levels of TTMPP are illustrated in Figure 4.15B. Especially in the early polymerization stage, ATRP is significantly accelerated upon increasing the amount of added TTMPP. This observation is in agreement with reported data for ATRP carried out in heterogeneous systems with anisole under otherwise similar conditions.<sup>53</sup>

$\text{Br-Fe}^{\text{III}}/\text{L}$  was monitored between wavelengths of 15 000 and 9000  $\text{cm}^{-1}$  as illustrated in Figure 4.15C. This absorption is highest at time zero, prior to adding TTMPP. The  $\text{Br-Fe}^{\text{III}}/\text{L}$  absorption band almost completely disappears upon addition of 1 equiv of TTMPP due to the rapid reaction of  $\text{Br-Fe}^{\text{III}}/\text{L}$  with TTMPP. The associated formation of the

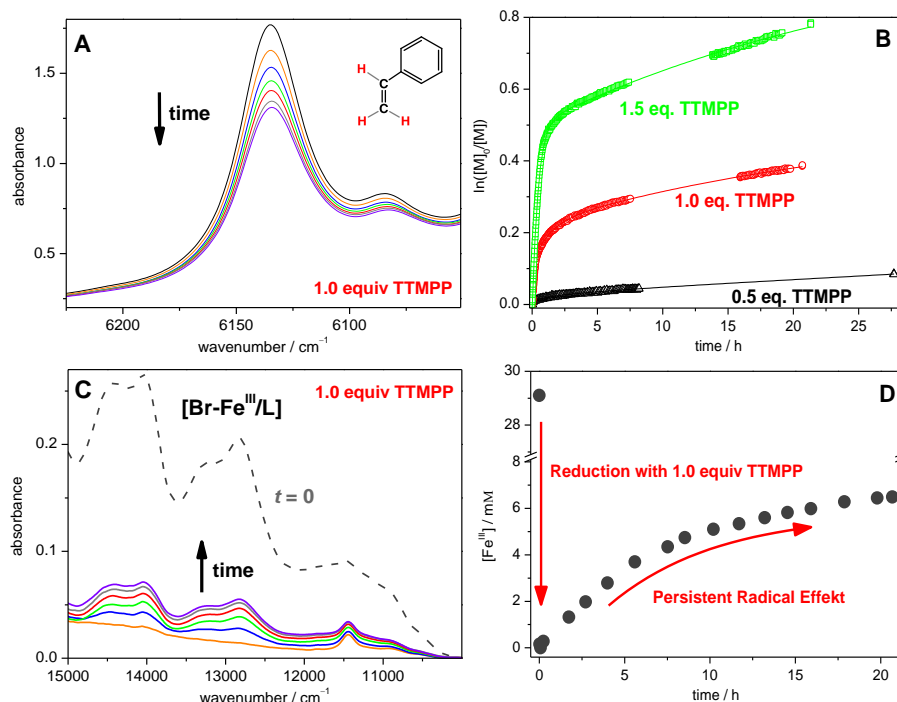


**Figure 4.15:** Kinetics of ATRP monitored via online NIR spectroscopy: (A) Monomer conversion measured between 6250 and 6000  $\text{cm}^{-1}$ ; (B)  $\ln([M]_0/[M])$  vs time traces measured at three levels of TTMPP; (C) Br-Fe<sup>III</sup>/L monitored between 15 000 and 9000  $\text{cm}^{-1}$ ; (D) Br-Fe<sup>III</sup>/L is first reduced by TTMPP and accumulates with reaction time, resulting from radical termination and following the PRE.

Fe<sup>II</sup> redox partner may be evidenced via the absorption between 9000 and 5000  $\text{cm}^{-1}$  (Figure S4) underlying the intense monomer band in Figure 4.15A.<sup>228</sup> No monomer conversion was observed prior to the formation of Fe<sup>II</sup> which indicates that ATRP is initiated via the Fe<sup>II</sup> catalyst complex. The subsequent increase in Br-Fe<sup>III</sup>/L absorption is consistent with the PRE.<sup>156</sup> The measured Br-Fe<sup>III</sup>/L concentration vs time curve is plotted in Figure 4.15D.

The absorption pattern in Figure 4.15C, measured prior to adding TTMPP, was tentatively assigned to Br-Fe<sup>III</sup>/L and is actually due to  $[\text{FeBr}_4]^-$ ,<sup>184,228</sup> the expected primary species present in the absence of

additives:  $[\text{FeBr}_4]^- : [\text{Fe}(\text{Solv})_6]^{3+} \approx 3 : 1$ .<sup>228,166</sup> Quantitative formation of  $[\text{FeBr}_4]^-$  from  $\text{FeBr}_3$  requires additional bromide. The  $\text{Fe}^{\text{II}}$  bromide complex, i.e., the redox partner in ATRP, may serve as a bromide source.<sup>228</sup>  $[\text{FeBr}_4]^-$  should be the only  $\text{Fe}^{\text{III}}$  species as soon as the formation of the  $\text{Fe}^{\text{II}}$  bromide complex allows for bromide transfer to  $\text{Fe}^{\text{III}}$ .<sup>228</sup> Interestingly, no major change in the shape of the  $\text{Fe}^{\text{III}}$  absorption band was observed after adding TTMPP, which suggests that  $[\text{FeBr}_4]^-$  remains the single  $\text{Fe}^{\text{III}}$  species present in the reaction medium.  $\text{Fe}^{\text{III}}$ /TTMPP complexes have not been detected, probably because the reduction of  $\text{Fe}^{\text{III}}$  presents the preferred reaction pathway in ATRPs conducted at elevated temperature. In the following discussion,  $[\text{FeBr}_4]^-$  is assumed to be the single  $\text{Fe}^{\text{III}}$  species present in the reaction medium, thus specifying the structure of the  $\text{Br-Fe}^{\text{III}}/\text{L}$  complex given in Scheme 4.3 and Figure 4.15. Calibration of the  $[\text{FeBr}_4]^-$  concentration vs time traces was performed as described in chapter 4.1.2.

The online spectroscopic measurements indicate that a higher TTMPP content yields progressively higher  $\text{Fe}^{\text{II}} : \text{Fe}^{\text{III}}$  ratios, thus enhancing the rate of the ATRP,  $R_p$ , according to Equation 4.2. The simultaneous measurement of both monomer conversion and  $[\text{FeBr}_4]^-$  concentration allows for the quantitative analysis of  $K_{\text{ATRP}}$  via Equation 4.2.<sup>36</sup>

$$R_p = -\frac{d[\text{M}]}{dt} = k_p \cdot [\text{R}_n^\bullet] \cdot [\text{M}] = k_p \cdot K_{\text{ATRP}} \cdot \frac{[\text{Fe}^{\text{II}}] \cdot [\text{R}_n\text{X}]}{[\text{Fe}^{\text{III}}]} \cdot [\text{M}] \quad (4.2)$$

The propagation rate coefficient is precisely known from pulsed-laser polymerization experiments<sup>97,98,229</sup> for systems of similar monomer-to-solvent composition.<sup>230,231</sup> The time-dependent concentrations of  $[\text{Fe}^{\text{II}}]$  and  $[\text{R}_n\text{-X}]$  are calculated from the following relationships:  $[\text{Fe}^{\text{II}}] = [\text{Fe}^{\text{III}}]_0 - [\text{Fe}^{\text{III}}]$  and  $[\text{R}_n\text{-X}] = [\text{R}_n\text{-X}]_0 - [\text{Fe}^{\text{III}}]$ .  $K_{\text{ATRP}}$  was found to be independent of TTMPP content, and no significant change of  $K_{\text{ATRP}}$  was observed within the range of monomer conversions under investigation. The so-obtained mean value for styrene at 100 °C amounts to  $K_{\text{ATRP}} = 7.6 \times 10^{-9}$  (Table 4.5). This value is by about a factor of two above the one found when using 1 equiv of triphenylphosphine (TPP),  $K_{\text{ATRP}} = 3.6 \times 10^{-9}$ , instead of TTMPP. Despite the level of uncertainty of about  $\pm 30\%$ , the higher  $K_{\text{ATRP}}$  suggests a weak interaction between  $\text{Fe}^{\text{II}}$  and TTMPP. Also listed in Table 4.5 are the associated values for BA

**Table 4.5:**  $K_{\text{ATRP}}$  for Fe-mediated ATRPs of different monomers with or without TTMPP as the additive.

entry	monomer / solvent	$T / ^\circ\text{C}$	equiv of TTMPP <sup>[a]</sup>	$K_{\text{ATRP}}$
1	MMA / NMP (1:1)	60 °C	-	$1.4 \times 10^{-8}$ [232]
2	MMA / NMP (1:1)	60 °C	1.5	$3.2 \times 10^{-8}$ [232]
3	Sty / DMF (2:1)	100 °C	0.5–1.5	$7.6 \times 10^{-9}$
4	Sty / DMF (2:1)	100 °C	1.1 <sup>[b]</sup>	$3.6 \times 10^{-9}$
5	BA : NMP (2:3)	100 °C	1	$9.0 \times 10^{-10}$

<sup>[a]</sup> Equivalents of TTMPP with respect to FeBr<sub>3</sub>. Polymerization without TTMPP (entry 1) was started with FeBr<sub>2</sub> instead of FeBr<sub>3</sub>. <sup>[b]</sup> TPP was used instead of TTMPP at the following initial molar ratios: [FeBr<sub>2</sub>] : [FeBr<sub>3</sub>] : [TPP] = 0.86 : 0.14 : 1.10.

polymerization at 100 °C,  $K_{\text{ATRP}} = 9.0 \times 10^{-10}$ , and for MMA polymerization at 60 °C,  $K_{\text{ATRP}} = 3.2 \times 10^{-8}$ , which were obtained via the same methodology using NMP instead of DMF as the highly polar solvent. The value of  $K_{\text{ATRP}}$  (entry 2) is slightly enhanced by the presence of TTMPP compared to the value measured with FeBr<sub>2</sub> in the absence of any additive,  $K_{\text{ATRP}} = 1.4 \times 10^{-8}$  (entry 1).<sup>232</sup> The known reaction enthalpies (cf. chapter 6.3.2) suggest that  $K_{\text{ATRP}}$  for the TTMPP-assisted ATRP of MMA should be around  $6.0 \times 10^{-7}$  at 100 °C, i.e., by about two orders of magnitude above the value for styrene. The increase of  $K_{\text{ATRP}}$  upon passing from BA to styrene and to MMA reflects the expectations based on the relative bond strengths of the associated alkyl halides.<sup>44,201,233</sup>

The polymerization rate, as visualized by the  $\ln([M]_0/[M])$  vs time plots, for homogeneous solutions in either DMF or NMP is enhanced as compared to heterogeneous polymerization with anisole.<sup>53</sup> Despite the rate enhancement in homogeneous polymerization, the ATRPs of styrene and MMA occurred in a controlled fashion. The dispersity values were  $\bar{D} = 1.49$  (PS) at 44 % and  $\bar{D} = 1.34$  (PMMA) at 76 % monomer conversion, respectively, with 1.5 equiv of TTMPP being added in each case (Figure S5). While the heterogeneous system may be the preferred option for synthesizing polymer due to the lower

dispersity values<sup>53</sup> and the minor toxicity concerns with the solvent anisole, the homogeneous system was selected as it enables the online NIR spectroscopic studies. The measured molar masses were in good agreement with the theoretical values calculated on the basis of the amount of initially added alkyl halide (MBriB or EBrPA), e.g.,  $M_{n,SEC} = 8900 \text{ g mol}^{-1}$  vs  $M_{n,theo} = 9200 \text{ g mol}^{-1}$  for polystyrene. This observation confirms that control over the polymerization was attained. No impact of initiation via the GAMA ATRP mechanism was observed, which would have resulted in a lower than predicted molar mass due to the formation of an additional amount of initiator. Under the conditions investigated, the reduction of  $[\text{FeBr}_4]^-$  by TTMPP is the dominant process, as detailed in the following section.

**Reduction of  $[\text{FeBr}_4]^-$  by TTMPP.** The rate of reduction of the  $[\text{FeBr}_4]^-$  complex by TTMPP was measured in monomer-free systems between 25 and 140 °C via online VIS spectroscopy (Figure 4.16A). An equivalent amount of TBA-Br was added to a solution of 30 mM  $\text{FeBr}_3$  in DMF to allow for quantitative formation of  $[\text{FeBr}_4]^-$ . After recording the first spectrum, 0.5 equiv of TTMPP were added. The subsequent reduction of  $[\text{FeBr}_4]^-$  in the presence of TTMPP was monitored via the associated absorption bands between 15 000 and 9000  $\text{cm}^{-1}$  as illustrated in the inset in Figure 4.16A.

At 25 °C, about 33 % of the total  $[\text{FeBr}_4]^-$  is immediately reduced after injecting 0.5 equiv of TTMPP into the reaction medium. However, no further reaction occurs for several hours. Figure 4.16B illustrates that 1.5 equiv of TTMPP are needed for complete reduction of  $[\text{FeBr}_4]^-$  at 25 °C (cf. Figure S6). Interestingly, the analogous reaction using TPP as the reducing agent requires more than 100 h for the reduction of ca. 85 %  $[\text{FeBr}_4]^-$  at 25 °C. The lower rate of reduction may be related to the weaker Lewis basic character of the unsubstituted triphenylphosphine. The resulting lower ratio of  $\text{Fe}^{\text{II}}:\text{Fe}^{\text{III}}$  in TPP-mediated ATRP would yield a lower polymerization rate than with TTMPP (cf. Equation 4.2), although  $K_{\text{ATRP}}$  is similar (see Table 4.5). This observation is consistent with the reported lowering of the ATRP rate with decreasing electron-donating character of the phosphine.<sup>52,53</sup>

As shown in Figure 4.16A, only 0.5 equiv of TTMPP are sufficient to almost quantitatively reduce  $[\text{FeBr}_4]^-$  at 140 °C within 4 to 5 h. TTMPP thus predominantly acts as a reducing agent for  $[\text{FeBr}_4]^-$  at elevated

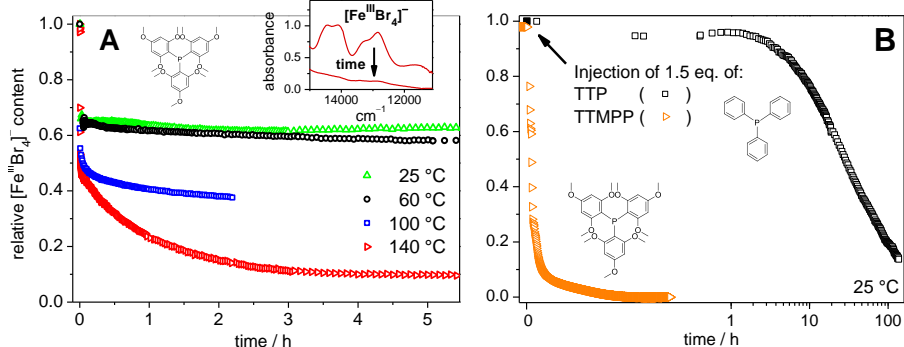


**Figure 4.16:** (A) Reduction of  $[\text{FeBr}_4]^-$  with 0.5 equiv of TTMPP in DMF at 25, 60, 100, and 140 °C monitored by online spectroscopy between 15 000 and 9000  $\text{cm}^{-1}$ , see the inset; (B) reduction of  $[\text{FeBr}_4]^-$  by 1.5 equiv of TTMPP or by 1.5 equiv of TPP monitored at 25 °C.

temperatures. At ambient temperature, more than stoichiometric amounts of the reducing agent are needed for complete reduction, which suggests that coordination of TTMPP to Fe also takes place. Because of the ability to reduce  $\text{Fe}^{\text{III}}$ , the coordination of TTMPP should almost exclusively occur to the  $\text{Fe}^{\text{II}}$  complex. Support for such coordination is provided by the fact that an equimolar mixture of  $\text{FeBr}_2$  and TTMPP is insoluble in less polar environments, such as 2-butanone and MMA, even though the individual components are soluble.<sup>228</sup>

$^{31}\text{P}$  NMR is particularly useful for deducing further information on the interaction of TTMPP and Fe. The spectra shown in Figure 4.17 were recorded in  $\text{DMF-d}_7$  at 25 °C; the  $^1\text{H}$  NMR spectra are shown in Figure S7. The chemical shift of TTMPP in the absence of Fe is  $-66.7$  ppm.<sup>234</sup> This signal disappears in a solution containing equivalent amounts of  $\text{FeBr}_2$  and TTMPP. It is assumed that the paramagnetism of the so-formed  $\text{Fe}^{\text{II}}/\text{TTMPP}$  complex does not allow for the detection of the associated  $^{31}\text{P}$  NMR signal. The signal of the free ligand at  $-66.7$  ppm returns when 2 equiv of TTMPP are added to  $\text{FeBr}_2$ , indicating that only one TTMPP molecule is coordinated to  $\text{Fe}^{\text{II}}$ , most likely due to steric limitations. A fourth spectrum has been recorded for a mixture of  $\text{FeBr}_3$  and 1.5 equiv TTMPP. A signal at  $-53.7$  ppm appears which is due to the presence of  $\text{TTMPP-Br}^+$ ,<sup>235</sup> i.e., the oxidized product of TTMPP associated with the reduction of  $\text{Fe}^{\text{III}}$ . Again no signal is observed for the



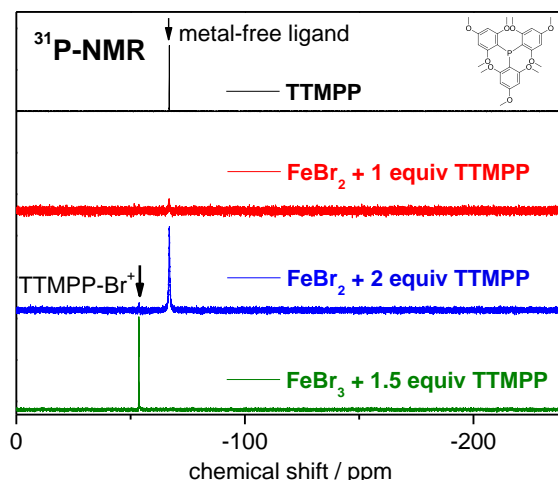
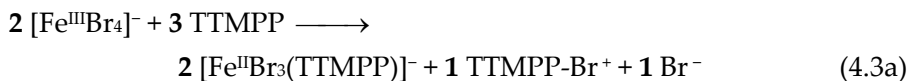


**Figure 4.17:**  $^{31}\text{P}$  NMR spectra of TTMPP in a metal-free DMF- $d_7$  solution (black), of 1 equiv of TTMPP with  $\text{FeBr}_2$  (red), of 2 equiv of TTMPP with  $\text{FeBr}_2$  (blue), and of 1.5 equiv of TTMPP with  $\text{FeBr}_3$  (green).

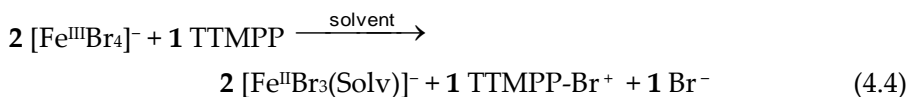
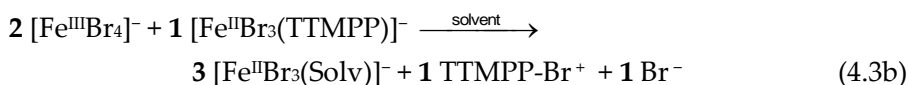
$\text{Fe}^{\text{II}}/\text{TTMPP}$  complex, which should also be present. Upon the addition of more than 1.5 equiv of TTMPP to  $\text{FeBr}_3$ , the signal of the free ligand at  $-66.7$  ppm is additionally observed (not shown).

Dunbar and Quillev re investigated the analogous reaction of  $\text{FeCl}_3$  with TTMPP and characterized the X-ray structure of the  $\text{TTMPP}\text{-Cl}^+$  ( $\text{P}^{\text{V}}$ ) product.<sup>226</sup> In addition to the NMR analysis, the bromine analogue  $\text{TTMPP}\text{-Br}^+$  was identified via ESI-MS (MeCN),  $m/z$  (%) = 611.1; 613.1 (10) for the reduction of  $\text{FeBr}_3$  with an excess of TTMPP,  $m/z$  (%) = 533.2 (88). The reported X-ray structure for the  $\text{Fe}^{\text{II}}/\text{TTMPP}$  complex is  $[\text{H}\text{-TTMPP}]_2[\text{Fe}_2\text{Cl}_6]$ .<sup>226</sup> The protonation of TTMPP ( $\text{P}^{\text{III}}$ ) occurs due to the presence of HCl, which is present in iron chloride as a contaminant.<sup>226</sup> In agreement with the X-ray structure, the peak position of the NIR absorbance, determined for the dissolved  $\text{Fe}^{\text{II}}/\text{TTMPP}$  complex, is also indicative of a tetrahedral  $\text{Fe}^{\text{II}}$  complex (Figure S4).<sup>228</sup> It is assumed that TTMPP predominantly occurs as non-protonated ligand in the solutions, since HCl is present only in subequivalent amounts. The non-protonated TTMPP may coordinate directly to  $\text{Fe}^{\text{II}}$ , which most likely yields monomeric complexes of otherwise analogous composition (cf. Equation 4.3a) as reported for the dimeric X-ray structure.

Monomeric complexes have already been described for the structurally similar  $[\text{FeCl}_3(\text{NMP})]^-$  and the  $[\text{FeCl}_3(\text{PMe}_3)]^-$  species.<sup>180,236</sup> Equation 4.3a illustrates the suggested mechanism for the reduction of  $[\text{FeBr}_4]^-$  by TTMPP at ambient temperature, assuming coordination of TTMPP to  $\text{Fe}^{\text{II}}$ .



At higher temperatures, TTMPP decoordinates from  $[\text{Fe}^{\text{II}}\text{Br}_3(\text{TTMPP})]^-$ , see Equation 4.3b. At 140 °C, the complex is apparently sufficiently labile, so that only 0.5 equiv TTMPP are required for complete reduction of  $[\text{Fe}^{\text{III}}\text{Br}_4]^-$ , see net Equation 4.4.



It is evident that the transformation of TTMPP to TTMPP-Br<sup>+</sup> is a two-electron process with TTMPP-Br<sup>•</sup> probably being the intermediate radical. EPR spectra of TPP-Br<sup>•</sup> radicals were reported for annealed glasses and single crystals.<sup>237,238</sup> Similar EPR features, which suggest the occurrence of TTMPP-Br<sup>•</sup> intermediates during the reaction of  $[\text{FeBr}_4]^-$  and TTMPP, were observed by recording EPR spectra of flash-frozen solutions at 140 K (Figure S8). An interaction of both TTMPP and TTMPP-Br<sup>•</sup> with  $\text{Fe}^{\text{II}}$  may contribute to the curvature of  $[\text{FeBr}_4]^-$  vs time trace observed at 140 °C (cf. Figure 4.16A) and may in turn make the determination of rate coefficients for the reduction of  $[\text{FeBr}_4]^-$  rather complicated. One may, however, conclude that TTMPP primarily acts as a reducing agent at the elevated temperatures typically used in Fe-mediated ATRPs.

In principle, similar mechanistic scenarios should also apply to other phosphines. TPP also reduces  $[\text{Fe}^{\text{III}}\text{X}_4]^-$ , even though the reaction is

much slower than with TTMPP. The reported coordination of TPP to Fe<sup>II</sup> <sup>48,239</sup> may be beneficial in enhancing the tolerance of the Fe<sup>II</sup> catalyst to the presence of functional groups.<sup>52</sup> Since TPP is a weaker base, even Fe<sup>III</sup>/TPP complexes are sufficiently stable for detection by both X-ray and low-temperature EPR spectroscopy.<sup>240</sup> In the absence of an alkyl halide, the TPP-mediated generation of activators by monomer addition (GAMA) should be considered.<sup>48</sup>

**Consequences for the Livingness of Fe-mediated ATRP.** The amount of the highly active reducing agent TTMPP in ATRPs at  $T > 100$  °C needs to be carefully selected: Equimolar amounts of alkyl halide, FeBr<sub>3</sub>, and the phosphine additive are commonly used in ATRP. In such a case, all [FeBr<sub>4</sub>]<sup>-</sup> is reduced in less than 2 min to a mixture of [Fe<sup>II</sup>Br<sub>3</sub>(Solv)]<sup>-</sup> and [Fe<sup>II</sup>Br<sub>3</sub>(TTMPP)]<sup>-</sup> species. The TTMPP ligand can be replaced by solvent and may reduce [FeBr<sub>4</sub>]<sup>-</sup>, resulting from radical termination and following the PRE. Such a continuous decrease of the [FeBr<sub>4</sub>]<sup>-</sup> deactivator content may, according to Scheme 4.3, produce large amounts of dead polymer, unless substoichiometric amounts of the catalyst are used. Such an unfavorable scenario may occur despite the formation of polymers with acceptable dispersity values well below 1.5. The consequences of catalyst regeneration in the phosphine-assisted ATRPs should be considered for the selection of suitable reaction conditions (*vide infra*).

With phosphine-containing Fe systems, even ATRP of acrylates is feasible (cf.  $K_{\text{ATRP}}$  in Table 4.1), despite the kinetic complications described in chapter 5.2.2. ATRPs with monomer conversion up to 86 % and dispersities below 1.2 have been achieved.<sup>53,55,214</sup> The overall ratio of reagents was modified to achieve a high degree of chain-end functionality (CEF) despite the catalyst regeneration via TTMPP. ATRP of BA was carried out in anisole (25 vol%) at 100 °C and initial molar ratios of [BA]:[MBriB]:[FeBr<sub>3</sub>]:[TTMPP] = 100 : 1.00 : 0.10 : 0.15, i.e., with just 5 mM FeBr<sub>3</sub>. The [FeBr<sub>4</sub>]<sup>-</sup> deactivator may be reduced and subsequently be regenerated twice, but according to Scheme 4.3, each regeneration is accompanied by an equivalent loss in CEF. However, due to the presence of excess R-Br initiator, MBriB, compared to overall Fe, the loss of CEF remains below 20 % of total R<sub>n</sub>-Br according to stoichiometric considerations. 40 % monomer conversion and poly(butyl acrylate) with a dispersity of  $\bar{D} = 1.56$  was obtained. The higher

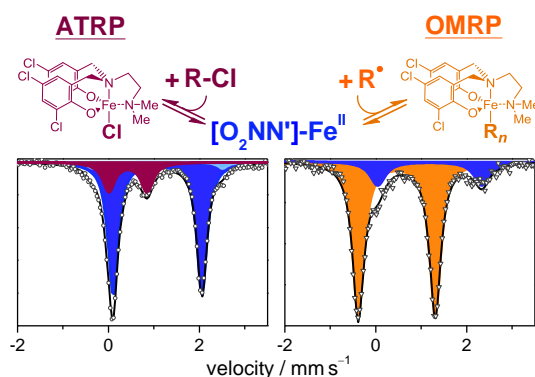
dispersity is a consequence of lowering the Fe content. More active Fe catalysts with a higher  $K_{\text{ATRP}}$  are required for achieving lower dispersity and higher degrees of BA conversion at a similarly high level of preserved chain-end functionality and at possibly even lower Fe concentrations. ATRP of MMA and styrene at ppm levels of the iron bromide catalyst is already feasible.<sup>57,58,67,83,84</sup>

Even though no significant enhancement of  $K_{\text{ATRP}}$  occurs, TTMPP is an attractive additive for Fe-based ATRP, as it serves as a convenient reducing agent for the stable  $\text{Fe}^{\text{III}}$  precursor. TTMPP is associated with minor toxicity concerns as opposed to the commonly used tin(II)-based reducing agents<sup>131</sup> and exhibits better solubility in the organic phase than ascorbic acid.

In an attempt to find even more active Fe-based catalysts, the following chapter explores amine-bis(phenolate)iron complexes,<sup>86,87</sup> which are not generated *in situ* from an  $\text{FeBr}_2$  or  $\text{FeBr}_3$  precursor. Even though the systems studied so far operated exclusively via ATRP, it should be considered that organometallic reactions may occur concurrently with ATRP.

# 5

## The Interface of ATRP and OMRP



The systems studied so far operate exclusively via ATRP, which involves deactivation of propagating radicals by the catalyst in the higher oxidation state, e.g.,  $Fe^{III}$ . The reaction of propagating radicals with the catalyst in the lower oxidation state,  $Fe^{II}$ , is not contained in the ATRP scheme, but such organometallic reaction may also play a role.

Chapter 5.1 presents a multi-spectroscopic analysis of RDRP mediated by amine-*bis*(phenolate)iron complexes centering around the question whether both equilibria, ATRP and OMRP, are operative. Chapters 5.2.1 and 5.2.2 present SP-PLP-EPR investigations into ATRP deactivation and organometallic reactions, respectively.

## 5.1 RDRP Mediated by Amine–bis(phenolate) Iron Complexes<sup>3</sup>

One of the most efficient<sup>86,87</sup> amine–bis(phenolate)iron catalysts (Figure 5.1) will be the subject of a detailed spectroscopic investigation involving online monitoring of styrene and MMA polymerizations by VIS/NIR spectroscopy combined with Mössbauer, EPR, and NMR spectroscopy. The results of polymerization reactions performed under both ATRP and OMRP control<sup>86,87,241</sup> will be discussed in the context of the findings from the spectroscopic studies.

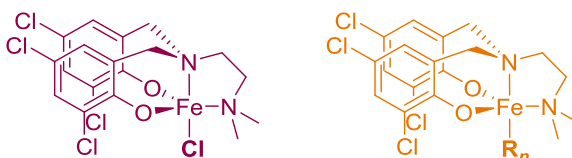
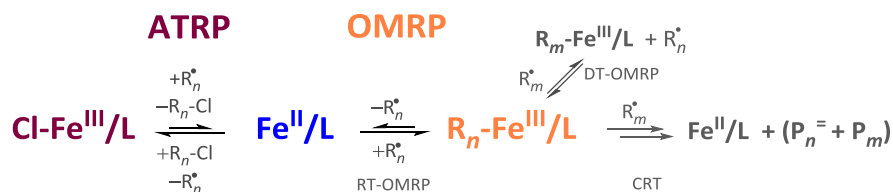


**Figure 5.1:** Structure of the ATRP deactivator,  $\text{Cl-Fe}^{\text{III}}/\text{L}$ ,<sup>28,40,41</sup> and the expected structure of the organometallic  $\text{R}_n\text{-Fe}^{\text{III}}/\text{L}$  complex.

Illustrated in Scheme 5.1 are equilibria implicated in Fe-mediated RDRP. It is evident that the  $\text{Fe}^{\text{II}}/\text{L}$  complex may participate in both ATRP and OMRP pathways. According to the ATRP equilibrium, activation of an alkyl chloride initiator by  $\text{Fe}^{\text{II}}/\text{L}$  generates radicals,  $\text{R}_n^\bullet$ , of chain length  $n$  along with the chain deactivator complex,  $\text{Cl-Fe}^{\text{III}}/\text{L}$ . In the OMRP equilibrium, the reaction of  $\text{Fe}^{\text{II}}/\text{L}$  with  $\text{R}_n^\bullet$  produces the organometallic species,  $\text{R}_n\text{-Fe}^{\text{III}}/\text{L}$ . This complex may undergo subsequent reactions, the most important of which, with respect to the present study, being the reverse reaction to  $\text{Fe}^{\text{II}}/\text{L}$ , known as reversible termination (RT) OMRP. In addition, degenerative transfer (DT) between  $\text{R}_m^\bullet$  and  $\text{R}_n\text{-Fe}^{\text{III}}/\text{L}$  may occur. The same reactants may also yield dead polymer and  $\text{Fe}^{\text{II}}/\text{L}$ . The net reaction is a catalytic termination of two radicals,  $\text{R}_m^\bullet$  and  $\text{R}_n^\bullet$ , via the  $\text{R}_n\text{-Fe}^{\text{III}}/\text{L}$  intermediate, which is referred to as Fe-catalyzed radical termination (Fe-CRT, see chapter 5.2.2).<sup>21,242</sup> Even though all of these organometallic reactions

<sup>3</sup> Reproduced with permission from Schroeder, H.; Lake, B. R. M.; Demeshko, S.; Shaver, M. P.; Buback, M. *Macromolecules* **2015**, *48*, 4329–4338, Copyright 2015 American Chemical Society. The synthesis of and OMRP with  $\text{Fe}^{\text{II}}$  was carried out by B. R. M. Lake and M. P. Shaver.



**Scheme 5.1:** Iron-mediated radical polymerization with a simultaneous ATRP and RT-OMRP equilibrium. Both reaction pathways involve the  $\text{Fe}^{\text{II}}/\text{L}$  activator complex and growing radicals,  $\text{R}_n^{\bullet}$ , of chain length  $n$ . Potential subsequent reactions such as degenerative transfer (DT) and catalytic radical termination (CRT) are also included.

proceed via  $\text{R}_n\text{-Fe}^{\text{III}}/\text{L}$ , the catalyst design determines which organometallic mechanism is dominant. The focus of the spectroscopic studies centers around the question whether ATRP and OMRP equilibria are both operating with the Fe catalyst under investigation, i.e., whether both species,  $\text{Cl-Fe}^{\text{III}}/\text{L}$  and  $\text{R}_n\text{-Fe}^{\text{III}}/\text{L}$ , are present during the reaction.

Both the  $\text{Fe}^{\text{II}}$  and the  $\text{Fe}^{\text{III}}$  catalyst under investigation are derived from a chloro-substituted amine-*bis*(phenolate) ligand.<sup>243</sup> The synthesis of the highly air- and moisture-sensitive  $\text{Fe}^{\text{II}}/\text{L}$  species from an  $\text{Fe}^{\text{II}}\text{-bis}(\text{amide})$  precursor,  $[\text{Fe}(\text{N}(\text{SiMe}_3)_2)_2]$ ,<sup>244</sup> has only very recently been reported.<sup>241</sup> The solution magnetic moment data,  $\mu_{\text{eff}} = 4.7\mu_{\text{B}}$ , suggests a high-spin electron configuration for this compound (see Figure 5.2 for the reported crystal structure),<sup>241</sup> which was found to crystallize as a  $(\mu\text{-OAr})_2$ -bridged dimer, along with two molecules of solvent THF.

**UV/VIS Spectroscopy.** Initial polymerization studies were performed with the stable (with respect to oxidation)  $\text{Fe}^{\text{III}}$  species, i.e.,  $\text{Cl}_{\text{Cl,NMe}_2}[\text{O}_2\text{NN}']\text{Fe}^{\text{III}}\text{Cl}$  ( $\text{Cl-Fe}^{\text{III}}/\text{L}$ , Figure 5.1). As illustrated in Scheme 5.2, polymerization is initiated by rapid decomposition of a thermal initiator. It should be noted that the structure of the primary radicals,  $\text{R}_1^{\bullet}$ , which add to monomer, depends on the choice of the thermal initiator and differs from the monomer-specific radicals,  $\text{R}_n^{\bullet}$ . Reaction of  $\text{R}_n^{\bullet}$  with the ATRP deactivator,  $\text{Cl-Fe}^{\text{III}}/\text{L}$ , yields alkyl halide and the reduced complex,  $\text{Fe}^{\text{II}}/\text{L}$ . In addition to the ATRP reaction, organometallic species may be formed from  $\text{Fe}^{\text{II}}/\text{L}$ , according to Scheme 5.1.

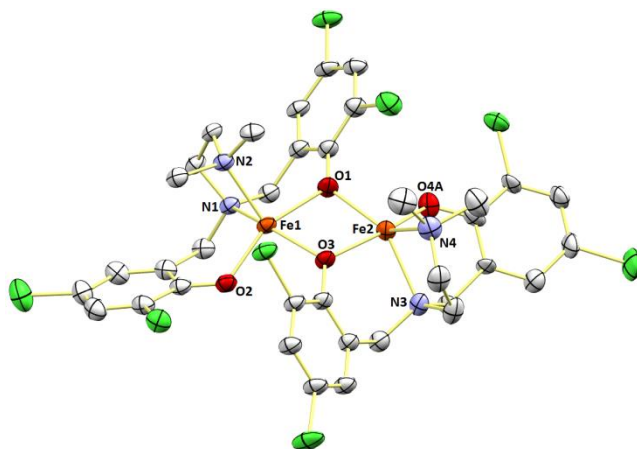
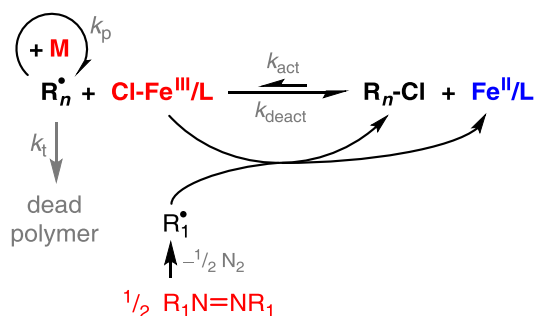


**Figure 5.2:** Crystal structure of the Fe<sup>II</sup>/L complex from ref. <sup>241</sup>. Ellipsoids are set to the 50% probability level. Hydrogen atoms and two molecules of co-crystallized THF have been omitted for clarity.



**Scheme 5.2:** Reverse ATRP mediated by the complexes Cl-Fe<sup>III</sup>/L and Fe<sup>II</sup>/L. The starting reagents are marked in red. Polymerization is initiated by the decomposition of the thermal initiator, R<sub>1</sub>N=NR<sub>1</sub>.

Polymerizations of styrene and MMA were monitored via online VIS spectroscopy (Figure 5.3). The styrene solution contained the ATRP deactivator, Cl-Fe<sup>III</sup>/L (2 mM), and AIBN (20 mM). The decomposition of AIBN at 90 °C ( $t_{1/2} \approx 34$  min) produces growing styryl radicals, R<sub>n</sub><sup>•</sup>, which react with Cl-Fe<sup>III</sup>/L according to Scheme 5.2 to yield Fe<sup>II</sup>/L and



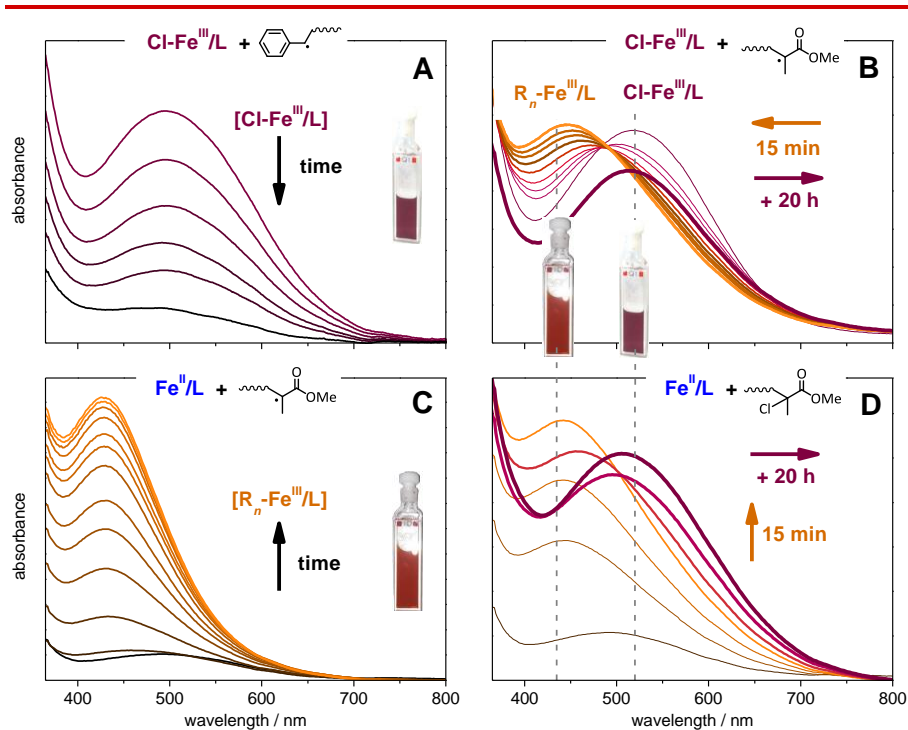
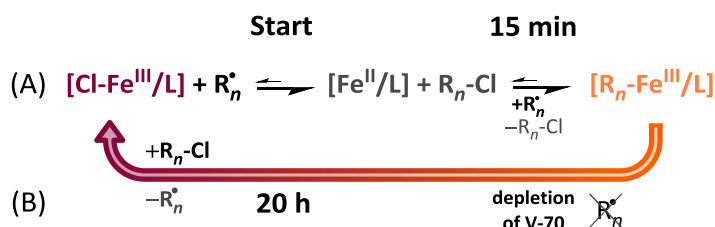


**Figure 5.3:** (A) The absorption of Cl-Fe<sup>III</sup>/L was monitored online at around 500 nm during styrene polymerization at 90 °C. Cl-Fe<sup>III</sup>/L is reduced via the reaction with styrene radicals. (B) In MMA polymerization, rapid transformation of Cl-Fe<sup>III</sup>/L to R<sub>n</sub>-Fe<sup>III</sup>/L at around 430 nm was observed as represented by the increasing line thickness and the color transition to orange. Cl-Fe<sup>III</sup>/L, monitored at 520 nm, is essentially formed back at extended reaction times up to 20 h. (C) The formation of R<sub>n</sub>-Fe<sup>III</sup>/L may also be evidenced by the direct reaction of Fe<sup>II</sup>/L with propagating radicals in the absence of alkyl halide. (D) In the presence of alkyl halide, both R<sub>n</sub>-Fe<sup>III</sup>/L and Cl-Fe<sup>III</sup>/L are formed from Fe<sup>II</sup>/L. After 20 h, Cl-Fe<sup>III</sup>/L turns out to be the dominant species.

R<sub>n</sub>-Cl. The associated reduction in the concentration of Cl-Fe<sup>III</sup>/L is monitored by a decrease in the absorbance at around 500 nm as illustrated in Figure 5.3A (only six out of a multitude of spectra recorded within 40 minutes are shown). The formation of the Fe<sup>II</sup>/L complex was evidenced via Mössbauer spectroscopy (*vide infra*). The

experimental procedure used in these online VIS spectroscopy studies is similar to the one commonly used in reverse ATRP (R-ATRP), except for the lower decomposition rate of the thermal initiator and the excess of AIBN being employed. An excess of AIBN was intentionally used to try and facilitate the formation and detection of organometallic species. However, neither  $R_n\text{-Fe}^{\text{III}}/\text{L}$  nor the  $R_1\text{-Fe}^{\text{III}}/\text{L}$  species involving the initiator fragment ( $n = 1$ ) were observed during styrene polymerization. The absence of organometallic species is further demonstrated by the Mössbauer measurements.

The polymerization of MMA under similar conditions was also examined using online VIS spectroscopy (Figure 5.3B). The ATRP deactivator,  $\text{Cl-Fe}^{\text{III}}/\text{L}$  (0.4 mM), was used as the initial Fe-containing species, giving the absorption at around 520 nm. An excess of the thermal initiator, V-70 (9 mM), was added to the polymerization at 70 °C ( $t_{1/2}(\text{V-70}) \approx 6$  min). The reaction scenario illustrated in Figure 5.3B clearly differs from the one in styrene polymerization, with the reaction sequence being represented by increasing line thickness. The spectra recorded within 15 min indicate that  $\text{Cl-Fe}^{\text{III}}/\text{L}$  is transformed into a different  $\text{Fe}^{\text{III}}$  species with peak absorbance at around 430 nm (orange line). The reaction was continued for 20 h at 80 °C, though only the final spectrum is shown in Figure 5.3B. The position of the peak in this spectrum (thick maroon line) is at 520 nm, indicating that the starting  $\text{Cl-Fe}^{\text{III}}/\text{L}$  complex has been re-formed. These observations are strongly indicative of both ATRP and OMRP equilibria imparting control over MMA polymerization initiated under R-ATRP conditions. In agreement with the Mössbauer analysis discussed below, the intermediate  $\text{Fe}^{\text{III}}$  species seems to be  $R_n\text{-Fe}^{\text{III}}/\text{L}$ . In contrast to styrene polymerization, the  $\text{Fe}^{\text{II}}/\text{L}$  complex, which is formed via the reduction of  $\text{Cl-Fe}^{\text{III}}/\text{L}$ , quickly reacts with MMA-type radicals,  $R_n\cdot$ , to produce  $R_n\text{-Fe}^{\text{III}}/\text{L}$  according to the mechanism proposed in Scheme 5.3A. It should be noted that alkyl halide,  $R_n\text{-Cl}$ , is also formed while transforming  $\text{Cl-Fe}^{\text{III}}/\text{L}$  to  $R_n\text{-Fe}^{\text{III}}/\text{L}$  (cf. Scheme 5.3A). After the depletion of the V-70 thermal initiator, the underlying RT-OMRP equilibrium (cf. Scheme 5.1) induces the decomposition of  $R_n\text{-Fe}^{\text{III}}/\text{L}$  back to  $\text{Fe}^{\text{II}}/\text{L}$  and  $R_n\cdot$  (Scheme 5.3B).  $\text{Fe}^{\text{II}}/\text{L}$  progressively reacts with  $R_n\text{-Cl}$  to produce  $\text{Cl-Fe}^{\text{III}}/\text{L}$ . Over time, all  $R_n\cdot$  species will disappear due to radical termination reactions, thus producing  $\text{Cl-Fe}^{\text{III}}/\text{L}$  as the final iron-containing compound after 20 h.



**Scheme 5.3:** Pathway for the reaction sequence illustrated in Figure 5.3B. (A)  $\text{Cl-Fe}^{\text{III}}/\text{L}$  reacts with  $\text{R}_n^\bullet$  to  $\text{Fe}^{\text{II}}/\text{L}$  and  $\text{R}_n\text{-Cl}$ .  $\text{Fe}^{\text{II}}/\text{L}$  subsequently reacts with excess  $\text{R}_n^\bullet$  to produce  $\text{R}_n\text{-Fe}^{\text{III}}/\text{L}$ . (B) The V-70 thermal initiator is depleted upon running the reaction for 20 h.  $\text{R}_n\text{-Fe}^{\text{III}}/\text{L}$  decomposes and  $\text{Cl-Fe}^{\text{III}}/\text{L}$  is formed back by the reverse reaction pathway.

With the  $\text{Fe}^{\text{II}}/\text{L}$  complex being accessible, the mechanistic interpretation was checked by two further experiments. First, V-70 (14 mM) was added to a solution of  $\text{Fe}^{\text{II}}/\text{L}$  (10 mM, i.e., 5 mM of the  $\text{Fe}^{\text{II}}/\text{L}$  dimer) in MMA/anisole (1:3, v/v) at 70 °C. Because of the absence of alkyl halide,  $\text{Cl-Fe}^{\text{III}}/\text{L}$  cannot be formed. Only  $\text{R}_n\text{-Fe}^{\text{III}}/\text{L}$ , which is produced by the reaction of  $\text{Fe}^{\text{II}}/\text{L}$  with propagating radicals, is observed in the VIS spectrum at around 430 nm (Figure 5.3C). This finding is in agreement with the Mössbauer analysis detailed below.

Secondly, an alkyl halide initiator, i.e., ethyl  $\alpha$ -chlorophenylacetate (ECIPA, 50 mM) was added to a solution of  $\text{Fe}^{\text{II}}/\text{L}$  (5 mM) in MMA/anisole (1:3, v/v) at 70 °C. Such a setup is, in general, typical for ATRP, where  $\text{Fe}^{\text{II}}/\text{L}$  activates the alkyl halide to produce  $\text{Cl-Fe}^{\text{III}}/\text{L}$  and primary radicals. However, in this system, the methacrylate-type radicals,  $\text{R}_n^\bullet$ , also react with the  $\text{Fe}^{\text{II}}/\text{L}$  complex to produce  $\text{R}_n\text{-Fe}^{\text{III}}/\text{L}$  along with  $\text{Cl-Fe}^{\text{III}}/\text{L}$ . In the absence of a thermal initiator, the formation of  $\text{R}_n\text{-Fe}^{\text{III}}/\text{L}$  is accompanied by the production of at least the same amount of  $\text{Cl-Fe}^{\text{III}}/\text{L}$ , since each  $\text{R}_n\text{-Fe}^{\text{III}}/\text{L}$  requires first the formation of  $\text{R}_n^\bullet$  and thus  $\text{Cl-Fe}^{\text{III}}/\text{L}$  via ATRP activation. This situation is illustrated by the net equation shown in Scheme 5.4. In what follows, the mechanistic scenario is identical to the one presented in Scheme 5.3:  $\text{R}_n\text{-Fe}^{\text{III}}/\text{L}$  decomposes as the reaction is continued for 20 h at 80 °C and  $\text{Cl-Fe}^{\text{III}}/\text{L}$  finally turns out to be the single  $\text{Fe}^{\text{III}}$  species. The reaction sequence is represented by increasing line thickness and a color transition from orange to maroon in Figure 5.3D.



**Scheme 5.4:** The net reaction for  $\text{Fe}^{\text{II}}/\text{L}$  and  $\text{R}_n\text{-Cl}$  illustrates that  $\text{R}_n\text{-Fe}^{\text{III}}/\text{L}$  may only be produced in equal amounts as  $\text{Cl-Fe}^{\text{III}}/\text{L}$ . The absence of a thermal initiator prevents the formation of excess  $\text{R}_n\text{-Fe}^{\text{III}}/\text{L}$ .

---

It should be noted that, in the case of styrene polymerization initiated in the presence of  $\text{Fe}^{\text{II}}/\text{L}$ , only species expected to be present due to the ATRP equilibrium are observed (Figure S9). In this instance, ATRP of styrene was initiated via the reaction of  $\text{Fe}^{\text{II}}/\text{L}$  with the alkyl halide initiator,  $\text{PECl}$ , which resulted in the formation of only a single observed  $\text{Fe}^{\text{III}}$  species,  $\text{Cl-Fe}^{\text{III}}/\text{L}$ . In the absence of alkyl halide, when styrene polymerization was initiated at 110 °C by *meso*-1,2-bis(1-phenylethyl)diazene (PEDA), which decomposes to styryl radicals, no formation of  $\text{R}_n\text{-Fe}^{\text{III}}/\text{L}$  from  $\text{Fe}^{\text{II}}/\text{L}$  was observed (Figure S10).

**Mössbauer Spectroscopy.**  $^{57}\text{Fe}$  Mössbauer spectroscopy provides direct information on the oxidation and spin states of Fe species, and thus was used to further corroborate the data provided by the online VIS spectroscopy studies. Another important facet of  $^{57}\text{Fe}$  Mössbauer spectroscopy is the provision of quantitative information on the relative amounts of Fe complexes, which could infer the relative importance of ATRP and OMRP equilibria in the RDRP of styrene and MMA. The experimental procedures to yield the polymer samples subjected to Mössbauer spectroscopy were similar to the ones for VIS spectroscopy, except that higher concentrations of each component were used. Thus, due to the specific adjustments required for each spectroscopic technique, a wide range of reaction conditions was covered within the experiments.

All Mössbauer spectra were recorded at 80 K, mostly on flash-frozen solutions. The Mössbauer spectrum of the  $\text{Fe}^{\text{II}}/\text{L}$  complex, shown in Figure 5.4A, is the only one recorded on powdered  $\text{Fe}^{\text{II}}/\text{L}$ . Two subfunctions have been used to fit the overall spectrum, both indicating typical parameters for a high-spin  $\text{Fe}^{\text{II}}$  species, i.e.,  $\delta = 1.09$  and  $1.16 \text{ mm s}^{-1}$ , respectively (Table S3).<sup>245</sup> The subfunction of lower intensity is assigned to a different molecular arrangement of the

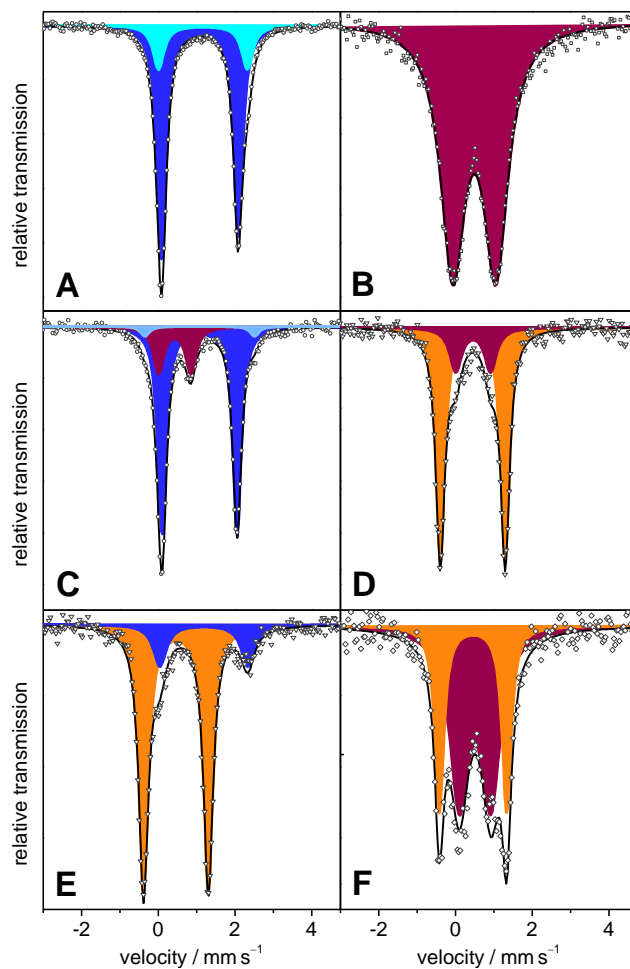


**Figure 5.4:**  $^{57}\text{Fe}$  Mössbauer spectra recorded at 80 K. (A) Powder spectrum of  $\text{Fe}^{\text{II}}/\text{L}$ . (B) Spectrum of  $\text{Cl-Fe}^{\text{III}}/\text{L}$  (100 mM) recorded on a flash-frozen styrene solution. (C) Spectrum of styrene polymerization indicating the presence of  $\text{Fe}^{\text{II}}/\text{L}$  (80 %) and of  $\text{Cl-Fe}^{\text{III}}/\text{L}$  (20 %). (D)–(F) were recorded from MMA polymerization with 66 vol% anisole. (D) was recorded on an MMA polymerization carried out with V-70 (200 mM) and  $\text{Cl-Fe}^{\text{III}}/\text{L}$  (50 mM). After 30 min at 70 °C, both  $\text{R}_i\text{-Fe}^{\text{III}}/\text{L}$  (80 %) and  $\text{Cl-Fe}^{\text{III}}/\text{L}$  (20 %) were observed. (E)  $\text{R}_i\text{-Fe}^{\text{III}}/\text{L}$  in 82 % yield also results from reaction of  $\text{Fe}^{\text{II}}/\text{L}$  (50 mM) with MMA-type radicals generated via V-70 (500 mM) at 60 °C. After 20 h at 80 °C (F),  $\text{Cl-Fe}^{\text{III}}/\text{L}$  (65 %) and  $\text{R}_i\text{-Fe}^{\text{III}}/\text{L}$  (35 %) were found.

otherwise identical complex: either two different topological isomers or a monomer/dimer equilibrium. Shown in Figure 5.4B is the spectrum of  $\text{Cl-Fe}^{\text{III}}/\text{L}$  (100 mM),  $\delta = 0.49 \text{ mm s}^{-1}$ , which was recorded on a flash-frozen styrene solution. The Mössbauer parameters (cf. Table S3) obtained from fitting the spectra in Figure 5.4A–B are used for the interpretation of the spectra recorded on the actual polymerization systems (Figure 5.4C–F). It turns out that the position of  $\text{Fe}^{\text{II}}/\text{L}$  and  $\text{Cl-Fe}^{\text{III}}/\text{L}$  is insensitive toward the type of solvents used within this work. The measured isomer shifts (cf. Table S3) are indicative of all  $\text{Fe}^{\text{III}}$  complexes being in the high-spin state.<sup>246-248</sup>

The spectrum shown in Figure 5.4C was measured on a flash-frozen solution from the polymerization of styrene at 85 °C initiated under reverse ATRP conditions, starting with V-70 (120 mM) and  $\text{Cl-Fe}^{\text{III}}/\text{L}$  (100 mM). The analysis indicates the presence of  $\text{Fe}^{\text{II}}/\text{L}$  (80 %) as the major component and of  $\text{Cl-Fe}^{\text{III}}/\text{L}$  (20 %, cf. Table S3). No further  $\text{Fe}^{\text{III}}$  species were observed, which confirms the online VIS spectroscopy data. It should be noted that the Mössbauer parameters of  $\text{Fe}^{\text{II}}/\text{L}$  are identical to the intense subfunction of the powder spectrum in Figure 5.4A, which suggests that the same dimeric  $\text{Fe}^{\text{II}}$  species is also present in the flash-frozen solution.

The spectra shown in Figure 5.4D–F were recorded on flash-frozen solutions from MMA polymerization in 66 vol% anisole. Figure 5.4D illustrates the catalyst speciation analysis in a polymerization performed at 70 °C with  $\text{Cl-Fe}^{\text{III}}/\text{L}$  (50 mM) and V-70 (200 mM), i.e., under reverse ATRP conditions. The spectrum was recorded after 30 min and indicates the presence of two different  $\text{Fe}^{\text{III}}$  species, assigned to  $\text{R}_n\text{-Fe}^{\text{III}}/\text{L}$  (80 %) and  $\text{Cl-Fe}^{\text{III}}/\text{L}$  (20 %). As shown in Figure 5.4E, the same  $\text{R}_n\text{-Fe}^{\text{III}}/\text{L}$  species (82 %) also resulted from reaction of  $\text{Fe}^{\text{II}}/\text{L}$  (50 mM) with MMA-type radicals formed via the decomposition of V-70 (500 mM) at 60 °C. The spectrum shown in Figure 5.4F was measured after running the reaction illustrated in Figure 5.4D for an extended time period (20 h at 80 °C). It is evident that  $\text{Cl-Fe}^{\text{III}}/\text{L}$  (65 %) is regenerated from  $\text{R}_n\text{-Fe}^{\text{III}}/\text{L}$  (35 %). Thus, the mechanistic conclusions drawn from the Mössbauer spectroscopic measurements are identical to the ones observed in the online VIS spectroscopic experiments (cf. Figure 5.4B–C), i.e., that the RDRP of styrene is controlled by an ATRP equilibrium, whereas control is imparted both by ATRP and OMRP equilibria during MMA polymerization.

**EPR spectroscopy.** Further verification of the mechanistic analysis of iron-mediated styrene and MMA polymerization was obtained via EPR spectroscopy. Both Fe<sup>III</sup> complexes, Cl-Fe<sup>III</sup>/L and R<sub>n</sub>-Fe<sup>III</sup>/L, may be detected in the solid state, i.e., on flash-frozen solutions of the polymerization systems.

A solution of Cl-Fe<sup>III</sup>/L (13.3 mM) and V-70 (12.0 mM) in styrene/anisole (1:1, v/v) was prepared. The initial spectrum (purple line) shown in Figure 5.5A was recorded at -163 °C, with the signal at ~1500 G being assigned to Cl-Fe<sup>III</sup>/L. The sample was heated at 80 °C for 4 min thus inducing a rapid decomposition of V-70. The second spectrum (gray line) was recorded after flash-freezing the sample, again to -163 °C. The signal around 1500 G almost entirely disappeared due to the reduction of Cl-Fe<sup>III</sup>/L to the Fe<sup>II</sup>/L complex, which is not observable by EPR spectroscopy. As with the other spectroscopic techniques, no other Fe<sup>III</sup> species were observed during styrene polymerization.

MMA polymerizations were studied in solution (50 vol% anisole) starting with 3.0 mM Cl-Fe<sup>III</sup>/L and 15 mM V-70. In between the measurements at -170 °C, the sample was heated to 70 °C for the given time interval to induce the decomposition of V-70. In contrast to the observation with styrene, the Fe<sup>III</sup> signal around 1500 G is transformed into a broader signal (Figure 5.5B) with a distinct shoulder indicating the presence of two Fe<sup>III</sup> species. This finding is in agreement with the observations from VIS and Mössbauer spectroscopy. The spectral change suggests partial transformation of Cl-Fe<sup>III</sup>/L to another Fe<sup>III</sup>-containing species, in all likelihood, R<sub>n</sub>-Fe<sup>III</sup>/L.

**Consequences of the Mechanistic Insight for Controlled Radical Polymerizations.** The mechanistic analysis suggests that styrene polymerizations using the investigated catalyst system operate via an ATRP mechanism. The occurrence of this single polymerization mechanism should be beneficial for the synthesis of polymeric materials due to only one type of chain-end functionality (CEF) being present, i.e., the chloride-capped radical species. This situation could be advantageous for subsequent modification of the polymer, e.g., for the synthesis of block copolymers.

To probe the CEF in the ATRP of styrene, a <sup>1</sup>H-NMR spectroscopic study was performed. R-ATRP reactions were initiated at 90 °C via decomposition of the thermal initiator, V-70. The crude polymer was

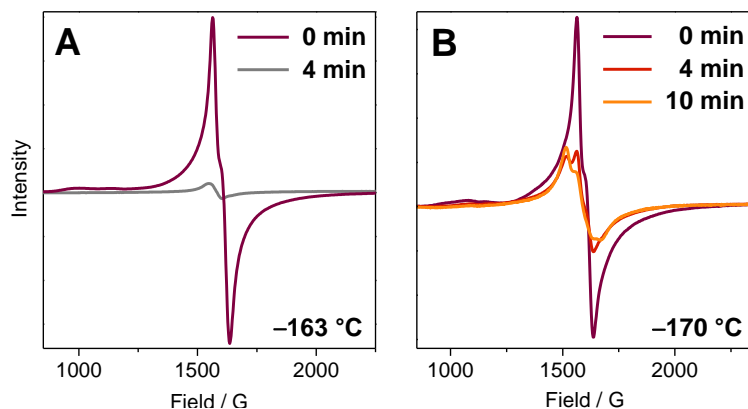


**Figure 5.5:** (A) The initial EPR spectrum (purple line) was recorded at  $-163\text{ }^{\circ}\text{C}$  on a flash-frozen solution of  $\text{Cl-Fe}^{\text{III}}/\text{L}$  (13.3 mM) and V-70 (12.0 mM) in styrene/anisole (1:1, v/v). The second spectrum (gray line) was recorded at  $-163\text{ }^{\circ}\text{C}$  after heating the sample at  $80\text{ }^{\circ}\text{C}$  for 4 min, thus inducing a rapid decomposition of V-70. The signal around 1500 G almost entirely disappeared due to the reduction of  $\text{Cl-Fe}^{\text{III}}/\text{L}$ . (B) Spectra recorded on a solution which initially contained  $\text{Cl-Fe}^{\text{III}}/\text{L}$  (3.0 mM) and V-70 (15 mM) in MMA/anisole (1:1, v/v). In between the measurements at  $-170\text{ }^{\circ}\text{C}$ , the sample was heated at  $70\text{ }^{\circ}\text{C}$  for the given time intervals to induce decomposition of V-70. The  $\text{Fe}^{\text{III}}$  signal around 1500 G is transformed into a broader signal with a distinct shoulder indicating partial transformation of  $\text{Cl-Fe}^{\text{III}}/\text{L}$  into  $\text{R}_i\text{-Fe}^{\text{III}}/\text{L}$ .

isolated by removing all solvents under reduced pressure. As illustrated in Figure 5.6A, the  $^1\text{H}$  NMR signals of the V-70 initiator fragment ( $-\text{OCH}_3$ ) at 3.08 ppm (3H) and of the proton at the Cl-functionalized carbon,  $-\text{CHCl}$ , at 4.35 ppm (1H) are well separated. The degree of  $-\text{CHCl}$  functionality may be calculated by comparing the integration of these two fragments, a process which assumes that all chains were initiated by the primary radicals of V-70.

The ratio of  $\text{Cl-Fe}^{\text{III}}/\text{L}$  and V-70 for the reverse ATRPs was selected such as to have sufficient halide for ATRP deactivation of all generated radicals. When ATRP was carried out with 45.6 mM  $\text{Cl-Fe}^{\text{III}}/\text{L}$  and 16.9 mM V-70 up to ca. 10 % monomer conversion, the degree of chlorine CEF amounted to 97 % (Figure 5.6B), thus being almost quantitative. This observation confirms that no other type of CEF, e.g.,



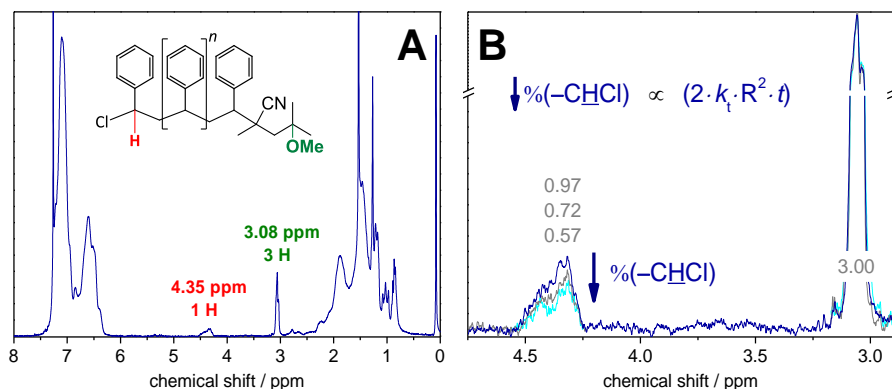


**Figure 5.6:** <sup>1</sup>H-NMR analysis of CEF in Cl-Fe<sup>III</sup>/L-mediated ATRP of styrene at 90 °C. (A) The <sup>1</sup>H-NMR signals for the  $-\text{OCH}_3$  fragment of the V-70 initiator at 3.08 ppm (3H) and of the proton at the Cl-functionalized carbon at 4.35 ppm (1H) are well separated. (B) Chlorine CEF amounts to 97 % for ATRP carried out with 45.6 mM Cl-Fe<sup>III</sup>/L and 16.9 mM V-70 up to ca. 10 % monomer conversion. The decrease in  $\%(-\text{CHCl})$  for spectra recorded at higher degrees of monomer conversion is consistent with expectations based on radical termination rate (see main text).

metal-capped radical species ( $R_n\text{-Fe}^{\text{III}}/\text{L}$ ), occurs to any significant extent. It should be noted that in ATRP, as in all radical polymerizations, radical-radical termination cannot be avoided. As a consequence, the degree of CEF decreases with time, i.e., toward higher degrees of monomer conversion. The loss in CEF, i.e., in the concentration of dead chains without chlorine functionality,  $[\text{T}]$ , may be estimated via Equation 5.1,<sup>249</sup> where  $[\text{T}]$  is a function of monomer conversion,  $\text{conv}$ , and time,  $t$ . The associated rate coefficients for termination,  $k_t$ ,<sup>250</sup> and propagation,  $k_p$ ,<sup>251</sup> are found in the literature. Monomer conversion was determined via NIR spectroscopy.<sup>105</sup>

The decrease in  $\%(-\text{CHCl})$  may be explained based on radical-radical termination rate and the associated conversion vs time profiles used to calculate  $[\text{T}]$  according to Equation 5.1. This observation

$$[\text{T}] = 2k_t \cdot [\text{R}_n^*]^2 \cdot t = \frac{2k_t \cdot d\ln(1 - \text{conv})^2}{k_p^2 \cdot dt} \quad (5.1)$$

confirms that no further loss of CEF via a different termination mechanism occurs. The Fe-CRT reaction (Scheme 5.1) does not appear to affect Cl-Fe<sup>III</sup>/L-mediated ATRP of styrene. In ATRP, it is generally desirable to obtain polymers with a high degree of CEF, which may be achieved by carrying out ATRP with an excess of alkyl halide as compared with the total amount of Fe (*vide infra*).

In contrast to styrene polymerizations, a dual control mechanism including ATRP and OMRP equilibria is operative in MMA polymerization. As illustrated by the VIS spectra in Figure 5.3D, both mechanisms contribute even in the presence of an excess of the ATRP initiator, R-Cl, relative to the Fe-mediator. Nevertheless, Cl-capped radical species should be the dominant type of CEF under such conditions, since the OMRP pathway has the obvious restriction of requiring stoichiometric amounts of Fe<sup>II</sup>/L and R<sub>n</sub>•.

Variation of temperature may favor one of the two mechanisms, even though both the ATRP of styrene (Figure S11A) and the OMRP of MMA (Figure S11B) are significantly accelerated at higher temperature. The rate enhancements are partially due to the increase in the associated propagation rate coefficients.<sup>251,252</sup> Moreover, both the ATRP and OMRP equilibria are expected to be shifted to the side of the active radical species. Nevertheless, both mechanisms are not equally important when simultaneously in operation. The R<sub>n</sub>-Fe<sup>III</sup>/L complex is quite labile in MMA polymerizations carried out above 90 °C. Under these conditions, ATRP should be the dominant mechanism, especially at increased polymerization times (Scheme 5.3). The polymerization temperature for OMRP-only processes, i.e., in the absence of alkyl halide, should also be selected carefully. Lower temperature increases the stability of R<sub>n</sub>-Fe<sup>III</sup>/L but also provides lower rates for the deactivation of R<sub>n</sub>• with Fe<sup>II</sup>/L.<sup>48</sup>

**Protocols for ATRP and OMRP.** As shown in Figure 5.6B, radical termination affects each RDRP in that the degree of CEF is progressively lowered toward increasing polymerization time. To synthesize polymer with a high degree of CEF, one should make use of the beneficial situation that ATRP does not require stoichiometric amounts of catalyst and initiator. Radical termination in ATRP results in the loss of chain-end functionalized alkyl halide and simultaneously in the loss of Fe<sup>II</sup>/L that is converted into persistent X-Fe<sup>III</sup>/L species. The polymerization will essentially cease when all of the Fe<sup>II</sup>/L mediator is converted to

X-Fe<sup>III</sup>/L. Therefore, the loss of CEF is small if an excess of the alkyl halide initiator as compared with the total Fe content is used. As an example, ATRP of styrene was carried out at 100 °C in solution of anisole (25 vol%) with the following molar ratios of reagents: [Sty] : [PECl] : [Fe<sup>II</sup>/L] : [Cl-Fe<sup>III</sup>/L] = 100 : 1.00 : 0.17 : 0.04. Based on stoichiometric considerations (17 % Fe<sup>II</sup>/L with respect to PECl), the degree of CEF will in any case be better than 83 %. After 23 h, 50 % monomer conversion was reached yielding polymer with a dispersity of  $D = 1.14$  (entry 1, Table 5.1) and an experimentally obtained number average molar mass,  $M_{n,SEC} = 6200 \text{ gmol}^{-1}$ , which is in reasonable agreement with the theoretical value,  $M_{n,theo} = 5350 \text{ gmol}^{-1}$ . Owing to the excellent catalytic performance of [O<sub>2</sub>NN']Fe in styrene polymerizations, ATRP may be carried out at even lower levels of the catalyst.<sup>87</sup>

Listed in Table 5.1 are further examples of polymerization reactions started with the Fe<sup>II</sup>/L mediator and performed under ATRP and/or OMRP control.<sup>241</sup> Polymerization of MMA at 120 °C initiated by an alkyl halide, PECl, operates under simultaneous ATRP and OMRP control yielding a dispersity of  $D = 1.22$  (entry 3).<sup>241</sup> An advantage of being able to isolate an RDRP mediator in its lower oxidation state, Fe<sup>II</sup>, is the possibility of using this compound under OMRP conditions in the absence of alkyl halide, where the intervention of an ATRP mechanism is not possible. Dispersities as low as 1.29 were reported in case of MMA using either AIBN or V-40 (entry 4) as the radical initiators at 110°C.<sup>241</sup> Control in OMRP was better at elevated temperatures.<sup>241</sup> As expected from the spectroscopic analysis, Fe<sup>II</sup>/L under OMRP conditions is not an efficient mediator of styrene polymerization (entry 2).<sup>241</sup>

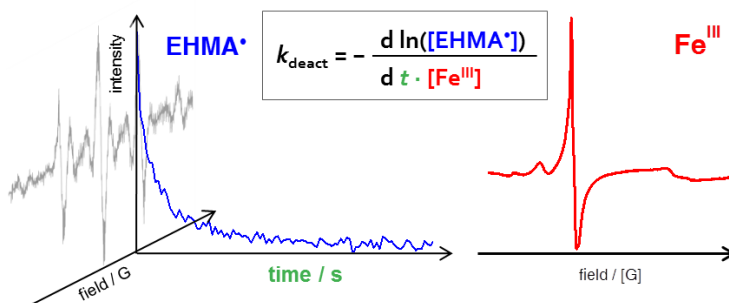
**Table 5.1:** Data for the polymerizations of styrene (Sty) and MMA under ATRP and/or OMRP control started with <sup>Cl,Cl,NMe<sub>2</sub></sup>[O<sub>2</sub>NN']Fe<sup>II</sup>.

entry	monomer	initiator	T / °C	mechanism	$\bar{D}$	ref.
1	Sty	PECl	100	ATRP	1.14	this work
2	Sty	V-40 or AIBN	110	uncontrolled	> 1.5	241
3	MMA	PECl	120	ATRP-OMRP	1.22	241
4	MMA	V-40 or AIBN	110	OMRP	1.29	241

## 5.2 Analysis of Rate Coefficients via SP–PLP–EPR

Because of the kinetic complexity, the precise knowledge of the mechanism and of the individual rate coefficients is necessary for improving Fe-mediated RDRP. The SP–PLP–EPR technique is particularly useful for investigations into the kinetics of radical polymerization, since the concentration of the propagating radical may be measured with high time resolution after pulsed-laser-induced radical production. Metal complexes with unpaired electrons such as  $\text{Cu}^{\text{II}}$  or high-spin  $\text{Fe}^{\text{III}}$  are also EPR-active.<sup>22,176,253</sup> One SP–PLP–EPR methodology has been developed for measuring ATRP deactivation rate, i.e., the reaction of  $\text{Fe}^{\text{III}}$  with propagating radicals. SP–PLP–EPR is also used for measuring the catalytic termination of radicals mediated by  $\text{Fe}^{\text{II}}$ , which presents one type of organometallic reaction.

### 5.2.1 ATRP Deactivation<sup>4</sup>



This chapter deals with an SP–PLP–EPR approach to measure ATRP deactivation rate for amine–bis(phenolate)iron-mediated polymerization of 2-ethylhexyl methacrylate (EHMA). As shown further below, the SP–PLP–EPR experiment is carried out so that ATRP deactivation kinetics is monitored without the interference by organometallic reactions.

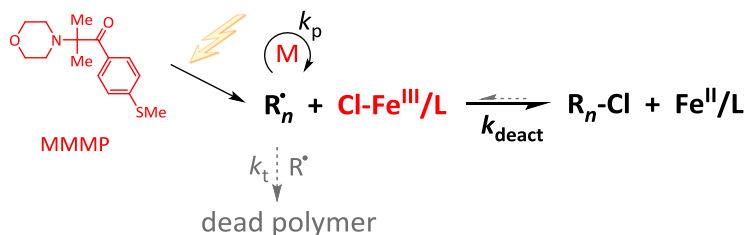
<sup>4</sup> Reproduced with permission from Schroeder, H.; Buback, M. *Macromolecules* **2015**, *48*, 6108–6113, Copyright 2015 American Chemical Society.

SP-PLP-EPR studies into  $k_{\text{deact}}$  are performed more easily in case that deactivation rate is much faster than termination, which is the reason why EHMA was selected as the monomer for this first study into Fe-mediated deactivation rate. EHMA radicals terminate by more than one order of magnitude slower than MMA radicals under otherwise identical conditions.<sup>143,202</sup> EPR is more sensitive toward the detection of methacrylate-type radicals compared with, e.g., styryl radicals, where the EPR intensity is spread over a multitude of lower-intensity peaks. Other than with acrylates, complications due to backbiting and thus midchain-radical formation are not met with methacrylates.

Illustrated in Scheme 5.5 is the scenario for measuring the ATRP deactivation rate coefficient,  $k_{\text{deact}}$ , which resembles the one of reverse ATRP in that the catalyst is employed in the higher oxidation state, i.e.,  $\text{Cl-Fe}^{\text{III}}/\text{L}$ . The starting reagents are marked in red. MMMP acts as the photoinitiator for producing primary radicals which rapidly add to monomer molecules,  $\text{M}$ . Propagating radicals,  $\text{R}_n^{\bullet}$ , of chain length  $n$ , react with the  $\text{Cl-Fe}^{\text{III}}/\text{L}$  complex to generate deactivated alkyl halide,  $\text{R}_n\text{-Cl}$ , and the  $\text{Fe}^{\text{II}}/\text{L}$  complex. In addition, the radicals may terminate and produce dead polymer.

The system under investigation involves 3.0 mM of the amine-*bis*(phenolate)iron(III) chloride complex,  $\text{Cl-Fe}^{\text{III}}/\text{L}$  (for the structure see Figure 5.7A), and 50 mM MMMP (for the structure see Scheme 5.5) in solution of a mixture of EHMA and anisole (25 vol%). MMMP<sup>254</sup> was chosen as the photoinitiator due to its strong absorption at the laser wavelength of 351 nm.

Shown in Figure 5.7A are EPR spectra of  $\text{Cl-Fe}^{\text{III}}/\text{L}$  with maximum intensity at around 1560 G. The spectra were recorded on flash-frozen solutions at  $-153\text{ }^{\circ}\text{C}$ , as this complex may only be detected in the solid state. After recording the initial spectrum (red line), the solution was heated to  $-40\text{ }^{\circ}\text{C}$ . At this temperature, the SP-PLP-EPR analysis for  $k_{\text{deact}}$  was carried out by applying up to 40 laser single pulses. Subsequently, the solution was flash-frozen back to  $-153\text{ }^{\circ}\text{C}$  and the conversion of  $\text{Cl-Fe}^{\text{III}}/\text{L}$  was measured via the double integral of the spectra in Figure 5.7A. The conversion of  $\text{Cl-Fe}^{\text{III}}/\text{L}$  per pulse sequence turned out to be well below 10 %. In the experiments at temperatures above  $-40\text{ }^{\circ}\text{C}$ , only about 15 pulses were applied to keep the overall  $\text{Cl-Fe}^{\text{III}}/\text{L}$  conversion below 5 %. Thus, only minor amounts of  $\text{Fe}^{\text{II}}/\text{L}$  are produced which ensures that the reverse reaction, ATRP activation, does not occur



**Scheme 5.5:** SP-PLP-EPR measurement of  $k_{\text{deact}}$ . The starting components, i.e., the photoinitiator MMMP, monomer M, and the Cl-Fe<sup>III</sup>/L complex are marked in red. The primary radicals generated via laser pulsing produce propagating radicals,  $\text{R}_n^*$ , of chain length  $n$ . Deactivation of  $\text{R}_n^*$  yields alkyl chloride,  $\text{R}_n\text{-Cl}$ , and Fe<sup>II</sup>/L. The scheme includes radical termination to dead polymer.

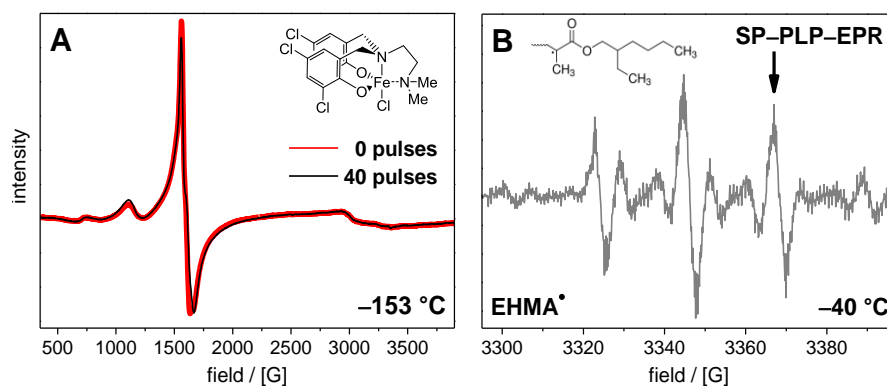


**Figure 5.7:** (A) EPR spectrum (red line) recorded on a flash-frozen solution of 3.0 mM Cl-Fe<sup>III</sup>/L and 50 mM MMMP in EHMA and anisole (3:1, v/v) at -153 °C (120 K). The second spectrum (black line) was recorded on the same solution and also at -153 °C, but after applying 40 laser pulses at -40 °C. (B) The spectrum of EHMA<sup>\*</sup> radicals was recorded at -40 °C using a pulse repetition rate of 20 Hz to identify the appropriate field position, indicated by the arrow, for time-resolved detection of EHMA<sup>\*</sup> concentration.

to a significant extent. This favorable situation is achieved due to the SP-PLP-EPR experiment being instationary, which does not require the activation-deactivation equilibrium state to be reached.

Shown in Figure 5.7B is the spectrum of EHMA radicals recorded between 3300 and 3400 G at  $-40\text{ }^{\circ}\text{C}$  using a pulse repetition rate of 20 Hz. This spectrum serves the purpose of identifying the appropriate field position for time-resolved detection of EHMA radicals (cf. Refs <sup>143,202</sup>), which is indicated by the arrow in Figure 5.7B. This spectrum may be recorded without interference by the broad absorption of the metal complex, since  $\text{Cl-Fe}^{\text{III}}/\text{L}$  only shows up in the EPR solid-phase spectrum. On the other hand, the EPR signal of  $\text{EHMA}^{\bullet}$  does not disturb the  $\text{Cl-Fe}^{\text{III}}/\text{L}$  spectrum shown in Figure 5.7A, as the  $\text{EHMA}^{\bullet}$  radicals quickly disappear after laser-pulsing.

Shown in Figure 5.8 are the  $[\text{EHMA}^{\bullet}]$  vs time traces recorded at  $-40\text{ }^{\circ}\text{C}$  (A) and  $+40\text{ }^{\circ}\text{C}$  (B). In each case, an intense burst of  $\text{EHMA}^{\bullet}$  evolves at time zero,  $t = 0$ , when the laser single pulse hits the sample. It should be noted that the time scale is much shorter for the experiments at higher temperature. At both temperatures (Figure 5.8A–B), the  $[\text{EHMA}^{\bullet}]$  vs time traces were recorded in the absence<sup>179</sup> and in the presence of  $\text{Cl-Fe}^{\text{III}}/\text{L}$ . In the absence of  $\text{Cl-Fe}^{\text{III}}/\text{L}$ , the decay of  $\text{EHMA}^{\bullet}$  concentration is entirely due to radical-radical termination (cf. Scheme 5.5). Interestingly, the decrease in  $\text{EHMA}^{\bullet}$  concentration at  $-40\text{ }^{\circ}\text{C}$  is not significantly accelerated by the presence of 3.0 mM  $\text{Cl-Fe}^{\text{III}}/\text{L}$  (Figure 5.8A). This observation indicates a relatively slow ATRP deactivation rate at  $-40\text{ }^{\circ}\text{C}$ . The situation is clearly different at  $+40\text{ }^{\circ}\text{C}$  (Figure 5.8B), where the decay in  $[\text{EHMA}^{\bullet}]$  with 3.0 mM  $\text{Cl-Fe}^{\text{III}}/\text{L}$  is significantly faster, which is the expected effect of an efficient ATRP deactivator. After 0.1 s, the  $\text{EHMA}^{\bullet}$  concentration in Figure 5.8B decreases below the EPR detection limit.

The initial  $\text{Cl-Fe}^{\text{III}}/\text{L}$  concentration of 3.0 mM was selected to obtain a clear and accurately measurable effect. Higher  $\text{Cl-Fe}^{\text{III}}/\text{L}$  concentration would be associated with higher deactivation rate, which may be difficult to analyze at  $+40\text{ }^{\circ}\text{C}$  and above with the currently available time resolution of the EPR setup. Moreover, initial  $\text{Cl-Fe}^{\text{III}}/\text{L}$  concentration and laser pulse intensity were balanced such as to generate only trace amounts of  $\text{Fe}^{\text{II}}/\text{L}$ , thus avoiding any interference by organometallic reactions between  $\text{Fe}^{\text{II}}/\text{L}$  and  $\text{R}_n^{\bullet}$ . Such trapping of  $\text{R}_n^{\bullet}$  by  $\text{Fe}^{\text{II}}/\text{L}$  would result in an enhanced decay of  $[\text{EHMA}^{\bullet}]$  vs time, which was, however,

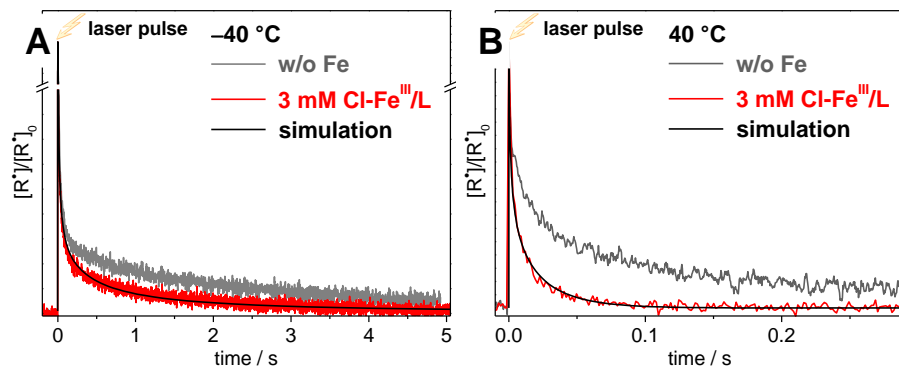


**Figure 5.8:** (A) Relative EHMA $\cdot$  radical concentration,  $[R\cdot]/[R\cdot]_0$ , vs time recorded at  $-40\text{ }^\circ\text{C}$  with the laser single pulse being applied at time zero. Two  $[R\cdot]/[R\cdot]_0$  vs time traces, one in the absence and one in the presence of 3.0 mM Cl-Fe $^{III}$ /L, were recorded. The black line illustrates the PREDICI $^\circ$ -simulated data for the experiment with Cl-Fe $^{III}$ /L. Figure 5.8B shows the results of the analogous experiments carried out at  $+40\text{ }^\circ\text{C}$ . Again, the black line is from PREDICI $^\circ$ -simulation. The experimental data for the iron-free systems, w/o Fe, are from ref. <sup>179</sup>.

not seen in experiments with 5, 10 or 15 applied laser pulses, neither at  $-40\text{ }^\circ\text{C}$ , nor at  $+40\text{ }^\circ\text{C}$ . Organometallic reactions may play a role at higher degrees of Cl-Fe $^{III}$ /L conversion, which were avoided in the present study. A particular advantage of measuring ATRP deactivation by SP-PLP-EPR relates to the fact that this technique enables the precise control of Cl-Fe $^{III}$ /L conversion by sensible selection of the number and intensity of applied laser pulses. Investigations into the kinetics of organometallic reactions may be carried out via SP-PLP-EPR experiments starting from the Fe $^{II}$ /L complex.<sup>242,255</sup>

As has been mentioned above, the analysis for  $k_{\text{deact}}$  benefits from an increase in the ratio of deactivation to termination rate. This is why EHMA, where termination is much slower than, e.g., with methyl methacrylate, has been selected for this study into  $k_{\text{deact}}$ .<sup>143</sup> Moreover, the low melting point and the high boiling point of the EHMA/anisole mixture allow for measuring  $k_{\text{deact}}$  within a wide temperature range.

Deactivation is a first-order reaction in  $[R\cdot]$ , whereas radical-radical termination is second order in  $[R\cdot]$ . As a consequence, termination may



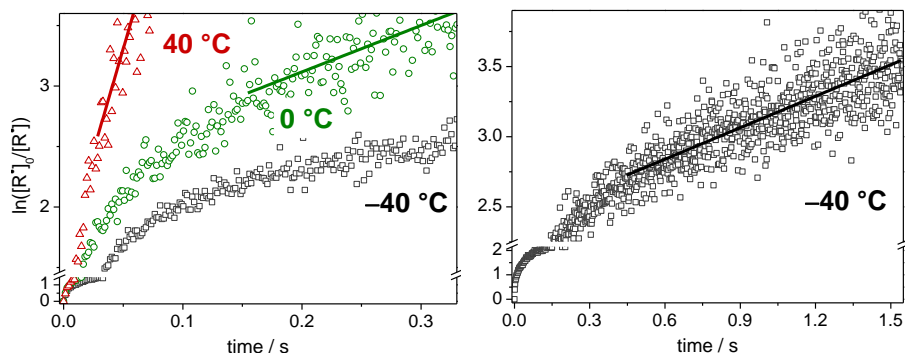
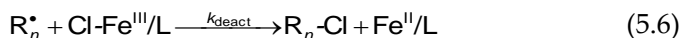
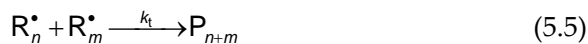


**Figure 5.9:**  $\ln([R^\bullet]_0/[R^\bullet])$  vs time traces for  $-40$ ,  $0$ , and  $+40$  °C. The curvature in the early time regime is indicative of significant contributions from radical–radical termination. Straight lines have been fitted to the data for later times where ATRP deactivation controls the decay of radical concentration.

control the kinetics in the early time period of the SP-PLP-EPR measurement, where radical concentration immediately after applying the laser pulse is very high. The analysis of  $k_{\text{deact}}$  was carried out in the region of lower radical concentration, i.e., at longer times after laser-pulse application, where radical–radical termination plays a minor role and may be ignored.

Shown in Figure 5.9 are  $\ln([R^\bullet]_0/[R^\bullet])$  vs time traces for experiments carried out at  $+40$ ,  $0$ , and  $-40$  °C. The curvature in the early time regime is indicative of significant contributions from radical–radical termination. Straight lines have been fitted to the data for the later time regime where ATRP deactivation controls the kinetics. The slope of the straight lines fitted to the  $\ln([R^\bullet]_0/[R^\bullet])$  vs time data yields the product  $k_{\text{deact}} \times [\text{Cl-Fe}^{\text{III}}/\text{L}]$  according to Equation 5.2. The  $\text{Cl-Fe}^{\text{III}}/\text{L}$  concentration does not vary significantly during the experiment. The mean value of  $\text{Cl-Fe}^{\text{III}}/\text{L}$  concentration measured before and after laser-pulse application via an EPR experiment as presented in Figure 5.7A, is used to calculate  $k_{\text{deact}}$ . The SP-PLP-EPR method is very convenient in that no calibration for absolute radical concentration is required. The estimate of  $k_{\text{deact}}$  is based on relative radical concentrations,  $[\text{EHMA}^\bullet]/[\text{EHMA}^\bullet]_0$ , and thus on relative EPR intensity.



**Scheme 5.6:** Reaction scheme used for the simulation of the  $[R^{\bullet}]/[R^{\bullet}]_0$  vs time traces from SP-PLP-EPR experiments.  $k_{p,1}$  was assumed to be  $10 \times k_p$ . All other rate coefficients were taken from literature for the particular polymerization temperature (see text).

$$\frac{d \ln([R_n^{\bullet}]_0/[R_n^{\bullet}])}{dt} = k_{deact} \cdot [Cl-Fe^{III}/L] \quad (5.2)$$

Although a similar evaluation strategy has been successfully applied toward analysis of iron(II) halide-mediated organometallic reactions,<sup>242</sup> we verified our procedure by simulation of  $[EHMA^{\bullet}]$  vs time traces on the basis of the reaction steps in Scheme 5.6 using the PREDICI<sup>®</sup> program.<sup>256</sup> The value of  $k_{deact}$  (40 °C) =  $(1.2 \pm 0.2) \times 10^4 \text{ L mol}^{-1} \text{ s}^{-1}$ , as determined from the first-order analysis, was introduced into the simulation. The average Cl-Fe<sup>III</sup>/L concentration was 2.97 mM.  $[I]_0$  was adopted and checked by modeling to be  $1.8 \times 10^{-5} \text{ mol L}^{-1}$ ,  $k_p$  (40 °C) amounts to  $740 \text{ L mol}^{-1} \text{ s}^{-1}$ ,<sup>257</sup> and the composite-model parameters<sup>143,144</sup> for chain-length-dependent  $k_t$  are:<sup>179</sup>  $\alpha_s = 0.61$ ,  $\alpha_l = 0.19$ , and  $i_c$  (40 °C) = 100. The termination rate coefficient,  $k_t^{1,1}$ , was varied by a factor of six to check whether this variation affects the first-order analysis of  $k_{deact}$ .

Shown in Figure 5.10 are five simulated  $\ln([R^{\bullet}]_0/[R^{\bullet}])$  vs time traces with  $k_t^{1,1}$  being varied between  $1.0 \times 10^7$  and  $6.0 \times 10^7 \text{ L mol}^{-1} \text{ s}^{-1}$ . Toward higher termination rate, the initial curved region of the  $\ln([R^{\bullet}]_0/[R^{\bullet}])$  vs  $t$  traces extends over a larger time range. Within the subsequent straight-line region, the  $\ln([R^{\bullet}]_0/[R^{\bullet}])$  vs  $t$  correlations are essentially parallel to each other. Thus, irrespective of the value adopted for the termination rate coefficient, the same number for  $k_{deact}$  as introduced into the simulation is obtained. Using  $k_t^{1,1} = 2.8 \times 10^7 \text{ L mol}^{-1} \text{ s}^{-1}$ , i.e., the bold value in Figure 5.10, yields an excellent agreement of experimental and simulated  $[R^{\bullet}]/[R^{\bullet}]_0$  vs time traces for 40 °C (Figure 5.8B). The simulation

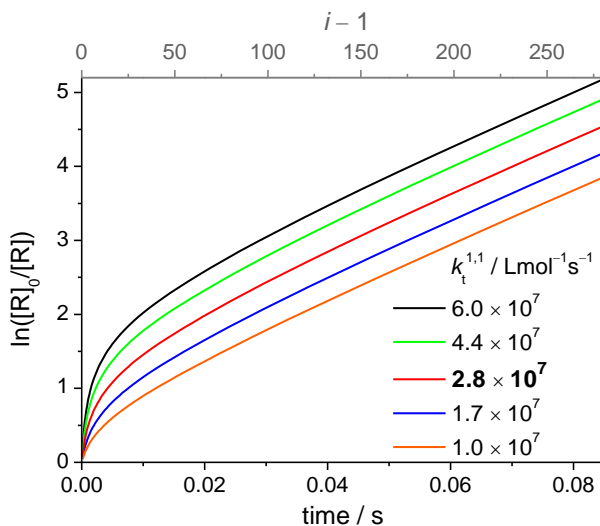


**Figure 5.10:** Simulation of  $\ln([R^\bullet]_0/[R^\bullet])$  vs time,  $t$ , and vs chain length,  $i$ , for an SP–PLP–EPR experiment at 40 °C.  $k_t^{1,1}$  was varied from  $1.0 \times 10^7$  to  $6.0 \times 10^7$  L mol<sup>-1</sup> s<sup>-1</sup>. Further parameters used for simulation are given in the text. Despite the differences in the early time regime, the  $\ln([R^\bullet]_0/[R^\bullet])$  vs  $t$  traces calculated with different termination rates become essentially parallel toward larger  $t$  and thus yield identical  $k_{\text{deact}}$ .

demonstrates that the linear part of the  $\ln([R^\bullet]_0/[R^\bullet])$  vs  $t$  correlation at later stages of the radical decay refers to kinetic control by ATRP deactivation. Analysis of this part of the highly time-resolved EPR trace thus allows for reliably measuring  $k_{\text{deact}}$ . As indicated by the upper abscissa scale in Figure 5.10, the measured  $\ln([R^\bullet]_0/[R^\bullet])$  vs time traces may allow for an analysis of rate coefficients as a function of chain length,  $i = k_p \times c_M \times t + 1$ . Our analysis suggests that  $k_{\text{deact}}$  is chain-length independent, at least within the range of chain lengths covered in the present study, i.e., for radicals up to  $i = 280$  (at 40 °C), since a single value of  $k_{\text{deact}}$  suffices for modeling each  $[R^\bullet]/[R^\bullet]_0$  vs  $t$  trace.

Further measurements of ATRP deactivation rate were carried out between -40 and +80 °C. Shown in Figure 5.11 is the Arrhenius plot of the so-obtained  $k_{\text{deact}}$  data. The associated activation energy was determined from the slope of the straight-line fit to be:  $E_a(k_{\text{deact}}) = (35 \pm 5)$  kJmol<sup>-1</sup>. Given in Equation 5.7 is the Arrhenius

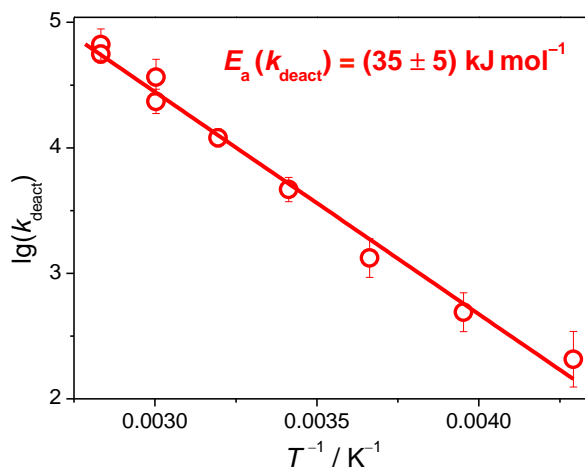


**Figure 5.11:** Arrhenius plot of  $k_{\text{deact}}$ . The activation energy associated with the slope of the straight line is  $E_a(k_{\text{deact}}) = (35 \pm 5) \text{ kJ mol}^{-1}$ .

expression for  $k_{\text{deact}}$ . The measured value at the lowest experimental temperature of  $-40^\circ\text{C}$  slightly exceeds the value given by the Arrhenius relation. This deviation is within experimental accuracy, but may also be due to the small size of  $k_{\text{deact}}$  which may induce some interference of radical–radical termination with the first-order analysis for deactivation. It should be noted that the value of  $k_{\text{deact}}$  at  $-40^\circ\text{C}$  given by the Arrhenius fit,  $k_{\text{deact}} = 1.4 \times 10^2 \text{ L mol}^{-1} \text{ s}^{-1}$ , provides excellent agreement of the simulated  $[\text{R}^\bullet]/[\text{R}^\bullet]_0$  vs time trace with the experimental data, as shown in Figure 5.8A.

$$\ln(k_{\text{deact}} / \text{L mol}^{-1} \text{ s}^{-1}) = 22.44 - \frac{4078}{T/\text{K}} \quad (5.7)$$

The high value of  $E_a(k_{\text{deact}})$  indicates that ATRP deactivation is a chemically controlled process which encompasses the cleavage of the iron–halogen bond and the structural reorganization of the complex.<sup>176</sup> *Ab initio* calculations carried out by Lin et al.<sup>258</sup> as well as theoretical and experimental investigations by Isse et al.<sup>259</sup> suggest that ATRP deactivation proceeds in a concerted fashion: The inner-sphere electron transfer (ISET) involves the transfer of an electron from the propagating radical,  $\text{R}^\bullet$ , to the metal center and the transfer of a halide ion.<sup>176</sup>

Interestingly,  $E_a(k_{\text{deact}})$  is significantly above the activation energy for EHMA propagation,  $E_a(k_p, \text{EHMA}) \approx 20 \text{ kJmol}^{-1}$ .<sup>257</sup> In contrast, the activation energy for the deactivation of DMA-type radicals by  $\text{Cu}^{\text{II}}\text{Br}_2(\text{HMTETA})$  was reported to be  $\approx 21.5 \text{ kJmol}^{-1}$  (cf. Table 5.2),<sup>176</sup> which is very close to  $E_a(k_p, \text{DMA}) \approx 22.4 \text{ kJmol}^{-1}$ .<sup>257,260,261</sup> RDRP involving the amine-*bis*(phenolate)iron chloride complex,  $\text{Cl,Cl,NMe}_2[\text{O}_2\text{NN}']\text{Fe}^{\text{III}}\text{Cl}$ , should thus be carried out at elevated temperature due to the beneficial increase of deactivation rate relative to propagation rate, which improves control and narrows molar mass distribution. Extrapolation via Equation 5.7 yields  $k_{\text{deact}} \approx 1.7 \times 10^5 \text{ Lmol}^{-1}\text{s}^{-1}$  at 120 °C, which is by about a factor of 50 above  $k_p(120 \text{ °C})$ .<sup>257</sup> This difference affords a balanced ratio of deactivation and propagation rate,  $k_{\text{deact}} \cdot [\text{Cl-Fe}^{\text{III}}/\text{L}] \cdot [\text{R}_n^\bullet] \approx k_p \cdot [\text{M}] \cdot [\text{R}_n^\bullet]$ , as the monomer content is well above  $\text{Cl-Fe}^{\text{III}}/\text{L}$  concentration. For RDRPs of MMA at 120 °C, dispersities as low as 1.2 have indeed been reported.<sup>86</sup>

Listed in Table 5.2 are reported  $k_{\text{deact}}$  values determined for ATRP systems involving polymeric methacrylate-type radical species.<sup>176,228</sup> At 60 °C,  $k_{\text{deact}}$  for the  $\text{Cl,Cl,NMe}_2[\text{O}_2\text{NN}']\text{Fe}^{\text{III}}\text{Cl}$  complex is by approximately one order of magnitude below the  $k_{\text{deact}}$  value reported for  $[\text{FeBr}_4]^-$  and by about two orders of magnitude below  $k_{\text{deact}}$  for  $\text{Cu}^{\text{II}}\text{Br}_2(\text{HMTETA})$ .<sup>176,228</sup> This difference decreases toward higher temperature because of the high  $E_a(k_{\text{deact}})$  for  $\text{Cl,Cl,NMe}_2[\text{O}_2\text{NN}']\text{Fe}^{\text{III}}\text{Cl}$ . Only minor effects on  $k_{\text{deact}}$  are expected to occur as a function of the size of the ester side chain, i.e., in between MMA, EHMA, and DMA, since deactivation occurs under chemical control and the side chain is located relatively far off the carbon-centered radical site. The  $k_p$  values, e.g., for EHMA and MMA at 60 °C also differ by less than a factor of 1.5.<sup>262,263</sup>

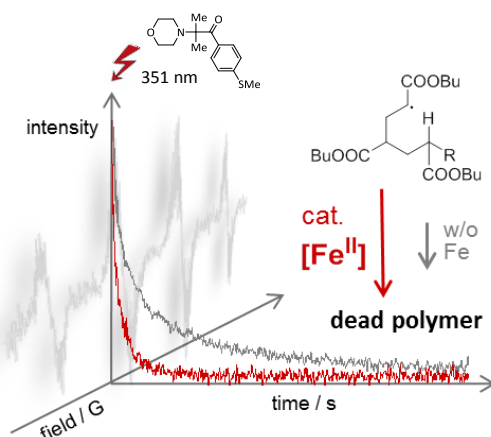
Of key impact on the size of  $k_{\text{deact}}$  is the strength of the metal-halogen bond, which strongly depends on the type of halogen. In Cu catalysis,  $k_{\text{deact}}$  for Cl complexes is by about one order of magnitude below the value for the associated Br species, as may be inferred from monomer-free systems involving methacrylate-type radicals of chain length unity.<sup>35</sup> The deactivation rate of the bromine analogue,  $[\text{O}_2\text{NN}']\text{Fe}^{\text{III}}\text{Br}$ , thus will be closer to the values for  $[\text{FeBr}_4]^-$  and  $\text{Cu}^{\text{II}}\text{Br}_2(\text{HMTETA})$  listed in Table 5.2. The size of  $k_{\text{deact}}$  makes amine-*bis*(phenolate)iron an attractive catalyst system for well-controlled RDRPs.<sup>86,87</sup>

**Table 5.2:**  $k_{\text{deact}}$  at 60 °C and activation energy,  $E_a(k_{\text{deact}})$ , for ATRP of methacrylate-type radicals mediated by different deactivator species.

entry	deactivator	monomer	$k_{\text{deact}}$ at 60 °C / $\text{Lmol}^{-1}\text{s}^{-1}$	$E_a$ / $\text{kJmol}^{-1}$	ref.
1	$\text{Cl}_2\text{NMe}_2[\text{O}_2\text{NN}']\text{Fe}^{\text{III}}\text{Cl}$	EHMA	$2.7 \times 10^4$	$35 \pm 5$	this work
2	$[\text{TBA}][\text{Fe}^{\text{III}}\text{Br}_4]$ [a]	MMA [c]	$5.0 \times 10^5$	-	228
3	$\text{Cu}^{\text{II}}\text{Br}_2(\text{HMTETA})$ [b]	DMA	$2.2 \times 10^6$	$21.5 \pm 5$	176

[a] TBA = tetrabutylammonium; [b] HMTETA = 1,1,4,7,10,10-hexamethyltriethylenetetramine; [c] PMMA-Br of molar mass  $8000 \text{ g mol}^{-1}$  dissolved in 2-butanone is used as the initiator.

### 5.2.2 Fe-Mediated Radical Termination<sup>5</sup>



The SP-PLP-EPR technique was used to study the catalytic termination of two propagating radicals by  $\text{Fe}^{\text{II}}$ . Even though polymerization with the  $[\text{Fe}^{\text{II}}\text{Br}_3(\text{Solv})]^-$  mediator is ATRP-controlled, the catalytic termination turns out to play a role for the ATRP of acrylates.

<sup>5</sup> Reproduced with permission from Schroeder, H.; Buback, M. *Macromolecules* **2014**, *47*, 6645–6651, Copyright 2015 American Chemical Society.

For the SP–PLP–EPR experiments, solutions of  $[\text{Fe}^{\text{II}}\text{Br}_3(\text{Solv})]^-$ , as obtained by combining  $\text{FeBr}_2 : \text{TBA-Br} = 1:1$ , and of the photoinitiator MMMP (ca. 46 mM) in BA and 2-butanone (15 vol%) were prepared. Experiments were carried out in the absence of alkyl halide, i.e., of the ATRP initiator, thus avoiding the ATRP activation reaction. SP–PLP–EPR experiments under such conditions focus on the potential organometallic reactions of propagating radicals with the  $\text{Fe}^{\text{II}}$  catalyst.

Shown in Figure 5.12A is an EPR spectrum recorded at  $-60\text{ }^\circ\text{C}$  under pseudo-stationary conditions at a laser pulse repetition rate of 20 Hz. The four-line spectrum is characteristic of secondary propagating radicals (SPRs) in BA polymerization (see Figure 5.12A).<sup>154,264</sup> Mid-chain radicals (MCRs) are not detected at this low temperature due to the high activation energy of the backbiting reaction of  $34.7\text{ kJmol}^{-1}$ , by which MCRs are produced from SPRs (the structure of MCRs is given further below).<sup>264</sup> The time-resolved concentration of SPRs was measured at the maximum intensity of the associated spectrum. As illustrated in Figure 5.12B, an intense burst of SPRs evolves at time  $t = 0$  when the laser single pulse is applied. The primary photoinitiator-derived radicals add to the monomer (Scheme 5.7). As is shown in Figure 5.12B, the subsequent decay in SPR concentration, which usually occurs via radical-radical termination, becomes much faster toward increasing  $\text{Fe}^{\text{II}}$  content. In the presence of 10 mM  $\text{Fe}^{\text{II}}$ , the decrease in SPR concentration to ca.  $10^{-7}\text{ molL}^{-1}$  is about ten times faster than in the absence of  $\text{Fe}^{\text{II}}$ . This observation suggests that the  $\text{Fe}^{\text{II}}$  species either induce an irreversible trapping or catalyze the termination of propagating radicals. The shorter lifetime of radicals in the presence of  $\text{Fe}^{\text{II}}$  has remarkable consequences on the molar mass distribution of the polymer obtained from PLP: Molar mass in PLP with  $\text{Fe}^{\text{II}}$  being present is by two orders of magnitude below the one from PLP without  $\text{Fe}^{\text{II}}$  (Figure 5.13).

The interaction of radicals with  $\text{Fe}^{\text{II}}$  species is not contained in the conventional ATRP scheme and thus requires closer inspection in order to elucidate the mechanistic scenarios and kinetic consequences for controlled polymerization.

Scheme 5.7 illustrates potential reactions of propagating radicals after laser pulsing. For BA polymerizations carried out at  $-60\text{ }^\circ\text{C}$ ,  $R_n^\bullet$  refers exclusively to SPRs due to the absence of MCRs. Scheme 5.7 includes radical-radical termination to dead polymer,  $P_{n+m}$ , with a chain-length-dependent (CLD) rate coefficient  $k_t^{i,i}$ .<sup>154</sup> The organometallic

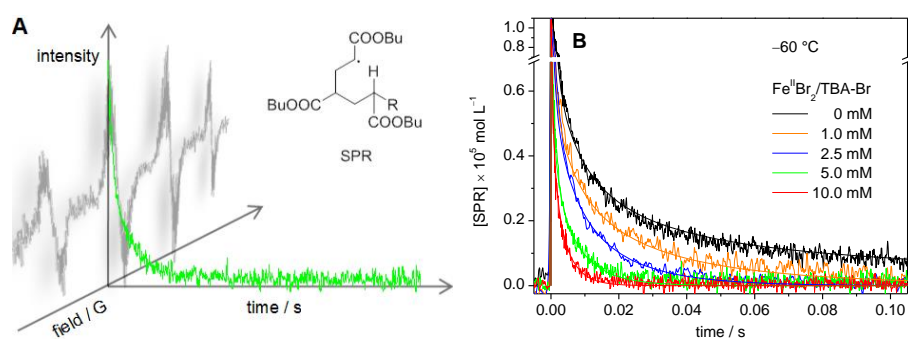


**Figure 5.12:** (A) Time-resolved SPR concentration measured at the position of maximum intensity of the four-line EPR spectrum. (B) SPR concentration vs time traces measured at  $-60\text{ }^{\circ}\text{C}$  with the laser single pulse being applied at time zero using MMMP as the photoinitiator in a solution of BA:2-butanone (85:15 v/v) at different levels of Fe<sup>II</sup> (including the equivalent amounts of TBA-Br, see text). The experimental data has been modeled (full lines) via PREDICI (see further below).

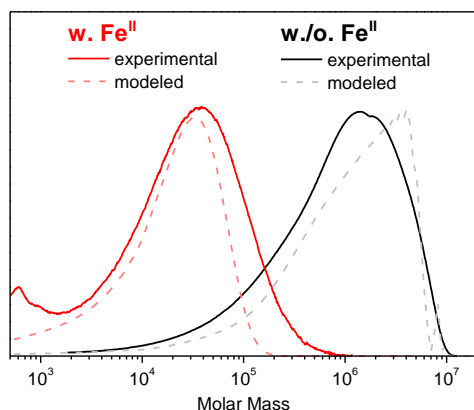
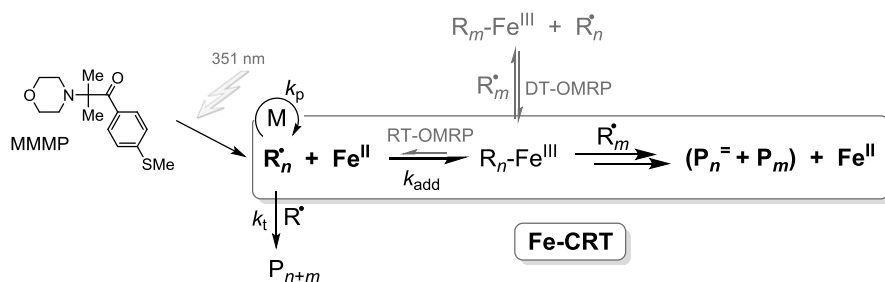


**Figure 5.13:** Molar mass distributions of poly(butyl acrylate) obtained from PLP of BA at  $25\text{ }^{\circ}\text{C}$  in solution of 2-butanone (15 vol%) in the presence (red full line) and in the absence (black full line) of  $[\text{TBA}][\text{Fe}^{\text{III}}\text{Br}_3(\text{Solv})]$  (10 mM). The dashed lines illustrate the distributions modeled with PREDICI.





**Scheme 5.7:** Potential reactions of propagating radicals generated by laser pulsing with MMMP acting as the photoinitiator. The scheme includes radical-radical termination, as well as RT-OMRP, DT-OMRP, and Fe-CRT to the  $P_n^=$  and  $P_m$  disproportionation products via  $R_n-Fe^{III}$ .

pathway,  $k_{add}$ , proceeds via an  $R_n-Fe^{III}$  intermediate. The formation of  $R_n-Fe^{III}$  may result in organometallic-mediated radical polymerization (OMRP) either via reversible termination (RT) or via degenerative transfer (DT). Moreover,  $R_n-Fe^{III}$  may induce Fe-CRT by reaction with another radical  $R_m^{\bullet}$  to form dead polymer. This CRT process is expected to proceed in a similar manner as  $Cu^I-CRT$ , i.e., via  $\beta$ -H elimination to produce disproportionation products,  $P_n^=$  and  $P_m$ . In contrast to the situation with  $Cu^I-CRT$ ,<sup>255</sup> the  $R_n-Fe^{III}$  intermediate could not be detected via EPR or NIR spectroscopy. In what follows, the mechanism of the organometallic pathway will be investigated by analyzing the experimental [SPR] vs time traces presented in Figure 5.12.

Other than conventional radical-radical termination, the organometallic reaction between  $R_n^{\bullet}$  and  $Fe^{II}$  is first order in  $[R_n^{\bullet}]$  (cf. Equations 5.8–5.9) and thus becomes the dominant reaction pathway toward lower radical concentration and higher  $Fe^{II}$  content (cf. Figure 5.12). The decay in radical concentration seen in the presence of  $Fe^{II}$  should follow first-order kinetics in two potential scenarios: when a stable  $R_n-Fe^{III}$  intermediate is irreversibly formed ( $R_n^{\bullet} + Fe^{II} \rightarrow R_n-Fe^{III}$ ) (Equation 5.8) or when subsequent CRT according to Scheme 5.7 takes place to regenerate  $Fe^{II}$  (Equation 5.9). The additional factor of two in Equation 5.9 results from two radicals being consumed in each Fe-CRT step. The rate coefficient for Fe-CRT,  $k_t^{Fe}$ , is defined as  $2k_{add}$  in order to remain consistent with the previous notation.<sup>255</sup> The essential difference between both scenarios is that the formation of stable  $R_n-Fe^{III}$

intermediates results in a gradual decrease in  $\text{Fe}^{\text{II}}$  concentration upon repetitive laser pulsing, whereas the  $\text{Fe}^{\text{II}}$  catalyst is regenerated by Fe-CRT. It was found that identical [SPR] vs time traces may be recorded even after several hundred pulses (Figure S13A). Although the amount of radicals produced by such a large number of pulses is well above the selected  $\text{Fe}^{\text{II}}$  concentration, there is no indication of any  $\text{Fe}^{\text{II}}$  consumption. The characteristic NIR absorbance of the  $\text{Fe}^{\text{II}}$  complex around  $4700\text{ cm}^{-1}$  (cf. chapter 4.1.1) before and after the PLP experiment with 600 laser pulses remained unchanged (Figure S13B). It may be concluded that the CRT mechanism observed in Cu-mediated ATRPs of BA also operates in the Fe-catalyzed system.

The fast CRT reaction prevents an efficient control of the polymerization by one of the two OMRP pathways presented in Scheme 5.7. The  $\text{R}_n\text{-Fe}^{\text{III}}$  intermediate is predominantly decomposed via the CRT pathway. In particular DT-OMRP requires stable  $\text{R}_n\text{-Fe}^{\text{III}}$  intermediates and thus the absence of significant contributions of Fe-CRT. It should further be noted that the occurrence of an OMRP equilibrium with an  $\text{R}_n\text{-Fe}^{\text{III}}$  intermediate would turn Fe-CRT into a second-order reaction (cf. Equation S8), which is also not observed. The interplay of ATRP and OMRP may thus be ruled out for polymerizations with the investigated catalyst.

$$-\frac{d\ln[\text{R}^{\bullet}]}{dt} = k_{\text{add}} \cdot [\text{Fe}^{\text{II}}] \quad (5.8)$$

or in case of a subsequent reaction of  $\text{R}_n\text{-Fe}^{\text{III}}$  with  $\text{R}_m^{\bullet}$ :

$$-\frac{d\ln[\text{R}^{\bullet}]}{dt} = 2 \cdot k_{\text{add}} \cdot [\text{Fe}^{\text{II}}] = k_{\text{t}}^{\text{Fe}} \cdot [\text{Fe}^{\text{II}}] \quad (5.9)$$

First-order kinetics were checked by plotting the  $\ln([\text{SPR}]_0/[\text{SPR}])$  vs time data from SP-PLP-EPR analysis for BA polymerizations at  $-60\text{ }^{\circ}\text{C}$  and different levels of  $[\text{Fe}^{\text{II}}]$  as illustrated in Figure 5.14A. With the exception of the initial time period where the high level of radical concentration significantly contributes to radical-radical termination, straight lines may be fitted to the data. The slopes of these straight lines are 240, 120, 54, and  $27\text{ s}^{-1}$  for experiments with 10.0, 5.0, 2.5, and 1.0 mM  $\text{Fe}^{\text{II}}$ , respectively, resulting in  $k_{\text{t}}^{\text{Fe}}$  values of  $2.4 \times 10^4$ ,  $2.3 \times 10^4$ ,  $2.2 \times 10^4$ , and  $2.7 \times 10^4\text{ Lmol}^{-1}\text{s}^{-1}$ , respectively, according to Equation 5.9.

The fitted data interval corresponds to chain lengths  $i = k_p \times c_M \times t + 1$  of about 15 to 200. Within this chain-length interval, no CLD of  $k_t^{\text{Fe}}$  was observed. The slightly larger  $k_t^{\text{Fe}}$  value at the lowest  $\text{Fe}^{\text{II}}$  concentration is probably due to radical-radical termination affecting the analysis as is also indicated by the larger range of non-linearity of the associated data (Figure 5.14A). The mean value for higher  $\text{Fe}^{\text{II}}$  content,  $2.3 \times 10^4 \text{ Lmol}^{-1}\text{s}^{-1}$ , was used for PREDICI modeling of the measured SP–PLP–EPR traces in Figure 5.14B according to Scheme S1. Close agreement of the experimental and modeled data was achieved by using identical rate coefficients for modeling SP–PLP–EPR traces within the entire range of  $\text{Fe}^{\text{II}}$  concentrations from 0 to 10 mM. The analysis of  $k_t^{\text{Fe}}$  via modeling (see Figure 5.12B) supports the evidence from the evaluation procedure via the pseudo first-order plots.

Shown in Figure 5.14B are four  $\ln([\text{SPR}]_0/[\text{SPR}])$  vs time traces for BA polymerization between  $-60\text{ }^\circ\text{C}$  and  $+50\text{ }^\circ\text{C}$  in the presence of 5 to 10 mM  $\text{Fe}^{\text{II}}$ . Favored by the high catalyst loading, Fe-CRT turns out to be the dominant termination pathway throughout most of the measured concentration regime, as evidenced by the linearity of these plots at larger  $t$ . In case of BA polymerization, both the backbiting rate,  $k_{\text{bb}} \times [\text{SPR}]$ , as well as the propagation rate of MCRs,  $k_p^t \times [\text{MCR}] \times [\text{M}]$ , need to be considered at higher temperature, see Equation 5.10.<sup>154</sup> Equation 5.10 reduces to the simple first-order expression, i.e., Equation 5.9, only in the case of very fast CRT, e.g., at high  $\text{Fe}^{\text{II}}$  loadings. Further determinations of  $k_t^{\text{Fe}}$  have thus been carried out at  $\text{Fe}^{\text{II}}$  contents of at least 5 mM, since backbiting and MCR propagation would otherwise complicate the analysis of  $k_t^{\text{Fe}}$ .

$$\frac{d[\text{SPR}]}{dt} = -k_t^{\text{Fe}} \cdot [\text{Fe}^{\text{II}}] \cdot [\text{SPR}] - k_{\text{bb}} \cdot [\text{SPR}] + k_p^t \cdot [\text{M}] \cdot [\text{MCR}] \quad (5.10)$$

In order to measure SPR concentration in the presence of MCRs, SPRs need to be monitored at a specific magnetic field position which is free from overlap with the MCR spectrum.<sup>154</sup> The simulated EPR spectra of SPRs and MCRs reported in the literature<sup>92</sup> suggest that it may be difficult in case of BA polymerization to find such an optimum field position for exclusively detecting SPRs. At  $50\text{ }^\circ\text{C}$ , SPR concentration was measured at the field position indicated in Figure 5.12A according to the procedure reported elsewhere.<sup>154</sup> The slope of the straight line fitted to

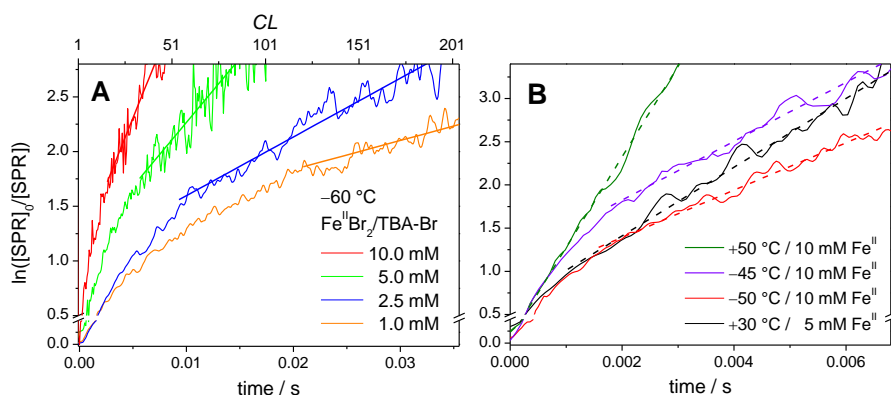


**Figure 5.14:**  $\ln([\text{SPR}]_0/[\text{SPR}])$  vs time traces recorded during SP-PLP-EPR measurements of BA at (A)  $-60\text{ }^\circ\text{C}$  with 1.0 to 10.0 mM  $\text{Fe}^{\text{II}}$  and (B) up to  $+50\text{ }^\circ\text{C}$  with 10 mM  $\text{Fe}^{\text{II}}$  or with 5 mM  $\text{Fe}^{\text{II}}$ . The data in Figure 5.14B has been recorded at lower time resolution. The linear fits are represented by the full (A) and dotted (B) lines.

the  $\ln([\text{SPR}]_0/[\text{SPR}])$  vs time data shown in Figure 5.14B results in the rate coefficient:  $k_t^{\text{Fe}}(50\text{ }^\circ\text{C}) = (1.0 \pm 0.1) \times 10^5 \text{ Lmol}^{-1}\text{s}^{-1}$ . A similarly suitable field position could not be found for experiments between  $-20\text{ }^\circ\text{C}$  and  $+20\text{ }^\circ\text{C}$ , probably due to an unfavorable shift of the MCR against the SPR spectrum.

MCR concentration may be measured at the maximum of the highest magnetic field position of the associated hyperfine structure (cf. Ref. <sup>154</sup>) without interference by the SPR spectrum. Such  $[\text{MCR}]$  vs time traces are shown in Figure 5.15 for  $+50\text{ }^\circ\text{C}$  and different levels of  $\text{Fe}^{\text{II}}$ . Additional measurements are included in Figure S21. Other than with the SPR traces in Figure 5.12B recorded under highly instationary conditions, no significant acceleration of decay rate is seen toward increasing  $\text{Fe}^{\text{II}}$  concentration. Some enhanced decay in MCR concentration toward high  $\text{Fe}^{\text{II}}$  content is seen, which is due to Fe-CRT of SPRs generated by the addition of monomer to MCRs. The data in Figure 5.15 suggests that Fe-CRT is not an important process for MCRs.

As Fe-CRT of SPRs affects the MCR kinetics, it should be possible to estimate  $k_t^{\text{Fe}}$  for SPRs, under the equilibrium conditions described in Appendix B, via the measurement of  $[\text{MCR}]$  vs  $t$  traces. The analysis for  $k_t^{\text{Fe}}$  via pseudo first-order plots of experimental  $[\text{MCR}]$  vs  $t$  data is

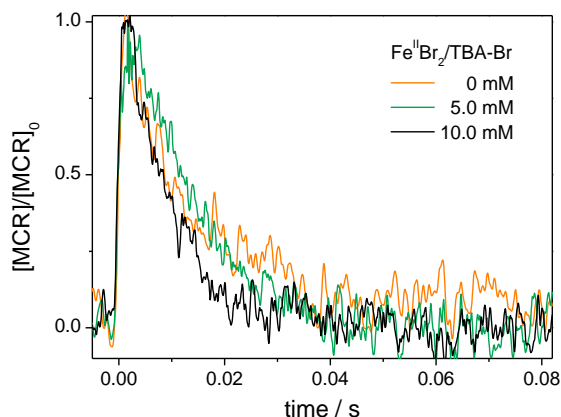


**Figure 5.15:**  $[MCR]/[MCR]_0$  vs time traces measured by SP-PLP-EPR experiments on BA containing 2-butanone (15 vol.%) at +50 °C and  $Fe^{II}$  concentrations of 0, 5, and 10.0 mM  $Fe^{II}$ , respectively.

detailed in Appendix B. As demonstrated by Equation S16, the analysis of  $k_t^{Fe}$  via time-resolved measurement of MCRs requires the knowledge of the rate coefficients for MCR propagation and backbiting,  $k_p^t$  and  $k_{bb}$ , respectively. For this reason, direct analysis of  $k_t^{Fe}$  via measuring SPR concentration is the preferred option. It is however gratifying to note that the numbers derived via both approaches are in close agreement (cf. Table S5).

**Methacrylate polymerization.** Based on the mechanistic insight into butyl acrylate polymerization, it appeared rewarding to check, whether organometallic reactions as contained in Scheme 5.7 also operate in Fe-mediated polymerization of methacrylates. Dodecyl methacrylate (DMA) was chosen as the monomer for the associated SP-PLP-EPR measurements. The dodecyl side chain significantly lowers the diffusion-controlled radical-radical termination rate coefficient,  $k_t^{d,i}$ ,<sup>143</sup> which even allows for the analysis of slower organometallic reactions. Shown in Figure 5.16 are two traces of relative radical concentration vs  $t$  measured on a DMA/2-butanone solution (70:30 v/v) at 0 °C, in the absence and in the presence of 10 mM  $FeBr_2/TBA-Br$ , respectively. With backbiting being absent in the case of methacrylates, radical

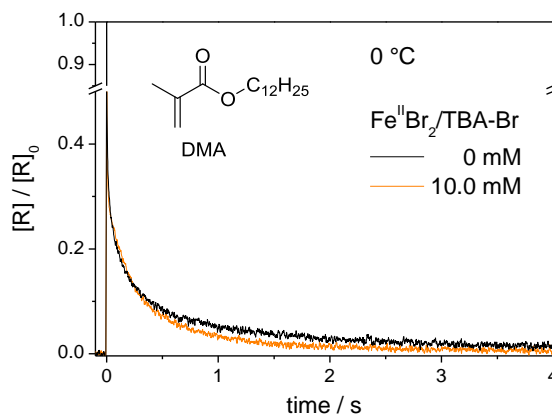


**Figure 5.16:**  $[R]/[R]_0$  vs time traces for the SP-PLP-EPR measurements of DMA at 0 °C with 10 mM  $\text{Fe}^{\text{II}}$  and without  $\text{Fe}^{\text{II}}$ .

concentration refers to the only one type of chain-end radicals. The radical concentration vs  $t$  traces in Figure 5.16 are more or less identical which indicates that an organometallic reaction such as Fe-CRT plays no major role with methacrylate polymerizations. Analysis for  $k_t^{\text{Fe}}$  (DMA) along the above lines yields  $k_t^{\text{Fe}}$  (DMA) =  $(60 \pm 10) \text{ Lmol}^{-1}\text{s}^{-1}$  at 0 °C, which is by about three orders of magnitude below the value found for SPRs in acrylate polymerization. A value similar to  $k_t^{\text{Fe}}$  (DMA) may apply to CRT behavior of the structurally similar MCRs in acrylate polymerization.

**Fe-CRT in ATRP.** Fe-CRT may also be measured during ATRP. According to the basic concept of ATRP, each termination step, irrespective of occurring with or without metal catalysis, leads to the accumulation of the ATRP deactivator species,<sup>155,156</sup> e.g., of  $[\text{Fe}^{\text{III}}\text{Br}_4]^-$ . Therefore, it appeared rewarding to expand the instationary SP-PLP-EPR experiments to the analysis of ATRPs of BA and MMA under stationary conditions, where radical concentration is below  $10^{-7} \text{ molL}^{-1}$ . Shown in Figure 5.17A are the NIR spectra for ATRP of BA with 17.7 mM  $\text{FeBr}_2$ , 17.7 mM TBA-Br, and 13.6 mM MBriB at 75 °C in solution of 2-butanone (50 vol%). Only five out of a multitude of spectra recorded within 90 h are shown. The concentrations of  $[\text{Fe}^{\text{III}}\text{Br}_4]^-$ , of

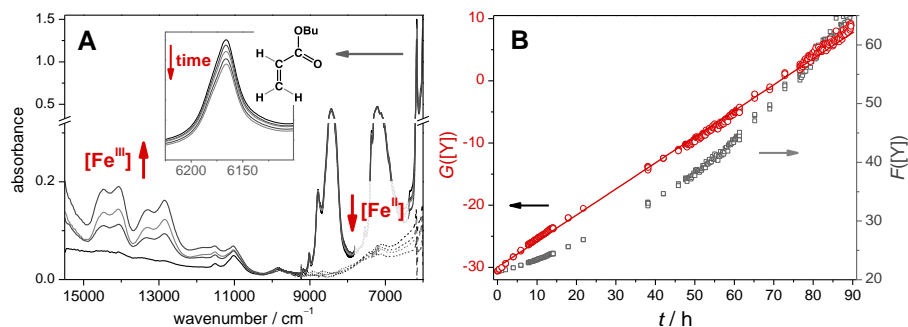


**Figure 5.17:** (A) Online NIR measurement of Fe<sup>III</sup>, of Fe<sup>II</sup>, and of monomer concentration during an ATRP of BA with 17.7 mM FeBr<sub>2</sub>, 17.7 mM TBA-Br, and 13.6 mM MBriB at 75 °C in solution of 2-butanone (50 vol%). Only five out of a multitude of spectra recorded within 90 h are shown. (B) Plot of the functions  $G(Y)$  and  $F(Y)$  vs time for the same reaction as in Figure 5.17A.

monomer, and of Fe<sup>II</sup> were monitored during the same experiment (see chapter 6.3.2 for details). The  $[\text{Fe}^{\text{II}}\text{Br}_3(\text{Solv})]^-$  contribution to absorption is obtained by subtraction of the solvent absorption via reference spectra taken at the same solvent composition, but in the absence of Fe<sup>II</sup>.

The concentration of  $[\text{Fe}^{\text{III}}\text{Br}_4]^-$  is easily determined as described in chapter 4.1.2, as no significant solvent absorption occurs in the 12 000 to 15 000  $\text{cm}^{-1}$  range. The  $[\text{Fe}^{\text{II}}\text{Br}_3(\text{Solv})]^-$  concentration may be determined with sufficient accuracy as to conclude that the decrease in Fe<sup>II</sup> is equivalent to the increase in Fe<sup>III</sup>. The increase in Fe<sup>III</sup> concentration caused by radical-radical termination should be represented by the modified Fischer Equation 4.1, for  $F([Y])$ .<sup>36</sup> The accumulation of  $[\text{Fe}^{\text{III}}\text{Br}_4]^-$  in the BA ATRPs under investigation is, however, much faster than predicted for conventional radical-radical termination, i.e.,  $d[\text{Br-Fe}^{\text{III}}] \gg 2k_t \times [\text{R}]^2 \times dt$ . This observation indicates that  $[\text{Fe}^{\text{III}}\text{Br}_4]^-$  is predominantly produced via Fe-CRT which is represented by the function  $G([Y])$  in Equation 5.11.<sup>255</sup> In order to remain consistent with previous work,  $[I]_0$  represents  $[\text{RX}]_0$ ,  $[C]_0$  refers to  $[\text{Fe}^{\text{II}}\text{Br}_3(\text{Solv})]^-$  at  $t = 0$ , and  $[Y]$  to  $[\text{Fe}^{\text{III}}\text{Br}_4]^-$ .<sup>36</sup> Only the  $G([Y])$  function results in a straight line plot of the experimental data, illustrated in Figure 5.17B. The linearity of the first-order function  $G([Y])$  further demonstrates that (RT-) OMRP is absent.

$$G([Y]) = \int_0^Y \frac{[Y]}{([I]_0 - [Y])([C]_0 - [Y])^2} d[Y] = k_t^{\text{Fe}} \cdot K_{\text{ATRP}} \cdot t \quad (5.11)$$

From  $G([Y])$ , the Fe-CRT rate coefficient has been determined to be:  $k_t^{\text{Fe}} (75 \text{ }^\circ\text{C}) = (1.1 \pm 0.2) \times 10^5 \text{ Lmol}^{-1}\text{s}^{-1}$ . The equilibrium constant,  $K_{\text{ATRP}}$ , required for this analysis has been determined by online NIR-spectroscopic measurement of monomer and catalyst concentration in the monomer conversion range between 2 and 21 per cent, see chapter 6.3.2 for details, to be:  $K_{\text{ATRP}} = (1.2 \pm 0.2) \times 10^{-9}$  (cf. Figure S14). The so-obtained  $k_t^{\text{Fe}}$  values for 60 and 75 °C are close to each other. The almost perfect agreement of  $k_t^{\text{Fe}}$  with the corresponding number from the above-mentioned SP-PLP-EPR experiments can also be seen in Figure 5.18 below.

$k_t^{\text{Fe}}$  for methacrylates was studied via online NIR-spectroscopic monitoring of MMA ATRPs in different solvent environments. In agreement with the results obtained via SP-PLP-EPR, the rate of CRT for methacrylates is well below the rate for acrylates. For ATRP in bulk MMA,  $k_t^{\text{Fe}}$  at 60 °C amounts to  $(8.0 \pm 3.0) \times 10^2 \text{ Lmol}^{-1}\text{s}^{-1}$ , which is by a factor of five below the value determined for DMA polymerization in solution of 2-butanone (cf. Table 5.3 below).

**Discussion.** The measured  $k_t^{\text{Fe}}$  values for DMA radicals and for SPRs of BA are summarized in Figure 5.18. The slope of the straight line fitted to the SPR-related data in the Arrhenius-type plot yields an activation energy,  $E_A(k_t^{\text{Fe}})$ , of  $(7.7 \pm 1.0) \text{ kJmol}^{-1}$ . The activation barrier is close to the activation energy of fluidity of BA,<sup>56</sup>  $E_A(\eta^{-1}) = 10.5 \text{ kJmol}^{-1}$ , and of 2-butanone,  $E_A(\eta^{-1}) = 7.2 \text{ kJmol}^{-1}$ .<sup>200</sup> The absolute value of  $k_t^{\text{Fe}}$  is, however, clearly below the one estimated for a diffusion-controlled process.

Interestingly,  $E_A(k_t^{\text{Fe}})$  for DMA radicals is significantly higher and amounts to  $(52 \pm 5) \text{ kJmol}^{-1}$ . CRT for both monomers occurs under chemical control. The difference in activation energy suggests that the relative importance of  $R_n\text{-Fe}^{\text{III}}$  formation and subsequent  $\beta$ -H elimination differs for acrylates and methacrylates. These reaction steps may also occur in a concerted fashion via H-Fe<sup>III</sup> intermediates.<sup>255</sup> Although the activation energy is high for methacrylates, the rate of Fe-CRT does not exceed the one of conventional radical-radical termination



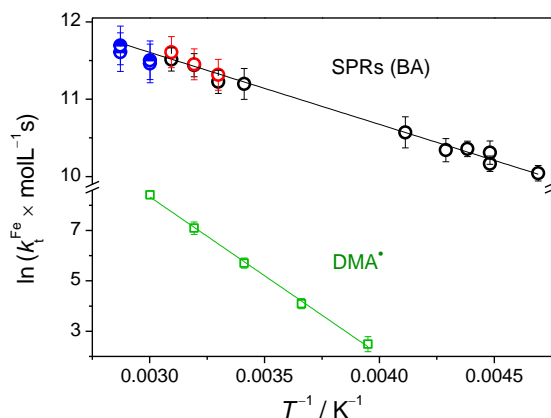


**Figure 5.18:** Arrhenius plot of  $k_t^{\text{Fe}}$  for SPRs of BA (circles) and for DMA in solution of 2-butanone (squares), determined via the SP-PLP-EPR method (empty symbols) and via online NIR spectroscopy of actual ATRPs (half-filled blue symbols). The data represented by red circles was deduced via the analysis of MCR concentration (cf. Table S5). Straight lines were fitted to the SP-PLP-EPR data.

at elevated polymerization temperatures, e.g., of 60 to 80 °C. Well-controlled ATRPs of methacrylates catalyzed by  $[\text{Fe}^{\text{II}}\text{Br}_3(\text{Solv})]^-$  may therefore be carried out even in the presence of high  $\text{Fe}^{\text{II}}$  catalyst loadings.<sup>81,82,105</sup> This statement also applies to such ATRPs in polar solvent environments, where  $k_t^{\text{Fe}}$  ( $\text{DMA}^*$ ) is reduced by about one order of magnitude in solution of 30 vol.% NMP (Table 5.3). The advantage of a decrease in  $k_t^{\text{Fe}}$  may, however, be accompanied by a decrease in catalyst activity, i.e., by a lowering of the ATRP equilibrium constant in a polar solvent environment (see chapter 4.1.3).

The CRT reaction also occurs in Cu-mediated ATRPs of acrylates, which are typically carried out in solution of MeCN.<sup>255,265</sup> In contrast to Fe, the organometallic species  $\text{R}_n\text{-Cu}^{\text{II}}/\text{TPMA}$  is stable at -40 °C and may be detected via both EPR and NIR (Figure S12) spectroscopy.<sup>255</sup> The stability of  $\text{R}_n\text{-Cu}^{\text{II}}/\text{TPMA}$  is due to the subsequent termination reaction being yet irrelevant at this lower temperature.<sup>179</sup> The rate coefficient for the formation of  $\text{R}_n\text{-Cu}^{\text{II}}/\text{TPMA}$  from radicals and  $[\text{Cu}^{\text{II}}\text{TPMA}]^+$  at -40 °C,  $k_{\text{add}} = (3.0 \pm 0.8) \times 10^5 \text{ L mol}^{-1} \text{ s}^{-1}$  (entry 1, Table 5.4),<sup>179</sup> is by a factor of 20 higher than  $k_{\text{add}}([\text{Fe}^{\text{II}}\text{Br}_3(\text{Solv})]^-) = (1.5 \pm 0.2) \times 10^4 \text{ L mol}^{-1} \text{ s}^{-1}$  in the

**Table 5.3:**  $k_t^{\text{Fe}}(\text{BA})$  at 60 °C and the associated activation energy,  $E_a$ , for different monomer/solvent environments.

entry	metal	monomer / solvent	$k_t^{\text{Fe}}$ at 60 °C / Lmol <sup>-1</sup> s <sup>-1</sup>	$E_a$ / kJmol <sup>-1</sup>
1	Fe <sup>II</sup>	BA / 2-butanone	$(1.0 \pm 0.1) \times 10^5$ [a]	$7.7 \pm 1.0$
2	Fe <sup>II</sup>	DMA / 2-butanone	$(4.0 \pm 0.5) \times 10^3$	$52 \pm 5$
3	Fe <sup>II</sup>	DMA / NMP	$(2.0 \pm 0.4) \times 10^2$	-

[a] Extrapolated from 50 °C.

2-butanone solution (entry 3), whereas  $k_{\text{add}} = (9 \pm 3) \times 10^3$  Lmol<sup>-1</sup>s<sup>-1</sup> for the [Cu<sup>I</sup>(PMDETA)]<sup>+</sup> complex (entry 2)<sup>179</sup> is very close to the value for the Fe-based system. Interestingly, [Cu<sup>I</sup>(PMDETA)]<sup>+</sup> and [Fe<sup>II</sup>Br<sub>3</sub>(Solv)]<sup>-</sup> are also characterized by similar ATRP activity, i.e., by similar size of  $K_{\text{ATRP}}$  (see chapter 4.1.3). There are, however, mechanistic differences in the Cu- and Fe-mediated organometallic reactions: In Cu catalysis, the formation of  $R_n\text{-Cu}^{\text{II}}/\text{TPMA}$  ( $k_{\text{add}}$ ) occurs at lower  $T$ , but without subsequent CRT. At higher  $T$ , both the reverse reaction,  $k_{\text{dis}}$ , and CRT are additionally in operation, which leads to more complex, non-first-order kinetics (cf. Appendix B)<sup>179</sup> and results in an effective lowering of the apparent Cu-CRT to  $k_t^{\text{Cu}}(25\text{ °C}) = (7.0 \pm 1.2) \times 10^3$  Lmol<sup>-1</sup>s<sup>-1</sup> for the [Cu<sup>I</sup>(TPMA)]<sup>+</sup> catalyst.<sup>179,255</sup>

Particularly in case of the fast Fe-CRT reaction in acrylate polymerization, ATRPs should be carried out at very low levels of catalyst concentration. High levels of Fe<sup>II</sup> will result in a rapid accumulation of the deactivator, [Fe<sup>III</sup>Br<sub>4</sub>]<sup>-</sup>, and in the simultaneous production of dead chains, which prevents ATRP reaching a high degree of monomer conversion and thus high molar masses. The percentage of dead chains,  $T_{\text{mol}\%}$ , produced by CRT may be estimated via Equation 5.12, which applies irrespective of the selected ATRP method, e.g., for normal, reverse or ICAR (initiators for continuous activator regeneration) ATRP. With typical catalyst loadings of a normal ATRP, such as the one described in Figure 5.17A,  $T_{\text{mol}\%}$  approaches 100 % already at the rather low degree of monomer conversion,  $X$ , of 26 % (as determined via  $k_p(75\text{ °C}) = 44\,100$  Lmol<sup>-1</sup>s<sup>-1</sup> [229]). This calculation may indicate why ATRPs of BA reaching higher conversions have rarely

**Table 5.4:**  $k_{\text{add}}(\text{BA})$  at  $-40\text{ }^{\circ}\text{C}$  for different Cu- and Fe-based complexes.<sup>[a]</sup>

entry	catalyst	$k_{\text{add}}$ at $-40\text{ }^{\circ}\text{C}$ / $\text{Lmol}^{-1}\text{s}^{-1}$	ref.
1	$[\text{Cu}^{\text{I}}(\text{TPMA})]^+$	$(3.0 \pm 0.8) \times 10$	179
2	$[\text{Cu}^{\text{I}}(\text{PMDETA})]^+$ <sup>[b]</sup>	$(9 \pm 3) \times 10^3$	179
3	$[\text{Fe}^{\text{II}}\text{Br}_3(\text{Solv})]^-$	$(1.5 \pm 0.2) \times 10^4$ <sup>[c]</sup>	this work

<sup>[a]</sup> Cosolvent: MeCN (Cu) and 2-butanone (Fe); <sup>[b]</sup> PMDETA = *N,N,N',N'',N'''*-pentamethyl-diethylenetriamine;  $k_{\text{add}} = 1/2 k_t^{\text{Fe}}$  (see Equation 5.9).

been reported with iron bromide catalysts.<sup>53</sup> An acceptable degree of chain-end functionality and thus of low  $T_{\text{mol}\%}$  is obtained when the  $\text{Fe}^{\text{II}}$  content is lowered to 0.5 mM, as may be targeted in ICAR ATRPs. In that case,  $T_{\text{mol}\%}$  may be reduced to less than 7 % at  $X = 80\%$ , if 25 mM of the initiator,  $[\text{RX}]_0$ , are used.

$$T_{\text{mol}\%} = \frac{k_t^{\text{Fe}} \cdot [\text{Fe}^{\text{II}}] \cdot [\text{R}^*] \cdot t}{[\text{RX}]_0} = \frac{k_t^{\text{Fe}} \cdot [\text{Fe}^{\text{II}}] \cdot \ln\left(\frac{1}{1-X}\right)}{k_p \cdot [\text{RX}]_0} \quad (5.12)$$

Improved Fe-mediated ATRP of acrylates would in general benefit from low  $k_t^{\text{Fe}}$  or more active catalysts (with higher  $K_{\text{ATRP}}$ ) to maintain narrow molar-mass distributions at a reduced  $\text{Fe}^{\text{II}}$  content. No or only a minor impact of CRT has been found for both Fe- and Cu-mediated<sup>255</sup> ATRPs of methacrylates so far. It remains to be studied whether CRT also operates in further Fe-based ATRP catalysts, e.g., the amine-bis(phenolate)  $\text{Fe}^{\text{III}}$  or hemin-based catalysts.<sup>86,87,266</sup> The SP-PLP-EPR analysis should be extended toward CRPs, where stable organometallic species (e.g.  $\text{R}_n\text{-Fe}^{\text{III}}$ ) are expected to occur, as with vinyl acetate polymerization.<sup>22</sup>



# 6

## Kinetics of RDRP up to High Pressure

### 6.1 Preface

Applying high pressure has marked effects on the rate coefficients of RDRP. The propagation rate coefficient is strongly enhanced ( $\Delta^\ddagger V(k_p) < 0$ , see Table 6.1) and the termination rate coefficient decreases ( $\Delta^\ddagger V(k_t) > 0$ ) upon pressurization.<sup>262</sup> The lowering of termination rate is due to diffusion control and is thus associated with an increase in viscosity. The pressure dependence of transfer reactions has been studied less frequently.<sup>267</sup> Of particular interest is the backbiting reaction, by which SPRs in acrylate polymerization are transformed into MCRs. Preliminary data from PLP-SEC experiments with BA indicates a large negative volume of activation,  $\Delta^\ddagger V(k_{bb}) \approx -20 \text{ cm}^3 \text{ mol}^{-1}$ .<sup>268</sup> This information was obtained by significant variation of laser-pulse repetition rate, i.e., by the so-called frequency-tuning method.<sup>153</sup> The experimentally monitored repetition rate, at which a lowering of the apparent propagation rate coefficient toward lower repetition rates is observed, is 79 Hz at 1 bar<sup>153</sup> and 175 Hz at 1000 bar.<sup>268</sup> At 2000 bar, repetition rates even above 400 Hz are needed to arrive at a constant apparent propagation rate. The consequences of the pressure-induced enhancement of backbiting for ATRP will be explored in chapter 6.2.

The lowering of termination rate enhances the living character of ATRP and leads to the formation of polymer with a higher degree of

**Table 6.1:** Reaction volumes,  $\Delta_r V$ , of  $K_{\text{ATRP}}$  and volumes of activation,  $\Delta^\ddagger V$ , of  $k_p$  for Cu-mediated ATRP of styrene and MMA and of associated monomer-free model system with TPMA being the ligand.

Entry	Solvent	Monomer	Initiator <sup>[a]</sup>	$\Delta_r V(K_{\text{ATRP}}) /$ $\text{cm}^3\text{mol}^{-1}$	$\Delta^\ddagger V(k_p) /$ $\text{cm}^3\text{mol}^{-1}$	Ref.
1	MeCN	Styrene	PEBr	-23	-12.1	36,97
2	MeCN	MMA	EBriB	-17	-16.7	98,103
3	MeCN	- [b]	EBriB	-17	-	104
4	MeCN	- [b]	PEBr	-17	-	102
5	MeCN	- [b]	MBrP	-16	-	102

<sup>[a]</sup> PEBr = 1-phenylethyl bromide, EBriB = ethyl 2-bromo-*iso*-butyrate, MBrP = methyl 2-bromopropionate; <sup>[b]</sup> monomer-free model system.

preserved chain-end functionality. ATRP of BA under high pressure was feasible with very low levels of the Cu catalyst in the absence of any additives. 100 ppm Cu is sufficient to yield poly(BA) with  $M_n = 112,000 \text{ gmol}^{-1}$ ,  $\mathcal{D} = 1.12$ , and more than 95 % preserved chain-end functionality at 5 kbar.<sup>269</sup> Furthermore,  $M_n = 625,000 \text{ gmol}^{-1}$  with  $\mathcal{D} = 1.25$  was obtained.<sup>269</sup> Applying pressure is also helpful for the synthesis of highly branched, dense molecular brushes formed via homopolymerization of macromonomers: The advantages are due to the increased ATRP rate despite the low catalyst content and to the beneficial lowering of the equilibrium monomer concentration at high pressure.<sup>270</sup>

In chapters 6.3–6.4, the kinetics of Fe-based ATRP will be studied up to 2500 and 6000 bar, respectively. Primary interest was directed toward the effect of pressure on the ATRP equilibrium and on the dispersity of the polymeric product. Higher pressure shifts chemical equilibria to the component side with smaller molar volume, thus favoring higher coordination and higher charged ions. In the Cu-based ATRP systems studied so far, the ATRP equilibrium was shifted toward the side of  $\text{Cu}^{\text{II}}$  and propagating radicals, which results in an enormous enhancement of ATRP rate due to the increase in both  $K_{\text{ATRP}}$  and  $k_p$ .<sup>102-104</sup> The results for  $\Delta_r V(K_{\text{ATRP}})$  with TPMA being the ligand to Cu are shown in Table 6.1.  $\Delta_r V(K_{\text{ATRP}})$  is almost insensitive toward the type of radical or initiator species, but essentially depends on the type of ligand to copper.<sup>102-104</sup>

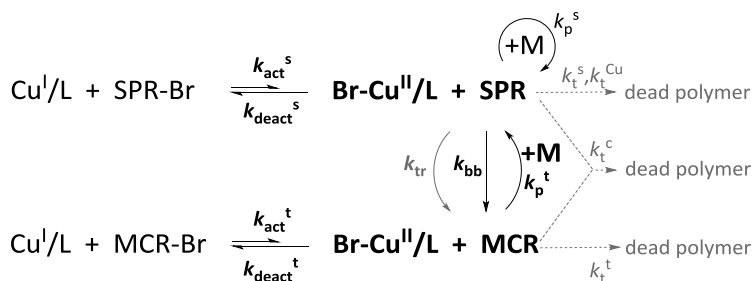
## 6.2 Modeling Cu-Mediated ATRP of Butyl Acrylate<sup>6</sup>

This chapter deals with the consequences of the backbiting reaction for rate and control of ATRP of BA toward higher pressure by means of PREDICI<sup>®271</sup> simulations. Modeling also provides estimates of the branching fraction of polymer obtained at higher pressure.

$K_{\text{ATRP}}$  in Cu-mediated ATRP significantly increases toward higher pressure.<sup>102-104</sup> As the size of  $\Delta_r V(K_{\text{ATRP}})$  is almost insensitive toward the type of radical or initiator species, one would expect  $\Delta_r V(K_{\text{ATRP}})$  of acrylates to be close to the numbers for styrene and MMA (cf. Table 6.1, chapter 6.1) in case of the same catalyst being used: Cu/TPMA. In the BA studies reported so far, the pressure-induced rate enhancement was, however, considerably lower than expected<sup>269</sup> and in some cases the rate enhancement was only associated with the increase in  $k_p$ .<sup>169</sup> It appeared rewarding to check whether this observation may be associated with the pressure-induced enhancement of backbiting rate in BA polymerization that was deduced from PLP experiments (see chapter 6.1).<sup>268</sup> The ratio of the associated radical species, SPRs and MCRs, was directly monitored via EPR spectroscopy at ambient pressure.<sup>154</sup> Such EPR measurements have, however, not been applicable toward higher pressure. Via NIR spectroscopy, which allows for monitoring monomer conversion in a wide pressure and temperature range, it is not possible to monitor or distinguish between SPRs and MCRs. The corresponding concentrations that affect experimental monomer and catalyst concentration-vs-time traces in high-pressure ATRP of BA may, however, be estimated via modeling of monomer and catalyst conversion.

Polymerization rate in BA ATRP essentially depends on the concentration of SPRs (and thus on  $K_{\text{ATRP}}^s$ ) and on the associated propagation rate coefficient  $k_p^s$  (Equation 6.1), since the propagation rate coefficient of MCRs is by about three orders of magnitude lower, i.e.  $k_p^t \ll k_p^s$ .<sup>153,154</sup> Analysis of  $K_{\text{ATRP}}^s$  from polymerization kinetics is complicated by the presence of the two types of radicals since, according to Equation 6.2, the concentration of SPR-X species, [SPR-X], needs to be

<sup>6</sup> Reproduced with permission from Schroeder, H.; Buback, J.; Schrooten, J.; Buback, M.; Matyjaszewski, K. *Macromol. Theory Simul.* **2014**, *23*, 279–287, Copyright 2015 Wiley-VCH. The software, which is further described in Appendix C, was developed by J. Buback.



**Scheme 6.1:** Cu-mediated ATRP of acrylates taking both secondary propagating radicals (SPRs) and mid-chain radicals (MCRs) into account.

known. As shown in Equation 6.3, [SPR-X] may be calculated according to the principle of halogen conservation.<sup>272</sup> If backbiting and thus MCR-X generation play no major role, [SPR-X] may be deduced from the evolution of Cu<sup>II</sup> concentration. Illustrated in Scheme 6.1 is the interplay of the activation–deactivation equilibria for both SPRs and MCRs and the interconversion of these two types of radicals by backbiting and propagation of mid-chain radicals.

$$R_p = -\frac{d[M]}{dt} = k_p^s \cdot [\text{SPR}] \cdot [M] + k_p^t \cdot [\text{MCR}] \cdot [M] \approx k_p^s \cdot [\text{SPR}] \cdot [M] \quad (6.1)$$

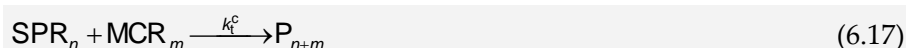
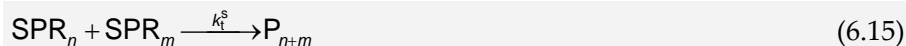
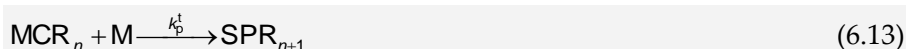
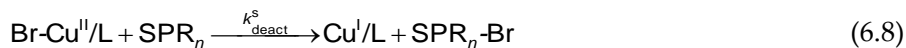
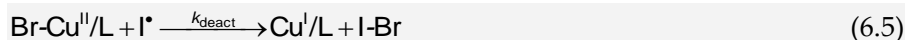
$$R_p = k_p^s \cdot K_{\text{ATRP}}^s \cdot \frac{[\text{Cu}^{\text{I}}] \cdot [\text{SPR-X}]}{[\text{Cu}^{\text{II}}]} \cdot [M] \quad (6.2)$$

$$[\text{SPR-X}] = [\text{I-X}]_0 + [\text{Cu}^{\text{II}}]_0 - [\text{Cu}^{\text{II}}] - [\text{MCR-X}] \quad (6.3)$$

The PREDICI<sup>®</sup> simulations were performed based on the reaction steps shown in Scheme 6.1 and Table 6.2. The scheme includes Cu<sup>I</sup>-CRT of SPRs.<sup>255</sup> As CRT of MCRs should be sterically hindered, this reaction was not taken into account. Moreover, intermolecular chain-transfer reactions may be neglected at low and moderate degrees of monomer conversion.<sup>146-148,273</sup>

The rate coefficients for ambient-pressure reactions are accessible from the literature (Table 6.3) with the exception of  $k_{\text{act}}^t$  and  $k_{\text{deact}}^t$ .  $K_{\text{ATRP}}^s$  for BA polymerization was reported for various solvent



**Table 6.2:** Reaction Scheme for PREDICT® simulations of BA ATRP.

environments.<sup>227</sup>  $k_{\text{deact}}$  was deduced from experiments on monomer-free model systems,<sup>35</sup> allowing for calculation of  $k_{\text{act}}^{\text{S}}$  via  $K_{\text{ATRP}}^{\text{S}}$ . It may be assumed that  $k_{\text{act}} = k_{\text{act}}^{\text{S}}$  (Equations 6.4 and 6.7) and  $k_{\text{deact}} = k_{\text{deact}}^{\text{S}}$  (Equations 6.5 and 6.8). The rate coefficients  $k_{\text{p}}^{\text{S}}$ <sup>229</sup> and  $k_{\text{p}}^{\text{t}}$ , for propagation of SPRs and MCRs, respectively,  $k_{\text{bb}}$  for backbiting,  $k_{\text{t}}^{\text{S}}$  and  $k_{\text{t}}^{\text{t}}$ , for radical-radical termination of two SPRs and MCRs, respectively, as well as  $k_{\text{t}}^{\text{C}}$  for cross termination have been studied via pulsed-laser experiments.<sup>153,154</sup> The known rate coefficients for ambient pressure indicate that under reaction conditions such as the ones of the present

**Table 6.3:** Rate coefficients and associated volumes of activation,  $\Delta^\ddagger V$ , used for modeling ATRP of BA in solution of MeCN at 22 °C and various pressures with TPMA as the ligand to Cu.

Entry	Rate Coefficient	$k$ at 22 °C/ Lmol <sup>-1</sup> s <sup>-1</sup>	Comments / Ref.	$\Delta^\ddagger V$ / cm <sup>3</sup> mol <sup>-1</sup>	Comments / Ref.
1	$k_{\text{act}}^{\text{s}}$ [a]	0.26	via $K_{\text{ATRP}}$ 227	$-16 \pm 3$	prediction 102,104
2	$k_{\text{deact}}^{\text{s}}$ [a]	$1.0 \times 10^7$	35,104	$0 \pm 3$	see ref. 104
3	$k_{\text{act}}^{\text{t}}$	1.0	via $K_{\text{ATRP}}$ 35,104	-	see Table 6.4
4	$k_{\text{deact}}^{\text{t}}$	$1.0 \times 10^6$	estimate [4,5,31]	-	see Table 6.4
5	$k_{\text{p}}^{\text{s}}$ [a]	15000	229	-11.5	229
6	$k_{\text{p}}^{\text{t}}$	10	153,154	-	see Table 6.4
7	$k_{\text{bb}}$	120 [b]	153,154	-	see Table 6.4
8	$k_{\text{t}}^{\text{Cu}}$	4500	this work	$-17 \pm 4$ [d]	this work
9	$k_{\text{t}}^{\text{s}}(1,1)$ [c]	$6.3 \times 10^8$	154		prediction via 274
10	$k_{\text{t}}^{\text{t}}(1,1)$ [c]	$3.9 \times 10^8$	154		prediction via 274
11	$k_{\text{t}}^{\text{c}}(1,1)$ [c]	$\approx 10^7$	154		prediction via 274

Further assumptions: [a]  $k_{\text{act}} = k_{\text{act}}^{\text{s}}$ ,  $k_{\text{deact}} = k_{\text{deact}}^{\text{s}}$ ,  $k_{\text{p}}^{\text{s}} = k_{\text{p}}^{\text{t}}$ ; [b] in s<sup>-1</sup>; [c] corrected for actual solvent viscosity;<sup>56,275</sup> [d] this preliminary data rests on a rather limited set of measurements at three pressures.

study, only about 0.1 % of the growing macroradicals are lost due to conventional radical termination (Equations 6.15–6.17). In contrast, about 2 % of the growing chains are lost due to Cu<sup>I</sup>-induced CRT (Equation 6.18) at moderate degrees of monomer conversion. The increase in the Cu<sup>II</sup> persistent radical concentration is thus almost entirely caused by CRT. The associated rate coefficient  $k_{\text{t}}^{\text{Cu}}$  was obtained from the analysis of high-pressure ATRP of BA using the reported protocol, which is based on monitoring the evolution of Cu<sup>II</sup> with time.<sup>255</sup>  $K_{\text{ATRP}}^{\text{t}}$  is estimated by comparison of the reported values for  $k_{\text{act}}$ ,  $k_{\text{deact}}$ , and overall  $K_{\text{ATRP}}$  of tertiary methacrylate-type radicals and secondary acrylate-type radicals.<sup>35,104,176</sup>

Modeling was carried out for the experimental data of BA ATRP at 22 °C from Ref. 269. The initial molar ratio of reactants was

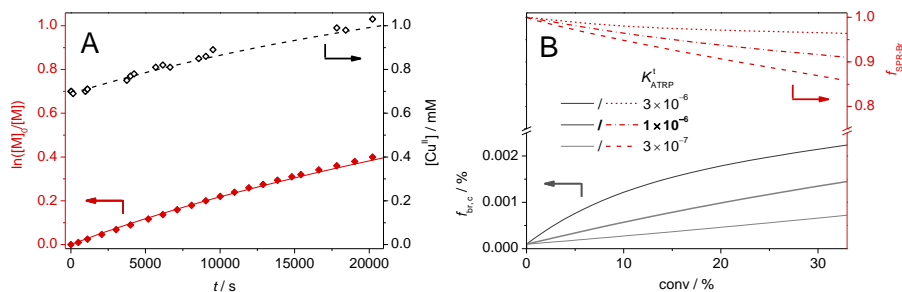


**Figure 6.1:** (A) Experimental (symbols) and simulated data (lines) of  $\ln([M]_0/[M])$  and  $[Cu^{II}]$  vs time for ATRP at initial molar ratios of BA :  $Cu^I$  :  $Cu^{II}$  : MBrP = 200 : 0.16 : 0.04 : 1.00 at 22 °C and 1 bar. (B) Model-based cumulative branching fraction,  $f_{br,c}$ , (full lines) and fraction of SPR-Br species,  $f_{SPR-Br}$ , (dashed lines) for ATRP at the above-mentioned conditions except for the variation of  $K_{ATRP}^t$  between  $3 \times 10^{-6}$  and  $3 \times 10^{-7}$ .

BA : MBrP : CuBr : CuBr<sub>2</sub> : TPMA = 200 : 1.00 : 0.16 : 0.04 : 0.24 in solution of 50 vol% MeCN (MBrP = methyl 2-bromopropionate). The modeled  $\ln([M]_0/[M])$  and  $Cu^{II}$  vs time traces closely fit the experimental data for the experiments carried out at ambient pressure (Figure 6.1A). At around 20 % monomer conversion, between 90 and 97 % of the growing macroradicals are reversibly deactivated as SPR-Br species (dashed lines Figure 6.1B). The fact that SPR-Br species dominate over MCR-Br species at ambient pressure facilitates the prediction of ATRP rate according to Equation 6.2. Even though the cumulated branching fraction (full lines in Figure 6.1B),  $f_{br,c}$ , is affected upon variation of  $K_{ATRP}^t$  within reasonable limits, i.e., between  $3 \times 10^{-6}$  and  $3 \times 10^{-7}$ ,  $f_{br,c}$  remains in all cases very low and amounts only to 0.05–0.2 % at 20 % monomer conversion. The prediction of low  $f_{br,c}$  is in agreement with reported measured values.<sup>276</sup>

**Modeling High-Pressure ATRP of BA.**  $k_p^s$  at high pressure may be estimated via the reported volume of activation given in Table 6.3.<sup>229</sup> The associated diffusion-controlled values for  $k_t^s$ ,  $k_t^t$ , and  $k_t^c$  were adjusted for high pressure via the estimated change in solvent viscosity. <sup>56,274,275</sup>  $k_t^{Cu}$  was determined to be 18 000 Lmol<sup>-1</sup>s<sup>-1</sup> as described above. Due to  $\Delta_r V(K_{ATRP})$  being rather insensitive toward the type of radical species,  $\Delta_r V(K_{ATRP})$  for both SPRs and MCRs may equally be estimated to

**Table 6.4:**<sup>[a]</sup> Parameter variation used for modeling ATRP of BA at 22 °C and 2000 bar with TPMA as the ligand to Cu.

Entry	$k_{bb} /$ $s^{-1}$	$k_p^t$ →	$k_t^{Cu}$ in $Lmol^{-1}s^{-1}$	$k_{act}^t$	$k_{deact}^t$ ←	$[Cu^I]_0:[Cu^{II}]_0:[IBr]_0$ / mM						
1	0	0	5000	0.03	$1 \times 10^7$	3.44 : 0.00 : 3.44						
2	300	15	10000	0.3	$1 \times 10^6$	2.75 : 0.69 : 17.2						
3	600	<b>20</b>	15000	1	$3 \times 10^5$	2.75 : 2.75 : 68.4						
4	900	35	<b>18000</b>	<b>3</b>	$1 \times 10^5$							
5	<b>1400</b>	50	20000	10	$1 \times 10^4$							
6	2100	75										
7	3000											
no. of scans:	7	×	6	×	5	×	5	×	5	×	3	= 15750

<sup>[a]</sup> Values in bold were used for the simulations shown in Figure 6.2 to 6.4 unless indicated otherwise.

be  $-16 \pm 3 \text{ cm}^3\text{mol}^{-1}$  based on the reported values for the same Cu/TPMA catalyst.<sup>102-104</sup>  $\Delta^\ddagger V$  ( $k_{deact}$ ) was reported to be close to zero.<sup>104</sup>

Pressure-dependent  $k_{bb}$  and  $k_p^t$  have not been reported so far. Modeling of BA polymerization under high pressure thus requires inspection of the consequences of modifying  $k_{bb}$  and  $k_p^t$ . In addition, variation of the activation–deactivation rate coefficients for MCRs,  $k_{act}^t$  and  $k_{deact}^t$ , should be considered, since the estimates for the ambient-pressure values as well as for the so-derived high-pressure values were based on the reported values for chain-end methacrylate-type radicals. Refinement of  $k_t^{Cu}$  had to be performed by simulation due to the scarcity of available data.

The entire data set subjected to parameter variation is given in Table 6.4. The variation of five rate coefficients at five to seven levels each in addition to three different initial concentrations results in  $7 \times 6 \times 5 \times 5 \times 5 \times 3 = 15750$  combinations and thus simulations to be performed. The enormous workload associated with manually processing all of these scans makes an automated parameter variation,

such as incorporated in the PREDICI<sup>®</sup> program, indispensable. In view of the extremely large number of required simulations and resulting data sets, an additional software based on Python programming was used (see Appendix C).

The following results refer to modeling based on the reported rate coefficients shown in Table 6.3 and, if not stated otherwise, the bold parameters given in Table 6.4, i.e.,  $k_{bb} = 1400 \text{ s}^{-1}$ ,  $k_p^t = 20 \text{ Lmol}^{-1}\text{s}^{-1}$ ,  $k_{act}^t = 3 \text{ Lmol}^{-1}\text{s}^{-1}$ ,  $k_{deact}^t = 1 \times 10^6 \text{ Lmol}^{-1}\text{s}^{-1}$ , and  $k_t^{Cu} = 18\,000 \text{ Lmol}^{-1}\text{s}^{-1}$ , which are based on fitting experimental data (see below). The essential difference between conventional radical polymerization and RDRP of BA consists of the interplay of activation and deactivation with the interconversion of SPRs and MCRs.<sup>277</sup> In case of fast backbiting, SPRs in ATRP are effectively converted and subsequently deactivated to MCR-Br species. The concentrations of both activated and deactivated SPR-Br species may thus be diminished significantly, which results in a lowering of polymerization rate according to Equation 6.1. This effect is illustrated in Figure 6.2A by modeling of ATRP under variation of  $k_{bb}$  between  $0 \text{ s}^{-1}$ , i.e., in the absence of backbiting, and  $k_{bb} = 3000 \text{ s}^{-1}$  at otherwise identical conditions.  $k_p^t$  was kept constant at  $20 \text{ Lmol}^{-1}\text{s}^{-1}$ . Polymerization rate, as deduced from the  $\ln([M]_0/[M])$  vs time traces, is reduced by a factor of two within this  $k_{bb}$  range. The range of  $k_{bb}$  values (except  $k_{bb} = 0 \text{ s}^{-1}$ ) is associated with a volume of activation of  $\Delta^\ddagger V(k_{bb}) = -11, -20, -25, -30, -35, \text{ and } -40 \text{ cm}^3\text{mol}^{-1}$ , respectively. In view of the general trend seen for the propagation rate coefficients, the size of  $k_p^t$  at 2000 bar should at least exceed the ambient-pressure value of  $k_p^t = 10 \text{ Lmol}^{-1}\text{s}^{-1}$ . Polymerization rate in Figure 6.2B is only moderately enhanced in passing from  $k_p^t = 15$  to  $75 \text{ Lmol}^{-1}\text{s}^{-1}$ , in particular at low degrees of monomer conversion. Within the limits of this parameter variation, increased  $k_p^t$  at high pressure cannot compensate a decrease in polymerization rate that would be induced by enhanced  $k_{bb}$ . The high backbiting rate may thus serve as an explanation for the diminished pressure-induced rate enhancement in BA polymerizations irrespective of the size of  $k_p^t$ .

The fraction of SPR-Br species,  $f_{SPR-Br}$ , also depends on the position of the ATRP equilibrium,  $K_{ATRP}^t$ , involving MCR-Br species. Shown in Figure 6.3A is the predicted change of  $f_{SPR-Br}$  at 30 % monomer conversion upon variation of  $K_{ATRP}^t$  and  $k_{deact}^t$  within about three orders of magnitude around the expected values of  $K_{ATRP}^t = 3 \times 10^{-6}$  and

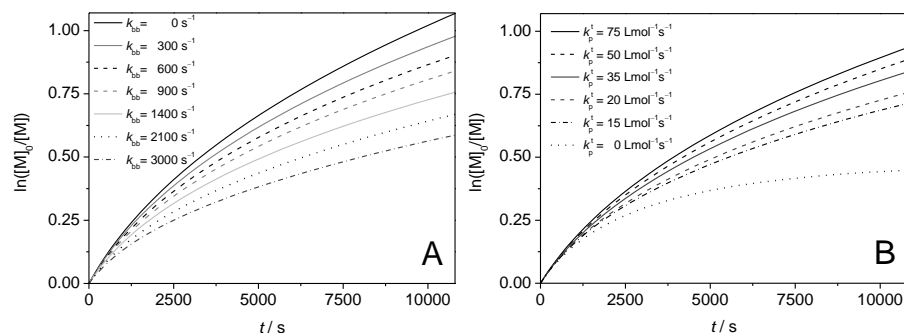


**Figure 6.2:** Simulated  $\ln([M]_0/[M])$  vs time traces for ATRP with BA : Cu<sup>I</sup> : Cu<sup>II</sup> : MBrP = 200 : 0.16 : 0.04 : 1.00 at 22 °C and 2000 bar in solution of 50 vol% MeCN. The bold values given in Table 6.4 were used in the simulations with different levels of  $k_{bb}$  as shown in (A) and of  $k_{bb}$  as shown in (B).

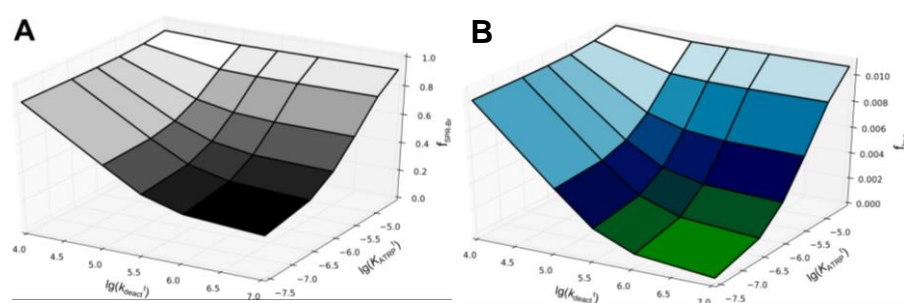


**Figure 6.3:** Predicted fraction of SPR-Br species,  $f_{\text{SPR-Br}}$ , (A) and of cumulative branching fraction,  $f_{\text{br,c}}$ , (B) at 30% monomer conversion in ATRP of BA with BA : Cu<sup>I</sup> : Cu<sup>II</sup> : MBrP = 200 : 0.16 : 0.04 : 1.00 at 22 °C and 2000 bar upon variation of  $K_{\text{ATRP}}^t$  and  $k_{\text{deact}}^t$ .

$k_{\text{deact}}^t = 1 \times 10^6 \text{ Lmol}^{-1}\text{s}^{-1}$ . The conversion of MCRs into SPRs may be hindered because of either high  $k_{\text{deact}}^t$  or low  $K_{\text{ATRP}}^t$  which lead to a permanent decrease in  $f_{\text{SPR-Br}}$ . Since propagation of MCRs is very slow as compared with propagation of SPRs, reactions with a large fraction of MCR-Br species may yield significant broadening of the molar-mass distribution. Narrow molar-mass distributions have, however, been

reported for actual BA ATRP even under high pressure.<sup>169,269</sup> They are also obtained by modeling with the predicted values of  $K_{\text{ATRP}}^t = 3 \times 10^{-6}$  and  $k_{\text{deact}}^t = 1 \times 10^6 \text{ Lmol}^{-1}\text{s}^{-1}$ , which thus appear to be appropriate estimates. Even higher  $K_{\text{ATRP}}^t$  or lower  $k_{\text{deact}}^t$  would result in a further increase in  $f_{\text{SPR-Br}}$ . At the same time, the cumulative branching fraction,  $f_{\text{br,c}}$ , will significantly increase for  $K_{\text{ATRP}}^t > 10^{-6}$  and  $k_{\text{deact}}^t < 10^6 \text{ Lmol}^{-1}\text{s}^{-1}$ , as is seen in Figure 6.3B for the same variation of parameters.

Shown in Figure 6.4A are the  $\ln([M]_0/[M])$  and  $[\text{Cu}^{\text{II}}]$  vs time traces (lines) for modeling BA ATRP at 22 °C and 2000 bar of the experimental data of Ref. <sup>269</sup> (symbols). The optimized rate coefficients, i.e., the bold numbers in Table 6.4, provide close agreement with the experimental data within the investigated range at moderate degrees of monomer conversion. As is shown in Figure 6.4B, polymerization rate decreases only slightly for low rates of backbiting and propagation of MCRs, i.e., for  $k_{\text{bb}} = 300 \text{ s}^{-1}$  and  $k_{\text{p}}^t = 10 \text{ Lmol}^{-1}\text{s}^{-1}$ , respectively, as compared to the hypothetical case of backbiting being absent, i.e.,  $k_{\text{bb}} = 0 \text{ s}^{-1}$ . In case of slow backbiting, the size of  $K_{\text{ATRP}}^t$  and  $k_{\text{deact}}^t$  does not significantly affect polymerization rate (not shown in Figure 6.4). To reproduce the experimental data, it is thus necessary to assume fast backbiting, e.g.,  $k_{\text{bb}} = 1400 \text{ s}^{-1}$  ( $\Delta^\ddagger V(k_{\text{bb}}) = -30 \text{ cm}^3\text{mol}^{-1}$ ). The initial curvature of the  $\ln([M]_0/[M])$  vs time traces is already indicative of rapid conversion of active SPR-Br to less active MCR-Br species. This curvature also rules out that the experimental data may be modeled via a slow backbiting rate in conjunction with a  $K_{\text{ATRP}}^s$  value that is considerably below the predicted number for 2000 bar. A large negative volume of activation for backbiting,  $\Delta^\ddagger V(k_{\text{bb}}) \approx -20 \text{ cm}^3\text{mol}^{-1}$ , has also been found from PLP-SEC experiments, which were carried out in bulk.

The interpretation of the high-pressure data for ATRP of BA suggests that the initial concentration of initiator,  $[\text{IBr}]_0$ , should be chosen such as to prevent a large fraction of SPR-Br species from being rapidly converted into MCR-Br species. It appeared rewarding to check by variation of  $[\text{IBr}]_0$  to 3.44, 17.2, and 69.0 mM whether the pressure-induced rate enhancement in passing from 1 bar to 2000 bar would meet the expectations. Along with  $[\text{IBr}]_0$ ,  $[\text{Cu}^{\text{II}}]_0$  was also increased to keep polymerization rate, SPR concentration, and thus backbiting rate, almost constant. As seen from Table 6.5, the expected rate enhancement in the absence of backbiting, i.e.  $k_{\text{bb}} = 0 \text{ s}^{-1}$ , is about a factor of 7 to 8 between 1

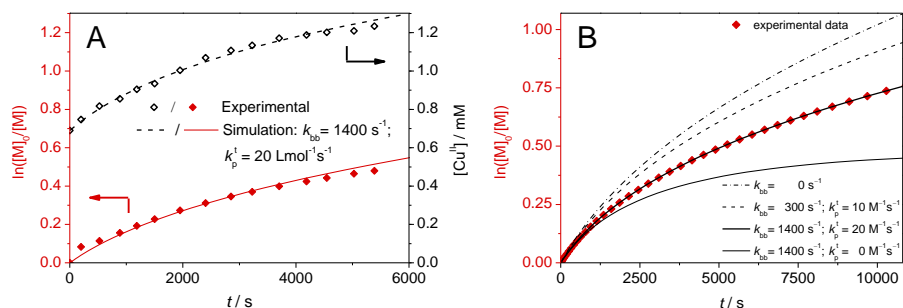


**Figure 6.4:** Experimental (symbols) and modeled data (lines) of  $\ln([M]_0/[M])$  and  $[Cu^I]$  vs time for ATRP with BA:  $Cu^I$ :  $Cu^{II}$ :  $MBrP = 200 : 0.16 : 0.04 : 1.00$  at 22 °C and 2000 bar in solution of 50 vol% MeCN. The optimized values shown in Table 6.4 were used for the simulations shown in (A). The  $\ln([M]_0/[M])$  vs time traces in (B) refer to simulation results obtained with the same parameters and reaction conditions, but at different levels of  $k_{bb}$  and  $k_p^t$ .

**Table 6.5:** Propagation rate,  $R_p$ , at 2000 bar relative to  $R_p^{1\text{ bar}}$  at 20 % monomer conversion for the simulated ATRPs of BA with different initial concentrations of initiator and Cu catalyst.

$[IBr]_0:[Cu^I]_0:[Cu^{II}]_0$ / mM	$\frac{R_p^{2000\text{ bar}}}{R_p^{1\text{ bar}}}$	$\frac{R_p^{2000\text{ bar}}}{R_p^{1\text{ bar}}}$
	$k_{bb} = 0\text{ s}^{-1}$	$k_{bb} = 1400\text{ s}^{-1}$
68.4 : 2.75 : 2.75	8.3	7.5
17.2 : 2.75 : 0.69	7.9	5.5
3.44 : 3.30 : 0.14	7.0	3.5

and 2000 bar, which is mainly due to the increase in both  $k_p$  and  $K_{ATRP}$  (for the simulated  $\ln([M]_0/[M])$  and [SPR] vs time traces see Figure S15).

For the highest initiator concentration,  $[IBr]_0 = 69.0\text{ mM}$ , the rate enhancement, i.e.  $R_p^{2000\text{ bar}}/R_p^{1\text{ bar}}$ , amounts to a factor of 7.5 even in case of fast backbiting,  $k_{bb} = 1400\text{ s}^{-1}$ . For the lowest  $[IBr]_0$ , however,  $R_p^{2000\text{ bar}}/R_p^{1\text{ bar}}$  is only 3.5 which is almost as low as the typical increase given by the pressure-induced enhancement of  $k_p(\text{BA})$ ,



$k_p^{2000 \text{ bar}}/k_p^{1 \text{ bar}} = 2.6$ , only. These results are in agreement with the experimental observations for the same catalyst and initiator concentrations.<sup>169</sup> The effect is due to most SPR-Br species being rapidly converted to MCR-Br species in case of low  $[\text{IBr}]_0$ . Higher  $[\text{IBr}]_0$  may also be helpful to reduce  $f_{\text{br,c}}$ . For example, the predicted  $f_{\text{br,c}}$  amounts to 1.0 and 0.4% at 20% monomer conversion with  $[\text{IBr}]_0 = 3.44$  and 17.2 mM, respectively, but remains as low as 0.1% in case of  $[\text{IBr}]_0 = 69.0$  mM. ATRP experiments for BA at 22 °C between 500 and 2000 bar with BA : Cu<sup>I</sup> : Cu<sup>II</sup> : MBrP = 60.0 : 0.05 : 0.04 : 1.00 in solution of 50 vol% MeCN confirmed that high initiator concentrations are necessary to observe a significant pressure-induced rate enhancement which corresponds to the expectations based on the reported  $\Delta_r V(K_{\text{ATRP}})$  and  $\Delta^\ddagger V(k_p)$  values.

The origin for the reduced branching level ( $f_{\text{br,c}}$ ) in ATRP (and in other RDRP procedures) of acrylates as compared to conventional radical polymerization is currently still under dispute in the literature.<sup>276-280</sup> These discussions are centered around the question whether the interplay of the activation–deactivation equilibria for SPRs and MCRs and the interconversion of these by backbiting and propagation of MCRs (cf. Scheme 6.1) are responsible for the observed lowering of  $f_{\text{br,c}}$ . This modeling study cannot prove beyond doubt the origin of the reduced  $f_{\text{br,c}}$ . The study was directed toward the kinetics of BA ATRP, which may in fact be precisely modeled in an extended pressure range based on the mechanistic scenario in Scheme 6.1. The results suggest that the extent to which dormant MCR-X species affect ATRP rate, in particular at high pressure, depends on the size of  $K_{\text{ATRP}}^\ddagger$ , and thus on the type of ATRP catalyst being used. Modeling may be helpful to identify ATRP conditions, which allow for the actual detection of MCR-Br species, perhaps even at ambient pressure. Tertiary dormant species have already been detected in nitroxide mediated polymerization.<sup>281</sup>

## 6.3 Iron-Halide-Mediated ATRP up to High Pressure

### 6.3.1 Monomer-Free Model Systems<sup>7</sup>

In this chapter,  $K_{\text{model}}$  for FeBr<sub>2</sub>/α-bromoester model systems is studied in an extended pressure and temperature range. A speciation analysis under high pressure was carried out to explore the reasons for the observed shift of  $K_{\text{model}}$  with pressure.

Quantitative analysis of  $K_{\text{model}}$  is carried out in solution of either NMP or MeCN via high-pressure online NIR spectroscopic monitoring the formation of the [Fe<sup>III</sup>Br<sub>4</sub>]<sup>-</sup> species as detailed in chapter 4.1.2. Along these lines, the slope of the so-obtained  $F([Y])$  function (Figure S16) yields  $K_{\text{model}}$  once the termination rate coefficient,  $k_t$ , is known. With  $k_t$  being assumed to occur under diffusion control, solvent viscosity,  $\eta$ ,<sup>203-205,275,282,283</sup> allows for estimating  $k_t$ .<sup>158</sup> Pressure-dependent viscosities are estimated via Equation 6.19, where  $\eta_0$  refers to viscosity at ambient pressure and  $\alpha$  to the incremental change of viscosity per unit pressure.<sup>274</sup> The value of  $\alpha = 6.24 \cdot 10^{-4} \text{ bar}^{-1}$  for MeCN is known from the literature<sup>274</sup> and  $\alpha = 5.0 \cdot 10^{-4} \text{ bar}^{-1}$  for NMP was adopted as the mean value of data reported for several polar organic solvents.<sup>274</sup>

$$\eta(\rho) = \eta_0 \cdot [1 + \alpha \cdot (\rho - \rho_0)] \quad (6.19)$$

This procedure has been used to measure  $K_{\text{model}}$  as a function of pressure for reaction of 10.0 mM FeBr<sub>2</sub> with several EBrPA concentrations (for the structure see Figure 6.5) in MeCN and in NMP at 60 °C. The resulting  $K_{\text{model}}$  data is shown in Figure 6.6. In the pressure range under investigation, i. e., up to 4000 bar,  $K_{\text{model}}$  decreases by a factor of five. The measurements have been restricted to 4 kbar, as the rate of Fe<sup>III</sup> accumulation becomes insignificant at very high pressure due the decrease in both  $k_t$  and  $K_{\text{model}}$ . The slope of the straight lines in

<sup>7</sup> Reproduced in part with permission from Schroeder, H.; Buback, J.; Demeshko, S.; Matyjaszewski, K.; Meyer, F.; Buback, M. *Macromolecules* **2015**, *48*, 1981–1990, Copyright 2015 American Chemical Society, and from Schroeder, H.; Yalalov, D.; Buback, M.; Matyjaszewski, K. *Macromol. Chem. Phys.* **2012**, *213*, 2019–2026, Copyright 2015 Wiley-VCH.

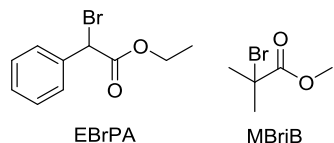


**Figure 6.5:** ATRP initiators under investigation: ethyl  $\alpha$ -bromophenylacetate (EBrPA) and methyl 2-bromo-*iso*-butyrate (MBriB).

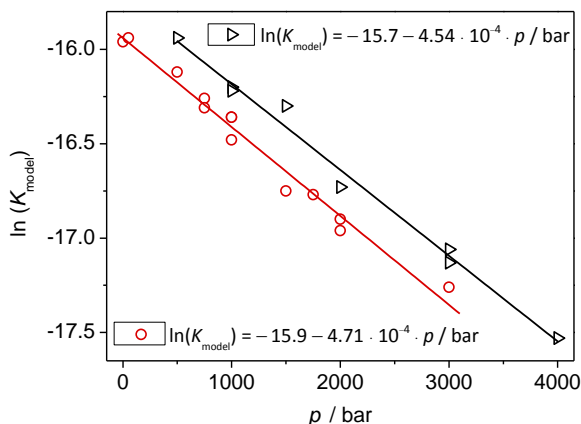


**Figure 6.6:** Pressure dependence of  $K_{\text{model}}$  for the system  $\text{FeBr}_2$  and EBrPA in solution of MeCN ( $\blacktriangleright$ ) and NMP ( $\circ$ ) at 60 °C.

**Table 6.6:** Equilibrium constants,  $K_{\text{model}}$ , at ambient pressure and 60 °C, reaction enthalpies,  $\Delta_r H$ , and reaction volumes,  $\Delta_r V$ , for  $\text{FeBr}_2$ -based model systems in solution of NMP and MeCN.

entry	metal salt	solvent/ligand	initiator	$K_{\text{model}}$ at 60 °C	$\Delta_r H / \text{kJmol}^{-1}$	$\Delta_r V / \text{cm}^3\text{mol}^{-1}$
1	$\text{FeBr}_2$	NMP	EBrPA	$1.2 \cdot 10^{-7}$	$37 \pm 4$	$13 \pm 3$
2	$\text{FeBr}_2$	MeCN	EBrPA	$1.5 \cdot 10^{-7}$	$36 \pm 4$	$13 \pm 3$
3	$\text{FeBr}_2$	NMP	MBriB	$1.8 \cdot 10^{-10}$	$43 \pm 4$	-

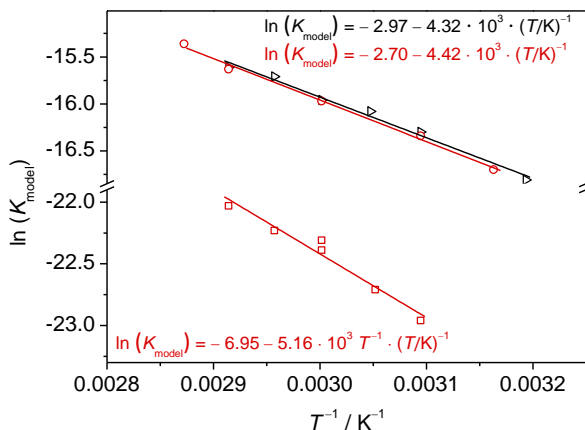
$$\left[ \frac{\partial \ln(K_{\text{model}})}{\partial p} \right]_T = - \frac{\Delta_r V}{R \cdot T} \quad (6.20)$$

Figure 6.6 yields the reaction volume,  $\Delta_r V$ , according to Equation 6.20. For reaction in both solvents,  $\Delta_r V = 13 \pm 3 \text{ cm}^3 \cdot \text{mol}^{-1}$  is obtained. Equilibrium constants, reaction enthalpies, and reaction volumes are tabulated in Table 6.6.  $\Delta_r V$  is assumed to be independent of temperature within the range of investigation (see below).

Equilibrium constants,  $K_{\text{model}}$ , were measured for the temperature range 40 to 75 °C at ambient pressure (Figure 6.7). The  $K_{\text{model}}$  data for reaction of FeBr<sub>2</sub> and EBrPA in MeCN and in NMP as well as for FeBr<sub>2</sub> and MBriB in NMP closely fit Arrhenius lines. Almost the same values are found for reaction of FeBr<sub>2</sub> and EBrPA in the two solvents. For reaction of FeBr<sub>2</sub> and MBriB,  $K_{\text{model}}$  is clearly different in both absolute value and temperature dependence. Reaction enthalpies,  $\Delta_r H$ , for the iron-mediated systems are larger than the ones reported for Cu-based model systems with Me<sub>6</sub>TREN (4 kJmol<sup>-1</sup>), TPMA (7 kJmol<sup>-1</sup>) or PMDETA (22 kJmol<sup>-1</sup>) being the ligand to Cu.<sup>104</sup> ATRP with iron catalysis thus should be strongly affected by temperature with catalyst activity being enhanced toward higher temperature.

The most striking effect with the iron-based ATRP systems is the decrease of  $K_{\text{model}}$  with pressure, whereas  $K_{\text{model}}$  increases upon pressurization with the copper-mediated systems investigated so far.<sup>102-104</sup> As a consequence, the reaction volumes for iron catalysis are positive and are negative for copper catalysis (cf. chapter 6.1).<sup>102-104</sup> According to Equation 6.20, higher pressure shifts chemical equilibria to the side with smaller molar volume. Therefore, high pressure mostly favors higher coordination and higher charged ions, such as Cu<sup>II</sup> over Cu<sup>I</sup>.

To reveal the origin of the unexpected decrease in  $K_{\text{model}}$  upon pressurization, the speciation analysis of the individual Fe<sup>II</sup> and Fe<sup>III</sup> species detailed in chapter 4.1.1 was expanded to higher pressure. The [Fe<sup>III</sup>Br<sub>4</sub>]<sup>-</sup> complex seems to be stable toward higher pressure, whereas marked changes in the distribution of [Fe<sup>II</sup>Br<sub>*u*</sub>(Solv)<sub>*v*</sub>] complexes may be observed via NIR spectroscopy. The spectra shown in Figure 6.8A were measured on a solution of FeBr<sub>2</sub> in NMP at 60 °C and pressures of 1, 1000, and 2000 bar. Figure 6.8A exhibits an isosbestic point at ca. 8100 cm<sup>-1</sup>, which consists of [Fe<sup>II</sup>(Br)<sub>*u*</sub>(NMP)<sub>*v*</sub>] absorption toward lower wavenumbers, and of [Fe(NMP)<sub>6</sub>]<sup>2+</sup> absorption at higher wavenumbers. For better illustration of the [Fe(NMP)<sub>6</sub>]<sup>2+</sup> contribution to absorbance, the absorption band of [Fe(NMP)<sub>6</sub>]<sup>2+</sup> obtained by dissolving Fe(OTf)<sub>2</sub> in NMP with a peak maximum at 9255 cm<sup>-1</sup> is also shown (gray line).



**Figure 6.7:** Temperature dependence of  $K_{\text{model}}$  for the systems FeBr<sub>2</sub> and EBrPA in MeCN ( $\blacktriangleright$ ) and in NMP ( $\circ$ ) as well as for FeBr<sub>2</sub> and MBriB in NMP ( $\square$ ) at ambient pressure and temperatures between 40 and 75 °C.

As expected for such species bearing an inversion center, the extinction coefficient is only around  $5 \text{ Lmol}^{-1}\text{cm}^{-1}$ ,<sup>166</sup> which in turn complicates the detection of this complex in the presence of, e.g., the tetrahedral  $[\text{Fe}^{\text{II}}(\text{Br})_u(\text{NMP})_v]_{u+v=4}$  species ( $\epsilon = 37 \text{ Lmol}^{-1}\text{cm}^{-1}$  at  $4820 \text{ cm}^{-1}$ ). The isobestic point, however, indicates that the intensity of  $[\text{Fe}(\text{NMP})_6]^{2+}$  increases toward higher pressure at the expense of the  $[\text{Fe}^{\text{II}}(\text{Br})_u(\text{NMP})_v]$  species.<sup>166</sup> The associated pressure-induced redistribution of these tetrahedral species was analyzed by deconvolution of the spectra measured for the  $\text{CDCl}_3/\text{CD}_3\text{CN}$  (87.5/12.5) mixture in the lower-wavenumber range (Figure 6.8B). Gaussian functions (dashed lines) were fitted to the data measured from 10 to 2000 bar. The positions of the fitted functions are in full agreement with the speciation analysis shown in Figure 6.8. Pressure favors the transformation of the neutral  $[\text{FeBr}_2\text{L}_2]$  complex to  $[\text{FeL}_6]^{2+}$  and to  $[\text{FeBr}_4]^{2-}$  retaining the overall balance of charges. The concentration of the  $[\text{FeBr}_3\text{L}]^-$  complex turns out to be almost insensitive toward pressure. The rearrangement in favor of the charged Fe<sup>II</sup> complexes is more pronounced in polar solvents such as NMP or acetonitrile, which are stronger ligands in  $[\text{FeL}_6]^{2+}$ .<sup>105,166</sup> The pressure-induced formation of octahedral  $[\text{FeL}_6]^{2+}$  and tetrahedral  $[\text{FeBr}_4]^{2-}$  from  $[\text{FeBr}_2\text{L}_2]$  is due to the lower molar volume of the charged species.<sup>105</sup> Furthermore, this

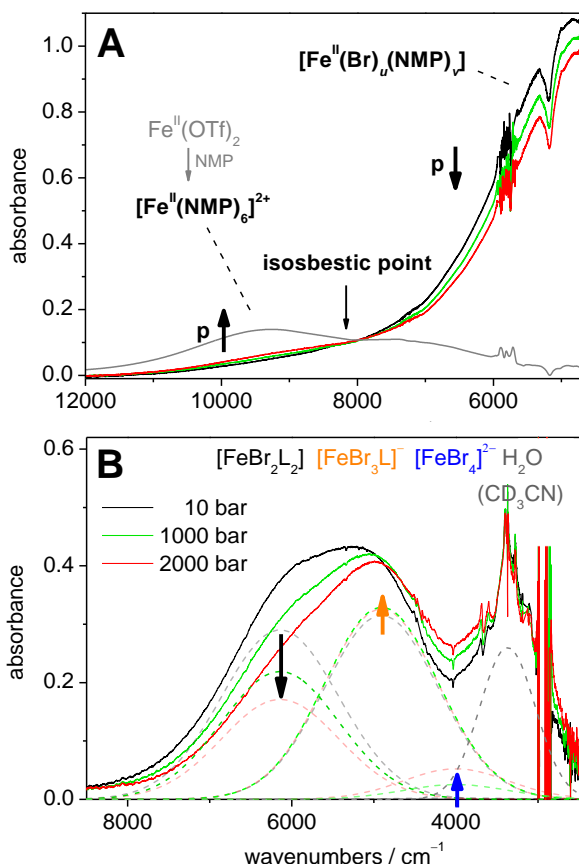


**Figure 6.8:** (A) FT-NIR spectra of 50.0 mM  $\text{FeBr}_2$  in NMP at 60 °C and an optical path length of  $d = 5.81$  mm; (B) of 30 mM  $\text{FeBr}_2$  in  $\text{CDCl}_3/\text{CD}_3\text{CN}$  (87.5/12.5) at ambient temperature and  $d = 4.4$  mm. Spectra of both solutions have been measured at 10, 1000, and 2000 bar. The Gaussian functions (dashed lines in Figure 6.8B) indicate the redistribution of tetrahedral  $\text{Fe}^{\text{II}}$  species under high pressure. The arrows illustrate the direction of change upon applying pressure.

redistribution to doubly charged  $\text{Fe}^{\text{II}}$  complexes lowers the overall molar volume of  $\text{Fe}^{\text{II}}$  with respect to  $[\text{Fe}^{\text{III}}\text{Br}_4]^-$ . This situation also results in the decrease in  $K_{\text{model}}$  with pressure according to Equation 6.20.<sup>105</sup> In the next chapter,  $K_{\text{ATRP}}$  is also studied under polymerization conditions to arrive at a detailed understanding of the kinetics of ATRP under high pressure.

### 6.3.2 ATRP of MMA up to High Pressure<sup>8</sup>

Iron-halide-mediated ATRP of MMA has been investigated in various solvents at pressures up to 2500 bar, which allows for deducing reaction volumes,  $\Delta_r V(K_{\text{ATRP}})$ , and for deducing the effect of pressure on the dispersity of the polymeric product.

MMA was selected as a suitable monomer for these studies, because methacrylates, in contrast to acrylates, exhibit only one type of (chain-end) radicals. According to Equation 6.21 polymerization rate depends on  $k_p$ , monomer concentration,  $[M]$ , and on radical concentration,  $[R_n^\bullet]$ , which may be expressed by  $K_{\text{ATRP}}$  multiplied by the actual catalyst and initiator concentrations (see r.h.s. of Equation 6.21).<sup>36</sup>  $k_p$  may vary with solvent composition: The solvent effect primarily acts on the Arrhenius pre-exponential factor of  $k_p$ , which is governed by the extent of internal rotational mobility of the transition state structure.<sup>263,284-286</sup> Literature values for  $k_p$  of MMA bulk polymerization<sup>98</sup> have been corrected for the concentration of NMP as the cosolvent and adjusted to the experimental  $p$  and  $T$  conditions. The so-obtained  $k_p$  values are tabulated in Table S4.

$$R_p = -\frac{d[M]}{dt} = k_p \cdot [R_n^\bullet] \cdot [M] = k_p \cdot K_{\text{ATRP}} \cdot \frac{[\text{Fe}^{\text{II}}] \cdot [\text{R}_n\text{X}]}{[\text{Fe}^{\text{III}}]} \cdot [M] \quad (6.21)$$

Time-dependent  $[M]$  (and thus  $R_p$ ) and  $[\text{Fe}^{\text{II}}]$  are measured via online high-pressure NIR spectroscopy.  $[\text{Fe}^{\text{III}}]$  was obtained from the difference of initial  $\text{Fe}^{\text{II}}$  concentration,  $[\text{Fe}^{\text{II}}]_0$ , and measured actual  $[\text{Fe}^{\text{II}}]$ , while  $[\text{R}_n\text{X}]$  was estimated via  $[\text{R}_n\text{X}] = [\text{R}_n\text{X}]_0 - [\text{Fe}^{\text{II}}]_0 + [\text{Fe}^{\text{II}}] = [\text{R}_n\text{X}]_0 - [\text{Fe}^{\text{III}}]$ . Molar extinction coefficients are required for the determination of  $[\text{Fe}^{\text{II}}]$  during ATRP. They were obtained by measuring the absorbance of initial  $\text{Fe}^{\text{II}}$  concentration,  $[\text{Fe}^{\text{II}}]_0$ , on the same monomer-to-solvent mixture, but without ATRP initiator. The  $\text{Fe}^{\text{II}}$  absorption results from an overlap of tetrahedral  $[\text{Fe}^{\text{II}}\text{Br}_u(\text{NMP})_v]_{u+v=4}$  species ( $u = 2, 3, \text{ or } 4$ , cf. chapter 4.1.1). Nevertheless, Beer-Lambert's law may be used under equilibrium conditions to deduce  $\text{Fe}^{\text{II}}$  catalyst concentration from overall  $\text{Fe}^{\text{II}}$  absorption.  $K_{\text{ATRP}}$  was evaluated at ca. 20 % monomer conversion, where  $[\text{Fe}^{\text{II}}]$  is still very close to  $[\text{Fe}^{\text{II}}]_0$ .

<sup>8</sup> Reproduced with permission from Schroeder, H.; Buback, M.; Matyjaszewski, K. *Macromol. Chem. Phys.* **2014**, *215*, 44–53, Copyright 2015 Wiley-VCH.

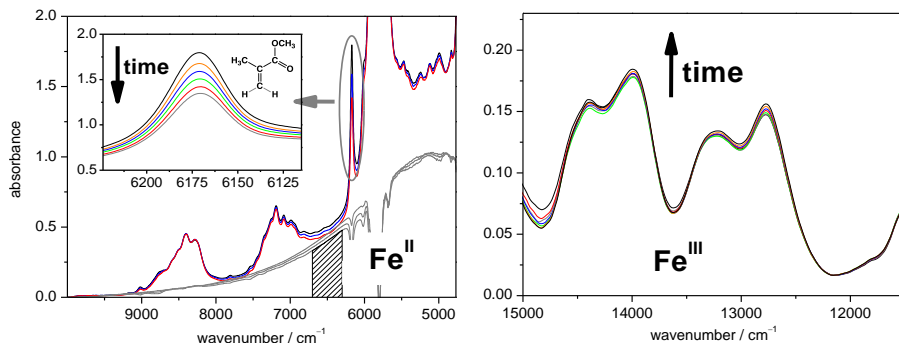


**Figure 6.9:** (A) Spectral series for solution polymerization of MMA in the presence of 16.2 mol% NMP at 60 °C and 2000 bar with MMA : EBrPA : FeBr<sub>2</sub> = 150 : 1.50 : 1.00 at an optical path length of  $d = 4.54$  mm. The decrease in MMA concentration with time was analyzed via the peak absorbance around 6171 cm<sup>-1</sup>. The underlying Fe<sup>II</sup> absorption (gray lines) is obtained by subtraction of the solvent absorption. Integration of the associated absorbance slice has been carried out between 6700 cm<sup>-1</sup> and 6300 cm<sup>-1</sup> (hatched area). (B) The increase in Fe<sup>III</sup> (= [FeBr<sub>4</sub>]<sup>-</sup>) concentration was recorded at  $d = 26.82$  mm under otherwise identical reaction conditions.

Figure 6.9A shows NIR spectra of MMA polymerization in 16.2 mol% NMP at 60 °C and 2000 bar for initial molar ratios of MMA : EBrPA : FeBr<sub>2</sub> = 150 : 1.50 : 1.00. The decrease in both monomer and Fe<sup>II</sup> concentration may be simultaneously monitored during ATRP. Monomer concentration is determined around 6171 cm<sup>-1</sup> (see inset to Figure 6.9A). Spectra were recorded within 2.8 h up to 40 % monomer conversion. To simplify the presentation, only six out of a multitude of spectra recorded within 2.8 h are shown in Figure 6.9A. The underlying NIR absorption of the Fe<sup>II</sup> species (gray lines) is obtained by subtraction of solvent absorption (including *n*-heptane as pressurization medium) measured for the same ratio of MMA and NMP at identical  $p$  and  $T$  conditions and optical path length. Integration for Fe<sup>II</sup> concentration is carried out on the absorbance slice between 6700 cm<sup>-1</sup> and 6300 cm<sup>-1</sup> as indicated in Figure 6.9A. No strong solvent absorption occurs in this wavenumber range.

As shown in chapter 4.1, the predominant Fe<sup>III</sup> species is [Fe<sup>III</sup>Br<sub>4</sub>]<sup>-</sup>. The additional bromide is provided by halide transfer from Fe<sup>II</sup> ([Fe<sup>II</sup>Br <sub>$u$</sub> (NMP) <sub>$v$</sub> ] <sub>$u+v=4$</sub> ). Molar extinction coefficients were therefore



determined in mixtures of Fe<sup>III</sup> with Fe<sup>II</sup> (see chapter 4.1.2). Only small amounts of Fe<sup>III</sup>, i. e., around 5–10 % of the Fe<sup>II</sup> concentration are generated. Thus Fe<sup>III</sup> absorption is too weak to be accurately determined at the optical path length required for measuring monomer concentration. Figure 6.9B shows the increase in Fe<sup>III</sup> absorption with time as monitored in a separate experiment at larger optical path length,  $d = 26.82$  mm. The measurement was stopped at 20 % monomer conversion. The spectra are shifted such as to yield identical absorbance at  $12\,140\text{ cm}^{-1}$ . The initial Fe<sup>III</sup> band reflects radical termination during the time period required for sample preparation and for reaching polymerization conditions. Between 6 and 20 % monomer conversion, Fe<sup>III</sup> concentration increases only slightly, from 3.77 to 4.10 mm. This minor increase in persistent radical concentration, [Fe<sup>III</sup>], reflects the high living character of the polymerization. Only 1 % of the growing chains undergo termination in this conversion range. Termination thus essentially occurs during the time interval required for reaching the targeted pressure. Ca. 7 % of total Fe<sup>II</sup> are consumed in this transition period. Also the separately measured Fe<sup>III</sup> concentration vs time traces were used for  $K_{\text{ATRP}}$  determination. It is gratifying to note that the so-obtained  $K_{\text{ATRP}}$  values are close to the associated  $K_{\text{ATRP}}$  data from analysis of the Fe<sup>II</sup> concentration vs time traces monitored at lower optical path length. The  $K_{\text{ATRP}}$  values deduced from the two concentration vs time profiles agree within 30 %, which is the estimated accuracy of  $K_{\text{ATRP}}$ .

Figure 6.10 shows a plot of  $\ln([M]_0/[M])$  vs time  $t$  for an MMA polymerization at reaction conditions as in Figure 6.9, for pressures from 1 to 2400 bar. The time required for reaching the target pressure was almost the same for all pressures. Except for the initial time period of the experiment at 1 bar, the data may be accurately fitted by straight lines. The slope of this line represents the product of  $k_p \times [R_i]$ . As  $k_p$  is constant for a given pressure, the straight line behavior indicates that also  $[R_i]$  remains more or less unchanged in the conversion range under investigation. This finding is in agreement with the observed minor increase in persistent radical concentration (see Figure 6.9B) and confirms the high living character of the ATRP reaction. Figure 6.10 further illustrates the significant enhancement of polymerization rate upon applying pressure under otherwise identical conditions. Pressurization from 1 to 1000 bar increases polymerization rate by about a factor of two and by almost a factor of four up to 2400 bar.

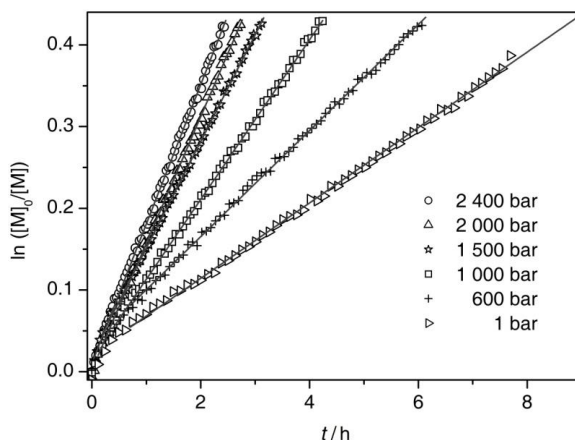


**Figure 6.10:**  $\ln([M]_0/[M])$  vs time,  $t$ , for iron-mediated ATRP of MMA in the presence of 16.2 mol% NMP for MMA : EBrPA :  $\text{Fe}^{\text{II}}$  = 150 : 1.50 : 1.00 at 60 °C and pressures between 1 and 2400 bar.  $\ln([M]_0/[M])$  and  $t$  refer to the first spectrum recorded after pressurization being taken as the time zero spectrum. Straight lines were fitted to the data.

The data in Figure 6.10 refer to samples which have been polymerized up to about 40 % monomer conversion. The experimental molar masses are in close agreement with the theoretical values (Table 6.7). The favorable low dispersity,  $D$ , for 1 bar is in agreement with the reported ambient-pressure value.<sup>82</sup> Since the same catalyst loading was used, radical concentration is already indicative of relative  $K_{\text{ATRP}}$  for a given pressure. Absolute values of  $K_{\text{ATRP}}$  have been determined at 20 % monomer conversion. It has been verified that  $K_{\text{ATRP}}$  remains almost constant up to high degrees of monomer conversion, see Figure S18 in the Appendix.

Both radical concentration and  $K_{\text{ATRP}}$  remain more or less unchanged upon carrying out ATRPs of MMA in the presence of 16.2 mol% NMP at pressures from 1 to 2400 bar (see lower part of Figure 6.11). The beneficial effect of pressure on polymerization rate is thus entirely due to the impact on  $k_p$ . The rate enhancement is not counterbalanced by any unfavorable increase in dispersity (see upper part of Figure 6.11).

Beyond the impact on  $k_p$  and  $K_{\text{ATRP}}$ , the effect of pressure on diffusion-controlled  $k_t$  is of interest. Since radical concentration is almost

**Table 6.7:** Experimental and theoretical molar masses,  $M_{n,SEC}$  and  $M_{n,theo}$ , respectively, and dispersity,  $D$ , of PMMA samples polymerized at different pressures up to the indicated degree of monomer conversion for MMA : EBrPA : Fe<sup>II</sup> = 150 : 1.50 : 1.00 in solution of 16.2 mol% NMP at 60 °C.

$p$ / bar	conversion / %	$M_{n,SEC}$ / gmol <sup>-1</sup>	$M_{n,theo}$ / gmol <sup>-1</sup>	$D$
1	34	4200	3640	1.25
600	38	4500	4040	1.24
1000	40	4700	4240	1.23
1500	46	5400	4840	1.21
2000	40	4600	4240	1.28
2400	42	4900	4440	1.26

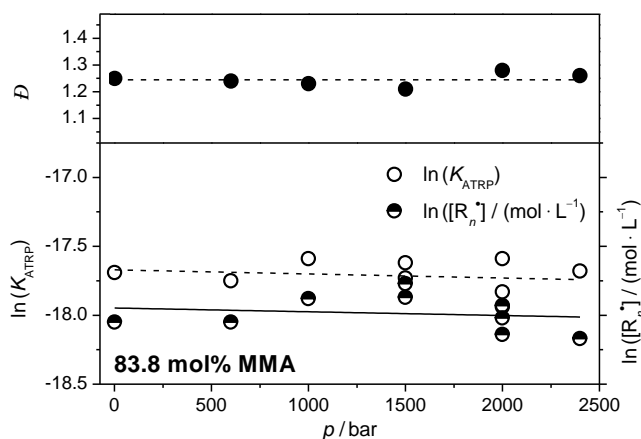


**Figure 6.11:** Pressure dependence of dispersity (filled symbols),  $D$ , radical concentration (half-filled symbols),  $[R\cdot]$ , and  $K_{ATRP}$  (open symbols) for ATRP of MMA/NMP (83.8/16.2 mol%) with MMA : EBrPA : Fe<sup>II</sup> = 150 : 1.50 : 1.00 at 60 °C. Straight lines were fitted to the data. The dashed line through the  $D$  vs  $p$  data represents the mean value of  $D$ .

insensitive toward pressure and no favorable effect of pressure on dispersity is observed, pressure-induced lowering of termination rate appears to play no major role. The decrease of termination rate toward higher pressure, however, turns out to be important in the early reaction period, i.e., during the time interval required for reaching the targeted polymerization conditions. Figure 6.12 shows relative monomer concentration plotted vs time for two ATRPs under identical conditions with only the time interval required for pressurization up to 2000 bar being significantly different. Upon fast pressurization, i.e., within one minute, the resulting  $\text{Fe}^{\text{III}}$  concentration is much lower,  $1.5 \text{ mmol L}^{-1}$  vs  $3.6 \text{ mmol L}^{-1}$  in case of slow pressurization, i.e., within about three minutes, and remains at this lower level throughout the entire ATRP. As a consequence,  $[\text{R}_i]$  (and thus polymerization rate) are significantly increased by faster pressurization. As well-controlled ATRP requires  $\text{Fe}^{\text{III}}$  deactivator species to be present, the amount of  $\text{Fe}^{\text{III}}$  can, however, not be reduced arbitrarily and should be between 0.5 and 1.0 mM  $\text{Fe}^{\text{III}}$ . This minimum  $\text{Fe}^{\text{III}}$  concentration limits the extent of pressure-induced rate enhancement.

It appeared rewarding to examine the solvent dependence of  $K_{\text{ATRP}}$  for iron-catalyzed ATRP of MMA.  $K_{\text{ATRP}}$  was investigated within a wide  $p$  and  $T$  range at different initial NMP contents, including measurements in the absence of NMP: either in bulk MMA, with 0.1 M TBA-OTf being added to ensure the solubility of the catalyst (cf. chapter 4.1.3), or in MMA/anisole (1:1, v/v) with 1 equiv TBA-Br being added. Illustrated in Figure 6.13 is the pressure dependence of  $\lg(K_{\text{ATRP}})$  with TBA-Br (gray symbols), with TBA-OTf (black), and in the presence of 16.2 (orange), 35.4 (blue), 68.7 (red) and 91.8 mol% (green) NMP. The decadic logarithm ( $\lg$ ) is more easily associated with decimal numbers, and is thus used instead of the natural logarithm ( $\ln$ ). The reaction volume,  $\Delta_r V$ , was deduced from the slope of the straight lines to the  $\lg(K_{\text{ATRP}})$  vs  $p$  data.

It stands out that  $K_{\text{ATRP}}$  at a given pressure varies significantly with the amount of the polar solvent component, NMP (see Figure 6.13 below). This effect has already been seen for the monomer-free model systems discussed in chapter 4.1.3. In passing from 91.8 % NMP solution polymerization to bulk MMA with the TBA-OTf additive,  $K_{\text{ATRP}}$  is increased by about three orders of magnitude at ambient pressure. The additional increase with TBA-Br being added is due to the quantitative

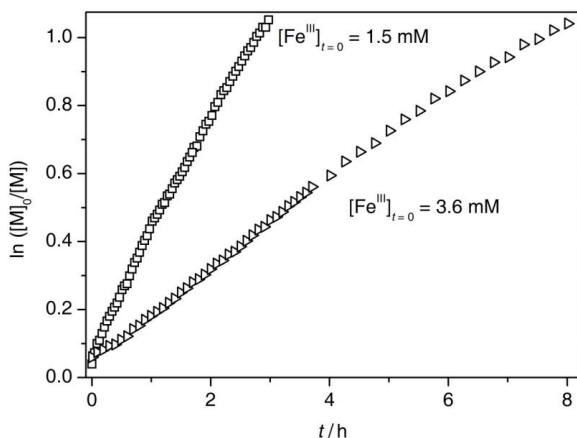


**Figure 6.12:**  $\ln([M]_0/[M])$  vs time,  $t$ , for iron-mediated ATRP of MMA in the presence of 16.2 mol% NMP for MMA : EBrPA :  $\text{Fe}^{\text{II}}$  :  $\text{Fe}^{\text{III}}$  = 150 : 1.50 : 1.00 : 0 at 60 °C and 2000 bar. The two experiments differ in the time required for reaching 2000 bar. The  $\ln([M]_0/[M])$  vs  $t$  data refer to the first spectrum recorded after pressurization.

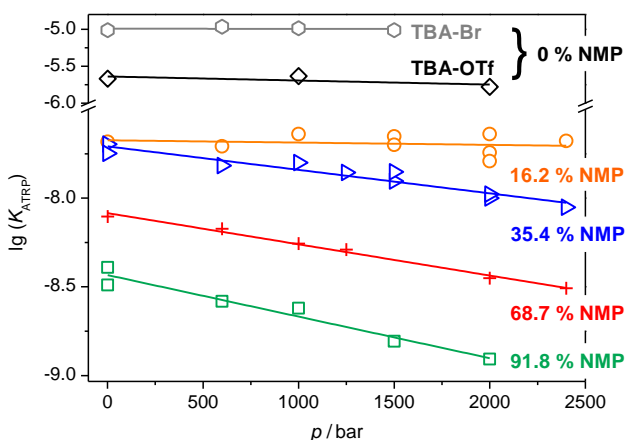


**Figure 6.13:**  $\lg(K_{\text{ATRP}})$  vs pressure,  $p$ , for iron-mediated ATRP of MMA at 60 °C with 1 equiv TBA-Br (gray symbols), with 0.1 M TBA-OTf (black), and in the presence of 16.2 (orange), 35.4 (blue), 68.7 (red) and 91.8 mol% (green) NMP.

formation of the active catalyst species  $[\text{Fe}^{\text{II}}\text{Br}_3(\text{Solv})]^-$  and  $[\text{Fe}^{\text{III}}\text{Br}_4]^-$  (see chapter 4.1.3). The changes in  $K_{\text{ATRP}}$  with solvent composition are accompanied by changes in  $\Delta_r V$ . Polymerizations carried out in 91.8 mol% NMP are close to the situation of the model systems in pure NMP without monomer being present, for which  $\Delta_r V$  has been found to be  $13 \pm 3 \text{ cm}^3 \text{ mol}^{-1}$ . This positive reaction volume describes the decrease of  $K_{\text{model}}$  toward high pressure due to the pressure-induced formation of octahedral  $[\text{FeL}_6]^{2+}$  and tetrahedral  $[\text{FeBr}_4]^{2-}$  from  $[\text{FeBr}_2\text{L}_2]$  due to the lower molar volume of the charged species.<sup>105</sup>  $\Delta_r V$  of the monomer-free model system in NMP is close to the value of MMA polymerization in the presence of 91.8 mol% NMP,  $\Delta_r V = 15 \pm 3 \text{ cm}^3 \text{ mol}^{-1}$  (Figure 6.13). The lowering of  $K_{\text{ATRP}}$  with pressure occurs to almost the same extent as the simultaneous increase in  $k_p$  ( $\Delta^\ddagger V(k_p) = -16.7 \text{ cm}^3 \text{ mol}^{-1}$ ), which results in only a minor rate enhancement of ATRP for this solvent composition.

In passing from 91.8 mol% NMP to 16.2 mol% NMP polymerization, the values for  $\Delta_r V$  decrease to  $1 \pm 2 \text{ cm}^3 \text{ mol}^{-1}$  (see Table 6.8 and Figure 6.13). This observation suggests that pressure-induced formation of  $[\text{Fe}(\text{NMP})_6]^{2+}$  becomes less likely in case that only small amounts of NMP are available. No further change in  $\Delta_r V$  is observed for polymerizations in the absence of NMP (entries 1–2 in Table 6.8).

Conversely, absolute  $K_{\text{ATRP}}$  is already significantly reduced with only small amounts of NMP being added as illustrated in Figure 6.14. This situation results from changes in Gibbs energy of  $[\text{Fe}^{\text{II}}\text{Br}_3(\text{Solv})]^-$  when NMP coordinates to Fe<sup>II</sup> to yield  $[\text{Fe}^{\text{II}}\text{Br}_3(\text{NMP})]^-$  instead of  $[\text{Fe}^{\text{II}}\text{Br}_3(\text{MMA})]^-$  (cf. chapter 4.1.3). The  $K_{\text{ATRP}}$  values in Figure 6.14 are plotted vs the NMP-to-metal ratio,  $\chi_{\text{NMP}}/\chi_{\text{Fe(II)}}$  for 60 °C and 2000 bar. The value of  $\chi_{\text{NMP}}/\chi_{\text{Fe(II)}} = 206$  refers to the monomer-free model system at  $\chi_{\text{NMP}} = 1$  using poly(MMA)-Br as the macroinitiator (see further below). ATRPs with low  $\chi_{\text{NMP}}/\chi_{\text{Fe(II)}}$  (■) have been carried out with TBA-OTf. The decrease in  $K_{\text{ATRP}}$  in Figure 6.14 at low values of  $\chi_{\text{NMP}}/\chi_{\text{Fe(II)}} = 1.1, 2.8, 5.2,$  and  $14.2$  reflects the association of NMP as a ligand to iron. At  $\chi_{\text{NMP}}/\chi_{\text{Fe(II)}} = 2.8$ ,  $K_{\text{ATRP}}$  is already by about one order of magnitude below the value determined during ATRP of bulk MMA. The data set may be linearized by a double logarithmic plot (Figure S19 and cf. Figure 4.9).

**Table 6.8:** Equilibrium constants,  $K_{\text{ATRP}}$ , at 2000 bar and 60 °C, reaction enthalpies,  $\Delta_r H$ , and reaction volumes,  $\Delta_r V$ , for MMA polymerization at different NMP contents.

entry	NMP / mol%	$K_{\text{ATRP}}$ At 60 °C / 2 kbar	$\Delta_r H /$ kJmol <sup>-1</sup>	$\Delta_r V /$ cm <sup>3</sup> mol <sup>-1</sup>
1	0 <sup>[a]</sup>	$9.7 \times 10^{-6}$	-	$1 \pm 2$
2	0 <sup>[b]</sup>	$1.7 \times 10^{-6}$	$62 \pm 7$	$3 \pm 2$ <sup>[c]</sup>
3	16.2	$2.0 \times 10^{-8}$	$54 \pm 6$	$1 \pm 2$
4	35.4	$1.1 \times 10^{-8}$	$58 \pm 6$	$8 \pm 2$
5	68.7	$3.6 \times 10^{-9}$	$60 \pm 6$	$11 \pm 3$
6	91.8	$1.2 \times 10^{-9}$	$50 \pm 5$	$15 \pm 3$

<sup>[a]</sup> With 1 equiv TBA-Br; <sup>[b]</sup> with 0.1 M TBA-OTf; <sup>[c]</sup> the value for  $\Delta_r V$  rests on a rather limited set of measurements.

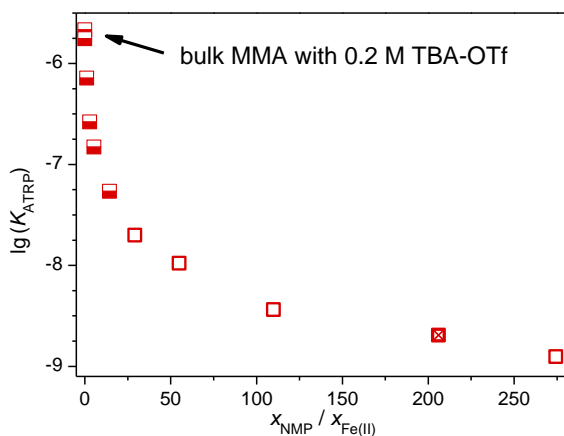


**Figure 6.14:**  $\lg(K_{\text{ATRP}})$  vs  $x_{\text{NMP}}/x_{\text{Fe(II)}}$  ( $\square$ ) for iron-mediated MMA polymerization at 60 °C and 2000 bar. The value of  $x_{\text{NMP}}/x_{\text{Fe(II)}} = 206$  refers to the monomer-free model system which is discussed in the next section. Values for small  $x_{\text{NMP}}/x_{\text{Fe(II)}}$  ( $\blacksquare$ ) have been obtained from MMA polymerization with 0.1–0.2 M TBA-OTf being present to ensure homogeneity of the solution.

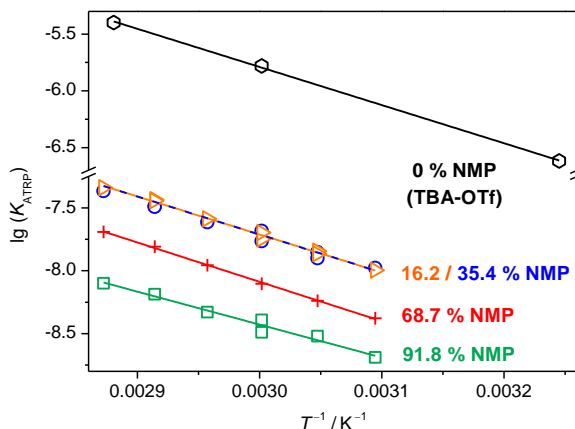


**Figure 6.15:**  $\lg(K_{\text{ATRP}})$  vs  $T^{-1}$  for Fe-mediated ATRP of MMA at ambient pressure and NMP contents of between 16.2 and 91.8 mol%. Measurements without NMP but with 0.1 M TBA-OTf were carried out at 2000 bar.

Shown in Figure 6.15 is the temperature dependence of  $K_{\text{ATRP}}$  at ambient pressure. The resulting reaction enthalpies,  $\Delta_r H$ , are listed in Table 6.8. The estimated uncertainty of  $\Delta_r H$  is primarily attributed to the rather small experimental temperature range of 50 to 75 °C. A few measurements for the system with TBA-OTf have also been carried out between 35 and 74 °C, but at 2000 bar.  $\Delta_r H$  is more or less insensitive toward NMP concentration. As with the model systems, the large  $\Delta_r H$  indicates that ATRP rate is strongly accelerated with temperature.

**Comparison of  $K_{\text{model}}$  and  $K_{\text{ATRP}}$ .** Summarized in Table 6.9 (cf. Figure S20) are equilibrium constants and reaction volumes measured during MMA polymerization and on a model system with a poly(MMA)-Br initiator ( $M_n \approx 8000 \text{ g mol}^{-1}$ , see chapter 8.3) in binary mixtures of NMP with either toluene or 2-butanone as a cosolvent.  $K_{\text{model}}$  with toluene as the cosolvent to NMP is almost identical to  $K_{\text{ATRP}}$  for MMA polymerization (with the same amount of NMP being present, entry 1–3). Irrespective of absolute  $K_{\text{model}}$ , both binary model system adequately reflect the trend of increasing  $K_{\text{model}}$  in passing from 100 to 18 mol% NMP.  $\Delta_r V_{\text{model}}$  and  $\Delta_r V_{\text{ATRP}}$  are also in close agreement.



**Table 6.9:** Equilibrium constants,  $K_{\text{model}}$  and  $K_{\text{ATRP}}$  at 1 bar and 60 °C as well as reaction volumes,  $\Delta_r V$ , for iron-catalyzed ATRP model systems studied in solution containing quite different amounts of NMP.

entry	mol% NMP	$K_{\text{model}}$ 2-Bu <sup>[a]</sup>	$K_{\text{model}}$ toluene <sup>[b]</sup>	$K_{\text{ATRP}}$ MMA	$\Delta_r V_{\text{model}} /$ $\text{cm}^3\text{mol}^{-1}$	$\Delta_r V_{\text{ATRP}} /$ $\text{cm}^3\text{mol}^{-1}$
1	18	$5.6 \times 10^{-8}$	$2.1 \times 10^{-8}$ <sup>[c]</sup>	$2.1 \times 10^{-8}$	$2 \pm 2$ <sup>[a]</sup>	$1 \pm 2$
2	38	$4.3 \times 10^{-8}$	$1.4 \times 10^{-8}$	$1.9 \times 10^{-8}$	-	$8 \pm 2$
3	62	-	$7.3 \times 10^{-9}$	$7.9 \times 10^{-9}$	-	$11 \pm 3$
4	100/92 <sup>[d]</sup>	$6.0 \times 10^{-9}$	$6.0 \times 10^{-9}$	$3.7 \times 10^{-9}$	$13 \pm 3$ <sup>[f]</sup>	$15 \pm 3$

<sup>[a]</sup> in 2-butanone as the cosolvent, <sup>[b]</sup> in toluene as the cosolvent, <sup>[c]</sup> with 1 equiv. TBA-OTf, <sup>[d]</sup> 100 mol% NMP in case of  $K_{\text{model}}$ , 91.8 mol% NMP and 9.2 mol% MMA in case of  $K_{\text{ATRP}}$ , <sup>[e]</sup> estimate based on the value with MBriB as the initiator (chapter 6.3.1), <sup>[f]</sup> Estimate via  $\Delta_r V$  with EBrPA.<sup>105</sup>

**Perspective.** Even though  $\Delta_r V(K_{\text{ATRP}})$  in iron-halide-mediated ATRP may be as low as ca.  $1 \text{ cm}^3\text{mol}^{-1}$ , negative numbers as in Cu catalysis are not observed. Tetrahedral  $[\text{Fe}^{\text{II}}\text{Br}_u\text{L}_v]$  species also mediate ATRP in the presence of additives such as phosphines (TTMPP), carbenes, and multidentate amines (TPMA\*), see chapter 4.2.<sup>228</sup> Hence, it does not come as a surprise that, within further experiments, the pressure dependence of  $K_{\text{ATRP}}$  with these systems turned out to be similar as compared to the iron halide catalyst operating without these additives in the same solvent mixture.

In the following chapter, amine-bis(phenolate)iron-mediated ATRP was examined in an attempt to identify reaction conditions under which  $K_{\text{ATRP}}$  is enhanced with pressure as with Cu-mediated systems. If both  $K_{\text{ATRP}}$  and  $k_p$  increase upon pressurization, full advantage may be taken of iron-mediated high-pressure ATRP. With such systems, experiments up to the maximum pressure of the setup should be particularly rewarding.

## 6.4 Kinetics with Amine–bis(phenolate) Iron Complexes<sup>9</sup>

### 6.4.1 ATRP up to High Pressure

ATRP of styrene (cf. chapter 5.1) catalyzed by chloro-substituted amine–bis(phenolate)iron complexes<sup>86,87,241</sup> (Figure 6.16) was investigated via online vis/NIR spectroscopy up to 6000 bar. Primary interest was directed toward the effect of pressure and temperature on  $K_{\text{ATRP}}$  and on the dispersity of the polymeric product.

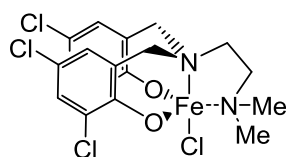
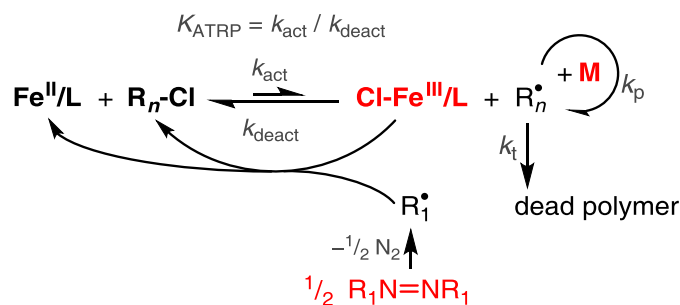


**Figure 6.16:** Structure of the investigated amine–bis(phenolate)iron(III) chloride catalyst.

As the catalyst is more readily handled in the higher  $\text{Fe}^{\text{III}}$  oxidation state, ATRPs of styrene were started in the reverse fashion (R-ATRP), as shown in Scheme 6.2, where alkyl halide and the  $\text{Fe}^{\text{II}}/\text{L}$  catalyst are produced *in situ* via decomposition of an azo initiator,  $\text{R}_1\text{N}=\text{NR}_1$ . The type of azo initiator was selected according to the targeted reaction temperature: 2,2'-azo-bis(4-methoxy-2,4-dimethyl valeronitrile) (V-70) was used for ATRPs between 70 and 90 °C, 2,2'-azo-bis(2,4-dimethyl valeronitrile) (V-65) at 100 and 110 °C, and 2,2'-azo-bis(2-methylpropionitrile) (AIBN) at 120 °C. The differences in the temperature stability of these azo initiators thus provide rapid initiator decomposition at each polymerization temperature and allows for an immediate initiation of the chain-growth reaction.

The system under investigation consisted of the amine–bis(phenolate)iron(III) chloride complex (Figure 6.16),  $\text{Cl-Fe}^{\text{III}}/\text{L}$ , and of 0.6 equiv of the azo initiator,  $\text{R}_1\text{N}=\text{NR}_1$ , in solution of styrene. The  $\text{Cl-Fe}^{\text{III}}/\text{L}$  concentration was monitored via the associated absorbance between 27 000 and 12 000  $\text{cm}^{-1}$  (Figure 6.17A). The spectra were

<sup>9</sup> Reproduced with permission from Schroeder, H.; Buback, M.; Shaver, M. P. *Macromolecules* 2015, 48, 6114–6120, Copyright 2015 American Chemical Society.



**Scheme 6.2:** Reverse ATRP catalyzed by Cl-Fe<sup>III</sup>/L and Fe<sup>II</sup>/L complexes. The starting materials are indicated in red. Polymerization is initiated by the decomposition of the thermal initiator, R<sub>1</sub>N=NR<sub>1</sub>. The structure of the primary radicals, R<sub>1</sub><sup>•</sup>, depends on the type of the thermal initiator and differs from the monomer-specific radicals, R<sub>n</sub><sup>•</sup>.

calibrated against the absorbance measured at known Cl-Fe<sup>III</sup>/L content in the absence of the thermal initiator (dashed-dotted line in Figure 6.17A). After addition of the thermal initiator, this absorption almost entirely disappears due to the rapid reduction of Cl-Fe<sup>III</sup>/L (fullred line). The initiator efficiency, i.e., the fraction of successful chain-initiation events, should be around 83 % at 120 °C, since 0.60 equiv of the azo initiator, i.e., 1.2 equiv of R<sub>1</sub> are required for the initial reduction of Cl-Fe<sup>III</sup>/L. The formation of the reduced iron complex, Fe<sup>II</sup>/L, was evidenced via Mössbauer spectroscopy as shown in chapter 5.1. During the subsequent polymerization, the Cl-Fe<sup>III</sup>/L concentration increases with time according to the PRE.<sup>155</sup> Nine out of a multitude of recorded spectra are shown in Figure 6.17A for clarity.

The full Cl-Fe<sup>III</sup>/L absorption band may be recorded via UV/VIS spectroscopy within the experiments at ambient pressure. The high-pressure equipment has been designed for FT-NIR spectroscopic studies and affords detection at wavenumbers up to 15 800 cm<sup>-1</sup> (cf. chapter 8.2), i.e., in the shaded area at wavenumbers below the one given by the dashed vertical line in Figure 6.17A. At 15 800 cm<sup>-1</sup>, the Cl-Fe<sup>III</sup>/L absorbance amounts to about one third of the intensity in the peak maximum, which is, however, sufficient to accurately determine Cl-Fe<sup>III</sup>/L concentration in the high-pressure experiments, in particular, as increased optical path lengths were used to compensate for the

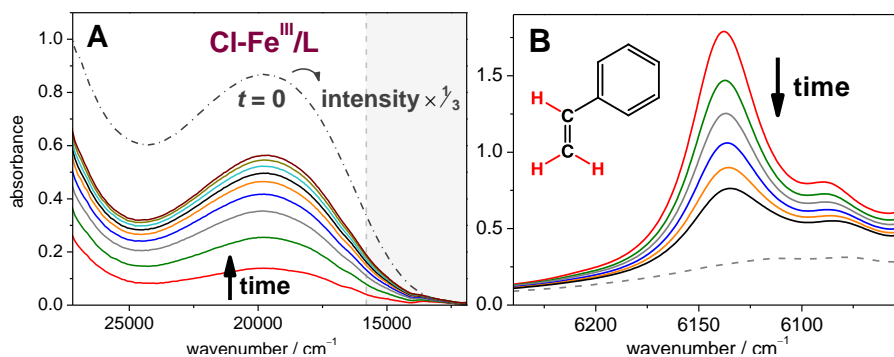


**Figure 6.17:** (A) Online vis/NIR spectroscopic measurement of an R-ATRP carried out at 90 °C and 1 bar starting with 14.5 mM Cl-Fe<sup>III</sup>/L and 8.7 mM V-70 in solution of styrene/anisole (1:1, v/v). Cl-Fe<sup>III</sup>/L concentration is measured between 27 000 and 12 000 cm<sup>-1</sup> at an optical path length of 0.5 mm. The initial spectrum (dashed-dotted line) was recorded in the absence of the thermal initiator. For better presentation, the intensity of this spectrum was reduced by a factor of three. (B) Styrene concentration monitored via the characteristic peak absorbance at around 6137 cm<sup>-1</sup> at an optical path length of 5 mm. The spectral series was recorded at 2000 bar and 120 °C. The dashed line represents the reference absorbance for full conversion of styrene.

reduced absorbance. The quantitative analysis for Cl-Fe<sup>III</sup>/L is thus straightforward, as this deactivator complex is the single Fe species occurring in this wavenumber range.<sup>241</sup>

Monomer concentration was determined from the characteristic peak absorbance at around 6137 cm<sup>-1</sup>, which is associated with the first overtone of the C–H stretching modes at an unsaturated carbon atom (Figure 6.17B). For clarity, only six out of a multitude of recorded spectra are shown in Figure 6.17B. The dashed line represents the reference spectrum for full conversion of styrene. A second autoclave<sup>104,166,167</sup> with larger optical path length has been used for online NIR detection of ATRPs at pressures above 2000 bar. In this experimental setup, styrene concentration was monitored at around 8980 cm<sup>-1</sup> via the second overtone of C–H stretching modes at an unsaturated carbon atom.

The  $\ln([M]_0/[M])$  vs time,  $t$ , traces for ATRPs of styrene carried out in bulk at 120 °C and pressures of 1, 1000, 2000 and 5000 bar are shown in

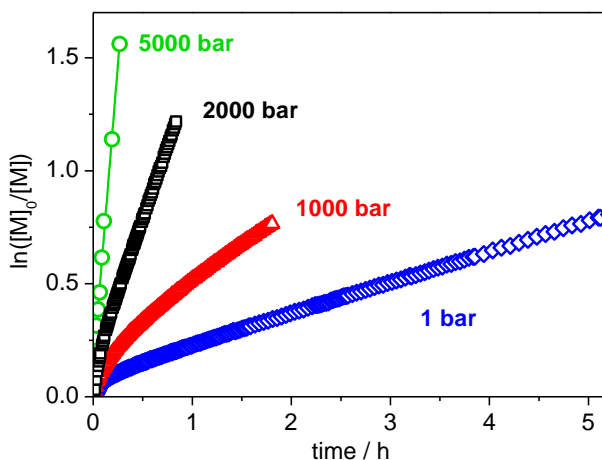


**Figure 6.18:**  $\ln([M]_0/[M])$  vs  $t$  for ATRPs of styrene carried out at 120 °C and 1, 1000, 2000, and 5000 bar. The initial molar ratios of reagents were:  $[\text{Sty}] : [\text{Cl-Fe}^{\text{III}}/\text{L}] : [\text{R}_1\text{N}=\text{NR}_1] = 1000 : 1.00 : 0.60$  with the exception of the reaction at 5000 bar, where only 0.40 equiv  $\text{R}_1\text{N}=\text{NR}_1$  have been employed.

Figure 6.18. The molar ratios of the reagents were:  $[\text{Sty}] : [\text{Cl-Fe}^{\text{III}}/\text{L}] : [\text{R}_1\text{N}=\text{NR}_1] = 1000 : 1.00 : 0.60$ , with the exception of the reaction at 5000 bar, where 0.40 equiv of  $\text{R}_1\text{N}=\text{NR}_1$  relative to  $\text{Cl-Fe}^{\text{III}}/\text{L}$  were employed. After an initial reaction period, the increase in  $\ln([M]_0/[M])$  vs  $t$  exhibits a straight-line behavior, which is indicative of a constant level of radical concentration.

At ambient pressure, radicals produced from styrene via self-initiation<sup>287</sup> may compensate the loss of growing chains due to termination reactions, thus yielding linear  $\ln([M]_0/[M])$  vs  $t$  traces over an extended time period (> 5h). Within the short duration of the high-pressure experiments, e.g., of about 40 min at 120 °C and 2000 bar, it was verified experimentally that the amount of radicals produced by self-initiation is negligible. Termination reactions and the simultaneous accumulation of  $\text{Cl-Fe}^{\text{III}}/\text{L}$  typically result in a slight curvature of  $\ln([M]_0/[M])$  vs  $t$  such as seen for the data at 1000 bar. The observed linearity of the  $\ln([M]_0/[M])$  vs  $t$  plots for 2000 and 5000 bar is thus assigned to the beneficial lowering of termination rate toward high pressure.<sup>99-101</sup>

ATRP is significantly accelerated toward higher pressure as is seen from the increase in the slope of the  $\ln([M]_0/[M])$  vs  $t$  correlations, by about one order of magnitude, in passing from 1 to 2000 bar (cf. Figure 6.18). This effect significantly exceeds the expected rate enhancement associated with the pressure dependence of  $k_p$ .<sup>97</sup> The additional rate enhancement must be due to the increase in  $[R_n^*]$  with pressure (cf. Equation 6.21, chapter 6.3.2).  $[R_n^*]$  may be estimated by rearranging Equation 6.21 to  $[R_n^*] = -d \ln[M]/(k_p \cdot dt)$ . The measured rate data, together with the known  $k_p(p)$ , suggest that, in passing from 1 to 1000 and to 2000 bar,  $[R_n^*]$  increases from  $1.4 \times 10^{-8}$  to  $2.5 \times 10^{-8}$  and  $4.8 \times 10^{-8} \text{ molL}^{-1}$ , respectively, with these numbers being determined at 33 % monomer conversion. The  $\ln([M]_0/[M])$  vs  $t$  trace at 5000 bar was recorded at a reduced ratio of initiator to Fe concentration to counterbalance the otherwise enormous pressure-induced rate enhancement. The adjustment was necessary to maintain a low degree of monomer conversion during the time interval required for reaching the targeted pressure and temperature and to provide sufficient time for online reaction monitoring.

The increase in  $[R_n^*]$  with pressure is assigned to the enhancement of  $K_{\text{ATRP}}$ . The online spectroscopic analysis of both  $\text{Fe}^{\text{III}}$  concentration and monomer conversion allows for analyzing  $K_{\text{ATRP}}$  according to Equation 6.21.<sup>36</sup> The time-dependent concentrations of  $\text{Fe}^{\text{II}}$  and  $R_n\text{-Cl}$  during the R-ATRP may be calculated from the relationship:  $[\text{Fe}^{\text{II}}] = [R_n\text{-Cl}] = [\text{Fe}^{\text{III}}]_0 - [\text{Fe}^{\text{III}}]$ . The propagation rate coefficient is known from pulsed-laser polymerization experiments up to 2800 bar.<sup>97</sup> The reported activation volume,  $\Delta^\ddagger V(k_p) = (-12.1 \pm 1.1) \text{ cm}^3 \text{ mol}^{-1}$ ,<sup>97</sup> was used for estimating  $k_p$  up to 6000 bar.

Plotted in Figure 6.19 are the so-obtained values of  $\lg(K_{\text{ATRP}})$  vs pressure (red symbols). According to Equation 6.20, the reaction volume,  $\Delta_r V$ , was deduced from the slope of the straight line to be  $(-17 \pm 2) \text{ cm}^3 \text{ mol}^{-1}$ , reflecting an increase in  $K_{\text{ATRP}}$  by a factor of 20 upon increasing pressure from 1 to 6000 bar. Due to the simultaneous increase in  $k_p$ , ATRP rates increase by two orders of magnitude within this extended pressure range. The simultaneous pressure-induced lowering of the termination rate allows for a high living character of amine-*bis*(phenolate)iron-mediated ATRP.

The large negative  $\Delta_r V(K_{\text{ATRP}})$  is assigned to the stronger contraction of the ligand sphere<sup>104</sup> of the  $\text{Cl-Fe}^{\text{III}}/\text{L}$  complex in solution, which may

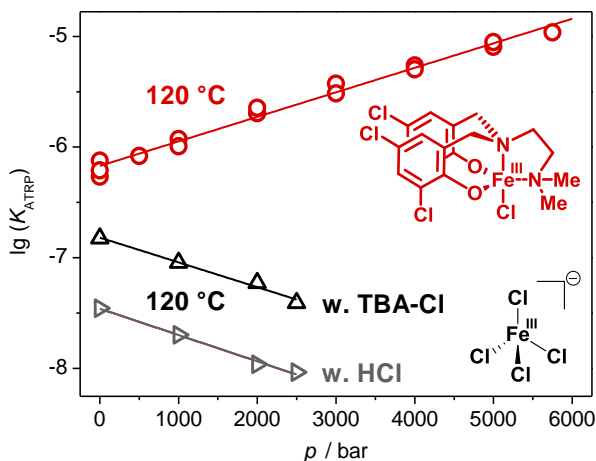


**Figure 6.19:**  $\lg(K_{\text{ATRP}})$  vs pressure,  $p$ , for ATRPs of styrene at 120 °C mediated by either the amine-*bis*(phenolate)iron(III) catalyst (upper part) or by  $[\text{FeCl}_4]^-$  (lower part) with TBA-Cl (black symbols) or HCl (gray symbols) being added for catalyst formation. Straight lines were fitted to the data.

be understood in terms of  $\text{Cl-Fe}^{\text{III}}/\text{L}$  being a stronger Lewis acid than  $\text{Fe}^{\text{II}}/\text{L}$ . The reaction volume is similar to the numbers reported for Cu-ligand ATRP systems,<sup>102-104</sup> where high pressure also shifts the ATRP equilibrium toward the metal species of higher charge, i.e., to  $\text{Fe}^{\text{III}}$  or  $\text{Cu}^{\text{II}}$ , respectively. The only exception to this behavior was the iron bromide system (see chapter 6.3) complexed by bromide and solvent molecules:  $[\text{Fe}^{\text{II}}\text{Br}_u(\text{Solv})_v]^{(2-u)}$ , which is due to the pressure-induced rearrangement of the  $\text{Fe}^{\text{II}}$  species.

In order to check whether the iron chloride complexes  $[\text{Fe}^{\text{II}}\text{Cl}_u(\text{Solv})_v]^{(2-u)}$  exhibit the same behavior as the bromide complexes, and to enable a direct comparison of  $K_{\text{ATRP}}$  with the amine-*bis*(phenolate)iron catalyst,  $^{\text{Cl,Cl,NMe}_2}[\text{O}_2\text{NN}']\text{FeCl}$ , ATRPs of styrene were conducted with iron chlorides in the absence of a specific ligand. The reactions were carried out at 120 °C and pressures between 1 and 2500 bar with the following initial molar ratio of reagents in solution of DMF (33 vol%):  $[\text{Sty}] : [\text{ECIPA}] : [\text{FeCl}_2] : [\text{TBA-Cl}] = 200 : 1.00 : 1.00 : 1.00$ , where ECIPA is ethyl  $\alpha$ -chlorophenylacetate and TBA-Cl is tetrabutylammonium chloride. TBA-Cl provides the additional chloride for the formation of the catalyst species,  $[\text{Fe}^{\text{II}}\text{Cl}_3(\text{Solv})]^-$  and  $[\text{Fe}^{\text{III}}\text{Cl}_4]^-$ ,

which are predominant at ambient pressure.<sup>228</sup> Alternatively, HCl was added as a chloride source. The ATRPs with the iron chloride catalyst turned out to be also well-controlled, e.g., yielding  $\bar{D} = 1.17$  at 75 % monomer conversion after 15 h at ambient pressure. However, the activity of the  $^{Cl,Cl,NMe_2}[O_2NN']FeCl$  catalyst is significantly higher with  $K_{ATRP}$  being a factor of 5 and 20 above  $K_{ATRP}$  for  $[Fe^{III}Cl_4]^-$  with added TBA-Cl and HCl, respectively. Based on relative  $K_{ATRP}$ , TBA-Cl seems to be the more effective chloride source than HCl in organic media. Irrespective of the added chloride component,  $K_{ATRP}$  for  $[Fe^{III}Cl_4]^-$  decreases toward higher pressure (Figure 6.19) yielding  $\Delta_r V(K_{ATRP}) = (17 \pm 3)$  and  $(18 \pm 3) \text{ cm}^3\text{mol}^{-1}$ , respectively (Table 6.10). Consequently, the difference in  $K_{ATRP}$  between  $^{Cl,Cl,NMe_2}[O_2NN']FeCl$  and  $[Fe^{III}Cl_4]^-$  enormously increases with pressure.

The experiments at elevated pressure demonstrate that the  $^{Cl,Cl,NMe_2}[O_2NN']FeCl$  catalyst does not undergo any competing solvent coordination or undesirable complex rearrangements. The amine-*bis*(phenolate) ligand affords Fe catalysis with enhanced  $K_{ATRP}$ . It was found that ATRP using this catalyst system may be carried out in bulk and in anisole solutions without any effect on  $K_{ATRP}$ . The reaction enthalpy of ATRP with  $^{Cl,Cl,NMe_2}[O_2NN']FeCl$  is  $25 \pm 5 \text{ kJ mol}^{-1}$  (Figure 6.20) and thus considerably below the enthalpy of  $58 \text{ kJ mol}^{-1}$  measured for ATRP of MMA with iron halides.<sup>105</sup> The temperature and pressure dependence of  $K_{ATRP}$  for  $^{Cl,Cl,NMe_2}[O_2NN']FeCl$  deduced from the styrene polymerization experiments is given by Equation 6.22.

$$\lg(K_{ATRP}) = -2.86 - \frac{1310}{T/K} + \frac{0.0888}{T/K} (p/\text{bar} - 1) \quad (6.22)$$

The effect of pressure on the dispersity of the polymeric product is also of interest. For this purpose, another series of ATRP experiments were carried out using a simultaneous reverse & normal initiation (SR&NI) principle: In addition to alkyl halide formation by *in situ* reduction of  $Cl-Fe^{III}/L$  with a thermal initiator, the alkyl halide initiator, ECIPA, was added to the system. ATRPs were conducted at  $120 \text{ }^\circ\text{C}$  in solution of anisole (25 vol%) with an identical initial molar ratio of reagents at all investigated pressures:  $[Sty]:[Cl-Fe^{III}/L]:[ECIPA]:[R_1N=NR_1] = 300:1.00:1.00:0.13$ . The SR&NI methodology was used because the small amount of thermal initiator means that only about



**Table 6.10:** Equilibrium constants,  $K_{\text{ATRP}}$ , at 1 bar and 120 °C, reaction enthalpy,  $\Delta_r H$ , and reaction volumes,  $\Delta_r V$ , for styrene ATRP mediated by the indicated catalyst.

entry	Fe <sup>III</sup> catalyst	$K_{\text{ATRP}}$ at 120 °C / 1 bar	$\Delta_r H /$ kJ mol <sup>-1</sup>	$\Delta_r V /$ cm <sup>3</sup> mol <sup>-1</sup>
1	Cl,Cl,NMe <sub>2</sub> [O <sub>2</sub> NN']FeCl	$6.8 \times 10^{-7}$	$25 \pm 5$	$-17 \pm 2$
2	[TBA][FeCl <sub>4</sub> ]	$1.5 \times 10^{-7}$	-	$17 \pm 3$
3	[H <sub>3</sub> O][FeCl <sub>4</sub> ]	$3.5 \times 10^{-8}$	-	$18 \pm 3$

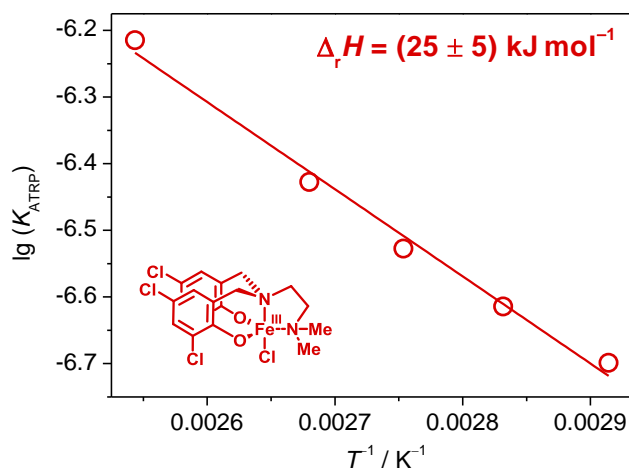


**Figure 6.20:**  $\lg(K_{\text{ATRP}})$  vs  $T^{-1}$  for the ATRP of styrene at 120 °C mediated by Cl,Cl,NMe<sub>2</sub>[O<sub>2</sub>NN']FeCl. A straight line was fitted to the data with the slope yielding the reaction enthalpy,  $\Delta_r H = 25 \pm 5$  kJmol<sup>-1</sup>.

20 % of Cl-Fe<sup>III</sup>/L is converted to Fe<sup>II</sup>/L. This provides a high Cl-Fe<sup>III</sup>/L deactivator concentration throughout the entire ATRP reaction. The excess of ECIPA as compared to Fe<sup>II</sup>/L essentially yields polymer with a high degree of chain-end functionality. Listed in Table 6.11 are the experimental and theoretical molar masses,  $M_{n,\text{SEC}}$  and  $M_{n,\text{theo}}$ , respectively, and the dispersity,  $\mathcal{D}$ , of polystyrene samples produced between 1 and 6000 bar. The experimental molar masses are in

**Table 6.11:** Experimental and theoretical molar masses,  $M_{n,SEC}$  and  $M_{n,theo}$ , respectively, and dispersity,  $D$ , of polystyrene produced at different pressures and up to the indicated degree of monomer conversion.<sup>[a]</sup>

$p /$ bar	conv. / %	$M_{n,SEC} /$ $g\text{mol}^{-1}$	$M_{n,theo} /$ $g\text{mol}^{-1}$ [a]	$D$
1	38	9400	9880	1.18
2000	37	9100	9620	1.21
3000	39	9300	10140	1.20
4000	45	10000	11700	1.22
5000	38	8600	9880	1.24
6000	54	11400	14040	1.28

<sup>[a]</sup> Conditions:  $[\text{Sty}] : [\text{Cl-Fe}^{\text{III}}/\text{L}] : [\text{ECIPA}] : [\text{R}_1\text{N}=\text{NR}_1] = 300 : 1.00 : 1.00 : 0.13$ , styrene : anisole = 3:1 (v/v), 120 °C.  $M_{n,theo} = [\text{Sty}]_0 / ([\text{ECIPA}]_0 + [\text{R}_1\text{N}=\text{NR}_1]_0 \times 1.7) \times M(\text{Sty}) \times \text{conversion} + M(\text{ECIPA})$ .

reasonable or even excellent agreement with the theoretical values. It is particularly gratifying to note that, despite the enormous rate enhancement toward higher pressure, ATRP may still be operated in a well-controlled fashion at 6000 bar with the dispersity being  $D = 1.28$ . Nevertheless dispersity increases from 1.18 to 1.28 in passing from 1 to 6000 bar (Figure 6.21). The associated broadening of the molar-mass distribution is illustrated in Figure 6.22. This effect is attributed to a relative lowering of deactivation to propagation rate toward higher pressure. The situation may be similar to the one with Cu-based ATRP systems, for which the activation volume,  $E_a(k_{\text{deact}})$ , was found to be close to zero,<sup>27</sup> whereas propagation rate is strongly enhanced. The consequences of such relative changes in deactivation to propagation rate are more vigorous at lower Cl-Fe<sup>III</sup>/L content: An ATRP started with 2 mM Cl-Fe<sup>III</sup>/L occurs in a controlled fashion ( $D < 1.3$ ) at ambient pressure, whereas the dispersity in ATRP at 5000 is significantly affected by lowering initial Cl-Fe<sup>III</sup>/L concentration from 22 mM to 8 mM and 2 mM, which yields an increase in dispersity from  $D = 1.24$  to 1.50 and to  $> 2.5$ , respectively.

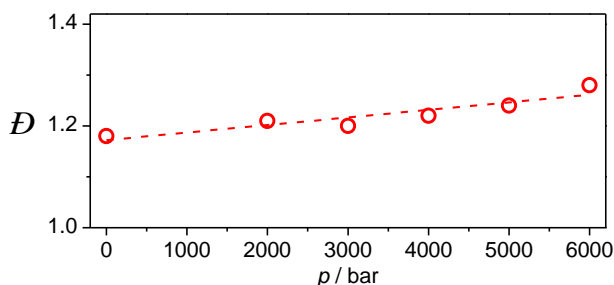


**Figure 6.21:** Dispersity as a function of pressure of polystyrene synthesized via ATRP (see text). The dashed line serves the purpose of guiding the eye.

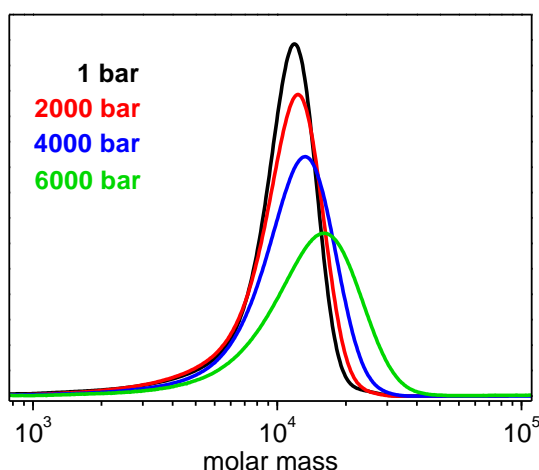


**Figure 6.22:** SEC-derived molar-mass distributions (MMDs) of polystyrene produced via ATRP (see text) at 120 °C and pressures from 1 to 6000 bar. The MMDs were scaled to identical area under the curves.

Applying high pressure turns out to be helpful once  $\text{Cl}_2\text{Cl}_2\text{NMe}_2[\text{O}_2\text{NN}']\text{FeCl}$  is used at further optimized conditions: To reach higher degrees of polymerization and thus higher molar masses, the concentration of growing chains and thus of ATRP initiator needs to be reduced. Such ATRPs are more feasible under high pressure due to the

beneficial lowering of termination rate. E.g., a number-average molar mass  $M_n = 103,000 \text{ g mol}^{-1}$  ( $D = 1.4$ ) was obtained after only 1 h by carrying out an R-ATRP of styrene at 120 °C and 5000 bar with 2 mM AIBN as the single initiator.

After this detailed kinetic study into styrene ATRP mediated by  $\text{Cl,Cl,NMe}_2[\text{O}_2\text{NN}']\text{FeCl}$ , other monomers should be investigated along the same lines. The reported reaction volumes for a variety of Cu–ligand systems were found to be almost independent of the type of propagating radical and of the associated alkyl halide,<sup>102-104</sup> despite the differences in absolute  $K_{\text{ATRP}}$ .<sup>44,102,103,201,233</sup>

### 6.4.2 OMRP up to High Pressure

With methacrylates, the investigated  $\text{Cl,Cl,NMe}_2[\text{O}_2\text{NN}']\text{Fe}$  catalyst operates simultaneously via ATRP and OMRP equilibria (cf. chapter 5.1).<sup>86,87,241</sup> The OMRP activation,  $\text{R}_n\text{-Fe}^{\text{III}}/\text{L} \rightarrow \text{R}_n^\bullet + \text{Fe}^{\text{II}}/\text{L}$ , should be disfavored toward higher pressure, since  $\text{R}_n\text{-Fe}^{\text{III}}/\text{L}$  is converted into two species,  $\text{R}_n^\bullet$  and  $\text{Fe}^{\text{II}}/\text{L}$ . With ATRP, on the other hand, activation is not associated with a change in the number of reacting species. Moreover, ATRP activation yields the higher charged iron species, which is mostly accompanied by a lower molar volume. Applying pressure may thus affect the relative importance of ATRP and OMRP with a preference for radical production and control by ATRP.

MMA polymerizations may also be operated exclusively via OMRP control (cf. chapter 5.1). The associated  $\text{R}_n\text{-Fe}^{\text{III}}/\text{L}$  activator complex was produced *in situ* according to the procedure detailed below Figure S11. OMRP was started by adding monomer to the solution containing about 8.2 mM  $\text{R}_n\text{-Fe}^{\text{III}}/\text{L}$  and 1.8 mM of the  $\text{Fe}^{\text{II}}/\text{L}$  complex.  $\text{R}_n\text{-Fe}^{\text{III}}/\text{L}$  cannot be monitored, since the high-pressure equipment was designed for NIR-spectroscopic detection below  $15\,800 \text{ cm}^{-1}$ , whereas the peak maximum of  $\text{R}_n\text{-Fe}^{\text{III}}/\text{L}$  occurs at  $23\,250 \text{ cm}^{-1}$  as deduced via ambient-pressure UV/VIS spectroscopy (chapter 5.1). The concentration and thus NIR intensity associated with  $\text{Fe}^{\text{II}}/\text{L}$  is too low to be monitored accurately. Therefore, only the initial catalyst concentrations are precisely known. To allow for an interpretation of the effect of pressure on polymerization rate, OMRPs at 1 and 4000 bar were started with identical concentrations of  $\text{R}_n\text{-Fe}^{\text{III}}/\text{L}$  (8.2 mM) and  $\text{Fe}^{\text{II}}/\text{L}$  (1.8 mM). Equilibration

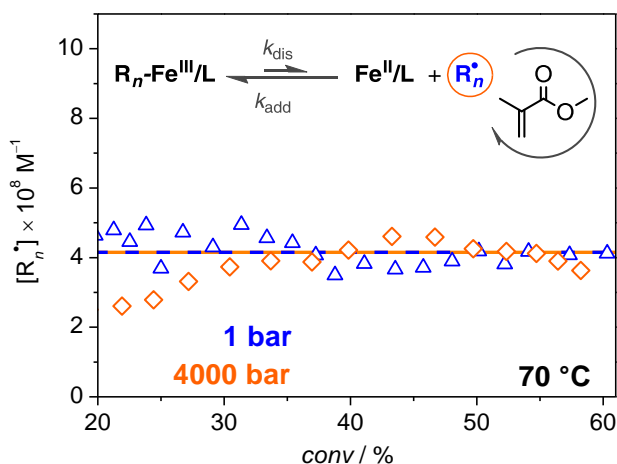


**Figure 6.23:**  $[R_n^\bullet]$  vs monomer conversion,  $\text{conv}$ , in OMRP of MMA carried out at 70 °C and 1 bar (blue symbols) and at 4000 bar (orange symbols). The dashed line serves the purpose of guiding the eye. Further details of the polymerization procedure are found in Figure S11.

should primarily affect the reaction partner with the smallest concentration, i.e., the radicals,  $R_n^\bullet$ . The changes in  $R_n^\bullet$  with pressure should be indicative of the changes in the position of the OMRP equilibrium, similarly as the changes in  $R_n^\bullet$  indicate the changes in  $K_{\text{ATRP}}$  with pressure as shown before.  $R_n^\bullet$  was determined from measured  $\ln([M]_0/[M])$  vs time traces and known  $k_p(p)$ . Within first investigations into OMRP of MMA at 70 °C, no increase in radical concentration toward higher pressure was observed in passing from 1 to 4000 bar (Figure 6.23). This observation supports the idea that if both the ATRP and OMRP mechanism operate simultaneously, high pressure should favor radical production and control via ATRP.



# 7

## Closing Remarks

ATRP equilibrium constants,  $K_{\text{ATRP}}$ , were determined for a variety of Fe–ligand combinations. Illustrated in Figure 7.1 is an overview of the  $K_{\text{ATRP}}$  values for MMA (squares), styrene (circles) and BA (triangles), representing three main monomer classes, as well as for ethyl phenylacetate radicals (diamonds), which are produced from the EBrPA initiator. Each color refers to the indicated type of Fe catalyst.  $K_{\text{ATRP}}$  values represented by solid symbols were directly measured, whereas the open symbols refer to data estimated on the basis of relative bond strengths of the associated alkyl halides.<sup>44,201,233</sup> Values represented by dotted symbols also result from such estimates but refer to systems, where an interplay with OMRP or CRT needs to be considered.

Figure 7.1 demonstrates that the  $K_{\text{ATRP}}$  values for Fe catalysis cover a broad range. The same is true for Cu catalysis, for which  $K_{\text{ATRP}}$  values are included in Figure 7.1 as cross marks.<sup>35,103,169</sup> These numbers are mostly based on reported values<sup>103,169</sup> or were predicted from these values as described above.<sup>35,288</sup> Fe catalysts may be tuned as effectively as Cu catalysts for use in different ATRP procedures, e.g., normal, reverse, ICAR and ARGET ATRP, as well as with a wide range of monomers. In contrast to Cu, certain Fe catalysts operate without amine ligands and could thus be more amenable for acidic monomers.

The insights into the interplay between ATRP and OMRP as well as the methodologies applied in this work should be valuable in studying further Fe catalysts. It was recently found that the Fe-based catalase enzyme and a synthetic Fe/mesoheme catalyst may be used for

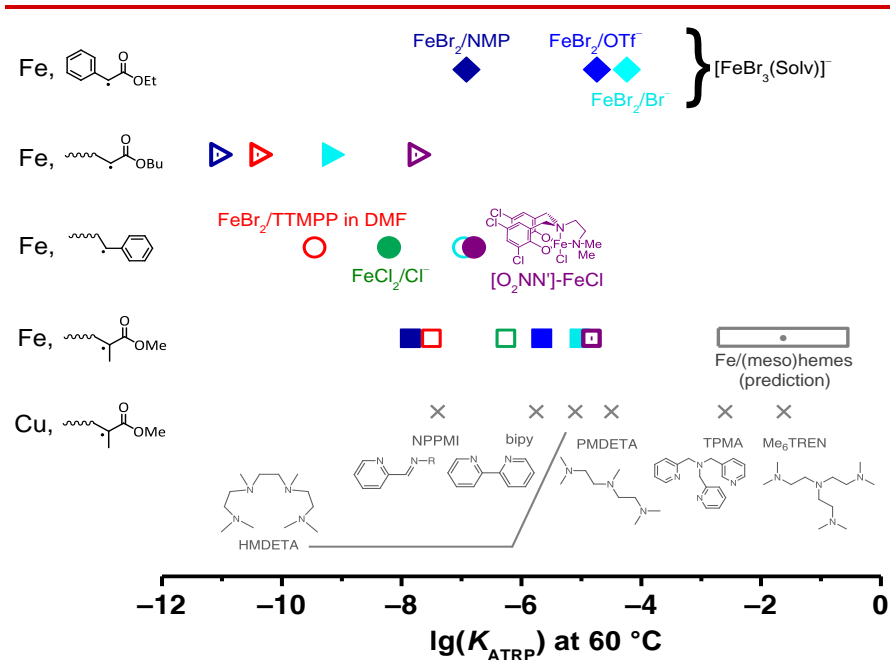


**Figure 7.1:**  $\lg(K_{\text{ATRP}})$  values at 60 °C for a selection of Fe–ligand systems and for MMA (squares), styrene (circles), BA (triangles) and for ethyl phenylacetate radicals (diamonds). Each color refers to the indicated type of Fe catalyst. Values in solid symbols were measured directly and those for open symbols estimated as described in the main text. The systems represented by dotted symbols operate via ATRP together with OMRP or CRT. Also,  $K_{\text{ATRP}}$  values for Cu catalysis are shown as cross marks.

controlled polymerization under bio-relevant conditions.<sup>266,289-291</sup> These catalysts allowed for the RDRP of water-soluble methacrylates, acrylates, and of *N*-isopropylacrylamide in aqueous phase under ambient conditions. It should be noted that Fe/heme systems may occur in various oxidation states<sup>292,293</sup> and that the kinetics in aqueous phase is particularly complex.<sup>294-297</sup> Nevertheless, these catalysts are projected to be very active, which seems to be partly due to an ATRP equilibrium with enhanced  $K_{\text{ATRP}}$ . The spectroscopic approaches applied in this work provide an essential framework for closer experimental inspection of such bio-relevant systems.



# 8

## Experimental

### 8.1 Chemicals

**Metal salts and solids.** FeBr<sub>2</sub> (ABCR, ultra dry, 99.995 % metals basis), FeBr<sub>3</sub> (ABCR, anhydrous, 99 %), FeCl<sub>2</sub> (anhydrous, 99.998 % metals basis, Aldrich), FeCl<sub>3</sub> (anhydrous, 98 %, ABCR), Fe(OTf)<sub>2</sub> (iron(II) trifluoromethanesulfonate, ABCR, 98 %), tetrabutylammonium trifluoromethanesulfonate (TBA-OTf, ABCR, 99 %), tetrabutylammonium bromide (TBA-Br, Fluka, ≥ 99.0 %), tris(2,4,6-trimethoxyphenyl)phosphine (TTMPP, ABCR, ≥ 97.0 %), triphenylphosphine (TPP, ABCR, 99 %), 1,3-bis(2,6-di-*i*-propylphenyl)-4,5-dihydroimidazol-2-ylidene (HIDipp, ABCR, 98 %), tris(2-pyridylmethyl)-amine (TPMA, Aldrich, 98 %) and 2,2,6,6-tetramethyl-1-piperidinyloxy (TEMPO, Aldrich, 99 %) were used as received. Tetrabutylammonium chloride (TBA-Cl, Aldrich, ≥ 97.0 %) was recrystallized from cold ethanol (Aldrich, p.a.) and dried under vacuum prior to use. Amine-*bis*(phenolate)iron complexes were prepared following literature procedures<sup>87,241,247,298-300</sup> and kindly provided by the Michael Shaver group at the University of Edinburgh. Tris([(4-methoxy-2,5-dimethyl)-2-pyridyl] methyl)amine (TPMA\*) was kindly provided by Kristin Schröder at the Carnegie Mellon University of Pittsburgh.<sup>210</sup>

**Initiators.** Ethyl  $\alpha$ -bromophenylacetate (EBrPA, ABCR, 97 %), methyl 2-bromo-*iso*-butyrate (MBriB, Fluka,  $\geq 99$  %), methyl 2-bromopropionate (MBrP, Fluka,  $\geq 97$  %), ethyl  $\alpha$ -chlorophenylacetate (ECIPA, Aldrich, 97 %), 1-phenyl-ethylchloride (PECl, ABCR, 98 %),  $\alpha$ -methyl-4-(methylmercapto)- $\alpha$ -morpholinopropiophenone (MMMP, Aldrich, 98 %) and 2,2'-azobis(4-methoxy-2,4-dimethyl valeronitrile) (V-70, Wako), 2,2'-azobis(2,4-dimethyl valeronitrile) (V-65, Wako) were used as received. 2,2'-Azobis(2-methylpropionitrile) (AIBN, Aldrich, 98 %) was recrystallized from cold ethanol (Aldrich, p.a.) and dried under vacuum prior to use. *Meso*-1,2-bis(1-phenylethyl)diazene (PEDA)<sup>301</sup> was kindly provided by Wibke Meiser at the University of Göttingen.

**Monomers and solvents.** 2-butanone (Acros, extra dry, 99.5 %), anisole (Aldrich, anhydrous, 99.7%), acetonitrile (MeCN, Acros, extra dry, over molecular sieve, 99.9 %), *N,N*-dimethylformamide (DMF, extra dry over molecular sieve, 99.8 %), tetrahydrofuran (THF, Aldrich, for HPLC,  $\geq 99.5$  %, inhibitor-free), *n*-heptane (Carl Roth,  $\geq 99$  %), *n*-hexane (Aldrich, p. a.), *n*-dodecane (Aldrich, anhydrous,  $\geq 99$  %), chloroform- $d_1$  (Deutero GmbH, 99.8 atom% D), DMF- $d_7$  (ABCR, 99.5 atom% D), acetonitrile- $d_3$  (Acros, 99.6 atom% D), and hydrochloric acid (Aldrich, 37 %) were used as received. Toluene (Aldrich, p. a.) was dried over molecular sieve (3 Å). Styrene (Aldrich,  $\geq 99.0$  %), methyl methacrylate (MMA, Fluka,  $> 99.0$  %), butyl acrylate (BA, Aldrich,  $\geq 99$  %), and *N*-methylpyrrolidin-2-one (Acros, ultra dry, 99.5 %) were passed through a column filled with Al<sub>2</sub>O<sub>3</sub> (Acros, neutral, Brockmann I, 50–200  $\mu$ m). 2-Ethylhexyl methacrylate (EHMA, Aldrich, 98 %) and *n*-dodecyl methacrylate (DMA, Fluka,  $> 95$  %) were treated with inhibitor remover (Aldrich).

**General considerations.** Monomers and solvents were degassed by several freeze–pump–thaw cycles. The solutions for Mössbauer, FT-NIR, and UV/VIS measurements were prepared under an argon atmosphere.

## 8.2 Spectroscopic Measurements

**High-Pressure Measurements.** The cells used for the FT-NIR measurements (IFS 88, Bruker) consisted of an MFA tube (modified fluoroalkoxy polymer, Reichelt GmbH&Co) closed on each side by a  $\text{CaF}_2$  window. A silicon diode, an indium antimonide (InSb), and a deuterated triglycine sulfate (DTGS) detector were used to obtain absorbance spectra for the range 15 800 to 1000  $\text{cm}^{-1}$ . The processing steps of the high-pressure experiments have been detailed elsewhere.<sup>104</sup> The spectra were analyzed via the OPUS 6.0 software (Bruker).

**Online FT-NIR spectroscopy** (IFS 66/S and IFS 88, Bruker) was carried out using a silicon diode (Si D510, Bruker) for detection between 9000 and 15 800  $\text{cm}^{-1}$ , a broad-band mercury cadmium telluride (MCT) below 10 000  $\text{cm}^{-1}$ , and a DTGS detector below 1000  $\text{cm}^{-1}$ .

**UV/VIS measurements** (Cary 300, Agilent) were carried out in sealed, thermostated quartz cells (e.g. 117-100-10-40/QS, Hellma). Measurements of  $k_{\text{act}}$  and  $k_{\text{deact}}$  were started by injecting 0.2 mL of a solution containing the initiator, e.g., 5 to 6 mM EBrPA, into 1.8 mL of a solution containing 0.5 to 1.5 mM  $\text{FeBr}_2$ , with or without added tetrabutylammonium bromide, (TBA-Br). Some experiments were carried out via stopped-flow injection procedures.<sup>227</sup>

**Samples for Mössbauer spectroscopy** were flash-frozen in liquid nitrogen. The spectra were obtained with a  $^{57}\text{Co}$  source embedded in a Rh matrix using an alternating constant acceleration Wissel Mössbauer spectrometer operated in the transmission mode and equipped with a closed-cycle helium cryostat (SHI 850, Janis). Isomer shifts are given relative to iron metal at ambient temperature. Symmetric Lorentzian doublets have been fitted to the zero-field spectra using the Mfit program.<sup>302</sup>

**EPR measurements** were performed on a Bruker EPR CW/transient spectrometer Elexsys-II 500T. The ER 41122SHQE-LC cavity (Bruker) was equipped with a grid through which the sample was irradiated by a

XeF laser (LPX 210 iCC, Lambda Physik) at 351 nm with about 60 mJ per pulse. The EPR spectrometer and the laser source were synchronized by a Quantum Composers 9314 pulse generator (Scientific Instruments). Temperature control was achieved via an ER 4131VT unit (Bruker) by purging the sample cavity with nitrogen. Experimental parameters, e.g., modulation amplitude and microwave energy, were optimized beforehand. Prior to the SP-PLP-EPR experiment at fixed magnetic field, the full EPR spectrum was recorded under pseudo-stationary conditions using a laser-pulse repetition rate of 20 Hz to identify the appropriate field position for time-resolved detection. To enhance signal-to-noise quality, several individual  $c_R(t)$  traces were measured at time intervals of up to 10 s and averaged. EPR intensity has been converted into absolute radical concentration by calibration against TEMPO as detailed elsewhere.<sup>92,177</sup>

**SEC Analysis.** Molar-mass distributions were determined with an SEC device consisting of an Agilent 1260 ALS G1329B autosampler, an Agilent 1260 Infinity ISO pump G1310B, three columns (PSS-SDV,  $8 \times 300$  mm each, particle diameter  $5 \mu\text{m}$ , pore sizes of  $10^6$ ,  $10^5$ , and  $10^3 \text{ \AA}$ , respectively), an Agilent 1260 refractive-index (RI) detector G1362A, and tetrahydrofuran (THF) at  $35 \text{ }^\circ\text{C}$  as the eluent at a flow rate of  $1 \text{ mL min}^{-1}$ . The setup was calibrated against PMMA and PS standards of narrow dispersity from Polymer Standard Services (PSS) with molar masses ranging from 800 to  $2\,000\,000 \text{ g mol}^{-1}$ .

**NMR spectra** (Avance DPX 300, Bruker) were recorded at ambient temperature and frequencies of 121.49 MHz ( $^{31}\text{P}$ ) and 300.13 MHz ( $^1\text{H}$ ). The spectra were calibrated against 85% phosphoric acid ( $^{31}\text{P}$ ) and tetramethylsilane ( $^1\text{H}$ ) as external standards and against the residual-proton signals of the deuterated solvent. A flip angle of  $30^\circ$  and a relaxation delay of 10 s were applied to measure polymer-containing samples.

**Determination of  $K_{\text{ATRP}}$  during MMA Polymerization** (Example): Dry NMP was degassed by repetitive freeze-pump-thaw cycles with a high-vacuum pump (Edwards, EXC 120).  $\text{FeBr}_2$  was added under an argon atmosphere. A second stock solution of the initiator EBrPA in MMA was prepared in the same way. The concentration of reactants in

the stock solutions and the relative amounts of the two solutions were chosen such as to obtain a reaction mixture composed of 23.4 mM FeBr<sub>2</sub> and 93.8 mM EBrPA in MMA/NMP (97/3 vol%), of 53.1 mM FeBr<sub>2</sub> and 79.8 mM EBrPA in MMA/NMP (85/15 vol%), of 62.5 mM FeBr<sub>2</sub> and 62.5 mM EBrPA in MMA with either 33 vol% or 66 vol% NMP, and of 33.8 mM FeBr<sub>2</sub> and 33.8 mM EBrPA in MMA/NMP (10/90 vol%). Additional processing steps and the two high-pressure devices, which differ in optical path length, have been detailed elsewhere.<sup>104,166</sup> Polymerization was stopped by rapid cooling to ambient temperature and pressure. The reaction mixture was subsequently passed through a column filled with neutral Al<sub>2</sub>O<sub>3</sub> to remove the iron catalyst. Residual monomer was evaporated under reduced pressure and the residual crude polymer analyzed by SEC.

**Determination of  $K_{\text{model}}$  for Monomer-Free Model Systems**  
(Example): Dry NMP was used for preparing a stock solution of FeBr<sub>2</sub> (150 to 300 mM) under an argon atmosphere. Similarly, a second stock solution of poly(MMA)-Br (7.47 to 15.0 mM) in either NMP, toluene or 2-butanone was prepared. The reaction was started by combining both solutions such that a solvent ratio between 15 and 100 vol% NMP was reached.

### 8.3 Synthesis of Poly(MMA)-Br via ICAR ATRP

A solution of MMA (83 mL), THF (42 mL), EBrPA (1.37 g, 5.64 mmol), FeBr<sub>3</sub> (22.2 mg, 75.1 μmol) and TBA-Br (48.4 mg, 150 μmol) was prepared under an argon atmosphere. The reaction was started by addition of AIBN (46.3 mg, 282 μmol). The initial molar ratio of reagents was [MMA]<sub>0</sub> : [EBrPA]<sub>0</sub> : [FeBr<sub>3</sub>]<sub>0</sub> : [TBABr]<sub>0</sub> : [AIBN]<sub>0</sub> = 138 : 1.00 : 0.01 : 0.02 : 0.03. The reaction mixture was heated to 65 °C and polymerized for 20.5 h up to a molar mass of  $M_n = 8050 \text{ g mol}^{-1}$  as determined by SEC. The crude reaction mixture was passed through a column filled with neutral Al<sub>2</sub>O<sub>3</sub>. The solvents were subsequently removed under reduced pressure and the residual polymer dissolved in toluene. The purified poly(MMA)-Br macroinitiator was obtained as a white powder after precipitation in *n*-hexane.

## 8.4 High-Pressure Equipment

Figure 8.1 illustrates the scheme of the high-pressure (HP) equipment for pressures up to 7 kbar.<sup>166</sup> Pressurization is performed in a stepwise fashion via an air-driven pump and two syringe-type pumps. The pressurizing medium is *n*-heptane or *n*-dodecane. The autoclave body consists of the nickel-based alloy RGT 601 (Figure 8.2), which has also been used for the construction of HP optical cells operated up to 3 kbar.<sup>167</sup> The essential difference between the components for experiments up to 7 kbar and the 3 kbar equipment is the significantly higher ratio of outer and inner diameter of the steel parts for 7 kbar. The equipment may be used in the temperature range 25 to 300 °C. The autoclave (Figure 8.2) is closed by a central bolt 2 on either side, which presses a steel ram 3 against the cell body. A sapphire window 4 is sealed against the ram. The probing light is transferred to the autoclave and back to the FT instrument by flexible fiber optics together with an optical adaptor 1. Via two borings, 7 and 8, at right angle to the cylindrical axis of the autoclave, the internal volume may be charged with the pressure-transmitting fluid (see above) and a sheathed thermocouple may be introduced into the internal cell volume.<sup>303</sup>

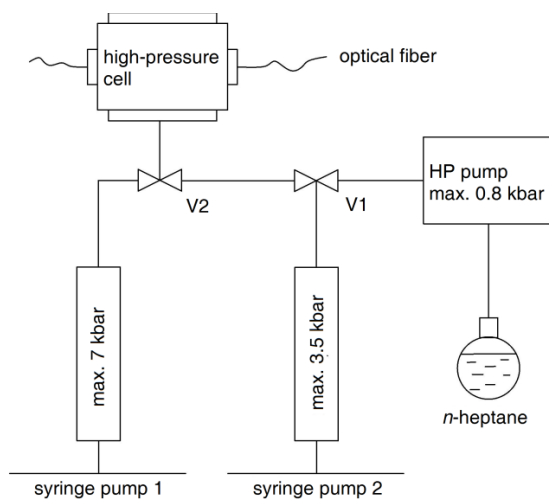


**Figure 8.1:** Schematic view of the setup for experiments up to 7 kbar with spectroscopic control.<sup>166</sup>

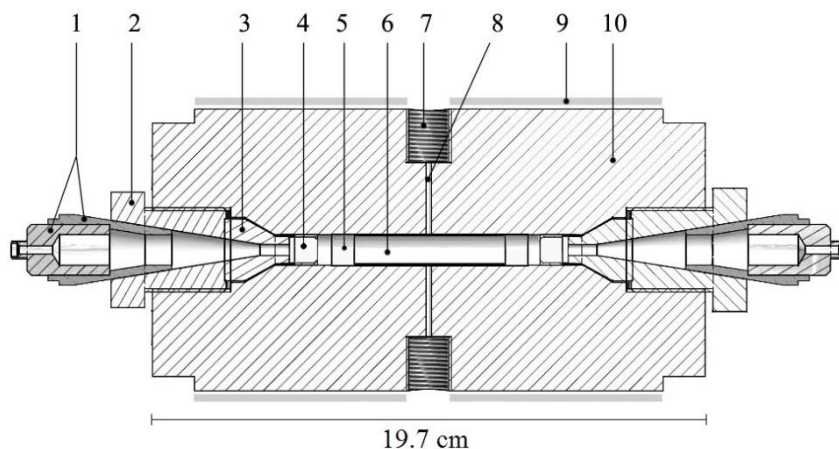


**Figure 8.2:** Cross section of the 7 kbar optical cell: (1) optical adaptor, (2) central bolt, (3) steel ram (4) sapphire window, (5) quartz window, (6) internal cell, (7) and (8) borings, (9) heating jacket, (10) cell body.<sup>166</sup>

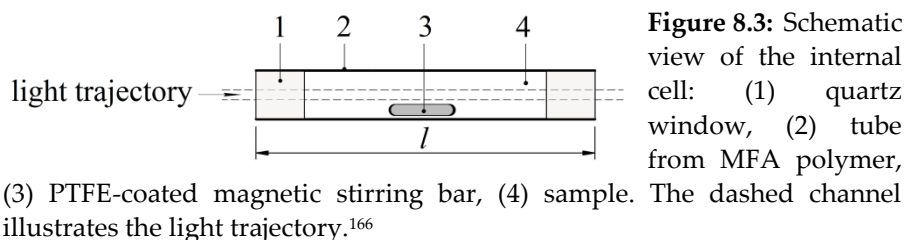


**Figure 8.3:** Schematic view of the internal cell: (1) quartz window, (2) tube from MFA polymer, (3) PTFE-coated magnetic stirring bar, (4) sample. The dashed channel illustrates the light trajectory.<sup>166</sup>

**Internal cell.**<sup>166</sup> The reaction mixture is contained in an internal cell of variable volume (max. 4 mL), which avoids catalytic action of the stainless steel walls and largely facilitates experimental operation. The internal cell consists of an MFA tube (modified fluoroalkoxy polymer, Reichelt GmbH&Co) of max. 82 mm length and 8.5 and 10.5 mm inner and outer diameter, respectively. The tube is closed on each side with a tightly fitting quartz window (Figure 8.3). The MFA tube ensures better gas impermeability than poly(tetrafluoroethylene) (PTFE), in particular at pressures above 1 kbar. A magnetic stir bar (MS) is positioned inside such that it rotates outside the optical light path. The stir bar is driven by a large magnet placed below the high-pressure cell.





## Appendix

### A Additional Figures, Tables, and Schemes

**Table S1:** Reduction rate and reduction efficiency for the indicated Cu and Fe complexes with different reducing agents at ambient conditions.

Metal/Ligand	Solvent	Reducing Agent	Reduction Rate
CuBr <sub>2</sub>	H <sub>2</sub> O	ascH <sub>2</sub>	Instant
CuBr <sub>2</sub> /bpy	H <sub>2</sub> O	ascH <sub>2</sub>	Instant
CuBr <sub>2</sub> /TPMA	MeCN/H <sub>2</sub> O	ascH <sub>2</sub>	Slow/Small Conv.
CuBr <sub>2</sub> /TPMA	H <sub>2</sub> O	Na <sub>2</sub> S <sub>2</sub> O <sub>4</sub>	Instant
Fe <sup>III</sup> /mesoheme	H <sub>2</sub> O/OEOMA	ascH <sub>2</sub>	Slow/Small Conv.
Fe <sup>III</sup> /mesoheme	H <sub>2</sub> O/OEOMA	Na <sub>2</sub> S <sub>2</sub> O <sub>4</sub>	Instant
Fe <sup>III</sup> /ABP	anisole	ascH <sub>2</sub> or NADH*	Slow

\*heterogeneous solution

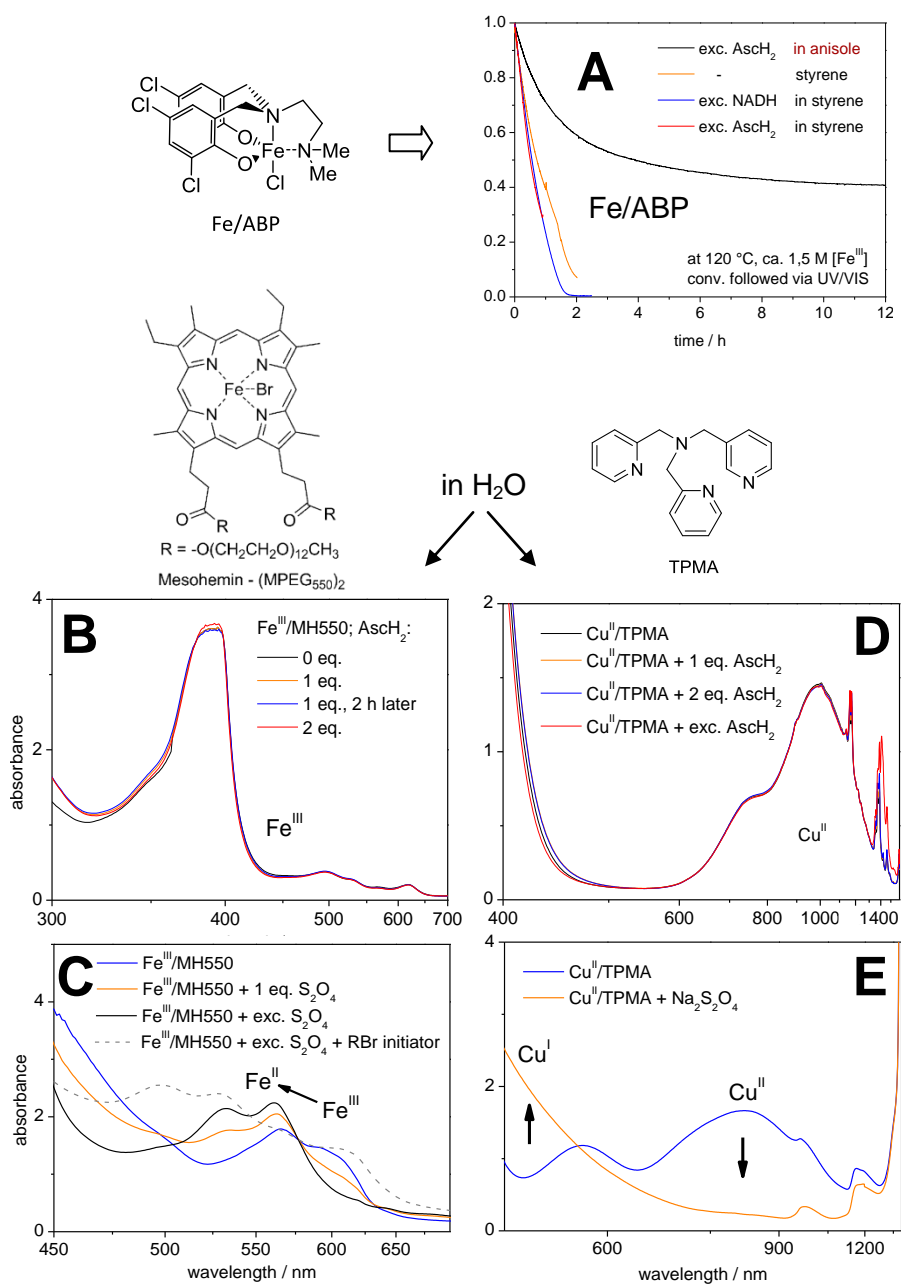


**Figure S1:** Reactions of the indicated Fe and Cu complexes with different reducing agents were monitored via UV/VIS spectroscopy.

(A)  $[\text{Fe}^{\text{III}}]_{\text{rel}}$  vs time for the reaction of amine-*bis*(phenolate)iron(III) chloride with  $\text{ascH}_2$  in anisole at 120 °C, and with  $\text{ascH}_2$  and NADH in styrene. Moreover, the reduction of  $\text{Fe}^{\text{III}}$  in styrene, which occurs in the absence of any external reducing agent, is due to the reaction with styrene radicals produced via self-initiation<sup>287</sup> at 120 °C. (B) Reaction of an  $\text{Fe}^{\text{III}}$ /mesohemin complex, MH 550,<sup>266</sup> with different amounts of ascorbic acid,  $\text{ascH}_2$  at 25 °C. Further spectra for the reduction by  $\text{S}_2\text{O}_4^{2-}$  are shown in (C). (D) Reaction of  $\text{Cu}^{\text{II}}$ /TPMA with different amounts of  $\text{ascH}_2$  at 25 °C. Further spectra for the reduction by  $\text{S}_2\text{O}_4^{2-}$  are shown in (E). The illustrated spectra indicate that reduction rates and efficiencies vary significantly: Less active ATRP catalysts such as  $\text{Cu}^{\text{II}}$ /bpy (cf. Table S1) are quickly reduced by  $\text{ascH}_2$ , whereas only a minor fraction of more active catalysts such as  $\text{Cu}^{\text{II}}$ /TPMA is reduced, since their redox potential is lower and thus closer to the one of  $\text{ascH}_2$ .<sup>35,44</sup> Similarly, only a minor fraction of the  $\text{Fe}^{\text{III}}$ /mesohemin complex is reduced. The reduction of amine-*bis*-(phenolate)iron(III) chloride by  $\text{ascH}_2$  and NADH is very slow. However,  $\text{Na}_2\text{S}_2\text{O}_4$ , which decomposes readily into  $\text{SO}_2\cdot^-$  radicals in aqueous phase, is able to quickly reduce  $\text{Cu}^{\text{II}}$ /TPMA and  $\text{Fe}^{\text{III}}$ /mesohemin. The latter is oxidized back to  $\text{Fe}^{\text{III}}$  as soon as R-Br is added.

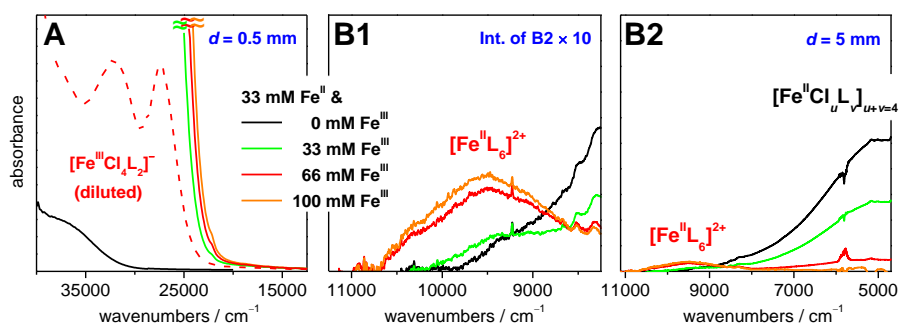


**Figure S2:** Spectra of 33 mM  $\text{FeCl}_2$  dissolved in NMP with different levels of  $\text{FeCl}_3$  ranging from 0 to 100 mM were recorded between 4700 and 40 000  $\text{cm}^{-1}$  via (A) UV/VIS and (B) FT-NIR spectroscopy. Full detection of  $[\text{Fe}^{\text{III}}\text{Cl}_4]^-$  above 25 000  $\text{cm}^{-1}$  is possible with diluted solutions as illustrated in Figure S2A. Due to the halogen transfer from  $[\text{Fe}^{\text{II}}\text{Cl}_i\text{L}_v]$  to  $[\text{Fe}^{\text{III}}\text{Cl}_4]^-$ ,  $[\text{Fe}^{\text{II}}\text{Cl}_i\text{L}_v]$  (Figure S2B-2) transforms into  $[\text{Fe}^{\text{III}}\text{L}_6]^{2+}$  (Figure S2B-1&2). In agreement with the stoichiometric expectation, the transfer is essentially complete when more than 2 equiv  $\text{FeCl}_3$  are added (Figure S2B).

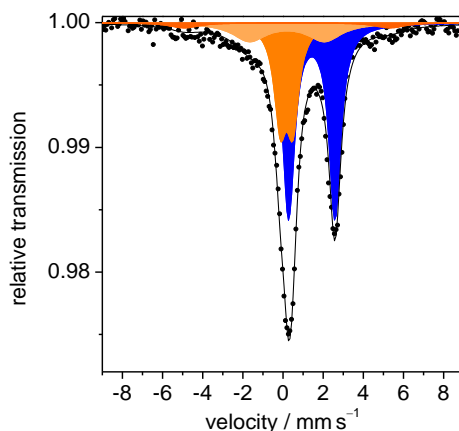


**Figure S3:**  $^{57}\text{Fe}$  Mössbauer spectrum of a frozen NMP solution of 150 mM  $\text{FeCl}_3$  and 50 mM  $\text{FeCl}_2$  measured at 6 K (full black symbols). Three functions representing  $\text{Fe}^{\text{III}}$  species (orange colors, see Table S2) with  $[\text{Fe}^{\text{III}}\text{Cl}_4]^-$  being the major  $\text{Fe}^{\text{III}}$  component and one function representing  $[\text{FeL}_6]^{2+}$  (blue) have been used for fitting the experimental data (cf. Table S2).

**Table S2:** Mössbauer parameters of  $\text{Fe}^{\text{III}}$  species and of  $[\text{Fe}^{\text{II}}\text{L}_6]^{2+}$  deduced from the spectrum in Figure S3;  $\delta$ ,  $\Delta E_Q$ , and  $\Gamma$  refer to isomer shift, quadrupole splitting, and line width, respectively.

entry	fitted species	$\delta /$ $\text{mm s}^{-1}$	$\Delta E_Q /$ $\text{mm s}^{-1}$	$\Gamma /$ $\text{mm s}^{-1}$	area / %
1	$\text{Fe}^{\text{III}}$	0.18	0.63	0.73	27
		0.20 <sup>[a]</sup>	3.74	2.06	14
		0.20 <sup>[a]</sup>	10.24	1.88	4
2	$[\text{Fe}^{\text{II}}\text{L}_6]^{2+}$	1.43	2.31	0.72	55

<sup>[a]</sup> not optimized.

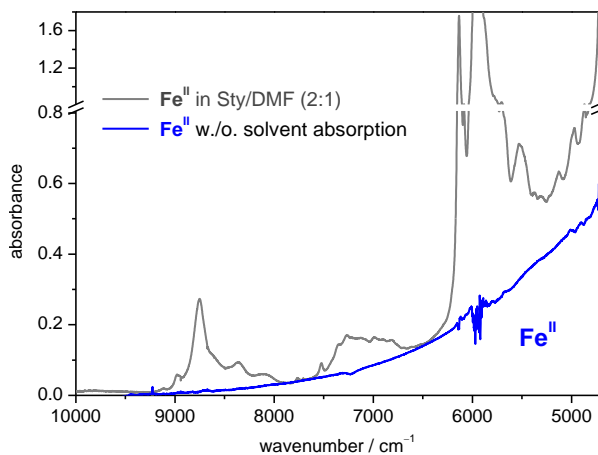


**Figure S4:** NIR absorbance spectra recorded during an ATRP of styrene at 100 °C in solution of DMF (33 vol%). The reduction of FeBr<sub>3</sub> (29.1 mM) by TTMPP (29.1 mM) results in the formation of the Fe<sup>II</sup> complex. The associated half-band is given by the blue curve. Solvent absorption was subtracted from the overall spectrum (gray line) via a reference spectrum measured at identical composition but without Fe. The position of the NIR absorbance is indicative of a tetrahedrally coordinated Fe<sup>II</sup> complex.

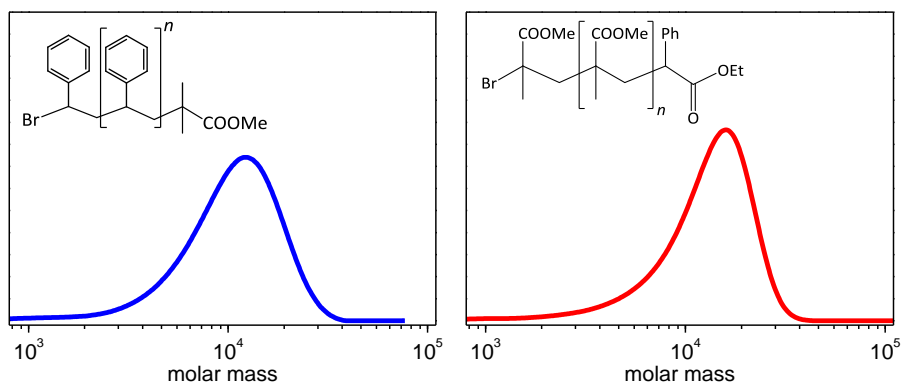


**Figure S5:** Molar-mass distributions of polystyrene (left) and poly(methyl methacrylate) (right). The polymers were obtained via the TTMPP-assisted ATRPs described in chapter 4.2.3.

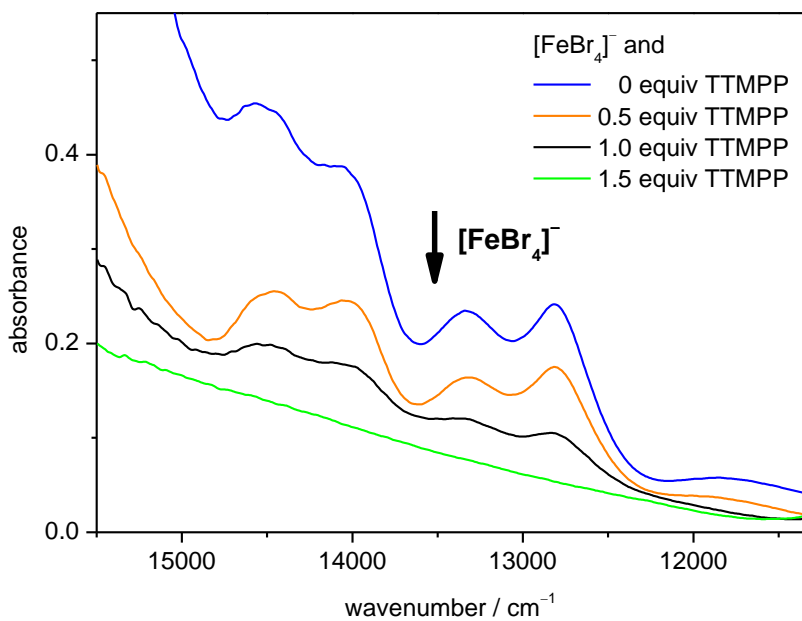


**Figure S6:** NIR spectra of  $[\text{FeBr}_4]^-$  measured for different amounts of TTMPP in solution of DMF at 25 °C. The decrease in the  $[\text{FeBr}_4]^-$  absorbance between 15 000 and 11 500  $\text{cm}^{-1}$  illustrates the reduction of  $[\text{FeBr}_4]^-$  upon progressively adding TTMPP.

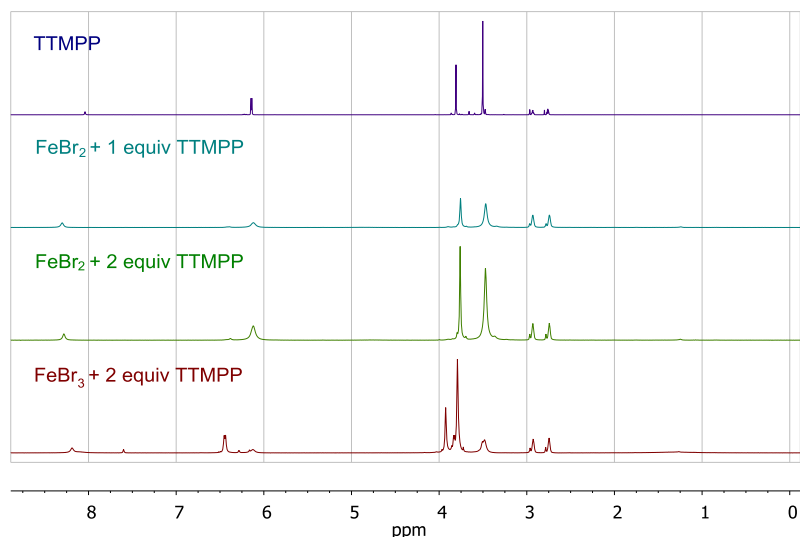


**Figure S7:** <sup>1</sup>H-NMR spectra for solutions of TTMPP, of TTMPP and FeBr<sub>2</sub>, and of TTMPP and FeBr<sub>3</sub> in DMF-d<sub>7</sub>. The upper spectrum was recorded in the absence of Fe. The signals between 3.4 and 7 ppm are associated with TTMPP. The signals below 3 ppm and above 8 ppm are due to the residual protons in DMF-d<sub>7</sub>. Only weak signals of TTMPP are observed for the equimolar solution of Fe<sup>II</sup> and TTMPP due to the formation of the paramagnetic Fe<sup>II</sup>/TTMPP complex, which is not seen in the NMR spectrum. The presence of this Fe<sup>II</sup>/TTMPP complex is, however, reflected in an increased line width of the TTMPP signals. The signals increase in intensity when 2 equiv TTMPP relative to FeBr<sub>2</sub> are present indicating that only one TTMPP molecule is coordinated to Fe<sup>II</sup>. FeBr<sub>3</sub> is reduced in the presence of 2 equiv TTMPP such that the associated signal for TTMPP-Br<sup>+</sup> additionally appears (bottom spectrum).

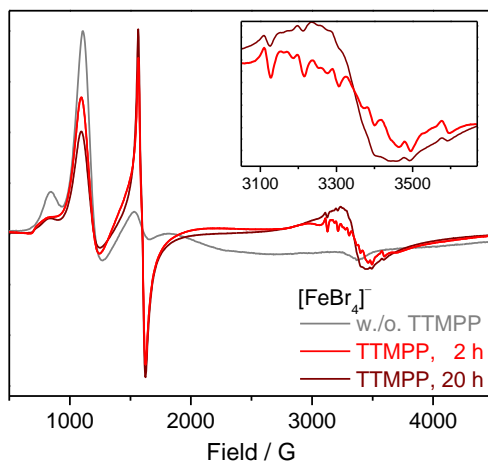


**Figure S8:** EPR spectra recorded during the reaction of [FeBr<sub>4</sub>][TBA] with TTMPP in DMF at 100 °C. For each measurement, the samples were flash-frozen to 140 K. The initial spectrum of [FeBr<sub>4</sub>][TBA] was recorded before adding TTMPP. Two further spectra were recorded after 2 and 20 h, respectively. All spectra were scaled by their maximum, which occurs either at 1100 or 1560 G. The quantitative analysis of Fe<sup>III</sup> concentration vs time is performed via NIR as described in chapter 4.2.3. The difference in the relative intensities at around 1100 and 1560 G may be an effect of the molecular arrangement in the flash-frozen samples. Also, TTMPP may potentially interact with Fe<sup>III</sup> at such low temperature thus affecting the molecular symmetry.

Illustrated in the insert is the hyperfine structure observed between 3100 and 3600 G, which is underlying the broad absorption of Fe<sup>III</sup>. This hyperfine structure and its relative changes suggest the occurrence of a TTMPP-Br<sup>•</sup> intermediate. The complex hyperfine structure may result from the nuclear spins of <sup>31</sup>P ( $I = 1/2$ ), <sup>79</sup>Br ( $I = 3/2$ ), and <sup>81</sup>Br ( $I = 3/2$ ).<sup>237,238</sup>



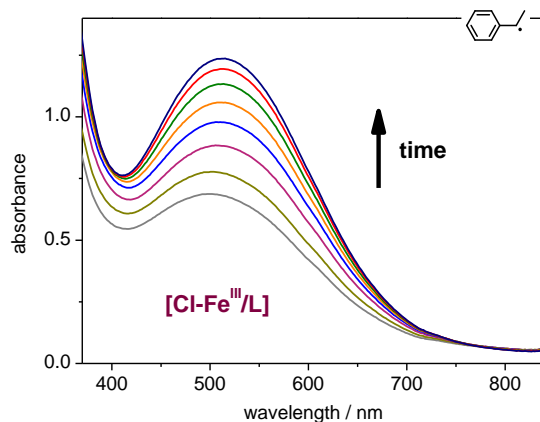


**Figure S9:** Increase in the absorbance of  $[\text{Cl-Fe}^{\text{III}}/\text{L}]$  with time during ATRP of styrene at  $100\text{ }^{\circ}\text{C}$  in anisole (25 vol%) with the following initial molar ratio of reagents: Sty : PECl :  $\text{Fe}^{\text{II}}/\text{L}$  :  $\text{Cl-Fe}^{\text{III}}/\text{L}$  = 100 : 1.00 : 0.17 : 0.04. The optical path length was 0.5 mm. ATRP was carried out up to 50 % monomer conversion.

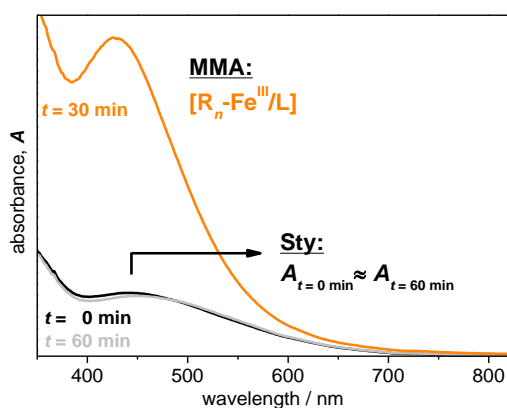


**Figure S10:**  $\text{R}_n\text{-Fe}^{\text{III}}/\text{L}$  is formed via the reaction of 10 mM  $\text{Fe}^{\text{II}}/\text{L}$  with MMA-type radicals in MMA polymerization initiated by V-70 (10 mM) at  $70\text{ }^{\circ}\text{C}$ . No such species is observed in styrene polymerization with 10 mM  $\text{Fe}^{\text{II}}/\text{L}$  and 38 mM PEDDA at  $110\text{ }^{\circ}\text{C}$ . After 60 min, which is close to the half life of PEDDA at  $110\text{ }^{\circ}\text{C}$ , no marked change in VIS absorbance occurred.

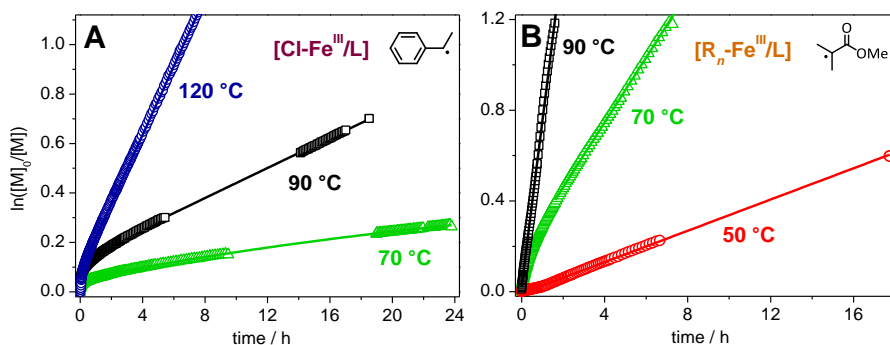


**Figure S11:** (A)  $\ln([M]_0/[M])$  vs time for the reverse ATRP of styrene at 70, 90, and 120 °C started with 14.5 mM Cl-Fe<sup>III</sup>/L and 5.8 mM of the thermal initiator. (B)  $\ln([M]_0/[M])$  vs time for the  $R_n$ -Fe<sup>III</sup>/L-induced OMRP of MMA at 50, 70, and 90 °C.  $R_n$ -Fe<sup>III</sup>/L was prepared by reaction of Fe<sup>II</sup>/L (50 mM, i.e., 25 mM of the Fe<sup>II</sup> dimer shown in chapter 5.1) and V-70 (250 mM) in solution of MMA/anisole (1:3, v/v) at 70–80 °C. The formation of  $R_n$ -Fe<sup>III</sup>/L was monitored via online VIS spectroscopy.  $R_n$ -Fe<sup>III</sup>/L is formed quickly due to the excess of the thermal initiator. After 1 h, V-70 is depleted (< ppm level). The solution now contains  $R_n$ -Fe<sup>III</sup>/L as well as a minor amount of the Fe<sup>II</sup>/L precursor and also traces of dead polymer, which was produced during the process. The reaction mixture was diluted to yield 10 mM solutions of total Fe at a composition of MMA/anisole = 2:1 (v/v). The solution was split into three parts for the polymerizations at 50, 70, and 90 °C to yield identical amounts of  $R_n$ -Fe<sup>III</sup>/L and Fe<sup>II</sup>/L in all cases. OMRPs were initiated by the decomposition of  $R_n$ -Fe<sup>III</sup>/L with no further source of radicals being present.

**Table S3:** Mössbauer parameters from Figure 5.4;  $\delta$ ,  $\Delta E_Q$ , and  $\Gamma$  refer to isomer shift, quadrupole splitting, and line width, respectively. The spectra were measured at 80 K.

Entry	Spectrum in Fig. 4	Solvent	Fitted species	$\delta / \rightarrow$	$\Delta E_Q / \text{mm s}^{-1}$	$\Gamma / \leftarrow$	Rel. Conc. /
1	A	-	Fe <sup>II</sup> /L	1.09	1.99	0.29	80
			Fe <sup>II</sup>	1.16	2.31	0.35	20
2	B	Sty	Cl-Fe <sup>III</sup> /L	0.49	1.12	0.77	100
3	C	Sty	Fe <sup>II</sup> /L	1.08	1.96	0.27	76
			Cl-Fe <sup>III</sup> /L	0.43	0.84	0.33	20
			Fe <sup>II</sup>	1.08	2.86	0.27	4
4	D	MMA /	R <sub>n</sub> -Fe <sup>III</sup> /L	0.45	1.69	0.28	80
		Anisole	Cl-Fe <sup>III</sup> /L	0.46	0.91	0.38	20
5	E	MMA /	R <sub>n</sub> -Fe <sup>III</sup> /L	0.46	1.69	0.30	82
		Anisole	Fe <sup>II</sup> /L	1.19	2.29	0.42	18
6	F	MMA /	R <sub>n</sub> -Fe <sup>III</sup> /L	0.46	1.75	0.29	35
		Anisole	Cl-Fe <sup>III</sup> /L	0.51	0.82	0.60	65

<sup>[a]</sup> correlated to Fe<sup>II</sup>/L.

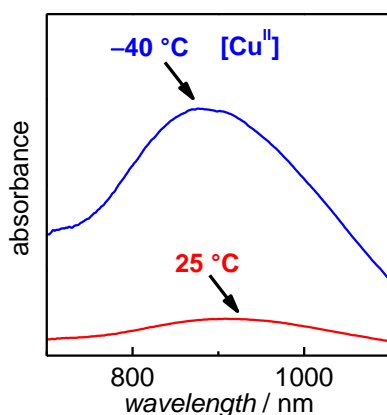


**Figure S12:** NIR measurement after reaction of 3.4 mM Cu<sup>II</sup>Br/TPMA with radicals generated by pulsed-laser application on a solution of BA/MeCN with MMMP as the initiator. The absorption is attributed to H-Cu<sup>II</sup>/TPMA and/or R-Cu<sup>II</sup>/TPMA complex, which is stable at -40 °C but readily decomposes upon heating to ambient temperature.

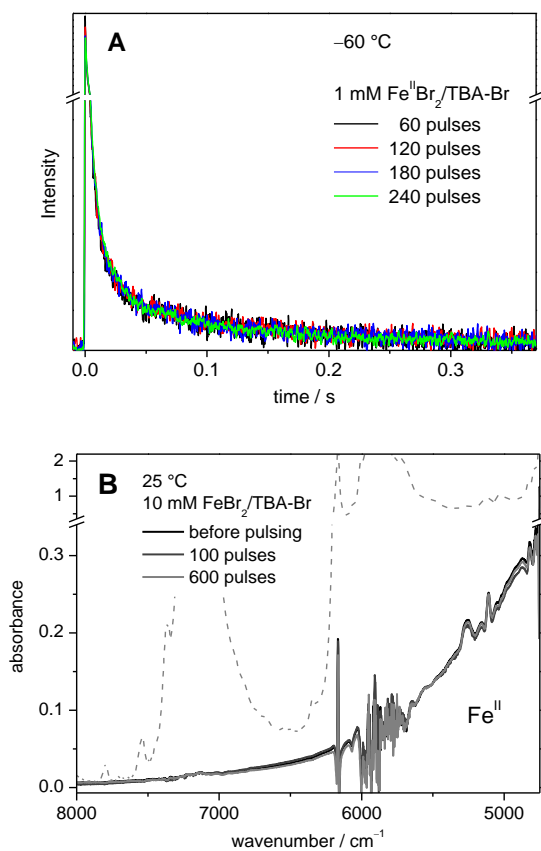
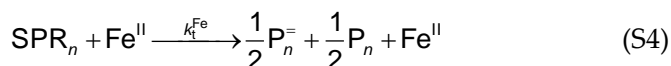
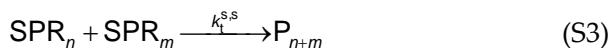
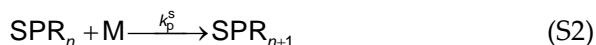


**Figure S13:** SP-PLP-EPR data for BA in solution of 2-butanone (15 vol%) with 1 mM FeBr<sub>2</sub>/TBA-Br at -60 °C (A) and NIR absorbance taken at 10 mM Fe<sup>II</sup> measured at 25 °C (B). Identical time-resolved EPR intensity of SPRs (A) and identical NIR absorption of Fe<sup>II</sup> (B) are observed after applying up to 600 pulses. The number of applied pulses corresponds to at least  $2.5 \times 10^{-3} \text{ molL}^{-1}$  of SPRs being produced, which is well above the Fe<sup>II</sup> concentration in this experiment (1 mM). The NIR absorption of the Fe<sup>II</sup> at 4700 cm<sup>-1</sup> is obtained by subtraction of the solvent absorption (dashed line) via reference spectra for the same solvent composition in the absence of Fe<sup>II</sup>.



**Scheme S1:** Reaction scheme for PREDICI<sup>®</sup> modeling of SP-PLP-EPR data for BA with backbiting being absent. The value of  $k_p = 980 \text{ Lmol}^{-1}\text{s}^{-1}$  was taken from literature,<sup>229</sup>  $I^{\bullet}$  was adjusted to experimental  $[SPR]_0$  in Figure 5.12 with  $k_{p,1}$  being assumed to be  $10k_p$ .  $k_t^{s,s}$  is calculated according to the composite model<sup>154</sup> with  $\alpha_s = 0.65$ ,  $\alpha_1 = 0.16$ ,  $i_c = 30$ , and  $k_t^{1,1} = (1.0 \pm 0.3) \times 10^8 \text{ Lmol}^{-1}\text{s}^{-1}$ .  $k_t^{Fe} = 2.3 \times 10^4 \text{ Lmol}^{-1}\text{s}^{-1}$  has been introduced as determined in this work.

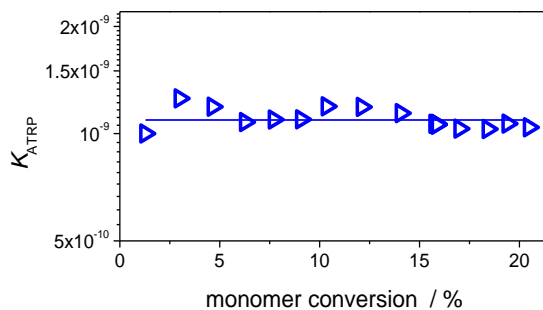


**Figure S14:**  $K_{ATRP}$  vs monomer conversion measured for ATRP at 75 °C with 17.7 mM  $FeBr_2$ , 17.7 mM TBA-Br, and 13.6 mM MBriB in solution of BA:2-butanone (1:1 v/v). The line represents the mean value of  $K_{ATRP} = 1.2 \times 10^{-9}$ .

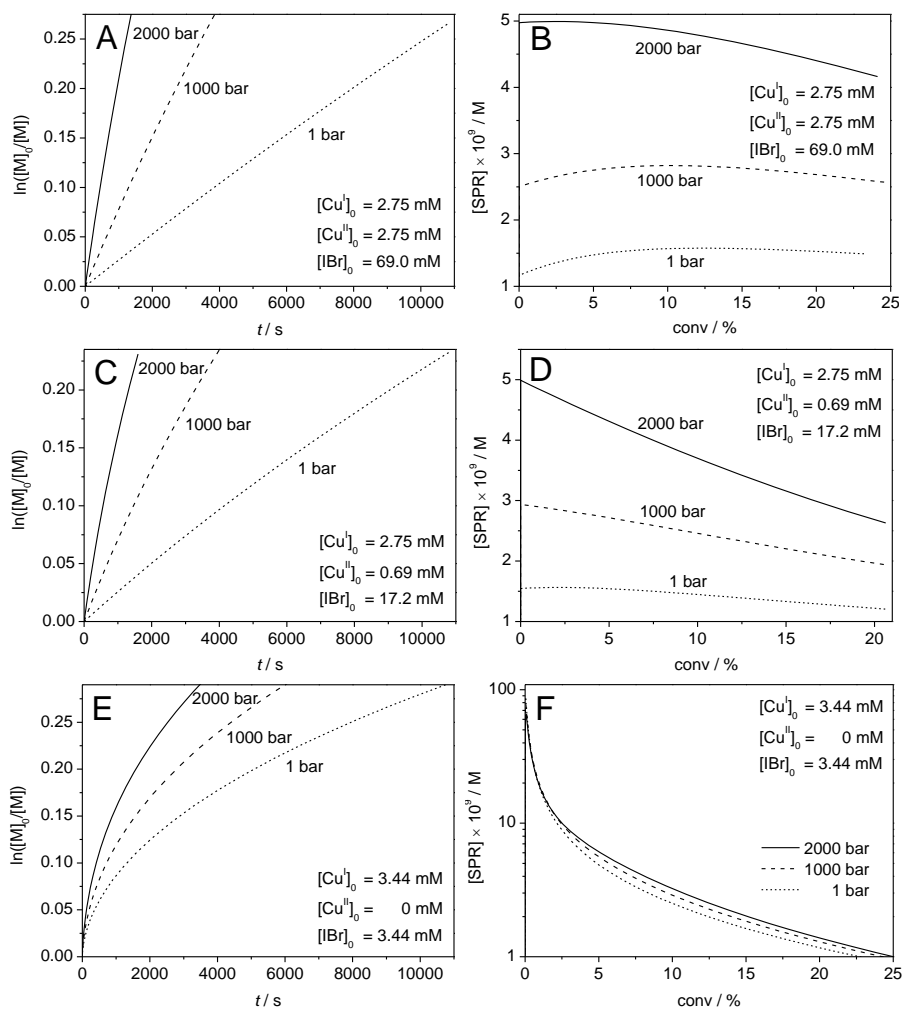


**Figure S15:** Predicted  $\ln([M]_0/[M])$  vs time traces (A, B, C) and SPR concentration vs time traces (B, D, F) for BA ATRP at 22 °C between 1 and 2000 bar in solution of 50 vol% MeCN.<sup>304</sup> The initial molar ratios of reactants were BA : Cu<sup>I</sup> : Cu<sup>II</sup> : MBrP = 50.0 : 0.04 : 0.04 : 1.00 (A, B), 200 : 0.16 : 0.04 : 1.00 (C, D), 1000 : 1.00 : 0 : 1.00 (E, F).

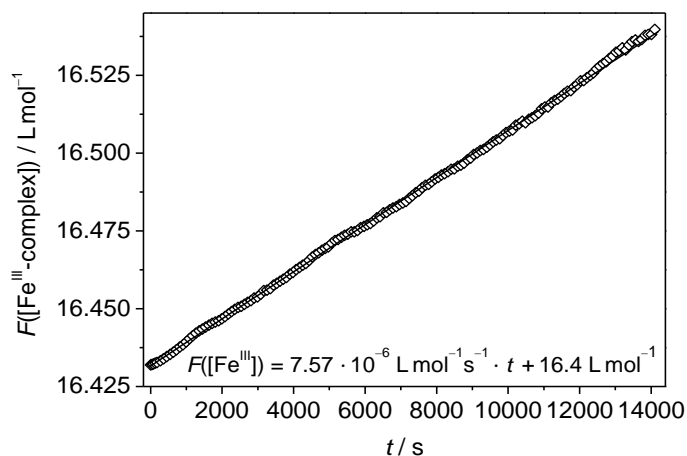


**Figure S16:** Plot of  $F([Y])$  vs time for the reaction of 10.0 mM FeBr<sub>2</sub> with 33.3 mM EBrPA in NMP at 60 °C and 1000 bar.

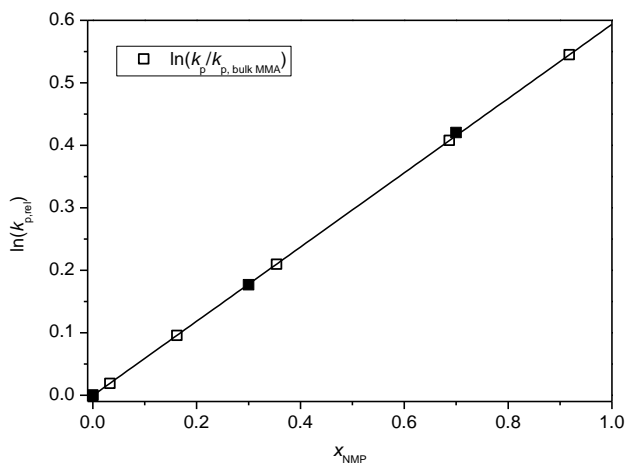


**Figure S17:**  $k_p$  values of MMA at 47.4 °C and ambient pressure as a function of NMP mole fraction,  $x_{\text{NMP}}$ , relative to  $k_p$  of MMA bulk polymerization. Filled symbols indicate measured literature data,<sup>230</sup> whereas the open symbols are from interpolation or extrapolation.

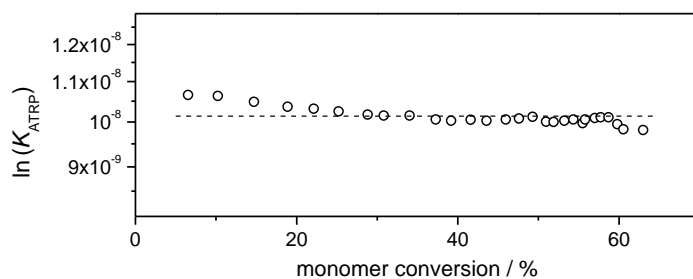
**Table S4:** Estimated  $k_p$  (in  $\text{L mol}^{-1} \text{s}^{-1}$ ) for MMA in mixtures with NMP (cf. Figure S17) as a function of both temperature,  $T$ , (at 1 bar) and pressure,  $p$ , (at 60 °C), respectively. Estimates between 50 and 75 °C are based on  $E_A(k_p) = 22.2 \text{ kJ mol}^{-1,98,305}$   $\Delta V^\ddagger(k_p) = (-16.7 \pm 1.1) \text{ cm}^3 \text{ mol}^{-1}$  [3] is assumed to be independent of NMP concentration and was used to estimate pressure-dependent  $k_p$  values.

$T$ ( $p = 1 \text{ bar}$ ) / °C	mol% NMP					
	0	3.3	16.2	35.4	68.7	91.8
50	618	631	681	763	930	1067
55	701	715	772	866	1055	1210
60	793	808	873	978	1192	1367
65	892	910	982	1101	1342	1539
70	1001	1021	1102	1235	1505	1727
75	1119	1142	1232	1381	1683	1931

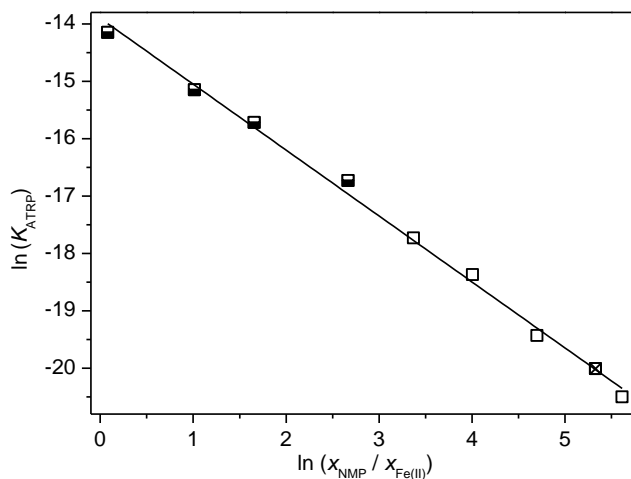
  

$p$ ( $T = 60 \text{ °C}$ ) / bar	mol% NMP					
	0	3.3	16.2	35.4	68.7	91.8
1	793	808	873	978	1192	1367
600	1138	1160	1252	1404	1711	1962
1000	1448	1477	1594	1787	2178	2498
1250	1684	1717	1854	2078	2532	2905
1500	1958	1997	2156	2416	2944	3378
2000	2647	2700	2915	3267	3981	4567
2400	3370	3436	3710	4158	5068	5813





**Figure S18:**  $K_{\text{ATRP}}$  vs. monomer conversion for ATRP of MMA in 35.4 mol% NMP with MMA : EBrPA :  $\text{Fe}^{\text{II}}$  = 100 : 1.00 : 1.00 at 60 °C and 2 000 bar. The dashed straight line indicates that  $K_{\text{ATRP}}$  remains almost constant up to ca. 64 % monomer conversion.



**Figure S19:**  $\ln(K_{\text{ATRP}})$  vs.  $\ln(x_{\text{NMP}} / x_{\text{Fe(II)}})$  ( $\square$ ) for iron-mediated MMA polymerization at 60 °C and 2 000 bar. Except for the logarithmic scale, the presentation is equivalent to Figure 6.14. Some data ( $\blacksquare$ ) have been obtained from MMA polymerization with 0.2 m TBA-OTf being added in order to ensure homogeneity of the solution.

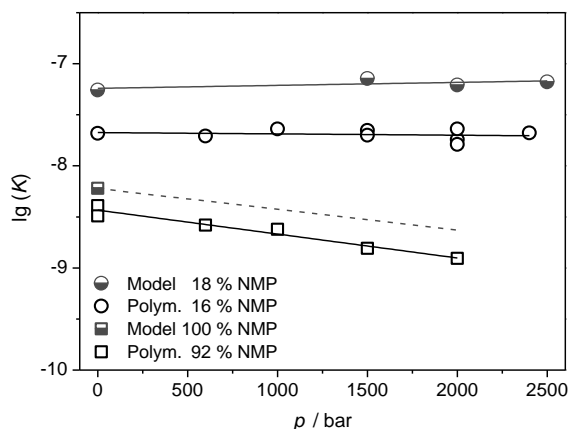


**Figure S20:** Pressure dependence of  $K_{\text{model}}$  in pure NMP ( $\blacksquare$ ) and in a mixture of NMP–2-butanone (18.5/81.5 mol%) ( $\bullet$ ). The associated  $K_{\text{ATRP}}$  values are given as open symbols. Straight lines were fitted to the data. The pressure dependence of  $K_{\text{model}}$  in pure NMP has been estimated based on  $\Delta_r V$  with EBrPA as the initiator. Chain-length dependent  $k_t$  values<sup>202</sup> required for the analysis of  $K_{\text{model}}$  were corrected for actual solvent viscosity<sup>200,203-209</sup> under high pressure.<sup>158,274</sup> It has been assumed that binary NMP–toluene mixtures exhibit the same variation of solvent viscosity as reported for NMP–ethyl benzene mixtures.<sup>208</sup> The pressure dependence of 2-butanone viscosity is adopted from the known variation of acetone viscosity with pressure.<sup>274</sup>

## B SP–PLP–EPR Measurement of Fe-CRT

$k_t^{\text{Fe}}$  via EPR Spectroscopy of SPRs. The decay in radical concentration vs time via Fe-CRT may be expressed by Equation S5.  $k_t^{\text{OM}}$  is the rate coefficient for termination of radicals,  $\text{R}^\bullet$ , via the organometallic R-Fe<sup>III</sup> intermediate.

$$-\frac{d[\text{R}^\bullet]}{dt} = k_{\text{add}} \cdot [\text{Fe}^{\text{II}}] \cdot [\text{R}] + k_t^{\text{OM}} \cdot [\text{R-Fe}^{\text{III}}] \cdot [\text{R}] + 2 \cdot k_t^{\text{ii}} \cdot [\text{R}^\bullet]^2 \quad (\text{S5})$$

The concentration of the R-Fe<sup>III</sup> intermediate becomes pseudo-stationary in case of fast Fe-CRT as shown by Equation S6, which is essentially equivalent to Equation 5.7 in chapter 5.2.2. The term for termination rate may be neglected toward lower radical concentration due to termination rate being second order in  $[\text{R}^\bullet]$ .

$$\frac{d[\text{R-Fe}^{\text{III}}]}{dt} \approx 0 = k_{\text{add}} \cdot [\text{Fe}^{\text{II}}] \cdot [\text{R}^\bullet] - k_t^{\text{OM}} \cdot [\text{R-Fe}^{\text{III}}] \cdot [\text{R}^\bullet] \quad (\text{S6a})$$

$$= \frac{d[\text{R}^\bullet]}{dt} + 2 \cdot k_{\text{add}} \cdot [\text{Fe}^{\text{II}}] \cdot [\text{R}^\bullet] \quad (\text{S6b})$$

In case of RT-OMRP being operative (Equation S7), the OMRP equilibrium  $K_{\text{OMRP}} = \frac{k_{\text{add}}}{k_{\text{dis}}} = \frac{[\text{R-Fe}^{\text{III}}]}{[\text{Fe}^{\text{II}}] \cdot [\text{R}^\bullet]}$  yields Equation S8 which, in contrast to the first-order Equations S5–6, is second order in  $[\text{R}^\bullet]$ .

$$-\frac{d[\text{R}^\bullet]}{dt} = k_{\text{add}} \cdot [\text{Fe}^{\text{II}}] \cdot [\text{R}^\bullet] - k_{\text{dis}} \cdot [\text{R-Fe}^{\text{III}}] + k_t^{\text{OM}} \cdot [\text{R-Fe}^{\text{III}}] \cdot [\text{R}^\bullet] \quad (\text{S7})$$

$$-\frac{d[\text{R}^\bullet]}{dt} = k_t^{\text{OM}} \cdot K_{\text{OMRP}} \cdot [\text{Fe}^{\text{II}}] \cdot [\text{R}^\bullet]^2 \quad (\text{S8})$$

**$k_t^{\text{Fe}}$  via EPR Spectroscopy of MCRs.** The backbiting reaction gives rise to two different kinds of radical species in BA polymerization, i.e., SPRs and MCRs. The MCR concentration increases toward higher temperature and reaches a sufficiently high level to be measured directly via EPR spectroscopy.<sup>154</sup>

To confirm the  $k_t^{\text{Fe}}$  values for BA polymerizations which were determined via SP–PLP–EPR measurement of SPR concentration,  $k_t^{\text{Fe}}$  may additionally be estimated via the analysis of the associated [MCR] vs time traces. Shown in Figure S21 are the [MCR] vs time traces for SP–PLP–EPR of BA at 50 °C with 1 to 10 mM Fe<sup>II</sup>. Also shown in Figure S21A is the [SPR] vs time trace for the reaction with 10 mM Fe<sup>II</sup>. The termination of SPRs with and without metal catalysis (not shown) is much faster for SPRs than for MCRs as may be seen from the rapid decrease of SPR concentration beyond EPR detection.

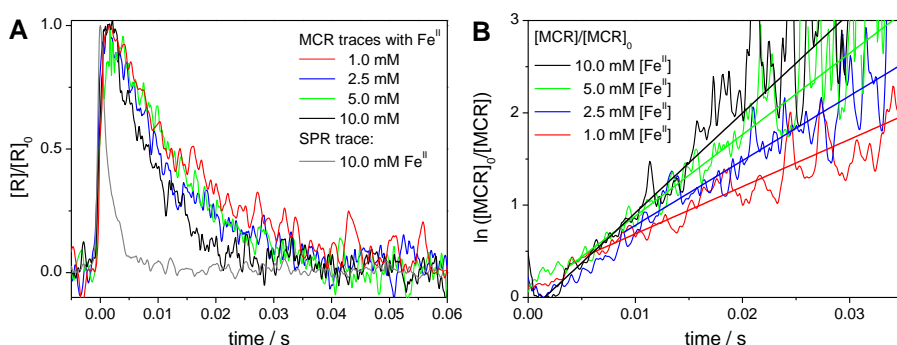


**Figure S21:**  $[R]/[R]_0$  (A) and  $\ln([R]_0/[R])$  (B) vs time for MCRs and SPRs during SP–PLP–EPR of BA at 50 °C in solution of 15 vol% 2-butanone measured at different levels of Fe<sup>II</sup>. Signal-to-noise ratio is lower for MCR than for SPR traces. Straight lines were fitted to the  $\ln([MCR]_0/[MCR])$  vs time data.

*Kinetic considerations.* After the initial rapid termination of SPRs, reaction rates equilibrate to yield a (nearly) constant ratio,  $C$ , of MCRs and SPRs (Eq. S9a). This occurs irrespective of the simultaneous decrease in both radical concentrations beyond EPR detection due to concurrent termination reactions. (Eq. S9b) applies as a consequence of eq. S6a.

$$\frac{[\text{MCR}]}{[\text{SPR}]} = C \quad (\text{S9a})$$

$$\frac{d \ln[\text{MCR}]}{d t} = \frac{d \ln[\text{SPR}]}{d t} + \ln C \quad (\text{S9b})$$

Due to the low SPR concentration at such equilibrium conditions, the rates of radical-radical termination for SPRs and MCRs, i.e.,  $R(k_t^{s,s})$ ,  $R(k_t^{s,t})$ , and  $R(k_t^{t,t})$ <sup>154</sup> are well below the rate of Fe-CRT, backbiting, and branching (given by  $R(k_t^{\text{Fe}})$ ,  $R(k_{\text{bb}})$ , and  $R(k_p^t)$ , respectively) (Eq. S10).

$$R(k_t^{s,s}), R(k_t^{s,t}), R(k_t^{t,t}) \ll R(k_t^{\text{Fe}}), R(k_{\text{bb}}), R(k_p^t) \quad (\text{S10})$$

As a consequence, the ratio of MCRs to SPRs,  $C$ , in the absence of  $\text{Fe}^{\text{II}}$ , may be derived by combining Eq. S9a and Eq. S11a to yield Eq. S11c.

$$k_{\text{bb}} \cdot [\text{SPR}] = k_p^t \cdot [\text{M}] \cdot [\text{MCR}] \quad (\text{S11a})$$

$$k_{\text{bb}} \cdot [\text{SPR}] = k_p^t \cdot [\text{M}] \cdot [\text{SPR}] \cdot C \quad (\text{S11b})$$

$$C = \frac{k_{\text{bb}}}{k_p^t \cdot [\text{M}]} \quad (\text{S11c})$$

Radical-radical termination in the absence of Fe-CRT is a second-order reaction. However, in the presence of  $\text{Fe}^{\text{II}}$ , the  $[\text{MCR}]$  vs time traces may obviously be represented by a first-order plot (Figure S21B), since termination proceeds mainly via Fe-CRT of those SPRs which are generated by propagation of MCRs. The associated rate laws are derived in Eq. S12–13. They apply when Eq. S10 holds. As mentioned in chapter 5.2.2, Fe-CRT of MCRs has not been observed and is therefore not included in the rate laws.

$$\begin{aligned}\frac{d[\text{MCR}]}{dt} &= k_{\text{bb}} \cdot [\text{SPR}] - k_{\text{p}}^{\text{t}} \cdot [\text{M}] \cdot [\text{MCR}] \\ &= k_{\text{bb}} \cdot [\text{MCR}] \cdot \frac{1}{C} - k_{\text{p}}^{\text{t}} \cdot [\text{M}] \cdot [\text{MCR}]\end{aligned}\quad (\text{S12a})$$

$$-\frac{d \ln[\text{MCR}]}{dt} = k_{\text{p}}^{\text{t}} \cdot [\text{M}] - k_{\text{bb}} \cdot \frac{1}{C} \quad (\text{S12b})$$

$$\frac{d[\text{SPR}]}{dt} = -k_{\text{t}}^{\text{Fe}} \cdot [\text{Fe}^{\text{II}}] \cdot [\text{SPR}] - k_{\text{bb}} \cdot [\text{SPR}] + k_{\text{p}}^{\text{t}} \cdot [\text{M}] \cdot [\text{SPR}] \cdot C \quad (\text{S13a})$$

$$-\frac{d \ln[\text{SPR}]}{dt} = -\frac{d \ln[\text{MCR}]}{dt} - \ln C = k_{\text{t}}^{\text{Fe}} \cdot [\text{Fe}^{\text{II}}] + k_{\text{bb}} - k_{\text{p}}^{\text{t}} \cdot [\text{M}] \cdot C \quad (\text{S13b})$$

As can be seen from Eq. S12b and Eq. S13b, the ratio of MCRs and SPRs,  $C$ , needs to be known to determine  $k_{\text{t}}^{\text{Fe}}$  from the slopes of the straight lines fitted to the 1<sup>st</sup>-order plots in Figure S21B. The ratio  $C$  may, however, not be measured directly via EPR, since SPR concentration quickly falls below the detection limit. It is helpful to combine Eq. S12b and Eq. S13b to Eq. S14a.

$$k_{\text{t}}^{\text{Fe}} \cdot [\text{Fe}^{\text{II}}] = k_{\text{p}}^{\text{t}} \cdot [\text{M}] \cdot (C + 1) - k_{\text{bb}} \cdot \left(1 + \frac{1}{C}\right) \quad (\text{S14a})$$

As  $C$  increases with  $k_{\text{t}}^{\text{Fe}} \times [\text{Fe}^{\text{II}}]$ , Eq. S14a simplifies to Eq. S14b-c in case of fast Fe-CRT, i.e., for the large  $k_{\text{t}}^{\text{Fe}}$  values as found for BA polymerization and for sufficiently high  $\text{Fe}^{\text{II}}$  concentration (e.g.:  $[\text{Fe}^{\text{II}}] \geq 2.5 \text{ mM}$ ).

$$k_{\text{t}}^{\text{Fe}} \cdot [\text{Fe}^{\text{II}}] = k_{\text{p}}^{\text{t}} \cdot [\text{M}] \cdot C - k_{\text{bb}} \quad (\text{S14b})$$

$$C = \frac{k_{\text{t}}^{\text{Fe}} \cdot [\text{Fe}^{\text{II}}] + k_{\text{bb}}}{k_{\text{p}}^{\text{t}} \cdot [\text{M}]} \quad (\text{S14c})$$

In the same way, division by  $C$  turns Eq. S14a into the pseudo first-order equations Eq. S15b-c for  $-\ln([MCR])/dt$  with  $m$  being the slope of the first-order plot.

$$k_t^{\text{Fe}} \cdot [\text{Fe}^{\text{II}}] \cdot \frac{1}{C} = k_p^t \cdot [\text{M}] \cdot \left(1 + \frac{1}{C}\right) - k_{\text{bb}} \cdot \left(\frac{1}{C} + \frac{1}{C^2}\right) \approx k_p^t \cdot [\text{M}] - k_{\text{bb}} \cdot \frac{1}{C} \quad (\text{S15a})$$

$$k_t^{\text{Fe}} \cdot [\text{Fe}^{\text{II}}] \cdot \frac{1}{C} \approx -\frac{d \ln[\text{MCR}]}{dt} \quad \text{cf. Eq. S12b} \quad (\text{S15b})$$

$$m \approx k_t^{\text{Fe}} \cdot [\text{Fe}^{\text{II}}] \cdot \frac{1}{C} = k_{\text{app}} \cdot [\text{Fe}^{\text{II}}] \quad (\text{S15c})$$

Equation Eq. S15c tells that  $C = k_t^{\text{Fe}} / k_{\text{app}}$ , which may be used to rearrange eq. Eq. S14c to Eq. S16 and thus to determine  $k_t^{\text{Fe}}$  via the straight line fit to  $-\ln([MCR])/dt$ . The required values of  $k_{\text{bb}}$  ( $390 \text{ s}^{-1}$  at  $50 \text{ }^\circ\text{C}$ ) and  $k_p^t$  ( $25 \text{ Lmol}^{-1}\text{s}^{-1}$  at  $50 \text{ }^\circ\text{C}$ ) for BA polymerization are reported in the literature.<sup>154</sup> The validity of these equations and the suggested evaluation procedure of SP-PLP-EPR experiments has been tested and verified by PREDICI simulations.

$$k_t^{\text{Fe}} = k_{\text{bb}} \cdot \left( \frac{k_p^t \cdot [\text{M}]}{k_{\text{app}}} - [\text{Fe}^{\text{II}}] \right)^{-1} \quad (\text{S16})$$

*Estimate of  $k_t^{\text{Fe}}$ .* The slopes,  $m = k_{\text{app}} \times [\text{Fe}^{\text{II}}]$ , of the straight lines fitted to the  $\ln([\text{MCR}]_0/[\text{MCR}])$  vs time data in Figure S21B may be used for estimating  $k_t^{\text{Fe}}$  according to Eq. S16, see Table S5.

**Table S5:**  $k_t^{\text{Fe}}$  determined between 30 and 50 °C via the  $\ln([\text{MCR}]_0/[\text{MCR}])$  vs time data for different levels of  $[\text{Fe}^{\text{II}}]$ .

$T / \text{°C}$	$[\text{Fe}^{\text{II}}] / \text{mM}$	$m / \text{s}^{-1}$	$k_{\text{app}} / \text{Lmol}^{-1}\text{s}^{-1}$	$k_t^{\text{Fe}} / \text{Lmol}^{-1}\text{s}^{-1}$
50	1.0	$51 \pm 3$	$5.1 \times 10^4$	$(2.1 \pm 0.2) \times 10^5$
50	2.5	$70 \pm 4$	$2.8 \times 10^4$	$(1.4 \pm 0.2) \times 10^5$
50	5.0	$88 \pm 5$	$1.8 \times 10^4$	$(1.2 \pm 0.2) \times 10^5$
50	10.0	$108 \pm 5$	$1.1 \times 10^4$	$(1.1 \pm 0.2) \times 10^5$
40	10.0	$68 \pm 4$	$6.8 \times 10^3$	$(9.4 \pm 1.9) \times 10^4$
30	10.0	$52 \pm 3$	$5.2 \times 10^3$	$(8.2 \pm 1.7) \times 10^4$

$k_t^{\text{Fe}}$  at 50 °C determined for the highest  $\text{Fe}^{\text{II}}$  concentration is very close to the value measured via time-resolved SP–PLP–EPR of SPRs, i.e.  $k_t^{\text{Fe}} = 1.0 \times 10^5 \text{ Lmol}^{-1}\text{s}^{-1}$ . The evaluation of  $k_t^{\text{Fe}}$  rests on the validity of Equation S10, which holds for sufficiently fast backbiting (e.g. above 20 °C) and fast Fe-CRT. The  $k_t^{\text{Fe}}$  value for the lowest  $\text{Fe}^{\text{II}}$  concentration, 1 mM, exceeds the expectation by a factor of two, since Eq. S10, S14c, and thus S16 do not exactly apply at such a low level of  $[\text{Fe}^{\text{II}}]$ .

It appears favorable to determine  $k_t^{\text{Fe}}$  via analysis of  $\ln([\text{SPR}]_0/[\text{SPR}])$  vs time traces, since this measurement is, under sensibly chosen conditions, independent of precisely knowing further rate coefficients. It is gratifying to note that the excellent agreement of  $k_t^{\text{Fe}}$  determined via the two approaches, i.e., via time-resolved SPR and MCR concentrations, respectively, demonstrates the quality of the  $k_{\text{bb}}$  and  $k_{\text{p}}^{\text{t}}$  values, which go into the analysis via MCR concentration.



---

## C Software for Modeling Procedures

### Details of the SCAN Program.

The python<sup>306,307</sup>-based software, which has been used for modeling in conjunction with the well-established PREDICI<sup>®</sup> program, will be introduced in the following section. SCAN and ANALYSIS were developed by *Johannes Buback*.<sup>304</sup>

A predefined PREDICI<sup>®</sup> model is read into the SCAN tool (Figure S22). SCAN allows for variation of rate coefficients, initial concentration of reagents and of recipes. As illustrated in Figure S22, parameter variation was prepared such as shown in Table 6.4 (chapter 6.2), i.e., there are six parameter dimensions being varied, including five rate coefficients each at five to seven levels, and one dimension for the combined variation of the overall initial concentrations. Moreover, recipes may be included and treated as parameter values. After each parameter study, the entire data set, including molar-mass distribution, may be stored on the hard-drive such that even a large amount of simulated data is readily available any time. The calculation mode for PREDICI<sup>®</sup> simulations may be selected in SCAN prior to starting the sequence of scans (Figure S23). The number of simultaneous PREDICI<sup>®</sup> processes may be defined in the SCAN system settings (Figure S24).

WINDOWS MESSAGES are used to load the PREDICI<sup>®</sup> model into SCAN and to start the integration process. The parameters are sent to PREDICI<sup>®</sup> such that an individual model including the targeted parameters is generated each time. SCAN obtains the simulated data by parsing the model and library log files generated by PREDICI<sup>®</sup>. This automated process is repetitively carried out until all simulations have been completed successfully. Optionally, a daemon may be started running under a different user to perform the calculations in the background.

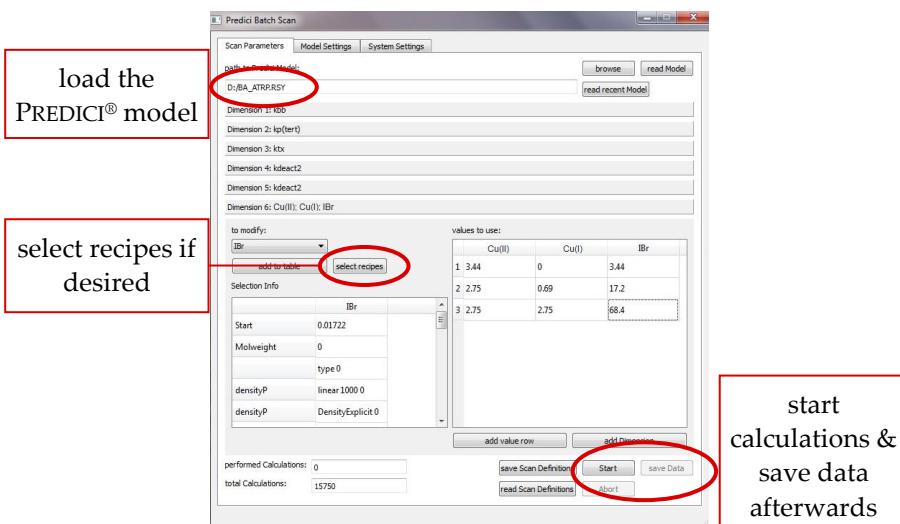


**Figure S22:** SCAN main window to prepare parameter variations for PREDICI® model files.

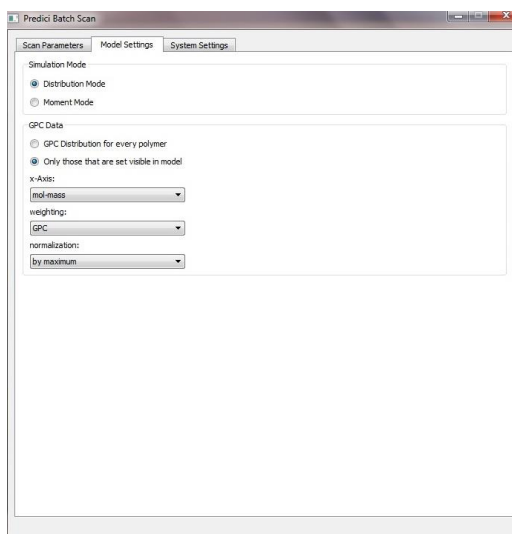


**Figure S23:** SCAN window to adjust the calculation mode in PREDICI® simulations.

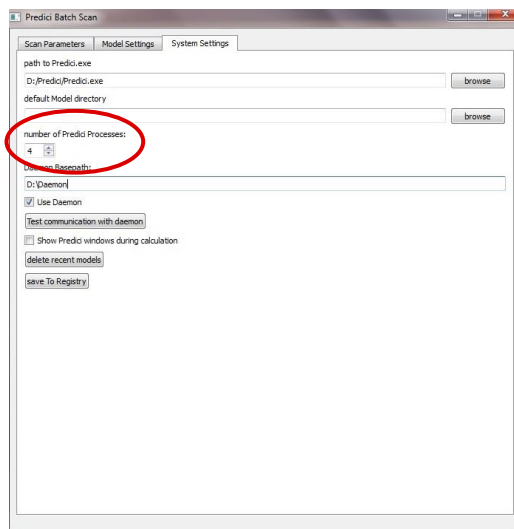


**Figure S24:** SCAN system settings where the number of simultaneous PREDICT® processes may be defined. A daemon may be started to perform the calculations in the background.

**Details of the ANALYSIS Program.** The SCAN file with all performed calculations may, traces, be loaded into ANALYSIS for data evaluation. A three-dimensional (Figure S25), two-dimensional (Figure S30) or a GPC plot (Figure S31) may be chosen for data representation. Shown in Figure S26 is the data selection for the three-dimensional plot to assign one parameter dimension to each ordinate (here:  $f_{br,c}$  vs  $k_{deact}^t$  and vs  $K_{ATRP}^t$  at  $x = 30\%$  monomer conversion). The  $x$  and  $z$  coordinates are defined in the "functions" window shown in Figure S27 which also allows mathematical operations to be applied (here: branching fraction  $f_{br,c}$ ) associated with reaction rates or reactivity ratios. Shown in Figure S28 are the labeling options. The plotted data may be exported to other programs or text files (Figure S29) or saved in numerous file formats.

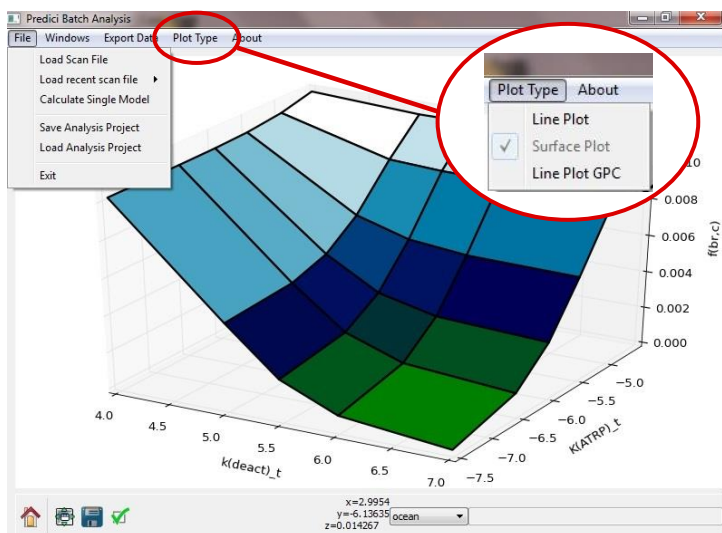


Figure S25: Three-dimensional plot in ANALYSIS.

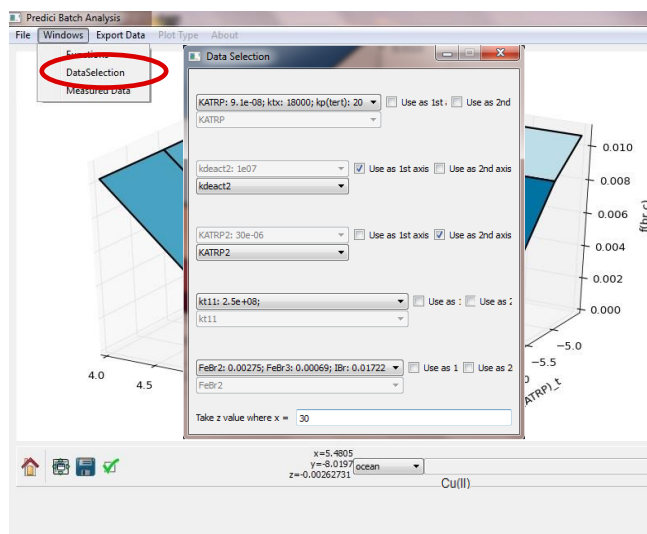


Figure S26: Data selection for three-dimensional plots in ANALYSIS.

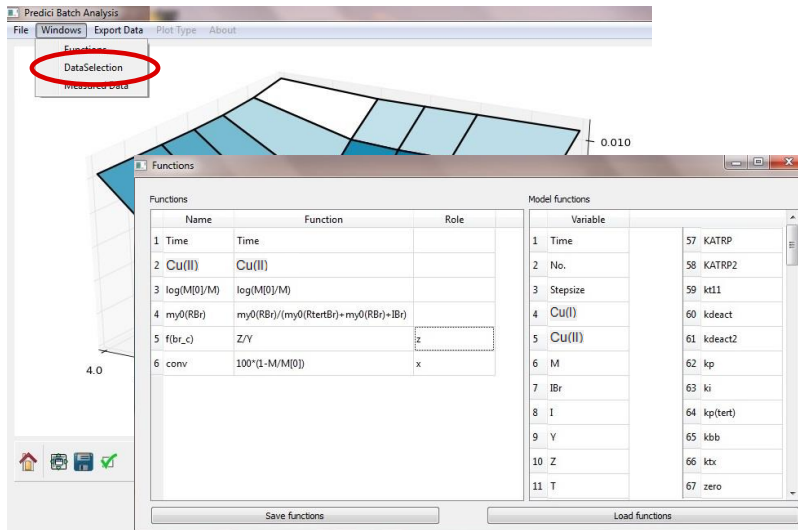


Figure S27: Functions including mathematical operations for plotting in ANALYSIS.

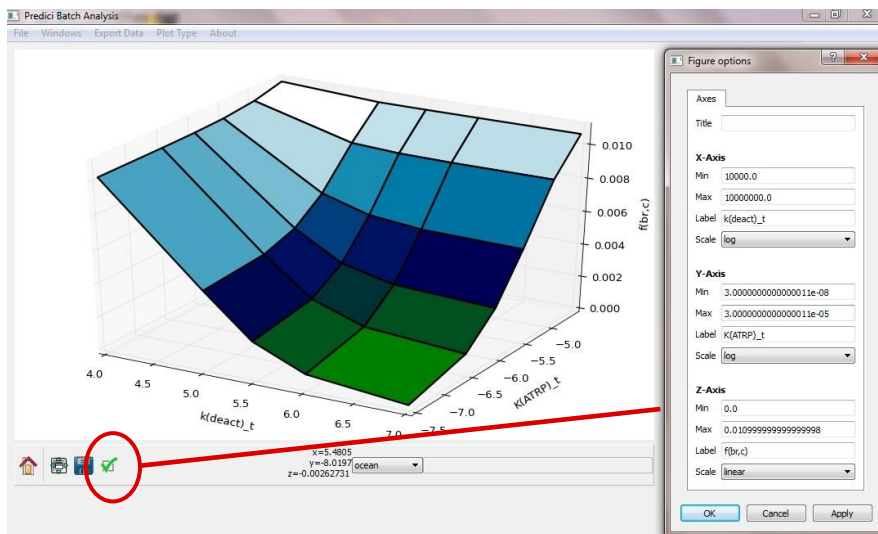
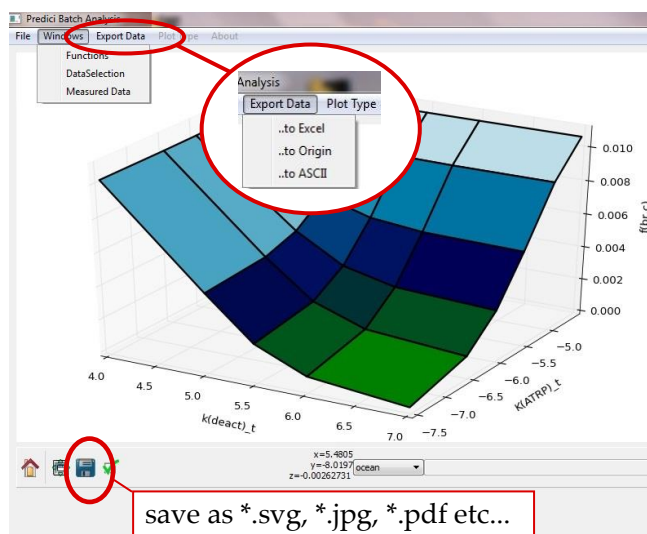
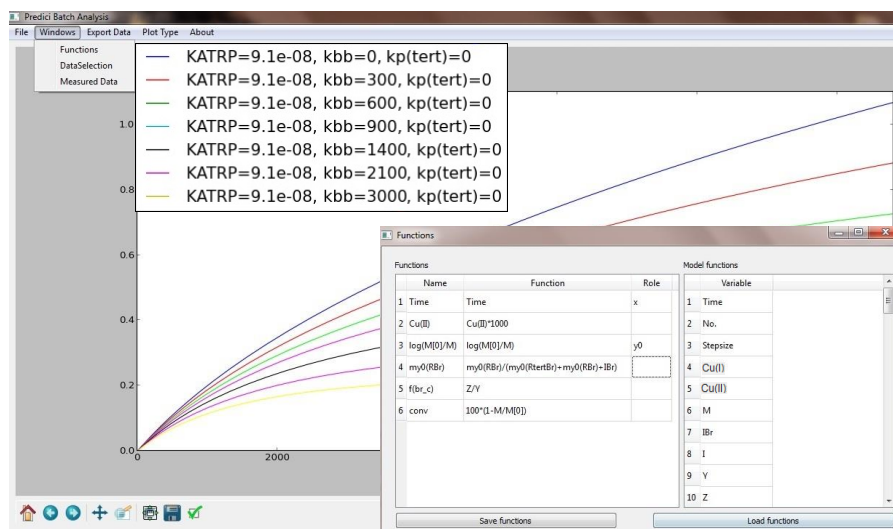


Figure S28: Figure options for plotting in ANALYSIS.



**Figure S29:** Data export and plot-saving options in ANALYSIS.



**Figure S30:** Two-dimensional plots Analysis, here:  $\ln([M]_0/[M])$  ( $\rightarrow y_0$ ) vs time ( $\rightarrow x$ ). In principle, several  $y$ -functions may be plotted simultaneously.

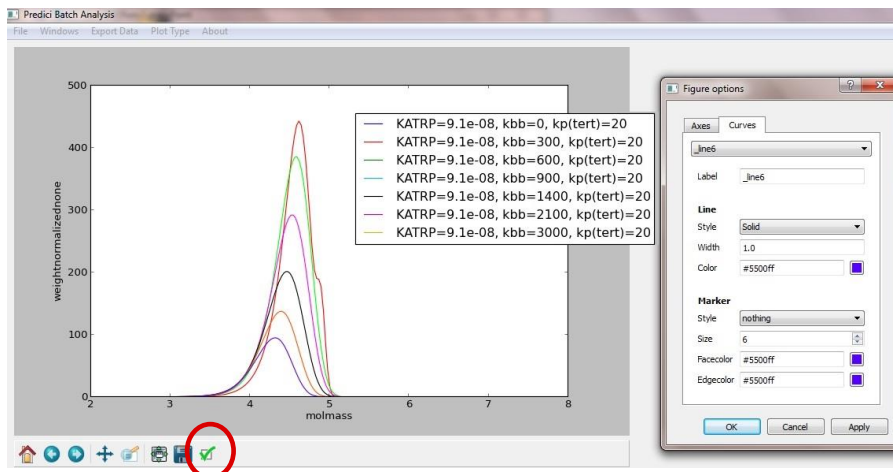


**Figure S31:** GPC plots in Analysis. Figure options such as color selection are also shown.

## D Abbreviations

$A$	absorbance
$A'$	pre-exponential factor
acac	acetylacetone
AIBN	2,2'-azobis(2-methylpropionitrile)
$\alpha$	relative variation of the viscosity with pressure
ATRA	atom-transfer radical addition
ATRP	atom-transfer radical polymerization
BA	butyl acrylate
BDE	bond-dissociation energy
$c$	concentration
$c'$	Y-intercept of the linearized function F[Y] for the non-equimolar case
$c''$	Y-intercept of the linearized function F[Y] for the equimolar case
CCT	catalytic chain transfer
CRP	controlled radical polymerization
CRT	catalytic radical termination
CV	cyclic voltammetry
$d$	optical pathway
DCM	dichloromethane
$\Delta G^\ddagger$	standard free energy of activation
$\Delta_r H$	reaction enthalpy
$\Delta V^\ddagger$	activation volume
$\Delta_r V$	reaction volume
DMF	dimethylformamide
$DP$	degree of polymerization
$E_A$	activation energy
EBrPA	ethyl $\alpha$ -bromophenylacetate
EPR	electron paramagnetic resonance
$\epsilon$	molar decadic extinction coefficient



---

equiv	equivalent
ESI	electrospray ionization
et al.	<i>et alii</i>
$\eta(T,p)$	solvent viscosity at the given temperature and pressure
$\eta_0$	solvent viscosity at the reference pressure $p_0$
EXAFS	extended X-ray absorption fine structure
$f$	initiator efficiency
FT	Fourier transform
GC	gas chromatography
$h$	Planck constant
HPLC	high-performance liquid chromatography
$i$	chain length
$k_{\text{act}}$	rate coefficient for the activation
$k_{\text{B}}$	Boltzmann constant
$K_{\text{ATRP}}$	ATRP equilibrium constant
$k_{\text{deact}}$	rate coefficient for the deactivation
$k_{\text{d}}$	rate coefficient of the initiator decay
$k_{\text{i}}$	rate coefficient of the monomer addition to the initiator radical
$K_{\text{model}}$	ATRP equilibrium constant in case of model systems
$k_{\text{p}}$	propagation rate coefficient
$k_{\text{p}}^1$	rate coefficient of the first propagation step
$K_{\text{poly}}$	ATRP equilibrium constant from polymerization kinetics
$k_{\text{t}}$	rate coefficient for the termination
$k_{\text{t,com}}$	rate coefficient of the termination by combination
$k_{\text{t,dis}}$	rate coefficient of the termination by disproportionation
$k_{\text{t}}^{1,1}$	rate coefficient for the termination of two monomer radicals
LMCT	ligand to metal charge transfer
M	monomer molecule
$m/z$	mass-to-charge ratio
MA	methyl acrylate

---

MBriB	methyl 2-bromoisobutyrate
MBrP	methyl 2-bromopropionate
MCR	mid-chain radical
MCT	mercury cadmium telluride
Me <sub>6</sub> TREN	tris(2-dimethylaminoethyl)amine
MeCN	acetonitrile
MFA	modified fluoralkoxy
MMA	methyl methacrylate
$M_n$	number-average molar mass
$M_w$	weight-average molar mass
MS	mass spectrometry
<i>n</i> Bu	<i>n</i> -butyl
NIR	near-infrared
NMP	<i>N</i> -methyl-2-pyrrolidone
NMR	nuclear magnetic resonance
OMRP	organometallic-mediated radical polymerization
OSET	outer sphere electron transfer
<i>p</i>	pressure
<i>p</i> <sub>0</sub>	reference pressure
PBA	poly(butyl acrylate)
<i>PDI</i>	dispersity
PE	polyethylene
PEBr	1-Phenylethyl bromide
Ph	phenyl
PID	proportional–integral–derivative controller
PLP	pulse-laser-induced polymerization
PMA	poly(methyl acrylate)
PMDETA	<i>N,N,N',N'',N'''</i> -pentamethyldiethylenetriamine
PMMA	poly(methyl methacrylate)
$P_{n+m}$	polymer generated by combination
$P_n^=$	unsaturated polymer generated by disproportionation
$P_m^H$	saturated polymer generated by disproportionation

---

PRE	<i>persistent radical effect</i>
PS	polystyrene
PSS	Polymer Standard Services
PVC	poly(vinyl chloride)
$R$	ideal gas constant
RAFT	reversible addition-fragmentation chain-transfer
RI	refractive index
$R_n\cdot$	radical consisting of $n$ monomer units
$R_p$	polymerization rate
$S$	entropy
SEC	size-exclusion chromatography
SRMP	stable-radical-mediated polymerization
SR&NI	simultaneous reverse and normal initiation
SP	single pulse
SPR	secondary propagating radical
$T$	temperature
TBABr	tetra( $n$ -butyl)ammonium bromide
TBAOTf	tetra( $n$ -butyl)ammonium triflate
TEMPO	2,2,6,6-Tetramethylpiperidin-1-oxidanyl
THF	tetrahydrofuran
TPMA	tris(2-pyridylmethyl)amine
TPMA*	tris([(4-methoxy-2,5-dimethyl)-2-pyridyl] methyl)amine
UV	ultraviolet
VIS	visible
$V$	volume
vol%	volume percent
wt%	weight percent



## Bibliography

- (1) *Plastics the facts 2013/2014*, <http://www.plasticseurope.co.uk/>, accessed July 12, **2015**.
- (2) Lechner, M. D.; Gehrke, K.; Nordmeier, E. H. *Makromolekulare Chemie*, 3<sup>rd</sup> ed., Birkhäuser, Basel, **2003**.
- (3) Shipp, D. A. *Polym. Rev.* **2011**, *51*, 99–103.
- (4) Poli, R.; Allan, L. E. N.; Shaver, M. P. *Prog. Polym. Sci.* **2014**, *39*, 1827–1845.
- (5) Tsarevsky, N. V.; Matyjaszewski, K. *Chem. Rev.* **2007**, *107*, 2270–2299.
- (6) Ouchi, M.; Terashima, T.; Sawamoto, M. *Chem. Rev.* **2009**, *109*, 4963–5050.
- (7) Matyjaszewski, K. *Macromolecules* **2012**, *45*, 4015–4039.
- (8) di Lena, F.; Matyjaszewski, K. *Prog. Polym. Sci.* **2010**, *35*, 959–1021.
- (9) Braunecker, W. A.; Matyjaszewski, K. *J. Mol. Catal. A: Chem.* **2006**, *254*, 155–164.
- (10) Matyjaszewski, K.; Xia, J. H. *Chem. Rev.* **2001**, *101*, 2921–2990.
- (11) Kamigaito, M.; Ando, T.; Sawamoto, M. *Chem. Rev.* **2001**, *101*, 3689–3745.
- (12) Kwak, Y.; Nicolay, R.; Matyjaszewski, K. *Macromolecules* **2008**, *41*, 6602–6604.
- (13) Braunecker, W. A.; Matyjaszewski, K. *Prog. Polym. Sci.* **2007**, *32*, 93–146.

- (14) Chiefari, J.; Chong, Y. K.; Ercole, F.; Krstina, J.; Jeffery, J.; Le, T. P. T.; Mayadunne, R. T. A.; Meijs, G. F.; Moad, C. L.; Moad, G.; Rizzardo, E.; Thang, S. H. *Macromolecules* **1998**, *31*, 5559–5562.
- (15) Moad, G.; Rizzardo, E.; Thang, S. H. *Aust. J. Chem.* **2005**, *58*, 379–410.
- (16) Moad, G.; Chong, Y. K.; Postma, A.; Rizzardo, E.; Thang, S. H. *Polymer* **2005**, *46*, 8458–8468.
- (17) Vana, P. *Macromol. Symp.* **2007**, *248*, 71–81.
- (18) Perrier, S.; Takolpuckdee, P. *J. Polym. Sci., Part A: Polym. Chem.* **2005**, *43*, 5347–5393.
- (19) Poli, R. *Eur. J. Inorg. Chem.* **2011**, 1513–1530.
- (20) Poli, R. *Angew. Chem. Int. Ed.* **2006**, *45*, 5058–5070.
- (21) Poli, R. *Chem. Eur. J.* **2015**, *21*, 6988–7001.
- (22) Xue, Z. G.; Poli, R. *J. Polym. Sci., Part A: Polym. Chem.* **2013**, *51*, 3494–3504.
- (23) Hawker, C. J.; Bosman, A. W.; Harth, E. *Chem. Rev.* **2001**, *101*, 3661–3688.
- (24) Georges, M. K.; Veregin, R. P. N.; Kazmaier, P. M.; Hamer, G. K. *Macromolecules* **1993**, *26*, 2987–2988.
- (25) Matyjaszewski, K.; Tsarevsky, N. V. *Nature Chem.* **2009**, *1*, 276–288.
- (26) Guimard, N. K.; Oehlenschlaeger, K. K.; Zhou, J. W.; Hilf, S.; Schmidt, F. G.; Barner-Kowollik, C. *Macromol. Chem. Phys.* **2012**, *213*, 131–143.
- (27) Destarac, M. *Macromol. React. Eng.* **2010**, *4*, 165–179.
- (28) Ding, M. Q.; Jiang, X. W.; Zhang, L. F.; Cheng, Z. P.; Zhu, X. L. *Macromol. Rapid Comm.* **2015**, DOI: 10.1002/marc.201500085.
- (29) Adali-Kaya, Z.; Bui, B. T. S.; Falcimaigne-Cordin, A.; Haupt, K. *Angew. Chem. Int. Ed.* **2015**, *54*, 5192–5195.
- (30) Wang, J. S.; Matyjaszewski, K. *J. Am. Chem. Soc.* **1995**, *117*, 5614–5615.
- (31) Kato, M.; Kamigaito, M.; Sawamoto, M.; Higashimura, T. *Macromolecules* **1995**, *28*, 1721–1723.
- (32) Gossage, R. A.; Van De Kuil, L. A.; Van Koten, G. *Acc. Chem. Res.* **1998**, *31*, 423–431.
- (33) Kharasch, M. S.; Jensen, E. V.; Urry, W. H. *Science* **1945**, *102*, 128–128.
- (34) Minisci, F. *Acc. Chem. Res.* **1975**, *8*, 165–171.
- (35) Tang, W.; Kwak, Y.; Braunecker, W.; Tsarevsky, N. V.; Coote, M. L.; Matyjaszewski, K. *J. Am. Chem. Soc.* **2008**, *130*, 10702–10713.

- 
- (36) Tang, W.; Tsarevsky, N. V.; Matyjaszewski, K. *J. Am. Chem. Soc.* **2006**, *128*, 1598–1604.
- (37) Seeliger, F.; Matyjaszewski, K. *Macromolecules* **2009**, *42*, 6050–6055.
- (38) Pintauer, T.; Braunecker, W.; Collange, E.; Poli, R.; Matyjaszewski, K. *Macromolecules* **2004**, *37*, 2679–2682.
- (39) Horn, M.; Matyjaszewski, K. *Macromolecules* **2013**, *46*, 3350–3357.
- (40) Braunecker, W. A.; Tsarevsky, N. V.; Gennaro, A.; Matyjaszewski, K. *Macromolecules* **2009**, *42*, 6348–6360.
- (41) Bortolamei, N.; Isse, A. A.; Di Marco, V. B.; Gennaro, A.; Matyjaszewski, K. *Macromolecules* **2010**, *43*, 9257–9267.
- (42) Pintauer, T.; Matyjaszewski, K. *Coord. Chem. Rev.* **2005**, *249*, 1155–1184.
- (43) De Paoli, P.; Isse, A. A.; Bortolamei, N.; Gennaro, A. *Chem. Commun.* **2011**, *47*, 3580–3582.
- (44) Tang, W.; Matyjaszewski, K. *Macromolecules* **2007**, *40*, 1858–1863.
- (45) Eckenhoff, W. T.; Biernesser, A. B.; Pintauer, T. *Inorg. Chim. Acta* **2012**, *382*, 84–95.
- (46) Bolm, C.; Legros, J.; Le Paih, J.; Zani, L. *Chem. Rev.* **2004**, *104*, 6217–6254.
- (47) Gopalaiah, K. *Chem. Rev.* **2013**, *113*, 3248–3296.
- (48) Xue, Z.; He, D.; Xie, X. *Polym. Chem.* **2015**, *6*, 1660–1687.
- (49) Enthaler, S.; Junge, K.; Beller, M. *Angew. Chem. Int. Ed.* **2008**, *47*, 3317–3321.
- (50) Correa, A.; Mancheño, O. G.; Bolm, C. *Chem. Soc. Rev.* **2008**, *37*, 1108–1117.
- (51) Mancheño, O. G. *Angew. Chem. Int. Ed.* **2011**, *50*, 2216–2218.
- (52) Nishizawa, K.; Ouchi, M.; Sawamoto, M. *Macromolecules* **2013**, *46*, 3342–3349.
- (53) Wang, Y.; Kwak, Y.; Matyjaszewski, K. *Macromolecules* **2012**, *45*, 5911–5915.
- (54) Xue, Z. G.; He, D.; Noh, S. K.; Lyoo, W. S. *Macromolecules* **2009**, *42*, 2949–2957.
- (55) Aoshima, H.; Satoh, K.; Umemura, T.; Kamigaito, M. *Polym. Chem.* **2013**, *4*, 3554–3562.
- (56) Xue, Z.; Linh, N. T. B.; Noh, S. K.; Lyoo, W. S. *Angew. Chem. Int. Ed.* **2008**, *47*, 6426–429.
- (57) Zhu, G. H.; Zhang, L. F.; Zhang, Z. B.; Zhu, J.; Tu, Y. F.; Cheng, Z. P.; Zhu, X. L. *Macromolecules* **2011**, *44*, 3233–3239.

- (58) Chen, X. X.; Khan, M. Y.; Noh, S. K. *Polym. Chem.* **2012**, *3*, 1971–1974.
- (59) Matyjaszewski, K.; Wei, M. L.; Xia, J. H.; McDermott, N. E. *Macromolecules* **1997**, *30*, 8161–8164.
- (60) Khan, M. Y.; Chen, X. X.; Lee, S. W.; Noh, S. K. *Macromol. Rapid Commun.* **2013**, *34*, 1225–1230.
- (61) Satoh, K.; Aoshima, H.; Kamigaito, M. *J. Polym. Sci., Part A: Polym. Chem.* **2008**, *46*, 6358–6363.
- (62) Xue, Z.; Noh, S. K.; Lyoo, W. S. *Macromol. Res.* **2007**, *15*, 302–307.
- (63) Zhang, L. F.; Cheng, Z. P.; Tang, F.; Li, Q.; Zhu, X. L. *Macromol. Chem. Phys.* **2008**, *209*, 1705–1713.
- (64) Moineau, G.; Dubois, P.; Jerome, R.; Senninger, T.; Teyssie, P. *Macromolecules* **1998**, *31*, 545–547.
- (65) Ando, T.; Kamigaito, M.; Sawamoto, M. *Macromolecules* **1997**, *30*, 4507–4510.
- (66) Wang, G.; Zhu, X. L.; Zhu, J.; Cheng, Z. P. *J. Polym. Sci., Part A: Polym. Chem.* **2006**, *44*, 483–489.
- (67) Zhang, L. F.; Miao, J.; Cheng, Z. P.; Zhu, X. L. *Macromol. Rapid Commun.* **2010**, *31*, 275–280.
- (68) Zhang, L. F.; Cheng, Z. P.; Lu, Y. T.; Zhu, X. L. *Macromol. Rapid Commun.* **2009**, *30*, 543–547.
- (69) Bai, L. J.; Zhang, L. F.; Zhu, J.; Cheng, Z. P.; Zhu, X. L. *J. Polym. Sci., Part A: Polym. Chem.* **2009**, *47*, 2002–2008.
- (70) Tao, M. X.; Zhang, L. F.; Jiang, H. J.; Zhang, Z. B.; Zhu, J.; Cheng, Z. P.; Zhu, X. L. *Macromol. Chem. Phys.* **2011**, *212*, 1481–1488.
- (71) Niibayashi, S.; Hayakawa, H.; Jin, R. H.; Nagashima, H. *Chem. Commun.* **2007**, 1855–1857.
- (72) Zhang, H. Q.; Schubert, U. S. *J. Polym. Sci., Part A: Polym. Chem.* **2004**, *42*, 4882–4894.
- (73) Shaver, M. P.; Allan, L. E. N.; Gibson, V. C. *Organometallics* **2007**, *26*, 4725–4730.
- (74) Shaver, M. P.; Allan, L. E. N.; Rzepa, H. S.; Gibson, V. C. *Angew. Chem. Int. Ed.* **2006**, *45*, 1241–1244.
- (75) O'Reilly, R. K.; Shaver, M. P.; Gibson, V. C.; White, A. J. P. *Macromolecules* **2007**, *40*, 7441–7452.
- (76) Gibson, V. C.; O'Reilly, R. K.; Wass, D. F.; White, A. J. P.; Williams, D. J. *Macromolecules* **2003**, *36*, 2591–2593.
- (77) Gibson, V. C.; O'Reilly, R. K.; Reed, W.; Wass, D. F.; White, A. J. P.; Williams, D. J. *Chem. Commun.* **2002**, 1850–1851.



- 
- (78) Ferro, R.; Milione, S.; Bertolasi, V.; Capacchione, C.; Grassi, A. *Macromolecules* **2007**, *40*, 8544–8546.
- (79) Sarbu, T.; Matyjaszewski, K. *Macromol. Chem. Phys.* **2001**, *202*, 3379–3391.
- (80) Teodorescu, M.; Gaynor, S. G.; Matyjaszewski, K. *Macromolecules* **2000**, *33*, 2335–2339.
- (81) Wang, Y.; Matyjaszewski, K. *Macromolecules* **2011**, *44*, 1226–1228.
- (82) Wang, Y.; Matyjaszewski, K. *Macromolecules* **2010**, *43*, 4003–4005.
- (83) Wang, Y.; Zhang, Y. Z.; Parker, B.; Matyjaszewski, K. *Macromolecules* **2011**, *44*, 4022–4025.
- (84) Mukumoto, K.; Wang, Y.; Matyjaszewski, K. *ACS Macro Lett.* **2012**, *1*, 599–602.
- (85) Claverie, J. P. *Res. Discl.* **1998**, *416*, 1595–1604.
- (86) Allan, L. E. N.; MacDonald, J. P.; Reckling, A. M.; Kozak, C. M.; Shaver, M. P. *Macromol. Rapid Commun.* **2012**, *33*, 414–418.
- (87) Allan, L. E. N.; MacDonald, J. P.; Nichol, G. S.; Shaver, M. P. *Macromolecules* **2014**, *47*, 1249–1257.
- (88) Allan, L. E. N.; Shaver, M. P.; White, A. J. P.; Gibson, V. C. *Inorg. Chem.* **2007**, *46*, 8963–8970.
- (89) Poli, R. *Angew. Chem. Int. Ed.* **2006**, *45*, 5058–5070.
- (90) Poli, R.; Shaver, M. P. *Chem. Eur. J.* **2014**, *20*, 17530–17540.
- (91) Poli, R.; Shaver, M. P. *Inorg. Chem.* **2014**, *53*, 7580–7590.
- (92) Kattner, H.; Buback, M. *Macromol. Symp.* **2013**, *333*, 11–23.
- (93) Barth, J.; Buback, M. *Macromol. React. Eng.* **2010**, *4*, 288–301.
- (94) Yamada, B.; Westmoreland, D. G.; Kobatake, S.; Konosu, O. *Prog. Polym. Sci.* **1999**, *24*, 565–630.
- (95) Arita, T.; Buback, M.; Janssen, O.; Vana, P. *Macromol. Rapid Commun.* **2004**, *25*, 1376–1381.
- (96) Buback, M.; Meiser, W.; Vana, P. *Aust. J. Chem.* **2009**, *62*, 1484–1487.
- (97) Buback, M.; Kuchta, F. D. *Macromol. Chem. Phys.* **1995**, *196*, 1887–1898.
- (98) Beuermann, S.; Buback, M.; Russell, G. T. *Macromol. Rapid Commun.* **1994**, *15*, 351–355.
- (99) Buback, M.; Kuchta, F. D. *Macromol. Chem. Phys.* **1997**, *198*, 1455–1480.
- (100) Buback, M.; Kuelpmann, A.; Kurz, C. *Macromol. Chem. Phys.* **2002**, *203*, 1065–1070.
- (101) Buback, M.; Barner-Kowollik, C.; Kuelpmann, A. *Macromol. Chem. Phys.* **2002**, *203*, 1887–1894.

- (102) Morick, J.; Buback, M.; Matyjaszewski, K. *Macromol. Chem. Phys.* **2011**, *212*, 2423–2428.
- (103) Morick, J.; Buback, M.; Matyjaszewski, K. *Macromol. Chem. Phys.* **2012**, *213*, 2287–2292.
- (104) Buback, M.; Morick, J. *Macromol. Chem. Phys.* **2010**, *211*, 2154–2161.
- (105) Schroeder, H.; Buback, M.; Matyjaszewski, K. *Macromol. Chem. Phys.* **2014**, *215*, 44–53.
- (106) Pietrasik, J.; Hui, C. M.; Chaladaj, W.; Dong, H. C.; Choi, J.; Jurczak, J.; Bockstaller, M. R.; Matyjaszewski, K. *Macromol. Rapid Commun.* **2011**, *32*, 295–301.
- (107) Mueller, L.; Jakubowski, W.; Matyjaszewski, K.; Pietrasik, J.; Kwiatkowski, P.; Chaladaj, W.; Jurczak, J. *Eur. Polym. J.* **2011**, *47*, 730–734.
- (108) Kwiatkowski, P.; Jurczak, J.; Pietrasik, J.; Jakubowski, W.; Mueller, L.; Matyjaszewski, K. *Macromolecules* **2008**, *41*, 1067–1069.
- (109) Arita, T.; Kayama, Y.; Ohno, K.; Tsujii, Y.; Fukuda, T. *Polymer* **2008**, *49*, 2426–2429.
- (110) Mueller, L. *PhD Thesis*, Carnegie Mellon University, Pittsburgh, **2010**.
- (111) Matyjaszewski, K.; Patten, T. E.; Xia, J. H. *J. Am. Chem. Soc.* **1997**, *119*, 674–680.
- (112) Mori, H.; Müller, A. H. E. *Prog. Polym. Sci.* **2003**, *28*, 1403–1439.
- (113) Grimaud, T.; Matyjaszewski, K. *Macromolecules* **1997**, *30*, 2216–2218.
- (114) Davis, K. A.; Paik, H. J.; Matyjaszewski, K. *Macromolecules* **1999**, *32*, 1767–1776.
- (115) Neugebauer, D.; Matyjaszewski, K. *Macromolecules* **2003**, *36*, 2598–2603.
- (116) Teodorescu, M.; Matyjaszewski, K. *Macromolecules* **1999**, *32*, 4826–4831.
- (117) Matyjaszewski, K.; Jo, S. M.; Paik, H. J.; Gaynor, S. G. *Macromolecules* **1997**, *30*, 6398–6400.
- (118) Tsarevsky, N. V.; Braunecker, W. A.; Brooks, S. J.; Matyjaszewski, K. *Macromolecules* **2006**, *39*, 6817–6824.
- (119) Konkolewicz, D.; Schröder, K.; Buback, J.; Bernhard, S.; Matyjaszewski, K. *ACS Macro Lett.* **2012**, *1*, 1219–1223.
- (120) Gromada, J.; Matyjaszewski, K. *Macromolecules* **2001**, *34*, 7664–7671.
- (121) Qin, J.; Cheng, Z. P.; Zhang, L. F.; Zhang, Z. B.; Zhu, J.; Zhu, X. L. *Macromol. Chem. Phys.* **2011**, *212*, 999–1006.

- 
- (122) He, W. J.; Zhang, L. F.; Bai, L. J.; Zhang, Z. B.; Zhu, J.; Cheng, Z. P.; Zhu, X. L. *Macromol. Chem. Phys.* **2011**, *212*, 1474–1480.
- (123) Min, K.; Jakubowski, W.; Matyjaszewski, K. *Macromol. Rapid Commun.* **2006**, *27*, 594–598.
- (124) Min, K.; Jakubowski, W.; Matyjaszewski, K. *Macromol. Rapid Commun.* **2006**, *27*, 982–982.
- (125) Tsarevsky, N. V.; Jakubowski, W. *J. Polym. Sci., Part A: Polym. Chem.* **2011**, *49*, 918–925.
- (126) Lou, Q.; Shipp, D. A. *Chem. Phys. Chem.* **2012**, *13*, 3257–3261.
- (127) Zhang, Y. Z.; Wang, Y.; Matyjaszewski, K. *Macromolecules* **2011**, *44*, 683–685.
- (128) Jakubowski, W.; Min, K.; Matyjaszewski, K. *Macromolecules* **2006**, *39*, 39–45.
- (129) Dong, H. C.; Tang, W.; Matyjaszewski, K. *Macromolecules* **2007**, *40*, 2974–2977.
- (130) Kwak, Y.; Magenau, A. J. D.; Matyjaszewski, K. *Macromolecules* **2011**, *44*, 811–819.
- (131) Yang, D. F.; He, D.; Liao, Y. G.; Xue, Z. G.; Zhou, X. P.; Xie, X. L. *J. Polym. Sci., Part A: Polym. Chem.* **2014**, *52*, 1020–1027.
- (132) Abreu, C. M. R.; Mendonca, P. V.; Serra, A. C.; Popov, A. V.; Matyjaszewski, K.; Guliyashvili, T.; Coelho, J. F. J. *ACS Macro Lett.* **2012**, *1*, 1308–1311.
- (133) Dong, H.; Matyjaszewski, K. *Macromolecules* **2008**, *41*, 6868–6870.
- (134) Tanaka, K.; Matyjaszewski, K. *Macromol. Symp.* **2008**, *261*, 1–9.
- (135) Chan, N.; Cunningham, M. F.; Hutchinson, R. A. *Macromol. Chem. Phys.* **2008**, *209*, 1797–1805.
- (136) Pintauer, T.; Matyjaszewski, K. *Chem. Soc. Rev.* **2008**, *37*, 1087–1097.
- (137) Yamamoto, S.-I.; Matyjaszewski, K. *Polym. J. (Tokyo)* **2008**, *40*, 496–497.
- (138) Tang, W. *PhD Thesis*, Carnegie Mellon University, Pittsburgh, **2008**.
- (139) Krys, P.; Schroeder, H.; Buback, J.; Buback, M.; Matyjaszewski, K., *in preparation*.
- (140) Mueller, L.; Jakubowski, W.; Tang, W.; Matyjaszewski, K. *Macromolecules* **2007**, *40*, 6464–6472.
- (141) Matyjaszewski, K. *J. Macromol. Sci., Pure Appl. Chem.* **1997**, *34*, 1785–1801.
- (142) Müller, A. H. E.; Zhuang, R. G.; Yan, D. Y.; Litvinenko, G. *Macromolecules* **1995**, *28*, 4326–4333.

- (143) Buback, M.; Müller, E.; Russell, G. T. *J. Phys. Chem. A* **2006**, *110*, 3222–3230.
- (144) Smith, G. B.; Russell, G. T.; Heuts, J. P. A. *Macromol. Theory Simul.* **2003**, *12*, 299–314.
- (145) Matyjaszewski, K.; Gnanou, Y.; Leibler, L. *Macromolecular Engineering: from Precise Macromolecular Synthesis to Macroscopic Materials Properties and Applications*, 1<sup>st</sup> ed., Wiley–VCH, Weinheim **2007**.
- (146) Barth, J.; Buback, M.; Hesse, P.; Sergeeva, T. *Macromol. Rapid Commun.* **2009**, *30*, 1969–1974.
- (147) Boschmann, D.; Vana, P. *Macromolecules* **2007**, *40*, 2683–2693.
- (148) Farcet, C.; Belleney, J.; Charleux, B.; Pirri, R. *Macromolecules* **2002**, *35*, 4912–4918.
- (149) Plessis, C.; Arzamendi, G.; Alberdi, J. M.; van Herk, A. M.; Leiza, J. R.; Asua, J. M. *Macromol. Rapid Commun.* **2003**, *24*, 173–177.
- (150) Asua, J. M.; Beuermann, S.; Buback, M.; Castignolles, P.; Charleux, B.; Gilbert, R. G.; Hutchinson, R. A.; Leiza, J. R.; Nikitin, A. N.; Vairon, J. P.; van Herk, A. M. *Macromol. Chem. Phys.* **2004**, *205*, 2151–2160.
- (151) Willemse, R. X. E.; van Herk, A. M.; Panchenko, E.; Junkers, T.; Buback, M. *Macromolecules* **2005**, *38*, 5098–5103.
- (152) Nikitin, A. N.; Hutchinson, R. A. *Macromolecules* **2005**, *38*, 1581–1590.
- (153) Nikitin, A. N.; Hutchinson, R. A.; Buback, M.; Hesse, P. *Macromolecules* **2007**, *40*, 8631–8641.
- (154) Barth, J.; Buback, M.; Hesse, P.; Sergeeva, T. *Macromolecules* **2010**, *43*, 4023–4031.
- (155) Fischer, H. *Chem. Rev.* **2001**, *101*, 3581–3610.
- (156) Fischer, H. *J. Polym. Sci., Part A: Polym. Chem.* **1999**, *37*, 1885–1901.
- (157) Goto, A.; Fukuda, T. *Prog. Polym. Sci.* **2004**, *29*, 329–385.
- (158) Schuh, H.; Fischer, H. *Int. J. Chem. Kinet.* **1976**, *8*, 341–356.
- (159) van Eldik, R.; Asano, T.; Le Noble, W. J. *Chem. Rev.* **1989**, *89*, 549–688.
- (160) Eyring, H. *Chem. Rev.* **1935**, *1935*, 65–77.
- (161) Asano, T.; Lenoble, J. *Chem. Rev.* **1978**, *78*, 407–489.
- (162) Troe, J. *J. Phys. Chem.* **1986**, *90*, 357–365.
- (163) Van Eldik, R. *Inorganic High Pressure Chemistry – Kinetics and Mechanism*, Vol. 7, Elsevier, Amsterdam, **1986**.

- 
- (164) Horne, R. A.; Frysinger, G. R.; Myers, B. R. *Inorg. Chem.* **1964**, *3*, 452–454.
- (165) Rickard, D. T.; Wickman, F. E. *Chemistry and Geochemistry of Solutions at High Temperatures and Pressures*, 1<sup>st</sup> ed., Pergamon Press: Oxford, **1981**.
- (166) Schroeder, H.; Yalalov, D.; Buback, M.; Matyjaszewski, K. *Macromol. Chem. Phys.* **2012**, *213*, 2019–2026.
- (167) Buback, M.; Lendle, H. *Z. Naturforsch. A* **1979**, *34*, 1482–1488.
- (168) Schroeder, H. *Master Thesis*, Georg-August-University, Göttingen, **2011**.
- (169) Morick, J. *PhD Thesis*, Georg-August-University, Göttingen, **2012**.
- (170) Weiss, D. *Master Thesis*, Georg-August-University, Göttingen, **2012**.
- (171) Mössbauer, R. L. *Naturwissenschaften* **1958**, *45*, 538–539.
- (172) Mössbauer, R. L. *Z. Physik* **1958**, *151*, 124–143.
- (173) Gütlich, P. *Z. Anorg. Allg. Chem.* **2012**, *638*, 15–43.
- (174) Jeschke, G. *Einführung in die ESR Spektroskopie*, Johannes-Gutenberg-University, Mainz, **1998**.
- (175) Kattner, H. *Master Thesis*, Georg-August-University, Göttingen, **2012**.
- (176) Soerensen, N.; Barth, J.; Buback, M.; Morick, J.; Schroeder, H.; Matyjaszewski, K. *Macromolecules* **2012**, *45*, 3797–3801.
- (177) Hesse, P. *PhD Thesis*, Georg-August-University, Göttingen, **2008**.
- (178) Barth, J. *PhD Thesis*, Georg-August-University, Göttingen, **2011**.
- (179) Soerensen, N. *PhD Thesis*, Georg-August-University, Göttingen, **2015**.
- (180) Ding, K. Y.; Zannat, F.; Morris, J. C.; Brennessel, W. W.; Holland, P. L. *J. Organomet. Chem.* **2009**, *694*, 4204–4208.
- (181) Meyer, S.; Orben, C. M.; Demeshko, S.; Dechert, S.; Meyer, F. *Organometallics* **2011**, *30*, 6692–6702.
- (182) Furlani, C.; Cervone, E.; Valenti, V. *Inorg. Nucl. Chem.* **1963**, *25*, 159–163.
- (183) Parellada, R.; Arenas, J. F.; Perezpena, J. J. *Mol. Struct.* **1979**, *51*, 1–7.
- (184) Gill, N. S. *J. Chem. Soc.* **1961**, 3512–3515.
- (185) Kim, Y. J.; Park, C. R. *Inorg. Chem.* **2002**, *41*, 6211–6216.
- (186) Vala, M. T.; McCarthy, P. J. *Spectrochim. Acta, Part A* **1970**, *26*, 2183–2195.
- (187) Vala, M.; McCarthy, P. J.; Mongan, P. J. *Chem. Soc., Dalton Trans.* **1972**, 1870–1875.
- (188) Ginsberg, A. P.; Robin, M. B. *Inorg. Chem.* **1963**, *2*, 817–822.

- (189) Lever, A. B. P. *Inorganic Electronic Spectroscopy*, Elsevier, Amsterdam, **1984**; pg. 450.
- (190) Wyrzykowski, D.; Kruszyński, R.; Klak, J.; Mroziński, J.; Warnke, Z. *Z. Anorg. Allg. Chem.* **2007**, *633*, 2071–2076.
- (191) Cai, H. L.; Zhang, Y.; Fu, D. W.; Zhang, W.; Liu, T.; Yoshikawa, H.; Awaga, K.; Xiong, R. G. *J. Am. Chem. Soc.* **2012**, *134*, 18487–18490.
- (192) Hay, M. T.; Geib, S. J. *Acta Crystallogr.* **2005**, *E61*, M190–M191.
- (193) Wyrzykowski, D.; Kruszyński, R.; Kucharska, U.; Warnke, Z. *Z. Anorg. Allg. Chem.* **2006**, *632*, 624–628.
- (194) Wyrzykowski, D.; Kruszyński, R.; Klak, J.; Mroziński, J.; Warnke, Z. *Inorg. Chim. Acta* **2008**, *361*, 262–268.
- (195) Allen, F. H. *Acta Crystallogr.* **2002**, *B58*, 380–388.
- (196) Neese, F. *Inorg. Chim. Acta* **2002**, *337*, 181–192.
- (197) Herber, R. H.; Nowik, I.; Kostner, M. E.; Kahlenberg, V.; Kreutz, C.; Laus, G.; Schottenberger, H. *Int. J. Mol. Sci.* **2011**, *12*, 6397–6406.
- (198) de Pedro, I.; García-Saiz, A.; González, J.; de Larramendi, I. R.; Rojo, T.; Afonso, C. A. M.; Simeonov, S. P.; Waerenborgh, J. C.; Blanco, J. A.; Ramajo, B.; Fernandez, J. R. *Phys. Chem. Chem. Phys.* **2013**, *15*, 12724–12733.
- (199) König, E.; Ritter, G. *Inorg. Chim. Acta* **1982**, *59*, 285–291.
- (200) Habibullah, M.; Rahman, I. M. M.; Uddin, M. A.; Iwakabe, K.; Azam, A.; Hasegawa, H. *J. Chem. Eng. Data* **2011**, *56*, 3323–3327.
- (201) Nanda, A. K.; Matyjaszewski, K. *Macromolecules* **2003**, *36*, 8222–8224.
- (202) Barth, J.; Buback, M. *Macromol. Rapid Commun.* **2009**, *30*, 1805–1811.
- (203) García-Abuín, A.; Gómez-Díaz, D.; La Rubia, M. D.; López, A. B.; Navaza, J. M. *J. Chem. Eng. Data* **2011**, *56*, 2904–2908.
- (204) Henni, A.; Hromek, J. J.; Tontiwachwuthikul, P.; Chakma, A. *J. Chem. Eng. Data* **2004**, *49*, 231–234.
- (205) Yang, C. S.; He, G. H.; He, Y. F.; Ma, P. S. *J. Chem. Eng. Data* **2008**, *53*, 1639–1642.
- (206) Assael, M. J.; Dalaouti, N. K.; Polimatidou, S. *Int. J. Thermophys.* **1999**, *20*, 1367–1377.
- (207) Ku, H. C.; Tu, C. H. *J. Chem. Eng. Data* **2005**, *50*, 608–615.
- (208) Yang, C. S.; Yu, W. L.; Ma, P. S. *J. Chem. Eng. Data* **2005**, *50*, 1197–1203.
- (209) Yang, C. S.; Xu, W.; Ma, P. S. *J. Chem. Eng. Data* **2004**, *49*, 1794–1801.
- (210) Schröder, K.; Mathers, R. T.; Buback, J.; Konkolewicz, D.; Magenau, A. J. D.; Matyjaszewski, K. *ACS Macro Lett.* **2012**, *1*, 1037–1040.

- 
- (211) Okada, S.; Park, S.; Matyjaszewski, K. *ACS Macro Lett.* **2014**, *3*, 944–947.
- (212) Xue, Z. G.; Oh, H. S.; Noh, S. K.; Lyoo, W. S. *Macromol. Rapid Commun.* **2008**, *29*, 1887–1894.
- (213) Przyojski, J. A.; Arman, H. D.; Tonzetich, Z. J. *Organometallics* **2012**, *31*, 3264–3271.
- (214) Kawamura, M.; Sunada, Y.; Kai, H.; Koike, N.; Hamada, A.; Hayakawa, H.; Jin, R. H.; Nagashima, H. *Adv. Synth. Catal.* **2009**, *351*, 2086–2090.
- (215) Zhang, H.; Schubert, U. S. *J. Polym. Sci. A: Polym. Chem.* **2004**, *42*, 4882–4894.
- (216) Mandon, D.; Machkour, A.; Goetz, S.; Welter, R. *Inorg. Chem.* **2002**, *41*, 5364–5372.
- (217) Britovsek, G. J. P.; England, J.; White, A. J. P. *Inorg. Chem.* **2005**, *44*, 8125–8134.
- (218) Benhamou, L.; Lachkar, M.; Mandon, D.; Welter, R. *Dalton Trans.* **2008**, 6996–7003.
- (219) He, D.; Xue, Z.; Khan, M. Y.; Noh, S. K.; Lyoo, W. S. *J. Polym. Sci., Part A: Polym. Chem.* **2010**, *48*, 144–151.
- (220) Zhang, L. F.; Cheng, Z. P.; Zhang, Z. B.; Xu, D. Y.; Zhu, X. L. *Polym. Bull.* **2010**, *64*, 233–244.
- (221) Bedri, B.; Cikilmazkaya, M.; Tunca, U.; Hizal, G. *Des Monomers Polym.* **2003**, *6*, 299–307.
- (222) Dutta, A.; Mahato, P. K.; Dass, N. N. *J. Macromol. Sci. Chem.* **1991**, *A28*, 1001–1008.
- (223) Dutta, A.; Mahato, P. K.; Dass, N. N. *Eur. Polym. J.* **1991**, *27*, 465–469.
- (224) Xue, Z. G.; Linh, N. T. B.; Noh, S. K.; Lyoo, W. S. *Angew. Chem. Int. Ed.* **2008**, *47*, 6426–6429.
- (225) Wada, M.; Higashizaki, S. *J. Chem. Soc., Chem. Commun.* **1984**, 482–483.
- (226) Dunbar, K. R.; Quillevéré, A. *Polyhedron* **1993**, *12*, 807–819.
- (227) Wang, Y.; Kwak, Y.; Buback, J.; Buback, M.; Matyjaszewski, K. *ACS Macro Lett.* **2012**, *1*, 1367–1370.
- (228) Schroeder, H.; Buback, J.; Demeshko, S.; Matyjaszewski, K.; Meyer, F.; Buback, M. *Macromolecules* **2015**, *48*, 1981–1990.
- (229) Buback, M.; Kurz, C. H.; Schmaltz, C. *Macromol. Chem. Phys.* **1998**, *199*, 1721–1727.
- (230) Zammit, M. D.; Davis, T. P.; Willett, G. D.; O'Driscoll, K. F. *J. Polym. Sci. Part A: Polym. Chem.* **1997**, *35*, 2311–2321.

- (231) Olaj, O. F.; Schnöll–Bitai, I. *Monatsh. Chem.* **1999**, *130*, 731–740.
- (232) Schroeder, H.; Buback, M.; Matyjaszewski, K. *Macromol. Chem. Phys.* **2013**, *215*, 44–53.
- (233) Gillies, M. B.; Matyjaszewski, K.; Norrby, P. O.; Pintauer, T.; Poli, R.; Richard, P. *Macromolecules* **2003**, *36*, 8551–8559.
- (234) Tschan, M. J. L.; García–Suárez, E. J.; Freixa, Z.; Launay, H.; Hagen, H.; Benet–Buchholz, J.; van Leeuwen, P. W. N. M. *J. Am. Chem. Soc.* **2010**, *132*, 6463–6473.
- (235) Godfrey, S. M.; McAuliffe, C. A.; Pritchard, R. G.; Sheffield, J. M. *J. Chem. Soc., Dalton Trans.* **1998**, 1919–1923.
- (236) Bleeke, J. R.; Hays, M. K. *Organometallics* **1987**, *6*, 486–491.
- (237) Berclaz, T.; Geoffroy, M.; Ginet, L.; Lucken, E. A. C. *Chem. Phys. Lett.* **1979**, *62*, 515–518.
- (238) Symons, M. C. R.; Petersen, R. L. *J. Chem. Soc., Faraday Trans.* **1979**, *75*, 210–219.
- (239) Pignolet, L. H.; Forster, D.; Horrocks, W. D. *Inorg. Chem.* **1968**, *7*, 828–830.
- (240) Walker, J. D.; Poli, R. *Inorg. Chem.* **1989**, *28*, 1793–1801.
- (241) Schroeder, H.; Lake, B. R. M.; Demeshko, S.; Shaver, M. P.; Buback, M. *Macromolecules* **2015**, *48*, 4329–4338.
- (242) Schroeder, H.; Buback, M. *Macromolecules* **2014**, *47*, 6645–6651.
- (243) Groysman, S.; Goldberg, I.; Kol, M.; Genizi, E.; Goldschmidt, Z. *Organometallics* **2004**, *23*, 1880–1890.
- (244) Andersen, R. A.; Faegri, K.; Green, J. C.; Haaland, A.; Lappert, M. F.; Leung, W. P.; Rypdal, K. *Inorg. Chem.* **1988**, *27*, 1782–1786.
- (245) Gütlich, P.; Bill, E.; Trautwein, A. X. *Mössbauer Spectroscopy and Transition Metal Chemistry*, Springer, Heidelberg, **2011**.
- (246) Dean, R. K.; Fowler, C. I.; Hasan, K.; Kerman, K.; Kwong, P.; Trudel, S.; Leznoff, D. B.; Kraatz, H.–B.; Dawe, L. N.; Kozak, C. M. *Dalton Trans.* **2012**, *41*, 4806–4816.
- (247) Reckling, A. M.; Martin, D.; Dawe, L. N.; Decken, A.; Kozak, C. M. *J. Organomet. Chem.* **2011**, *696*, 787–794.
- (248) Hasan, K.; Fowler, C.; Kwong, P.; Crane, A. K.; Collins, J. L.; Kozak, C. M. *Dalton Transactions* **2008**, 2991–2998.
- (249) Zhong, M. J.; Matyjaszewski, K. *Macromolecules* **2011**, *44*, 2668–2677.
- (250) Kattner, H.; Buback, M. *Macromolecules* **2015**, *48*, 309–315.
- (251) Buback, M.; Gilbert, R. G.; Hutchinson, R. A.; Klumperman, B.; Kuchta, F. D.; Manders, B. G.; O'Driscoll, K. F.; Russell, G. T.; Schweer, J. *Macromol. Chem. Phys.* **1995**, *196*, 3267–3280.



- 
- (252) Beuermann, S.; Buback, M.; Davis, T. P.; Gilbert, R. G.; Hutchinson, R. A.; Olaj, O. F.; Russell, G. T.; Schweer, J.; vanHerk, A. M. *Macromol. Chem. Phys.* **1997**, *198*, 1545–1560.
- (253) Caretti, I.; Dervaux, B.; Du Prez, F. E.; Van Doorslaer, S. J. *Polym. Sci., Part A: Polym. Chem.* **2010**, *48*, 1493–1501.
- (254) Buback, M.; Kuelpmann, A. *Macromol. Chem. Phys.* **2003**, *204*, 632–637.
- (255) Wang, Y.; Soerensen, N.; Zhong, M. J.; Schroeder, H.; Buback, M.; Matyjaszewski, K. *Macromolecules* **2013**, *46*, 683–691.
- (256) Wulkow, M. *Macromol. Theory Simul.* **1996**, *5*, 393–416.
- (257) Hutchinson, R. A.; Beuermann, S.; Paquet, D. A.; McMinn, J. H. *Macromolecules* **1997**, *30*, 3490–3493.
- (258) Lin, C. Y.; Coote, M. L.; Gennaro, A.; Matyjaszewski, K. *J. Am. Chem. Soc.* **2008**, *130*, 12762–12774.
- (259) Isse, A. A.; Gennaro, A.; Lin, C. Y.; Hodgson, J. L.; Coote, M. L.; Guliyshvili, T. *J. Am. Chem. Soc.* **2011**, *133*, 6254–6264.
- (260) Beuermann, S.; Buback, M.; Davis, T. P.; Gilbert, R. G.; Hutchinson, R. A.; Kajiwara, A.; Klumperman, B.; Russell, G. T. *Macromol. Chem. Phys.* **2000**, *201*, 1355–1364.
- (261) Buback, M.; Geers, U.; Kurz, C. H.; Heyne, J. *Macromol. Chem. Phys.* **1997**, *198*, 3451–3464.
- (262) Beuermann, S.; Buback, M. *Prog. Polym. Sci.* **2002**, *27*, 191–254.
- (263) Buback, M. *Macromol. Symp.* **2009**, *275–276*, 90–101.
- (264) Barth, J.; Buback, M.; Hesse, P.; Sergeeva, T. *Macromolecules* **2009**, *42*, 481–488.
- (265) Schröder, K.; Konkolewicz, D.; Poli, R.; Matyjaszewski, K. *Organometallics* **2012**, *31*, 7994–7999.
- (266) Simakova, A.; Mackenzie, M.; Averick, S. E.; Park, S.; Matyjaszewski, K. *Angew. Chem. Int. Ed.* **2013**, *52*, 12148–12151.
- (267) Jauer, S. *PhD Thesis*, Georg-August-University, Göttingen, **2012**.
- (268) Schrooten, J.; Kritzler-Kosch, M. *personal communications* **2012–2014**.
- (269) Wang, Y.; Schroeder, H.; Morick, J.; Buback, M.; Matyjaszewski, K. *Macromol. Rapid Commun.* **2013**, *34*, 604–609.
- (270) Cho, H. Y.; Krys, P.; Szcześniak, K.; Schroeder, H.; Park, S.; Jurga, S.; Buback, M.; Matyjaszewski, K. *Macromolecules* **2015**, *48*, 6385–6395.
- (271) Wulkow, M. *Macromol. React. Eng.* **2008**, *2*, 461–494.
- (272) Wang, Y.; Zhong, M.; Zhang, Y.; Magenau, A. J. D.; Matyjaszewski, K. *Macromolecules* **2012**, *45*, 8929–8932.

- (273) Yu–Su, S. Y.; Sun, F. C.; Sheiko, S. S.; Konkolewicz, D.; Lee, H. I.; Matyjaszewski, K. *Macromolecules* **2011**, *44*, 5928–5936.
- (274) Martin, M.; Guiochon, G. J. *Chromatogr. A* **2005**, *1090*, 16–38.
- (275) Nikam, P. S.; Shirsat, L. N.; Hasan, M. J. *Chem. Eng. Data* **1998**, *43*, 732–737.
- (276) Ahmad, N. M.; Charleux, B.; Farcet, C.; Ferguson, C. J.; Gaynor, S. G.; Hawket, B. S.; Heatley, F.; Klumperman, B.; Konkolewicz, D.; Lovell, P. A.; Matyjaszewski, K.; Venkatesh, R. *Macromol. Rapid Commun.* **2009**, *30*, 2002–2021.
- (277) Reyes, Y.; Asua, J. M. *Macromol. Rapid Commun.* **2011**, *32*, 63–67.
- (278) Konkolewicz, D.; Sosnowski, S.; D'Hooge, D. R.; Szymanski, R.; Reyniers, M. F.; Marin, G. B.; Matyjaszewski, K. *Macromolecules* **2011**, *44*, 8361–8373.
- (279) Konkolewicz, D.; Krys, P.; Matyjaszewski, K. *Acc. Chem. Res.* **2014**, *47*, 3028–3036.
- (280) Ballard, N.; Salsamendi, M.; Santos, J. I.; Ruipérez, F.; Leiza, J. R.; Asua, J. M. *Macromolecules* **2014**, *47*, 964–972.
- (281) Hlalele, L.; Klumperman, B. *Macromolecules* **2011**, *44*, 5554–5557.
- (282) Lide, D. R. *Handbook of Chemistry and Physics*, 87<sup>th</sup> ed., CRC Press, Boca Raton, **2006**.
- (283) Yang, C. S.; Liu, Z. G.; Lai, H. X.; Ma, P. S. *J. Chem. Thermodyn.* **2007**, *39*, 28–38.
- (284) Beuermann, S.; Buback, M.; Hesse, P.; Lacík, I. *Macromolecules* **2006**, *39*, 184–193.
- (285) Beuermann, S.; Buback, M.; Hesse, P.; Kukucková, S.; Lacík, I. *Macromol. Symp.* **2007**, *248*, 23–32.
- (286) Heuts, J. P. A.; Gilbert, R. G.; Radom, L. *Macromolecules* **1995**, *28*, 8771–8781.
- (287) Khuong, K. S.; Jones, W. H.; Pryor, W. A.; Houk, K. N. *J. Am. Chem. Soc.* **2005**, *127*, 1265–1277.
- (288) Smolne, S.; Buback, M. *Macromol. Chem. Phys.* **2015**, *216*, 894–902.
- (289) Ng, Y. H.; di Lena, F.; Chai, C. L. L. *Chem. Commun.* **2011**, *47*, 6464–6466.
- (290) Ng, Y. H.; di Lena, F.; Chai, C. L. L. *Polym. Chem.* **2011**, *2*, 589–594.
- (291) Sigg, S. J.; Seidi, F.; Renggli, K.; Silva, T. B.; Kali, G.; Bruns, N. *Macromol. Rapid Commun.* **2011**, *32*, 1710–1715.
- (292) Tabard, A.; Cocolios, P.; Lagrange, G.; Gerardin, R.; Hubsch, J.; Lecomte, C.; Zarembowitch, J.; Guillard, R. *Inorg. Chem.* **1988**, *27*, 110–117.

- 
- (293) Guillard, R.; Boisseliercocolios, B.; Tabard, A.; Cocolios, P.; Simonet, B.; Kadish, K. M. *Inorg. Chem.* **1985**, *24*, 2509–2520.
- (294) Wittenberg, N. F. G.; Buback, M.; Hutchinson, R. A. *Macromol. React. Eng.* **2013**, *7*, 267–276.
- (295) Schrooten, J.; Lacík, I.; Stach, M.; Hesse, P.; Buback, M. *Macromol. Chem. Phys.* **2013**, *214*, 2283–2294.
- (296) Barth, J.; Meiser, W.; Buback, M. *Macromolecules* **2012**, *45*, 1339–1345.
- (297) Santanakrishnan, S.; Tang, L.; Hutchinson, R. A.; Stach, M.; Lacík, I.; Schrooten, J.; Hesse, P.; Buback, M. *Macromol. React. Eng.* **2010**, *4*, 499–509.
- (298) Chowdhury, R. R.; Crane, A. K.; Fowler, C.; Kwong, P.; Kozak, C. M. *Chem. Commun.* **2008**, 94–96.
- (299) Velusamy, M.; Palaniandavar, M.; Gopalan, R. S.; Kulkarni, G. U. *Inorg. Chem.* **2003**, *42*, 8283–8293.
- (300) Qian, X.; Dawe, L. N.; Kozak, C. M. *Dalton Trans.* **2011**, *40*, 933–943.
- (301) Daub, G. H.; Cannizzo, L. F. *J. Org. Chem.* **1982**, *47*, 5034–5035.
- (302) Bill, E. *Mfit*, Max–Planck Institute for Chemical Energy Conversion, Mülheim/Ruhr, Germany, **2008**.
- (303) Beuermann, S.; Buback, M. *High Pressure Res.* **1997**, *15*, 333–367.
- (304) Schroeder, H.; Buback, J.; Schrooten, J.; Buback, M.; Matyjaszewski, K. *Macromol. Theory Simul.* **2014**, *23*, 279–287.
- (305) Hutchinson, R. A.; Aronson, M. T.; Richards, J. R. *Macromolecules* **1993**, *26*, 6410–6415.
- (306) Oliphant, T. E. *Computing In Science & Engineering* **2007**, *9*, 10–20.
- (307) Hunter, J. D. *Computing In Science & Engineering* **2007**, *9*, 90–95.



## Acknowledgements

Ein paar Worte in eigener Sprache.

Mein besonderer Dank gilt Herrn Prof. Dr. Michael Buback für die interessante und herausfordernde Themenstellung dieser Arbeit. Seine Unterstützung und unsere zahlreichen Diskussionen waren für mich besonders wertvoll. Bei Herrn Prof. Dr. Philipp Vana, MBA möchte ich mich für die Übernahme des Korreferats bedanken.

Außerdem bedanke ich mich bei Herrn Prof. Dr. Karlheinz Hoyerermann, Prof. Dr. Martin Suhm, PD Dr. Thomas Zeuch und Dr. Florian Ehlers für die Teilnahme am Prüfungskomitee.

Ein herzlicher Dank gebührt Prof. Dr. Krzysztof Matyjaszewski für unsere Kooperation während der gesamten Arbeit, die vielen hilfreichen Diskussionen und besonders für die Möglichkeit, meine Forschung durch Aufenthalte in seiner Arbeitsgruppe bereichern zu können. In diesem Zusammenhang möchte ich auch den Mitgliedern der Matyjaszewski-Gruppe für die schöne Zeit und die nette Aufnahme danken, besonders Dr. Yu Wang, Dr. Mingjiang Zhong, Pawel Krysz und Dr. Benjamin Hui.

Für eine weitere Kooperation und die stete Diskussionsbereitschaft bedanke ich mich bei Dr. Michael Shaver. Außerdem möchte ich Dr. Serhiy Demeshko für die Betreuung und das Interesse an meiner Arbeit, sowie für die Unterstützung bei Mössbauer spektroskopischen Messungen bedanken. Ich danke Dr. Johannes Buback für seine Hilfe, vor allem für das Programmieren der Modellierungssoftware.

Natürlich gebührt ein besonderer Dank dem Fonds der Chemischen Industrie für die finanzielle Unterstützung und für die Möglichkeit, am Stipendiatentreffen in Jena teilzunehmen.

Herrn Dr. Hans-Peter Vögele möchte ich ganz besonders für die immer rasche und kompetente Hilfe und den nützlichen Ratschlägen bei IR-technischen Fragen danken. Desweiteren möchte ich mich bei den Mitarbeitern unserer Institutswerkstätten für die Konstruktion und Hilfe bei der Hochdruckanlage bedanken.

Bei Aline Selke und Christoph Dierking bedanke ich mich für die engagierte Arbeit und Unterstützung bei den Experimenten im Rahmen ihrer Forschungsaufenthalte. Ein herzlicher Dank gebührt Sebastian Smolne, Christian Roßner, Patrick Drawe, Michael Gamalinda und Hendrik Kattner für die Hilfe bei der Korrektur dieser Arbeit. Außerdem möchte ich mich ganz herzlich bei allen weiteren Mitarbeitern der Arbeitskreise Buback und Vana für die freundliche Atmosphäre, die Hilfe und Unterstützung, Ratschläge und Motivation, und für die vielen schönen Momente bedanken.

Für ein erfolgreiches Studium sind Freunde und Familie unerlässlich. Meinen Freunden danke ich für eine unvergessene Zeit in Göttingen. Unser enger Zusammenhalt hat mir besonders viel Kraft verliehen. Ein besonderer Dank gebührt meiner Familie, vor allem meinen Eltern, die mich stets von ganzem Herzen unterstützt haben. Ihnen widme ich diese Arbeit.

## About the Author

**Hendrik Schröder**, \* November 29, 1985 in Oldenburg, German citizen

### Curriculum Vitae

- 1998 – 2005** Herbartgymnasium Oldenburg, final grade: *Abitur* (1.3)
- 2002 – 2003** Exchange student, Calvary Christian Academy,  
Albuquerque, NM, USA
- 2005 – 2006** Community Service at the Youth Hostel Esens–Bensersiel
- 2006 – 2009** *Bachelor of Science*, Georg–August–University Göttingen,  
final grade: 1.7, bachelor thesis in cooperation with  
BÜFA Reaktionsharze & Co. KG, Rastede, supervisor:  
Prof. Dr. M. Buback
- 09/2010 – 01/2011** Erasmus student, Kungliga Tekniska högskolan  
(KTH) Stockholm, Sweden
- 2009 – 2011** *Master of Science*, Georg–August–University Göttingen,  
final grade: 1.1 ("*with distinction*"), master thesis: "Atom–  
Transfer Radical Polymerization up to High Pressure",  
supervisor: Prof. Dr. M. Buback
- 2011 – 2015** Doctorate Studies, Georg–August–University Göttingen,  
supervisor: Prof. Dr. M. Buback, final grade: *summa cum  
laude*
- 04/2012 – 06/2012 and 10/2013** Visiting student, Carnegie Mellon University, Pitts–  
burgh, PA, USA, supervisor: Prof. Dr. K. Matyjaszewski

## Publications

- “SP–PLP–EPR Measurement of ATRP Deactivation Rate”  
Soerensen, N.; Barth, J.; Buback, M.; Morick, J.; Schroeder, H.; Matyjaszewski, K. *Macromolecules* **2012**, *45*, 3797–3801.
- “Activation–Deactivation Equilibrium Associated With Iron–Mediated Atom–Transfer Radical Polymerization up to High Pressure”  
Schroeder, H.; Yalalov, D.; Buback, M.; Matyjaszewski, K. *Macromol. Chem. Phys.* **2012**, *213*, 2019–2026.
- “Improving the 'Livingness' of ATRP by Reducing Cu Catalyst Concentration”  
Wang, Y.; Soerensen, N.; Zhong, M.; Schroeder, H.; Buback, M.; Matyjaszewski, K. *Macromolecules* **2013**, *46*, 683–691.
- “High–Pressure Atom Transfer Radical Polymerization of *n*–Butyl Acrylate”  
Wang, Y.; Schroeder, H.; Morick, J.; Buback, M.; Matyjaszewski, K. *Macromol. Rapid Commun.* **2013**, *34*, 604–609.
- “Pressure Dependence of Iron–Mediated Methyl Methacrylate ATRP in Different Solvent Environments”  
Schroeder, H.; Buback, M.; Matyjaszewski, K. *Macromol. Chem. Phys.* **2014**, *215*, 44–53.
- “Modeling Atom–Transfer Radical Polymerization of Butyl Acrylate”  
Schroeder, H.; Buback, J.; Schrooten, J.; Buback, M.; Matyjaszewski, K. *Macromol. Theory Simul.* **2014**, *23*, 279–287.
- “SP–PLP–EPR Measurement of Iron–Mediated Radical Termination in ATRP”  
Schroeder, H.; Buback, M. *Macromolecules* **2014**, *47*, 6645–6651.
- “Speciation Analysis in Iron–Mediated ATRP Studied via FT–Near–IR and Mössbauer Spectroscopy”  
Schroeder, H.; Buback, J.; Demeshko, S.; Matyjaszewski, K.; Meyer, F.; Buback, M. *Macromolecules* **2015**, *48*, 1981–1990.



- “Kinetics of Fe–Mediated ATRP with Triarylphosphines”  
Schroeder, H.; Matyjaszewski, K.; Buback, M. *Macromolecules* **2015**, *48*, 4431–4437.
- “A Synthetic and Multispectroscopic Speciation Analysis of Controlled Radical Polymerization Mediated by Amine–Bis(phenolate)iron Complexes”  
Schroeder, H.; Lake, B. R. M.; Demeshko, S.; Shaver, M. P.; Buback, M. *Macromolecules* **2015**, *48*, 4329–4338.
- “SP–PLP–EPR Measurement of Iron–Mediated ATRP Deactivation Rate”  
Schroeder, H.; Buback, M. *Macromolecules* **2015**, *48*, 6108–6113.
- “Kinetics of Amine–Bis(phenolate) Iron–Mediated ATRP up to High Pressure”  
Schroeder, H.; Buback, M.; Shaver, M. P. *Macromolecules* **2015**, *48*, 6114–6120.
- “Synthesis of Poly(OEOMA) using Macromonomers via 'Grafting–through' ATRP”  
Cho, H. Y.; Krys, P.; Szcześniak, K.; Schroeder, H.; Park, S.; Jurga, S.; Buback, M.; Matyjaszewski, K. *Macromolecules* **2015**, *48*, 6385–6395.

## Conference Presentations

- “Rate Coefficients for Atom–Transfer Radical Polymerization (ATRP) up to High Pressure”  
*Oral Presentation*, 44<sup>th</sup> IUPAC World Polymer Congress, “Macro2012”, Blacksburg, VA, USA, **June 2012**.
- “Rate Coefficients for ATRP up to High Pressure”  
*Oral & Poster Presentation*, JungChemikerForum, Göttingen, **July 2012**.
- “Unexpected Pressure Dependence for Iron–Mediated Atom–Transfer Radical Polymerization (ATRP)”  
*Poster*, Niedersächsisches Katalyse Symposium “NiKaS”, Göttingen, **October 2012**.

- “Modeling of Atom–Transfer Radical Polymerization of Butyl Acrylate Using a Novel Tool for Multiple–Parameter Variation”  
*Oral Presentation*, Annual Meeting of the American Institute of Chemical Engineers (AIChE), San Francisco, CA, USA, **November 2013**.
- “Kinetics of Butyl Acrylate ATRP up to High Pressure”  
*Oral Presentation*, 3<sup>rd</sup> Controlled / Living Polymerization Symposium “CLP’14”, Antalya, Turkey, **Mai 2014**.
- “Fe–Mediated Radical Polymerization Studied via EPR”  
*Poster*, Niedersächsisches Katalyse Symposium “NiKaS”, Göttingen, **August 2014**.

## Awards

- 2012** Bunsen Book Award for the master thesis "Atom–Transfer Radical Polymerization up to High Pressure"
- 2012** Oral Presentation Award, JungChemikerForum, Göttingen, for the presentation “Rate Coefficients for ATRP up to High Pressure”
- 2012 – 2014** Chemiefonds Scholarship granted by the *Fonds der Chemischen Industrie*